Experimental Investigation on the Flow Characteristics of Three-Dimensional Turbulent Offset Jets

by

Baafour Nyantekyi-Kwakye

A Thesis submitted to the Faculty of Graduate Studies of

The University of Manitoba

in partial fulfillment of the requirements of the degree of

DOCTOR OF PHILOSOPHY

Department of Mechanical Engineering

University of Manitoba

Winnipeg

ABSTRACT

An experimental study was designed to investigate the effect of different parameters on the development and structure of turbulent 3D offset jets. The present investigation considered the effects of offset height ratio, expansion ratio, surface roughness and rib placement on the flow dynamics of a turbulent 3D offset jet. The velocity measurements were performed using an acoustic Doppler velocimetry (ADV) and particle image velocimetry (PIV). Measurements were conducted within the symmetry and lateral planes. For the PIV technique, the measurements in the symmetry and lateral planes were conducted over a streamwise range of $0 \leq x/b_o \leq 80$ and $12 \leq x/b_o \leq 60$, respectively (where b_o is the nozzle height). Likewise, velocity measurements using the ADV technique were conducted over a range of $4 \leq x/b_o \leq 45$ in both the symmetry and lateral planes. The velocity measurements were analyzed using both one-point and multi-point statistics. The one-point statistics included profiles of the mean velocities, Reynolds stresses and some of the budget terms in the turbulent kinetic energy transport equation. The quadrant analysis technique was used to investigate the dominant events that contribute towards the Reynolds shear stress. The two-point correlation analysis was used to investigate how the turbulence quantities are correlated. Information obtained from the two-point correlation analysis was also used to investigate the inclination of vortical structures within the inner and outer shear layers of the 3D offset jet. The direction of the positive mean shear gradient played an active role in the inclination of these vortical structures within the inner and outer shear layers. The reattachment process resulted in the breakdown of these structures within the developing region. Similarly, various length scales were estimated from these structures. The proper orthogonal decomposition was used to examine the distribution of the turbulent kinetic energy within the offset jet flow. Also, the dynamic role of the large scale structures towards the turbulent intensities, turbulent kinetic energy and Reynolds shear stress was investigated.

ACKNOWLEDGEMENTS

I would first of all like to thank the almighty God for granting me the opportunity to study in this challenging research area. I would also like to express my sincere gratitude to my supervisors, Professor Mark F. Tachie and Dr. Shawn P. Clark for their continual support, guidance, patience, encouragement and constructive criticism to ensure a distinctive quality work.

I would like to express my gratitude to my examining committee members, Professor David S. Kuhn, Dr. Tricia Stadnyk and Professor Kamran Siddiqui for their excellent suggestion and comments on my research. I would also like to acknowledge the efforts of Dr. Jarrod Malenchak and Dr. Getnet Y. Muluye.

I am grateful for the financial support of the Natural Sciences and Engineering Research Council of Canada, Manitoba Hydro and the University of Manitoba.

I appreciate the prayers and support of my siblings Nana Agyei and Akwasi Asubonteng as well as my parents, Mr. Kofi Nyantekyi-Kwakye and Mrs. Paulina A. Nyantekyi. I am most grateful to my wife Afua Kesewa for her love, care, understanding and continual support. I am also grateful to my pastors, Dr. Deborah Olukoju and Dr. Akin S. Olukoju for their prayers and encouragement. I cannot overlook the support, cooperation and advice of Kwadwo Poku, P.Eng., Ebenezer E. Essel, Afua Adobea Mante, Zacharie Durand and all my colleagues as well as friends. The technical and friendly support of Paul Krueger and Alexander Wall are greatly appreciated.

DEDICATION

I would like to dedicate this thesis to my wife, Afua Kesewa, and my parents Mr. and Mrs. Nyantekyi-Kwakye for their love and patience.

List of Tables

List of Figures

Nomenclature

b_o = nozzle height (mm)

b = nozzle width (mm)

d = nozzle exit diameter (mm)

F = Froude number (-)

g = acceleration due to gravity (ms^{-2})

h = offset height (mm)

k = roughness height (mm)

L_e = reattachment length (mm)

Lx_{uu} = streamwise extent of R_{uu} (mm)

Lx_{vv} = streamwise extent of R_{vv} (mm)

Ly_{uu} = wall-normal extent of R_{uu} (mm)

Ly_{vv} = wall-normal extent of R_{vv} (mm)

p = pitch of 2D roughness (mm)

Re = Reynolds number (-)

R_{uu} = streamwise correlation function (-)

R_{vv} = wall-normal correlation function (-)

TKE = turbulent kinetic energy (m^2s^{-2})

U = streamwise mean velocity (ms^{-1})

U_o = bulk velocity (ms^{-1})

U_m = local streamwise maximum mean velocity (ms^{-1})

U_j = jet exit velocity (ms^{-1})

u = streamwise fluctuating velocity (ms^{-1})

u' = streamwise turbulence intensity (ms^{-1})

$\overline{u^2}$, $\overline{v^2}$, $\overline{w^2}$ = Reynolds normal stresses (m^2s^{-2})

$\overline{uv}$, $\overline{uw}$, $\overline{vw}$ = Reynolds shear stress (m^2s^{-2})

V = wall-normal mean velocity (ms^{-1})

v = wall-normal fluctuating velocity (ms^{-1})

v' = wall-normal turbulence intensity (ms^{-1})

W = lateral mean velocity (ms^{-1})

w = lateral fluctuating velocity (ms^{-1})

w' = lateral turbulence intensity (ms^{-1})

x_r = streamwise reference point for two-point correlation analysis (mm)

y_m = wall-normal location of U_m (mm)

y_r = wall-normal reference point for two-point correlation analysis (mm)

$y_{0.5}$ = wall-normal half width (mm)

y_t = tailwater depth (mm)

$z_{0.5}$ = lateral half width (mm)

Δx = streamwise spatial distance (mm)

Δy = wall-normal spatial distance (mm)

ν = kinematic viscosity (m^2s^{-1})

Declaration of academic achievement

The current thesis outline is the sandwich format which follows the guidelines stipulated by the Faculty of Graduate Studies, University of Manitoba. It is a collection of five individual articles prepared for publication in highly rated peer-reviewed journals. Chapters 1 and 2 provide a general introduction which highlights the problem statement and a thorough literature review on turbulent jets, respectively. Chapters 4 to 8 are manuscripts which discuss the contributions from my research. Some peer-reviewed articles were presented at international conferences and one is included in the thesis in Appendix B.

Baafour Nyantekyi-Kwakye contributed immensely to the preparation of all the papers. Specifically, I designed the test conditions for all the experiments; collected, processed and analyzed the data; prepared and submitted all the manuscripts; as well as responded to reviewers' comments. My co-authors contributed in developing the research idea, analyzing the data and preparing the manuscript for publication.

Copyright notices

- **Baafour Nyantekyi-Kwakye**, Mark F. Tachie, Shawn P. Clark, Jarrod Malenchak & Getnet Y. Muluye (2015) Experimental study of the flow structures of 3D turbulent offset jets, Journal of Hydraulic Research, 53:6, 773-786,

This is the authors accepted manuscript of an article published as the version of record in Journal of Hydraulic Research 06 Oct 2015

www.tandfonline.com/ www.tandfonline.com/doi/full/10.1080/00221686.2015.1076532

- **Baafour Nyantekyi-Kwakye**, Shawn P. Clark, Mark F. Tachie, Jarrod Malenchak & Getnet Muluye (2015) Flow characteristics within the recirculation region of three-dimensional turbulent offset jet, Journal of Hydraulic Research, 53:2, 230-242

This is the authors accepted manuscript of an article published as the version of record in Journal of Hydraulic Research 13 Oct 2014

www.tandfonline.com/ www.tandfonline.com/doi/full/10.1080/00221686.2014.950612

- **Baafour Nyantekyi-Kwakye**, Mark F. Tachie & Shawn P. Clark (2016) Flow characteristics of an offset jet over a surface mounted square rib, Journal of Turbulence, 17:8, 727-757

This is the authors accepted manuscript of an article published as the version of record in Journal of Turbulence 25 Mar 2016

http://www.tandfonline.com/doi/full/10.1080/14685248.2016.1174779

- **Baafour Nyantekyi-Kwakye**, Mark F. Tachie, Shawn P. Clark, Jarrod Malenchak & Getnet Y. Muluye (2016) Acoustic Doppler velocimeter measurements of a submerged three-dimensional offset jet flow over rough surfaces, Journal of Hydraulic Research,

This is the authors accepted manuscript for publication in the Journal of Hydraulic Research 14 Apr 2016

DOI:10.1080/00221686.2016.1212413

CHAPTER ONE

1 INTRODUCTION

1.1 Overview

A turbulent jet is generated when a high momentum fluid is discharged from a source into an ambient fluid. Turbulent jets can be either two-dimensional (2D) or three-dimensional (3D) in nature. Two-dimensional jets (hereafter referred to as plane jets) are formed when the discharged jet has an infinite width whereas 3D jets are formed from nozzles of finite width. One of the major differences between plane and 3D jets is the lateral spreading of the latter. Thus, the flow statistics of plane jets are statistically independent of lateral distance. Turbulent jets can be grouped into one of the following broad categories: free, wall, surface and offset jets. A free jet is formed when a discharged jet is sufficiently far from a boundary that would restrict its development. A schematic diagram of a free jet is shown in Figure 1.1a where the different flow regions are indicated. Figure 1.1a shows that the flow field of turbulent free jets can be divided into the potential core region, where the maximum mean velocity remains nearly constant as the jet exit velocity, transition region, which is characterized by intense mixing of the jet and leads to a decrease in the maximum mean velocity with streamwise distance and the fully developed region where the maximum velocity is inversely proportional to streamwise distance. The transitional and fully developed regions are characterized by large-scale vortices which facilitate momentum transport.

A wall jet is established when a discharged jet is confined on one side by a solid boundary as illustrated in Figure 1.1b. Since the flow is constantly attached to the solid boundary, the following two distinct shear layers develop: an inner shear layer and an outer shear layer. These

two shear layers have different turbulent characteristics with the outer shear layer dominated by large-scale structures which control mixing and entrainment of the ambient fluid. For a surface jet, the discharged jet is restricted on only one side by the free surface of the ambient fluid. An offset jet is formed when a jet is discharged into a medium at a certain distance from the boundary, which may either be a solid wall or a free surface. The proximity of the jet to the boundary permits the influence of the boundary on the discharged offset jet. The offset jet possesses characteristic features of both free jet (close to the nozzle exit) and wall jet (after reattachment of the discharged jet to the bottom of the channel). This makes the turbulence characteristics of an offset jet relatively more complex than observed in the limiting cases (i.e., free and wall jets).

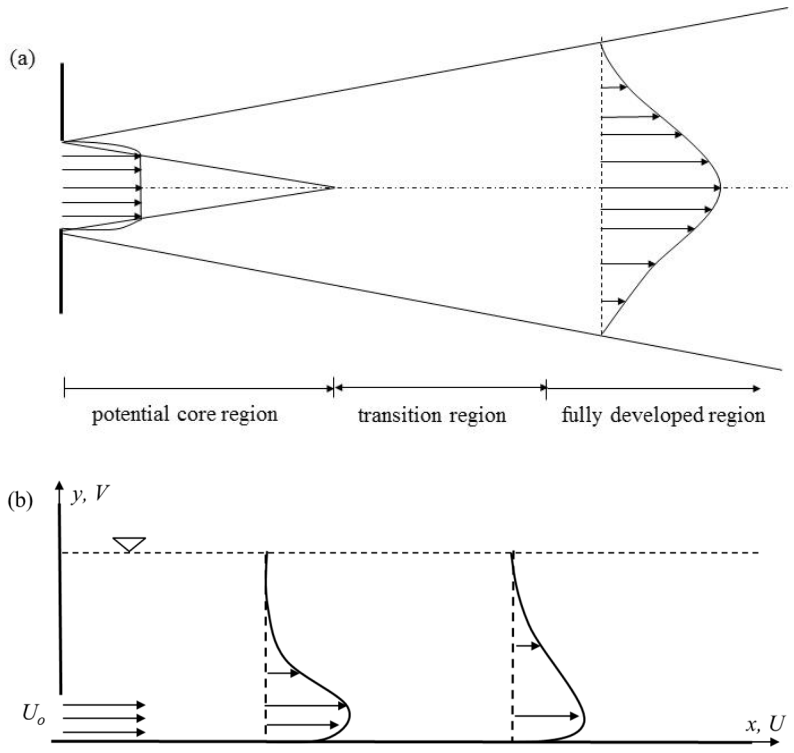

Figure 1.1 Schematic diagram of a discharged turbulent free jet (a) and wall jet (b)

Turbulent offset and wall jet flows are encountered in diverse industrial applications. Some of these applications include the techniques employed in cooling the combustion chamber of gas

turbines, heat transfer augmentation, air deflectors, automobile demisters, entrainment and mixing processes in boilers and combustion chamber of gas turbines, fuel injection systems, heating, ventilation and air conditioning systems and thrust augmenting ejectors for aircraft and the discharge of air for environmental control. Other applications in the field of water systems management include pollutant discharge, energy dissipation downstream of hydraulic structures (such as drop-structures, barrages, spillways, weirs and hydroelectric generation stations) and disposal of communal and industrial waste. Based on these applications, both offset and wall jets have attracted considerable research attention.

1.2 Description of the flow field of an offset jet

Figure 1.2 shows a typical flow field of a 3D offset jet. The streamwise, wall-normal and lateral directions are represented by x, y and z axis, respectively. The exit of the jet is at $x = 0$, the bottom of the channel is at $y = 0$, and $z = 0$ is located on the symmetry plane. The streamwise, wall-normal and lateral components of the mean velocities are denoted by U, V and W and their corresponding fluctuating components represented by u, v and w, respectively. The mean reattachment length of the offset jet (defined as the streamwise distance from the nozzle exit to the point where the jet reattaches to the bottom of the channel) is denoted by L_e. The notations U_o, b_o and h denote the bulk velocity at the jet exit, nozzle height and offset distance, respectively. The submerged offset jet entrains ambient fluid, resulting in the creation of a low pressure region between the jet and the bottom of the channel. This causes the jet to deflect towards the wall and subsequently reattach to the bottom of the channel. The velocity of the deflected jet reduces as it approaches the wall causing a pressure rise within the jet. The pressure increases inside the jet until it reaches a maximum at the reattachment point. Turbulent wall jet conditions are established beyond the reattachment point. It can be seen from Figure 1.2a that the offset jet has three distinct

flow regions: the recirculation region, developing region and the self-similar region. The recirculation region is comprised of backward deflection of the jet which results in the formation of reverse eddies and stretches from the jet exit (x/b_o = 0) to the reattachment point. The recirculation region is generally characterized by low velocities and high

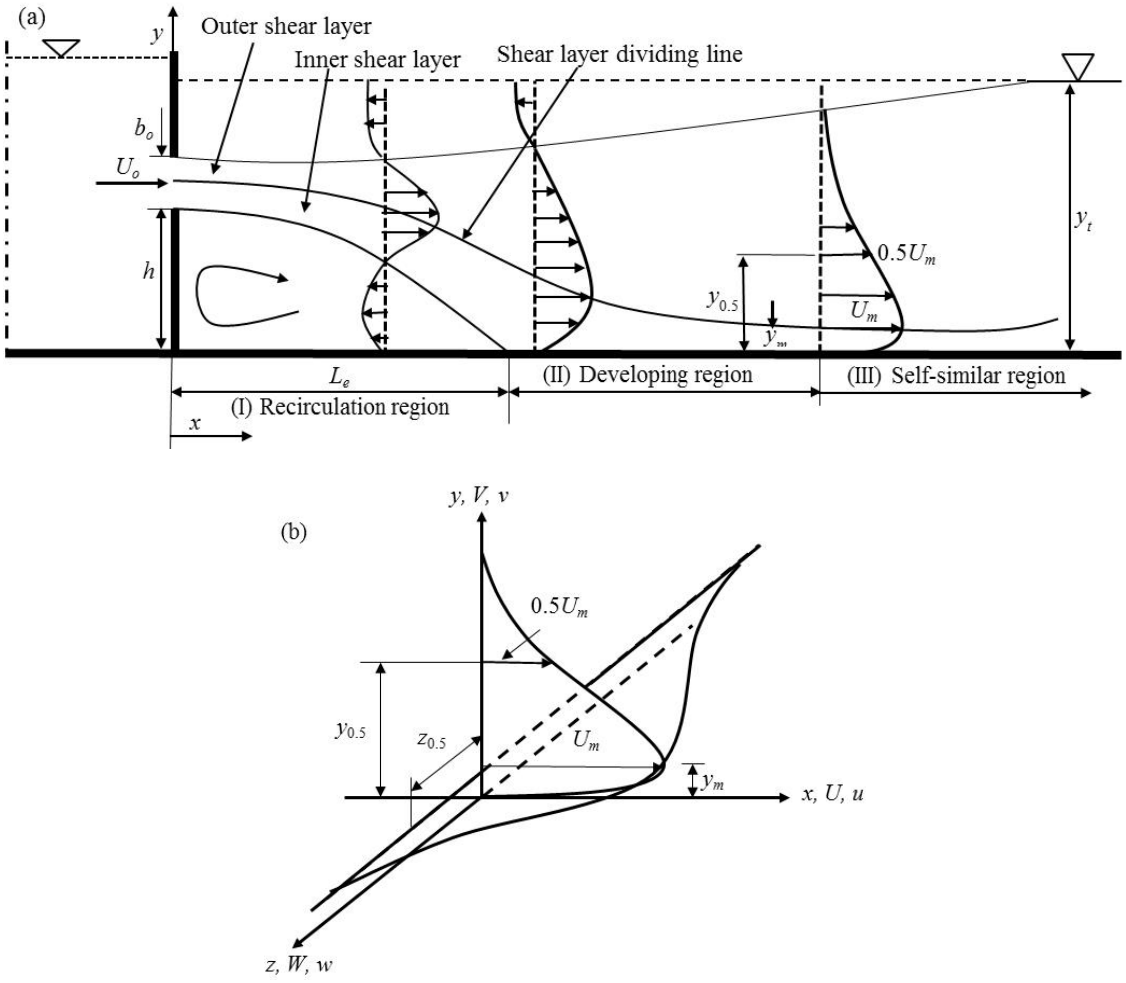

Figure 1.2 Schematic diagram of discharged turbulent offset jet into tailwater (a) and velocity characteristics of 3D turbulent jet (b)

local turbulence levels. The developing region extends from the reattachment point until the point where the flow properties of the jet become self-similar. The self-similar region is defined as the

flow region where the flow characteristics do not vary with streamwise distance when an appropriate scaling is applied. A schematic of the mean velocity profiles in the symmetry (x-y) and lateral (x-z) planes for a 3D wall jet are depicted in Fig. 1.2b. The symbols U_m, y_m, $y_{0.5}$ and $z_{0.5}$ correspond to the local maximum streamwise mean velocity, wall-normal location of U_m, wall-normal half-width and lateral half-width, respectively. The two half widths, $y_{0.5}$ and $z_{0.5}$, are defined as the wall-normal and lateral locations where $U = 0.5U_m$, respectively, and give a measure of the jet spread in the wall-normal and lateral directions of the flow. Similar to wall jets, the reattached offset jet also has two shear layers. The inner layer (which extends from the bottom of the channel to y_m) exhibits flow characteristics similar to a turbulent boundary layer, while the outer shear layer (which spans from y_m to the edge of the jet) has flow characteristics that resemble those of a free jet. One of the characteristic features of 3D jets is the larger lateral spreading compared to the wall-normal spreading. Due to their unique features, turbulent 3D jets are used as prototypical flows for investigating the physics of near wall and free shear turbulent flows. Moreover, the complex flow field of offset jets makes them suitable test cases for assessing the performance of different turbulence models (Kumar, 2015; Pramanik & Das, 2013; Rathore & Das, 2013; Nasr & Lai, 1998).

The discharge of effluents (which can be considered as a jet) in shallow waters is of significance in environmental fluid mechanics. This is because the mixing processes involved are influenced by the shallowness of the receiving water body. The mixing processes are complicated since the river bed influence the development of the flow. The presence of the bed produces significant difference in the wall-normal and lateral development of the discharged effluent. Due to the presence of the bed, there would be a reduction in entrainment of ambient fluid into the jet as a result of restricted volume of water below the jet. Based on this behavior, a considerable

number of studies have been conducted to elucidate the flow field of turbulent offset jets. Most of these studies focused on the evolution of plane offset jets leaving very little information on the turbulence structure of 3D offset jets, although the majority of these engineering applications behave in a 3D manner. For instance, the physical structures in 3D offset jet flow and their dynamics have been a challenge to investigate using single point measurement techniques due to the difficulties associated with obtaining multi-point measurements with high spatial resolution throughout the flow domain. In most instances, flow visualization techniques have been employed to give qualitative information about the flow. There is, therefore, the need to conduct refined experimental study to improve our fundamental understanding of this flow phenomenon using multi-point measurement technique.

1.3 Initial and boundary condition definitions

Previous experimental studies on turbulent jets have shown that the flow field is controlled by initial and boundary conditions. These initial and boundary conditions include the jet exit Reynolds number and the nozzle design parameters. The definition of Reynolds number is given below, with ν being the kinematic viscosity.

$$\mathrm{Re} = \frac{b_o U_o}{\upsilon} \tag{1.1}$$

It is to be noted that jets discharging from smoothly contoured nozzles have a top hat profile and as such the bulk velocity, U_o, is approximately equal to the jet exit velocity, U_j. In this regard, the Reynolds number can be defined as $\mathrm{Re} = b_o U_j/\nu$. The Reynolds number definition provided in Eqn. (1.1) is used in the present investigation.

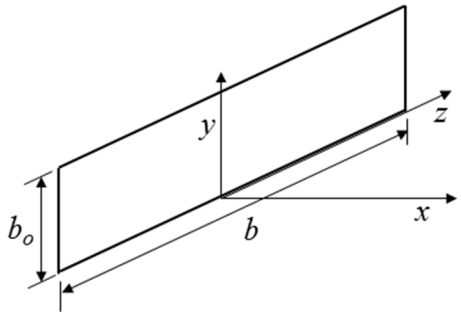

Figure 1.3 Schematic of a rectangular nozzle

The nozzle aspect ratio, *AR*, is defined as the ratio of the nozzle width, *b* (which is in line with the major axis, *z*) to nozzle height, b_o (in line with the minor axis, *y*) as indicated in Fig. 1.3. Thus $AR = b/b_o$ and this ratio has to be sufficiently large to maintain two-dimensionality of the jet. For 2D flows, the flow statistics are independent of the lateral coordinate, *z*. Pope (2000) suggested that for a plane jet, the nozzle *AR* should typically be greater than or equal to 50. It should be noted that the introduction of sidewalls on the edges of the discharge nozzle (placed in the $x - y$ plane) can force the jet to behave in a statistically 2D manner. That is, the sidewalls prevent interaction of the jet with its ambient in the lateral direction. Though the introduction of sidewalls imposes two-dimensionality, it also introduces a complex boundary condition on plane jets. Thus a boundary layer develops between the discharged jet and sidewalls.

The type of nozzle geometry used to generate the jet is of considerable importance since it influences the flow development. In order to understand the flow properties of turbulent jets, many investigations have been conducted for jets issuing from different nozzle geometries for free and surface jets (Quinn, 2006; Lee & Baek, 1994; Madnia & Bernal, 1994; Tsuchiya *et al*., 1986), wall jets (Agelinchaab & Tachie, 2011a; Abrahamsson *et al*., 1997; Irwin, 1973) and offset jets (Nyantekyi-Kwakye *et al.*, 2015a, b; Agelinchaab & Tachie, 2011b; Bhuiyan *et al*., 2011; Nozaki, 1983). Results from Madnia & Bernal (1994) have provided insight into the evolution and

interaction of the large-scale structures that play an active role in the mixing and entrainment processes of turbulent surface jets. The evolution and interaction of these structures create a complex 3D flow field. From these and many other studies, the nozzle geometry (e.g., round, elliptic, square or rectangular) has been observed to modify the flow dynamics of turbulent jets to some extent. For instance, the centerline mean velocity, U_c, of a jet issuing from a round jet varies as $U_c \sim x^{-1}$ whereas for a plane rectangular jet, the far field centerline velocity varies as $U_c \sim x^{-0.5}$ (Pope, 2000). This, therefore, shows that the nozzle geometry plays an important role in the mixing characteristics and determining the salient flow features of turbulent jets. The nozzle profile can be either sharp-edged, smooth/radial contour contraction or a long pipe flow. The flow through a smooth contraction nozzle produces a top hat exit velocity profile (Xu & Antonia, 2002) whiles a saddle-back exit velocity profile is generated for discharges through sharp-edged orifice nozzles (Quinn, 1992).

1.3.1 Equations of motion

The dynamics of turbulent flows is adequately described by the continuity and Navier-Stokes equations. For an incompressible flow, the continuity and Reynolds-averaged Navier-Stokes (RANS) equations in tensor notation are respectively given by:

$$\frac{\partial U_i}{\partial x_i} = 0 \tag{1.2}$$

$$\frac{\partial U_i}{\partial t} + U_j \frac{\partial U_i}{\partial x_j} = -\frac{1}{\rho}\frac{\partial P}{\partial x_i} + \frac{\partial}{\partial x_j}\left(\upsilon \frac{\partial U_i}{\partial x_j} - \overline{u_i u_j}\right) \tag{1.3}$$

The thermodynamic pressure is denoted by P, ρ is the fluid density and $\overline{u_i u_j}$ denotes the Reynolds stresses. The RANS equation contains the relevant physics of turbulent flows and as such understanding the various terms of the Eqn. (1.3) is very essential.

1.4 Research objectives

The flow characteristics (mean and turbulence fields) of an offset jet are affected by conditions at the upstream and downstream sections of the channel as has been outlined. The dimensions of the channel and discharge nozzle are vital to the downstream development of the flow as well. Subsequently, the elevation of the discharge nozzle from the bottom of the channel (h) also determines the extent of the recirculation region. For an open channel flow, the effect of gravitational force on the flow characteristics should also be taken into account. The channel bottom condition (smooth or rough) also may affect both the mean and fluctuating velocity fields of the flow. Thus, there should be a comprehensive set of quality benchmark data for validating results obtained from turbulence models. Therefore, the goal of the present study is to conduct detailed experimental studies on turbulent 3D offset jets. In the experimental studies, the effect of offset height ratio (h/b_o), rib placement, surface roughness (k), and nozzle expansion ratio (b/B, where b and B represent the nozzle and channel width, respectively) on the distribution of the mean and turbulence characteristics of a turbulent 3D offset jet were investigated. Detailed velocity measurements were conducted using a four receiver acoustic Doppler velocimeter and planar particle image velocimetry from which flow characteristics such as mean velocities, length of the recirculation region, shear layer growth and turbulence statistics were obtained.

1.5 Thesis format

The present experimental investigation on 3D offset jet is structured in a paper based format. The thesis begins with a thorough review of previous literature on turbulent jets provided in Chapter 2. This chapter is subdivided into two main sections. The first section reviews turbulent free jets followed by wall jets and subsequently offset jets. Both the near and far-field mean and turbulent characteristics are reviewed. The second section provides a review on selected techniques

used for identifying large-scale coherent structures that dominate turbulent flows. Specifically, attention is given to the quadrant analysis, two-point correlation and proper orthogonal decomposition. An overview of the experimental setup and measurement procedure is presented in Chapter 3. Chapters 4 to 8 are made up of a collection of journal articles obtained from the present work. The different articles are structured to investigate the parameters outlined in the objectives. Finally, conclusions and recommendations for future work are presented in Chapter 9.

CHAPTER TWO

2 LITERATURE REVIEW

2.1 Outline

Many flows found in nature and engineering applications are turbulent, and as a result considerable research efforts have been conducted in the past decades to thoroughly understand turbulence and its impact on mass, heat and momentum transport. In our quest to gain insight into the physics of turbulent flows, a lot of research has been conducted to examine the mean flow and fluctuating velocity fields. Recent discovery of large-scale coherent structures and rapid advancement in computing resources have had significant impact on turbulence research. The main motivation behind many of these studies is that these large-scale coherent structures dominate turbulent transport phenomena in fluid flows of technological and engineering interests (e.g., mixing and entrainment, heat transfer, turbulence production, aerodynamic noise and drag). This chapter provides an overview of previous investigations on turbulent free, wall and offset jets. The flow development and turbulence statistics are first presented for turbulent free jets. Then the flow characteristics (both mean and turbulence statistics) of a wall jet are reviewed. This is followed by a review of turbulent offset jets where the discussion will focus on the mean velocity distributions within the recirculation, developing and self-similar regions. Subsequently a review of the turbulence statistics of offset jets will be presented. Also, a brief review of multi-point statistics used for analyzing turbulence structures will be presented at the end of this chapter.

2.2 Turbulent free jets

Early studies concentrated on the flow characteristics of free jets (Quinn, 2006; Quinn & Militzer, 1988; Hussain & Clark, 1977; Wygnanski & Fiedler, 1969), primarily due to their

relatively simple flow configuration. The discharged jet entrains the surrounding ambient fluid thereby increasing the mass flux with streamwise distance. The shear layer of the jet is characterized by coherent structures of various sizes. These structures are responsible for the energy exchange between the mean flow and turbulence field.

2.2.1 Flow development of free jets

As indicated in the previous section, the flow field of turbulent free jet can be divided into three regions, namely, potential core, transition and the fully developed/self-similar regions. The potential core region exists predominantly for jets issuing from smooth contraction nozzles. The streamwise extent of the potential core region usually depends on initial conditions and has been observed to occur within a streamwise range of $0 \leq x/d \leq 7$ (where d is the nozzle exit diameter). Recent studies by Fellouah *et al*. (2009) observed that, for a turbulent free jet issuing from a smooth contraction nozzle, the potential core region persisted to about x/d = 5 to 6. The development of free jets through the different flow regions exhibits some level of dependence on initial conditions. A summary of relevant literature on turbulent free jets is provided in Table 2.1 (for round/circular jets) and Table 2.2 (for non-circular jets). The jet exit Reynolds number is denoted as Re, x/d is the normalized streamwise extent considered. The wall-normal and lateral spread rates are denoted as $dy_{0.5}/dx$ and $dz_{0.5}/dx$, respectively, and the decay rate constant and normalized kinematic virtual origin are represented as K and x_o/d, respectively. As shown in Tables 2.1 and 2.2, experiments on turbulent free jets have been conducted over a wide range of Reynolds numbers ($2.4\times10^3 \leq \mathrm{Re} \leq 208\times10^3$) and measurements taken over a large streamwise range ($0 \leq x/d \leq 150$).

Table 2.1 Relevant literature on turbulent round free jets

Author	**Technique**	$Re \times 10^3$	x/d	B	x_o/d	$dy_{0.5}/dx$
Xu & Antonia (2002)	HWA	86	1-75	0.154-0.179	2.6-3.7	0.086-0.095
Todde *et al*. (2009)	HWA	0.85-6.8	0-40	0.201-0.247	1.4-6.1	---
Mi *et al*. (2013)	HWA	4-20	0-30	0.159	---	0.085
Fellouah *et al*. (2009)	HWA	6-30	0-25	0.179	2.5	---
Hussein *et al*. (1994)	LDA, HWA	100	0-100	0.169	2.7	---
Bogey & Bailly (2009)	LES	11	0-150	0.156	---	0.087
Wygnanski & Fiedler (1969)	HWA	100	0-100	---	7	---
Boersma *et al*. (1998)	DNS	2.4	0-40	0.169	4.9	---

DNS–direct numerical simulation; *HWA*–hot-wire anemometry; *LDA*–laser Doppler anemometry; *LES*–large eddy simulation

The streamwise mean velocity distribution of a free jet have been observed to attain self-similarity beyond a certain streamwise distance. Early studies by Wygnanski & Fiedler (1969) showed that there was no variation in the distribution of the mean velocity beyond $x/d \geq 20$. Other studies have also reported self-similarity of free jets; for instance, Hussein *et al*. (1994) observed that the streamwise mean velocity became self-similar beyond $x/d \geq 30$. More recently, large eddy simulation by Bogey & Bailly (2009) reported that the mean velocity became self-similar beyond $x/d \geq 50$. Bogey & Bailly (2009) attributed the differences between their results and those reported by other researchers to the variations in the jets initial conditions; an observation which supported the conclusion made by Boersma *et al*. (1998) for a direct numerical simulation of a round jet. Xu & Antonia (2002) compared the flow characteristics of

Table 2.2 Relevant literature on turbulent free jets issuing from non-circular nozzles

Author	***Technique***	***Nozzle type***	***AR***	***Re_d × 10^3***	***B***	***$dy_{0.5}/dx$***	***$dz_{0.5}/dx$***
Faghani *et al*. (2009)	*k-ε* model	REC	1-4	0.8-25.6	---	---	---
Lee & Baek (1994)	3D LDV	ELP	1-8	40	---	---	---
Quinn (1992)	HWA	REC	2-20	208	0.199-0.240	0.074	0.119
Quinn (1989)	HWA	ELP	5	208	0.202	0.078	0.127
Sfeir (1976)	HWA	REC	10-30	122.2	0.156	0.113-0.125	0.145-0.150
Hashiehbaf & Romano (2013)	PIV	SQ, REC, ELP, TRI	1-3	8-35	0.17-0.26	---	---

ELP–elliptic; *PIV*–particle image velocimetry; *REC*–rectangular; Re_d–Reynolds number based on nozzle equivalent diameter; *SQ*–square; *TRI*–triangular

turbulent free jets issuing from a smooth contraction nozzle to that of a long pipe. The smooth contraction nozzle produced a top-hat velocity distribution at the nozzle exit whereas the long pipe produced a fully developed pipe flow velocity profile at the exit. These differences affected the streamwise extent at which the flow became self-similar. More specifically, the free jet generated from the smooth contraction nozzle reached self-similarity sooner (x/d = 20) than the jet produced from the pipe flow (x/d = 40). The difference between the smooth contraction and long pipe jets were associated with the thick initial shear layer and higher turbulence intensity level observed in the latter configuration.

2.2.1.1 Decay rate

As a result of entrainment of ambient fluid, the mean centerline velocity, U_c, of the free jet varies as a function of streamwise distance from the nozzle exit. For a self-preserving turbulent jet, the variation of U_c with streamwise distance is given by

$$\frac{U_j}{U_c} = B\frac{(x\text{-}x_o)}{d} \tag{2.1}$$

Studies by Todde *et al*. (2009) showed that the decay rate was independent of Reynolds number beyond 1600. The virtual origin also decreased drastically with increasing Reynolds number so long as Re was less than 1600. Beyond Re = 1600, the virtual origin was fairly constant. Mi *et al*. (2013) observed that the decay rate depended on Reynolds number for Re < 10^4. An experimental study by Fellouah *et al*. (2009) showed that the decay rate of U_c was independent of Re in the range $6 \times 10^3 – 30 \times 10^3$. Results from different experiments have revealed that the decay rate of turbulent free jets become independent of Reynolds number at high Re. It has been established from previous section that different initial conditions are produced when the jet issues from different nozzle geometries. Results from Xu & Antonia (2002) showed that the decay rate was dependent on the nozzle geometry. Lee & Baek (1994) reported that the decay rate of U_c for round jets was smaller than was observed for elliptic jets, and this was attributed to high levels of entrainment by the latter nozzle configuration. Turbulent free jets issuing from a smooth contraction nozzle decayed faster than those issuing through long pipes. For example, Xu & Antonia (2002) reported decay rate values of 0.179 and 0.154 for jets produced from a smooth contraction nozzle and long pipe, respectively. Also the decay rate is greater for sharp-edged nozzles compared to smooth contraction nozzles (Faghani *et al*., 2009), implying greater mixing and entrainment effects for sharp-edged nozzles than smooth contraction nozzle and long pipe.

2.2.1.2 Spread rate

Entrainment of the ambient fluid by the discharged jet leads it to spread in the wall-normal and/or lateral direction depending on the nozzle geometry. Entrainment by jets is a physical parameter that is significant in many practical applications. For instance, most mixing devices used in the chemical industry rely on optimal entrainment for their effectiveness. The entrainment properties of jets have also been widely reported to depend on factors such as nozzle geometry (Faghani *et al*., 2009; Quinn, 1992). For finite aspect ratio nozzles, the discharged jet spread differently in the major axis compared to the minor axis. The well-known axis switching phenomenon characterizes the spread behavior of jets issuing from finite aspect ratio nozzles. The axis switching phenomenon results in larger jet spread in the minor axis close to the nozzle exit with an initial decrease in spread in the major axis. A review by Ball *et al*. (2012) reported spread rates obtained from the far field data of round free jets to be in the range 0.086–0.097. The wall-normal spread rate for non-circular nozzles ranged from 0.074–0.125 as indicated in Table 2.2. However, larger lateral spread rates (0.119–0.150) have been reported for aspect ratio nozzles.

2.2.2 Turbulence statistics

In general, the turbulence intensity of a free jet initially increases rapidly with streamwise distance up to about $x/d \approx 3$–4. Farther downstream of the nozzle exit, the turbulence intensity decreases presumably as a result of the breakdown of primary vortical structures (Mi *et al*., 2013). Depending on the streamwise distance, the normalized intensities farther downstream attains a constant value; signifying self-similarity of the intensities. Fellouah *et al*. (2009) observed that in the near-field region of the free jet, the turbulence intensity increased as a result of large-scale coherent motions that dominate the shear layer. It was argued that the influence of these large-scale structures on the centerline intensities increase as they progress through the potential core

and eventually merge at the end of the potential core. Quinn & Militzer (1988) also attributed the rise in streamwise and wall-normal turbulence intensities within the initial regions of the jet to the high local shear in the streamwise mean velocity which led to high turbulence production. Similar to the mean velocity distribution, the turbulence intensities for free jets also attain self-similarity with streamwise distance. Numerical studies by Bogey & Bailly (2009) reported that both streamwise and wall-normal turbulence intensities (u' and v') became self-similar beyond $x/d \geq 60$. However, the experimental study of Wygnanski & Fiedler (1969) revealed that u' became self-similar beyond $x/d \geq 40$ whereas both v' and w' (where w' is the lateral turbulence intensity) attained self-similarity beyond $x/d \geq 70$. According to Wygnanski & Fiedler (1969), the turbulent free jet reaches a state of complete self-similarity only when all the turbulent components reach equilibrium. Wygnanski & Fiedler (1969) explained that since energy is transferred directly from the mean motion to u', and the pressure-velocity gradient correlations transfer part of the energy to v' and w', it was appropriate for self-similarity to be reached in steps. Based on their explanation, it follows that the mean velocity first reaches a state of self-similarity, thereby resulting in a certain production of u'. Once a balance is attained between these two quantities, only then can both v' and w' also attain a state of equilibrium.

2.3 Turbulent wall jets

Extensive research has been conducted to investigate the flow fields of turbulent wall jets. Investigations by Wygnanski *et al*. (1992), Abrahamsson *et al*. (1994, 1997) and Tachie *et al*. (2004) have provided significant insight into plane and 3D wall jets. Launder & Rodi (1981, 1983) provided an extensive review on the generation of streamwise vortices by the highly anisotropic turbulence fields of wall jets. A summary of relevant literature on wall jets is provided in Table 2.3. As shown in Table 2.3, the experiments were conducted over a wide range of Reynolds

numbers ($2\times10^3 \leq Re \leq 143.5\times10^3$) and over an extended streamwise distance ($0 \leq x/b_o \leq 200$). Table 2.3 also indicates that many of the earlier studies on turbulent wall jets were conducted using Pitot tubes and hotwire anemometry which are both pointwise measurements.

2.3.1.1 Flow development of wall jets

Similar to free jets, the flow field of a wall jet can be divided into the potential core, developing and the self-similar regions (Sforza & Herbst, 1970). The extents of these regions have already been defined in previous sections. It should be recalled that the wall jet is a two shear layer flow and that these layers are characterized by different turbulent scales. The interaction between these shear layers dictates the growth of the wall jet. For turbulent wall jets (both plane and 3D) the streamwise mean velocity has been observed to attain self-similarity beyond $x/b_o \geq 20$ when U_m and $y_{0.5}$ are used as the velocity and length scales, respectively (Bhuiyan *et al*., 2011; Agelinchaab & Tachie, 2011a). Agelinchaab & Tachie (2011a) observed that the wall jet with a top-hat profile reached self-similarity at a shorter streamwise extent than that with developed exit velocity profile. The observation by Agelinchaab & Tachie (2011a) supports findings of Sun & Ewing (2002) who also reported that the type of exit velocity profile affects the development of 3D wall jet. The decay and spread rates within the self-similar region can be used to examine the development of the flow field of turbulent wall jets and these are subsequently presented in the next section. Due to the presence of the solid boundary, the development of the wall jet with streamwise distance exhibits some characteristics different from those of free jets. A review of the turbulent statistics for wall jets is also presented to conclude the section for turbulent wall jets.

Table 2.3 Relevant literature on turbulent wall jets

Author	*Technique*	*Jet type*	*Re*×10^3	*x/b$_o$*	*n*	*dy$_{0.5}$/dx*	*dz$_{0.5}$/dx*
Rostamy *et al*. (2011)	LDA	2D	7.5	20-80	---	0.079	---
Dey *et al*. (2010)	ADV	2D	25.6	0-40	---	---	---
Ahlman *et al*. (2007)	DNS	2D	2	0-40	0.5	0.068	---
Wang & Tan (2007)	PIV	2D	10	0-30	0.47	---	---
Ead & Rajaratnam (2004)	PrT	2D	76-143.5	0-70	0.5	0.125	---
Tachie *et al*. (2004)	LDA	2D	5.9-12.5	0-130	---	0.085-0.09	---
Eriksson *et al*. (1998)	LDV	2D	9.6	5-200	1.08	0.078	---
Nyantekyi-Kwakye *et al*. (2015a)	PIV	3D	12	0-60	0.996	0.066	0.116
Agelinchaab & Tachie (2011a)	PIV	3D	5-20	0-120	1.15	0.054	0.255
Hall & Ewing (2007)	HWA	3D	89.6	0.1-25	---	0.051	0.281
Sun & Ewing (2002)	HWA	3D	65, 108	35-90	---	0.053-0.060	0.27-0.28
Abrahamsson *et al*. (1997)	HWA	3D	53-105	50-90	1.29	0.065	0.32
Padmanabham & Lakshmana Gowda (1991a,b)	PT, HWA	3D	95.4	0-100	1.12-1.16	0.040-0.045	0.22-0.25

ADV: acoustic Doppler velocimetry; *LDV*–laser Doppler velocimetry; *PT*– Pitot tube; *PrT*–Prandtl tube

2.3.1.1.1 Decay rate

The maximum velocity decay in the self-similar region can be described by a power law of the form:

$$\frac{U_m}{U_o} = a\left(\frac{x}{b_o}\right)^{-n} \tag{2.2}$$

where a and n are constants with n being the decay rate. A range of decay rate values have been reported for both plane and 3D wall jets. For 3D wall jets, reported values of n range from $n = 1$ to 1.29 as indicated in Table 2.3. The streamwise mean velocity of wall jets decays faster than for free jets. This is an expected behavior due to the loss of momentum induced by the shear stress imposed by the wall. Investigations by Padmanabham & Lakshmana Gowda (1991a) showed that the decay rate of 3D wall jets within the developing region is affected by nozzle geometry. Jets issuing from sharp-edged orifice nozzles had greater decay rate compared to nozzles with curved geometries. From their results, it was obvious that nozzle geometry affected the development of the 3D wall jet within the developing region. For instance, changing the nozzle geometry from circular to rectangular extended the developing region from $x/d = 10$ to 20. The effect of Reynolds number on the decay rate of 3D wall jets was investigated by Agelinchaab & Tachie (2011a) and Sun & Ewing (2002). The results by Sun & Ewing (2002) revealed that Reynolds number had no significant effect on the decay rate of the jets within the self-similar region. A similar conclusion was reached by Agelinchaab & Tachie (2011a) for the range of Reynolds number specified in Table 2.3. Law & Herlina (2002) also did not observe any Reynolds number (5.5×10^3–13.7×10^3) effect on decay rate.

2.3.1.1.2 Spread rate

The gradients of the jet half-width, $dy_{0.5}/dx$ and $dz_{0.5}/dx$, give an indication of the jet spread rate in the wall-normal and lateral directions, respectively. An experimental and theoretical investigation by Newman *et al*. (1972) showed that the two half-widths should grow linearly with streamwise distance. Launder & Rodi (1981, 1983) in a review of turbulent wall jet literature determined that wall-normal spread rate for both plane and 3D turbulent wall jets in the far-field

can be represented by Eqns. (2.3) and (2.4) respectively, with the lateral spread rate for 3D wall jets given in Eqn. (2.5).

$$\frac{dy_{0.5}}{dx} = 0.073 \pm 0.002 \tag{2.3}$$

$$\frac{dy_{0.5}}{dx} = 0.048 \pm 0.003 \tag{2.4}$$

$$\frac{dz_{0.5}}{dx} = 0.26 \pm 0.002 \tag{2.5}$$

The wall-normal spread rate of plane wall jets is observed to be greater than 3D wall jet as can be seen from Eqns. (2.3 and 2.4). This occurrence is associated with the corresponding lateral spreading of the 3D wall jet. It should be noted that the plane wall jet is restricted in the lateral plane and only entrains in the wall-normal plane. The wall-normal spread rate of plane wall jet is less than values obtained for turbulent free jets. Dejoan & Leschziner (2006) attributed this to the wall blocking effect which dampens the wall-normal fluctuations. From Table 2.3, the magnitude of the wall-normal spread rate appears to depend on initial conditions. Several studies have shown that the spread rate of the jet was independent of Reynolds number. For instance, Sun & Ewing (2002) investigated Reynolds numbers ranging from 65×10^3 to 108×10^3 and concluded that the spread rate of a wall jet was independent of Reynolds number. Experimental investigations by Rostamy *et al*. (2011) and Tachie *et al*. (2004) showed that the wall-normal spread rate of plane turbulent wall jets was independent of surface roughness. For 3D wall jets, the jet spread much faster in the lateral direction compared to the wall-normal direction. That is, the 3D wall jet spread about 5.4 times in the lateral direction compared to the wall-normal direction. The reason behind this mechanism has been a debate in 3D turbulent jet studies: Abrahamsson *et al*. (1997) attributed this to the presence of secondary flows but Launder & Rodi (1983) attributed it to the generation

of streamwise vortices. Anthony & Willmarth (1992) argued that the mechanism responsible for the larger lateral spreading is as a result of the creation of streamwise vortices, which arise from either bending of vortex lines or through inhomogeneity in the Reynolds stress field. The interaction between the jet and the wall involves large-scale coherent motion which results in the wall-normal component of motion towards or away from the wall and this is associated with lateral outflow or inflow along the wall. This motion provides a physical explanation for the larger lateral spreading rate for 3D wall jets. Measurements by Law & Herlina (2002) also revealed that the direction of wall-normal velocity within the symmetry plane was negative, meaning a downward motion of the flow towards the wall, supporting the existence of secondary mean motion. This secondary motion meant that the flow was directed towards the wall and then diverted laterally away from the symmetry plane. This in part explains the larger lateral spread rate compared to the wall-normal spread rate.

2.3.2 Turbulence statistics

Like the mean velocities, the turbulence intensities (u', v', and w') of turbulent wall jets also exhibit similarity with streamwise distance when the appropriate scaling is used (U_m and $y_{0.5}$ or $z_{0.5}$ representing velocity and length scales, respectively). Close to the nozzle exit, the turbulence intensities in the streamwise and wall-normal directions have double peaks with each occurring in the inner and outer shear layers. Higher turbulence intensities have been reported for wall jets compared to boundary layer flows. Investigations by Venas *et al*. (1999) on plane and 3D wall jets revealed peak values of the streamwise turbulence intensity, u' (near the point of maximum streamwise mean velocity) to be 20% and 27%, respectively, compared to 16% reported for boundary layers. The peak values of u' are observed to be greater than the wall-normal turbulence intensity, v', (Liu *et al*. 2004). The turbulence intensities require a longer streamwise distance to

become self-similar compared to the mean velocities. Agelinchaab & Tachie (2011a) reported that for 3D wall jets, the turbulence intensities collapsed fairly well beyond $x/d \geq 40$. For a wall jet, an antisymmetric distribution has been reported for the Reynolds shear stress, $\overline{uv}$, with negative and positive values dominating the inner and outer shear layers, respectively. An interesting feature arising from this distribution is the difference in wall-normal location of zero shear stress and the mean shear gradient. This difference arises as a result of strong interaction between the more turbulent outer shear layer on the less turbulent inner shear layer of the wall jet. Investigations by Banyassady & Piomelli (2014), Abrahamsson *et al*. (1997) and Padmanabham & Lakshmana Gowda (1991) revealed that due to the high turbulence levels within the outer shear layer of the jet, positive Reynolds shear stress is transported from the outer shear layer into the inner shear layer. This displaces the wall-normal location of zero shear stress closer to the wall compared to that of the mean shear gradient. The location of change in sign poses a challenge for turbulence models based on the eddy viscosity concept (e.g., k–ε model, where ε is turbulence dissipation) which assume that these two wall-normal locations to be equal.

Some studies have investigated the budget terms of the turbulent kinetic energy, k (or TKE), which is given as:

$$\underset{\text{I}}{U_j \frac{\partial k}{\partial x_j}} = \underset{\text{II}}{-u_i u_j \frac{\partial U_i}{\partial x_j}} \underset{\text{III}}{- \upsilon \frac{\partial u_i}{\partial x_j}\frac{\partial u_i}{\partial x_j}} + \underset{\text{IV}}{\frac{\partial}{\partial x_i}\left(-\frac{1}{\rho} p u_i - k u_i\right)} \tag{2.6}$$

where the individual terms are I – convection by the mean flow, II – turbulence production, III – turbulence dissipation and IV – turbulence diffusion. Investigations by Swamy & Bandyopadhyay (1981) estimated the production of turbulence from $-[(\overline{u^2}\text{-}\overline{v^2})\partial U/\partial x + \overline{uv}\partial U/\partial y]$ for a turbulent 3D wall jet and concluded that the major contributor was the $\overline{uv}\partial U/\partial y$ term.

Table 2.4 Relevant literature on turbulent offset jets

Author	h/b_o	*Technique*	*Jet type*	$Re_{bo}\times10^3$	*n*	$dy_{0.5}/dx$	$dz_{0.5}/dx$
Bhuiyan *et al*. (2011)	0-4	PrT	2D	64-273	0.52	0.172	---
Gao & Ewing (2007)	0.1-1	HWA	2D	44	---	---	---
Ead & Rajaratnam (2001)	5-100	PrT	2D	5-43	0.5	0.065	---
Nasr & Lai (1998, 1997)	2.125	LDA	2D	11	---	---	---
Yoon *et al*. (1993)	2.5-5	HWA	2D	39	0.5	0.076	---
Pelfrey & Liburdy (1986)	7	LDA	2D	15	---	---	---
Hoch & Jiji (1981)	3.0-8.7	HWA, Ptap	2D	3-18	---	---	---
Agelinchaab & Tachie (2011b)	0-3.5	PIV	3D	5-20	1.15-1.20	0.054-0.056	0.255-0.245
Davis & Winarto (1980)	0-3.5	HWA	3D	170	1.15	0.036-0.046	0.33-0.23
Nozaki *et al*. (1979)	10	HWA	3D	20-70	---	---	---

Re_{bo} – Reynolds number based on nozzle height

Studies by Abrahamsson *et al*. (1997) provided detailed analysis of the budget terms using a hot-wire anemometer technique. The production, convection and turbulent diffusion (neglecting the pressure diffusion term) terms were directly measured and the dissipation term was obtained as the imbalance of the TKE equation. Their investigation revealed that for the production term in the TKE equation, the major contributor was $\overline{uv}\partial U/\partial y$ which was consistent with previous studies.

2.4 Turbulent offset jets

Plane offset jets have received considerable research attention compared to their 3D counterpart. Detailed experimental investigations were reported by Bourque & Newman (1960), Ayukawa & Shakouchi (1976), Yaghoubi & Mahmoodi (2004). Nasr & Lai (1998) studied the effect of small offset height ratio (h/b_o = 2.125) on a turbulent plane offset jet both experimentally

and numerically. The experimental data set was compared to results obtained from the k-ε and Reynolds stress turbulence models. Both the k-ε and Reynolds stress models were able to predict the extent of the recirculation region of the offset jet reasonably well. Reattachment lengths of $4.8b_o$ and $5.3b_o$ were predicted by the k-ε and Reynolds stress model, respectively compared to the experimental value of $4.65b_o$. The turbulence models however, failed to predict the loci of the maximum streamwise mean velocity decay, wall-normal location of U_m, wall-normal half-width in the outer shear layer and the wall static pressure distribution. For instance, within the reattached region of the flow, the predicted normalized value of y_m by both k–ε and Reynolds stress models were 44% and 55% larger than the experimental value of about 0.45, respectively. The discrepancies between experimental and turbulence model results; especially for the k–ε models; can be partly attributed to the isotropic assumption made for the latter.

Until now, very few results are available in open literature for 3D turbulent offset jets. Table 2.4 provides a summary of relevant literature on previous studies of turbulent offset jets. The discussion of the offset jets will be categorized under pressure distribution within the recirculation region, velocity distribution within the three main regions specified in Figure 1.2 (namely, the recirculation, developing and self-similar regions) and turbulence statistics.

2.4.1 Pressure distribution

The discharged jet is deflected towards the bottom of the channel due to the Coanda effect. The reattached jet encloses a recirculation region characterized by negative streamwise mean velocities. Early studies by Sawyer (1963, 1960) and Bourque & Newman (1960) assumed uniform pressure distribution within the recirculation region of the jet. The assumption of uniform pressure however, does not hold according to subsequent studies by Bourque (1967) and Rajaratnam &

Subramanya (1968). It has been shown that within the recirculation region, the pressure rises within the jet and attains a maximum at the reattachment point (Yoon *et al*., 1993; Shakouchi, 1986). Nasr & Lai (1998) used a LDA to investigate the effect of Reynolds number on the static pressure distribution of the jet. The experiment was conducted at a Reynolds number range of 3.3×10^3 to 15.2×10^3. Their results revealed that the static pressure distribution was dependent on Reynolds number for flow with Reynolds number less than 11×10^3. However, there was no difference between results of static pressure distribution for flows with Reynolds number 11×10^3 and 15.2×10^3. This led to the conclusion that the static pressure distribution was independent of Reynolds number at sufficiently large Re.

2.4.2 Recirculation region

One of the significant characteristics of an offset jet is the length of the recirculation region or mean reattachment length (L_e). As already indicated in Figure 1.2, the mean reattachment length is the distance from the nozzle exit to the streamwise location where the jet reattaches to the bottom of the channel. The reattachment point of an offset jet can be determined using techniques such as 1) pressure measurement within the recirculation region, 2) contours or profile distribution of the mean velocities, 3) flow visualization (e.g., dye injection), 4) stream function technique and 5) forward-flow fraction technique. A brief description of these techniques is provided. Using the pressure measurement approach, the reattachment point can be estimated as the point where the maximum pressure occurs within the jet flow field. For the mean velocity contours, the reattachment point is determined as the point where the zero contour level intersects with the line indicating the bottom of the channel. Likewise, the stream function uses a similar approach to determine the reattachment point. Thus, the reattachment point is determined as the point where the zero streamline intersects with the bottom of the channel. Ra *et al*. (1990) defined the forward-

flow fraction, γ_p, as the fraction of time for which the flow is directed in the downstream direction. The main principle for a forward-flow fraction is, if $\gamma_p = 1$ then the flow is in the downstream direction all times whereas $\gamma_p = 0$ means the flow is in the reverse direction to the forward flow at all times. The reattachment point of the offset jet is estimated as the point where $\gamma_p = 0.5$. Various studies on separated and reattached flows have utilized one or a combination of these techniques to determine the mean reattachment length of the separated region.

The extent of the recirculation region of submerged offset jets may depend on factors such as, nozzle width, nozzle height, offset distance, exit bulk velocity, tailwater depth, fluid density, fluid dynamic viscosity, gravitational force and initial turbulence intensity (T_u). From dimensional analysis, the length of the recirculation region can be established to depend mainly on the dimensionless quantities listed in Eqn. (2.7).

$$\frac{L_e}{b_o} = f\left(\frac{1}{\mathrm{Re}},\ \frac{h}{b_o},\ \frac{1}{\mathrm{F}^2},\ \frac{y_t}{b_o},\ \frac{T_u}{U_o},\ \frac{b}{b_o}\right) \tag{2.7}$$

where F is the Froude number. Bhuiyan *et al*. (2011) observed that when an offset jet is discharged into tailwater, the effect of gravity on the reattachment length is reduced significantly. This makes other factors such as ambient fluid entrainment and the Coanda effect dominant on the extent of the recirculation region. At sufficiently large tailwater depth and fluid exit turbulent intensity, their effects on L_e can be neglected. Investigations by Bourque & Newman (1960) indicated that the reattachment point depended only on h/b_o at high Re (beyond 2.3×10^3) where viscous effects can be neglected. Similarly, the results by Agelinchaab & Tachie (2011b) for 3D offset jets revealed that L_e was independent of Re beyond 5×10^3, a result that supports earlier finding by Pani & Dash (1983). It is therefore apparent from these studies that at sufficiently large Re, fluid viscosity has

no significant effect on turbulent mixing. Based on these limiting conditions, the reattachment length of the jet will depend mainly on h/b_o and b/b_o (with the latter referred to as the nozzle aspect ratio). Therefore Eqn. (2.7) reduces to

$$\frac{L_e}{b_o} = f\left(\frac{h}{b_o}, \frac{b}{b_o}\right) \tag{2.8}$$

The reattachment length was described in a power law form by Nasr & Lai (1998) for offset height ratios less than 20 issuing from a constant nozzle aspect ratio and this is expressed in Eqn. (2.9).

$$\frac{L_e}{b_o} = 2.63\left(\frac{h}{b_o}\right)^{0.855} \tag{2.9}$$

Yoon *et al*. (1993) utilized flow visualization and forward-flow fraction technique to determine the reattachment length of an offset jet. Two offset height ratios of 2.5 and 5.0 were investigated at Re of 39×10^3. Using the split film method, the downstream distribution of the forward-flow fraction was measured at a distance 0.3 mm off the wall. Measurement of the probability distribution of the velocity fluctuation indicated a positive skew just downstream and negative skew just upstream of the reattachment point. Close to the reattachment point, Yoon *et al*. (1993) observed a symmetric probability distribution. Results from the two techniques revealed that the forward-flow fraction provided a more accurate way of estimating L_e. Agelinchaab & Tachie (2011b) also reported L_e of 1.5d, 3.2d and 6.4d for jets with h/b_o = 0.5, 1.5 and 3.5, respectively.

The mean velocity within the recirculation region has been investigated by different researchers. For a plane offset jet, Nasr & Lai (1998) measured the maximum reverse velocity within the recirculation region to be about 27% of the nozzle exit bulk velocity. Yoon *et al*. (1995)

reported a maximum reverse velocity of about 37% of the nozzle exit bulk velocity. The differences observed between the two results can be attributed to the variation in h/b_o. Ead & Rajaratnam (2001) observed that the maximum value of the reverse velocity within the recirculation region decrease with increasing h/b_o which is in contrast to previous reports. For 3D offset jets, Agelinchaab & Tachie (2011b) reported maximum reverse velocities of 0.17%, 0.59% and 0.38% of the exit velocity jets with h/b_o of 0.5, 1.5 and 3.5, respectively. These results show that larger reverse velocities are generated within the recirculation region of plane offset jets compared to 3D offset jets. The maximum streamwise mean velocity decays faster within the recirculation region for both plane and 3D offset jets.

2.4.3 Developing region

The developing region extends from the reattachment point to the commencement of the self-similar region. The flow behavior within this region shares similarity with other reattaching shear layer flows such as flow over a backward facing step. Since the jet evolves with streamwise distance, the flow within the developing region is sensitive to the different initial conditions that affect the flow dynamics. For instance, the decay of the maximum streamwise mean velocity within the developing region is dependent on initial conditions and h/b_o (Rajaratnam & Subramanya, 1968). Studies by Gao & Ewing (2007) revealed that the developing region is characterized by a rapid decay of U_m and an increase in $y_{0.5}$. A slower decay of U_m was observed within this region by Nasr & Lai (1998) for an offset jet than for a free jet but higher than that of a wall jet. Although the flow within the developing region is sensitive to initial conditions, majority of previous investigations focused on the self-similar region, and not much has been done to elucidate the flow physics in the developing region.

2.4.4 Self-similar region

The self-similar region is characterized by flow quantities which are independent of streamwise distance with the appropriate scaling. This region occurs further downstream of the nozzle exit and beyond the developing region. The decay rate estimated within the self-similar of an offset jet was observed to be similar to that obtained for classical wall jets (Rajaratnam & Subramanya, 1968). Studies by Agelinchaab & Tachie (2011) revealed that the decay rate of U_m within the self-similar region for 3D offset jets was slightly dependent on h/b_o, with decay rate values of 1.15, 1.16, 1.17 and 1.20 for jets with h/b_o = 0, 0.5, 1.5 and 3.5 respectively. In order to establish complete similarity (inner and outer shear layers) the profiles of U are usually scaled with U_m. However, two different length scales have been widely used to scale the wall-normal location; $y/y_{0.5}$ and mixed scaling consisting of y_m and $y_{0.5}$ (i.e., $(y\text{-}y_m)/(y_{0.5}\text{-}y_m)$). The profiles of U collapsed within the inner shear layer beyond $x/d \geq 40$ and 60 for offset jets with h/b_o = 1.5 and 3.5, respectively (Agelinchaab and Tachie, 2011). When the mixed scaling was used, profiles of U collapsed at all streamwise locations beyond reattachment, $2 \leq x^*/d \leq 80$ (where $x^* = x - L_e$, Agelinchaab & Tachie, 2011). Scaling with both length scales indicated that the mixed scaling was an appropriate choice for the streamwise mean velocities of the offset jets.

Davis & Winarto (1980) and Agelinchaab & Tachie (2011b) provided detailed investigations on the flow characteristics within the self-similar region of 3D offset jets. According to Agelinchaab & Tachie (2011b), increasing h/b_o from 0.5 to 3.5 yielded wall-normal spread rates of 0.054 and 0.056, respectively. The results by Agelinchaab & Tachie (2011b) revealed that the wall-normal spread rate ($dy_{0.5}/dx$) was nearly independent of h/b_o. However, studies by Davis & Winarto (1980) showed a considerable increase in $dy_{0.5}/dx$ with h/b_o. A wall-normal spread rate of 0.036 and 0.046 was obtained for offset jets with h/b_o of 0.5 and 3.5

respectively. Their results, however, revealed that $dy_{0.5}/dx$ was independent of this parameter for small h/b_o (i.e., $h/b_o \leq 2$). The results from both studies also revealed a decrease in lateral spread rate ($dz_{0.5}/dx$) with increasing h/b_o. For instance, Agelinchaab & Tachie (2011b) reported lateral spread rate values of 0.255 and 0.245 for offset jets with $h/b_o = 0$ and 3.5, respectively. The results from both Davis & Winarto (1980) and Agelinchaab & Tachie (2011b) revealed larger lateral spread rates compared to the wall-normal components. The ratio of ($dz_{0.5}/dx$)/ ($dy_{0.5}/dx$) for offset jets with $h/b_o = 0$, 0.5 and 1.5 were 4.7, 4.7 and 4.5 respectively (Agelinchaab & Tachie, 2011b). These values are comparable to 5.4 reported by Launder & Rodi (1983) for generic 3D wall jets.

2.4.5 Turbulence statistics

Numerous studies focused on the evolution of the mean velocity field and pressure distribution within the flow field of plane offset jets. However, several investigators reported turbulent quantities for both 3D (Agelinchaab & Tachie, 2011b; Davis & Winarto, 1980; Nozaki *et al*., 1979) and plane (Gao & Ewing, 2007; Nasr & Lai, 1997, 1998; Yoon *et al*., 1993; Pelfry & Liburdy, 1986) offset jets. Yet still, the vast majority of these measurements were conducted for plane offset jets. Prior to investigations by Agelinchaab & Tachie (2011b), only the turbulence intensities and Reynolds shear stresses had been reported for 3D offset jets. Quantities such as the triple velocity correlations, budget terms of the TKE equation and multi-point statistics were scarce in open literature for 3D offset jets. This section therefore provides a summary of previous results on the turbulence intensities, Reynolds stresses, triple velocity products and some budgets terms of the TKE equation.

Investigations by Pelfrey (1984) revealed significant differences between the turbulence intensities located within the upper and lower sides of the dividing streamline. Results presented

by Agelinchaab & Tachie (2011b) revealed that, closer to the nozzle exit, the streamwise turbulence intensities had double peaks. These double peaks disappeared with streamwise distance. For jets with small offset height ratios (e.g., h/b_o = 0.5), the double peak occurred close to the nozzle and disappeared at x^*/d = 6 (where x^* is x-L_e). Profiles of the turbulence intensities had no double peaks when h/b_o was increased from 1.5 to 3.5. The turbulence intensities for the 3D offset jets were larger than those reported for 3D wall jets. The investigation by Agelinchaab & Tachie (2011b) reported that high turbulence levels within the outer shear layer of the jet penetrated into the inner shear layer, causing higher values of the turbulence characteristics across the shear layer. Davis & Winarto (1980) reported that there was a significant decrease in turbulence levels within the developing and self-similar regions up to about 25% of U_m. The peak values of the turbulence intensities increased monotonically with streamwise distance, with peak values of about 20% and 24% of U_m at x/d = 32 for h/b_o = 1.5 and 3.5, respectively. The results presented by Nasr & Lai (1998) showed that the location of the maximum streamwise turbulence intensity within the inner shear layer occurred closer to the dividing streamline and immediately upstream of the reattachment point. This location also corresponded to the location of the maximum Reynolds shear stress. This is an indication of interaction between the flow in the recirculation region and the inner shear layer of the jet within the vicinity of the reattachment point. These findings are similar to those reported by Eaton & Johnston (1981) for separated and reattached flows. According to Nasr & Lai (1997, 1998), the streamwise development of the turbulence intensities and Reynolds shear stresses indicate that offset jets have significant suppression effects on the turbulence field within the recirculation and developing regions of the flow. The effect of exit turbulence levels on the flow dynamics of offset jets was investigated by Nozaki *et al*. (1979) and it was reported that for turbulence levels greater than 6%, the flow characteristics were independent

of the jet exit turbulence levels. Similarity in the turbulence intensities was investigated by Agelinchaab & Tachie (2011b) and they observed that the turbulence intensity profiles collapsed beyond $x^*/d \geq 40$ and 60 for jets with h/b_o of 1.5 and 3.5, respectively.

Profiles for the triple correlations can provide guidance for modeling the turbulence diffusion term in the transport equations. Thus far the only report on the triple velocity correlations for 3D offset jets has been presented by Agelinchaab & Tachie (2011a, b). The quantities reported by Agelinchaab & Tachie (2011b) include $\overline{u^3}$, $\overline{v^3}$, $\overline{u^2v}$ and $\overline{uv^2}$. Their studies revealed negative values of these correlations close to the wall ($y/y_{0.5} \leq 0.2$), but predominantly positive further away from the wall. In addition, the peak values of the triple velocity correlations for 3D offset jets were larger than those reported for 3D wall jets. This result implies that both the TKE and Reynolds shear stress are largely transported from the outer shear layer to the wall and outer edge of the jet. Within the developing region, Agelinchaab and Tachie (2011b) observed slightly higher turbulence production levels for 3D offset jets compared to wall jets. The level of turbulence production within the self-similar region was comparable for both offset and wall jets.

2.5 Eduction of turbulence structures

Turbulent flows are characterized by organized motions referred to as coherent structures which play a dynamic role in the mixing, entrainment and momentum transport. The formation of these large-scale structures is greatly affected by nozzle geometry. The interaction of these structures (pairing or tearing) with streamwise distance has been investigated in previous studies. The process of characterizing the properties of these structures is widely referred to as eduction. Several methods have been used to describe and identify these structures. These techniques include the quadrant analysis, two-point correlation and proper orthogonal decomposition (POD). A

comprehensive review of most of these and many other methods was undertaken by Alfonsi (2006). An overview of a few of these methods that are implemented in the present study is provided in the following sections.

2.5.1 Quadrant analysis

Quadrant analysis can be used to decompose the active motions that contribute to the Reynolds shear stress. This involves investigating the relationship between the fluctuating velocity components, u and v and sorting them into four different quadrants. The first quadrant, $Q1$, normally referred to as outward interaction, (where $u > 0$, $v > 0$) denotes events where high speed fluid moves away from the wall. The ejection event, $Q2$ ($u < 0$, $v > 0$) is characterized by low speed fluid which moves away from the wall. The third quadrant, $Q3$, inward interaction, ($u < 0$, $v < 0$) denotes an event in which low speed fluid moves toward the wall and the sweep event representing the fourth quadrant, $Q4$ ($u > 0$, $v < 0$) is characterized by an event where high speed fluid moves toward the wall. Following the methodology proposed by Lu & Willmarth (1973), the Reynolds shear stress at each grid point is decomposed into contributions from the four quadrants excluding a hyperbolic hole size, H, as follows:

$$\overline{uv}_Q(x,y,H) = \frac{1}{N}\sum_{i=1}^{N} u_i(x,y)v_i(x,y)I_Q(x,y,H) \tag{2.10}$$

where N is the total number of instantaneous velocity vectors at each grid point and I_Q is the indicator function given by

$$I_Q(x\,y,H) = \begin{cases} 1, \; when \; |u_i(x,y)v_i(x,y)|_Q \geq Hu'(x,y)v'(x,y) \\ 0 \end{cases} \tag{2.11}$$

where u' and v' are the streamwise and wall-normal turbulence intensities, respectively.

2.5.2 Two-point correlation

The two-point correlation is a useful multi-point technique for investigating the salient features of coherent structures and integral length scales. The two-point correlation function, R_{ab}, is defined at a reference point (x_r, y_r) between two arbitrary quantities; a and b separated in the streamwise and wall-normal directions by Δx and Δy, respectively, as:

$$R_{ab} = \overline{a(x_r,y_r)b(x_r+\Delta x,\, y_r+\Delta y)} \big/ a'(x_r,y_r)b'(x_r+\Delta x,y_r+\Delta y) \tag{2.12}$$

where a' and b' are the root mean square values of a and b, respectively. The arbitrary quantities a and b can either be the streamwise or wall-normal fluctuating velocity components.

This technique has been extensively used in turbulent boundary layer research to quantify the average extent and shape as well as inclination of hairpin-like vortex packets (e.g., Volino *et al*., 2007; Adrian *et al*., 2000; Krogstad & Antonia, 1994). Results obtained from DNS studies by Moin & Kim (1985) indicate that the size of these vortex packets increased with wall-normal distance. The angle of inclination of the hairpin-like vortices was found to vary from 10° to 20° for Re (based on momentum thickness) range of 1015–7705 (Tomkins & Adrian, 2003). For canonical turbulent wall-bounded flows (e.g., Volino *et al*., 2007; Krogstad & Antonia, 1994), results from experimental investigations indicate that the average inclination of the hairpin-like vortex packets is approximately 15° ±5°. Agelinchaab & Tachie (2011b) used the two-point correlation to investigate how the turbulence structures are correlated in the developing and self-similar regions of 3D offset jets. The results showed that the hairpin-like structures are larger in size within the outer shear layer compared to the inner shear layer of the flow. Increasing h/b_o also increased the size of the large-scale structures. The inclination of these hairpin-like structures within the inner layer of the flow was 11.2° ±0.6° and decreased with wall-normal distance. Gao

& Ewing (2007) investigated the correlation between fluctuating wall pressure distribution and velocity. Their results revealed that the large-scale structures within the attaching shear layers convected along the wall after reattachment of the offset jet. The pressure-velocity correlations also suggested that both small and large-scale structures within the flow merge and travel downstream in the self-similar region.

2.5.3 Proper orthogonal decomposition (POD)

The POD technique has been used to extract the dominant features and identify coherent structures within the flow fields of turbulent flows. The uniqueness of the POD technique is its ability to decompose the flow field into a set of basis functions which are optimal in terms of energy. That is, the dominant structures of the flow can be satisfactorily captured within the first few modes. Since its introduction, the POD technique has been applied to investigate coherent structures in boundary layers (Volino *et al*., 2007), separated flows (Shah & Tachie, 2009) and turbulent offset jets (Nyantekyi-Kwakye *et al*., 2015b). The snapshot approach proposed by Sirovich (1987) was adopted. The snapshot POD method was described in detail by Meyer *et al*. (2007) and as such only a brief overview will be presented herein. The snapshot POD method considers each instantaneous data set as a snapshot of the flow with the total number of snapshots denoted by N. The POD analysis is performed on the fluctuating velocity field (u_j^n, v_j^n) which is obtained by subtracting the mean velocity from the instantaneous velocity. The index n runs through the N snapshots and j runs through M, which is the total number of velocity vectors in each snapshot. The fluctuating velocities for N are arranged in a matrix U. The $N \times N$ auto-covariance matrix is obtained from $C = U^T U$. From the auto-covariance matrix, a set of N eigenvalues λ^i (which represents the kinetic energy) and corresponding set of orthonormal

eigenvectors A^i that satisfy $CA^i = \lambda^i A^i$, with i spanning from 1 to N, are evaluated. The evaluated eigenvalues are ordered by decreasing values as follows: $\lambda^1 > \lambda^2 > \ldots > \lambda^N > 0$. The normalized POD modes, ϕ^i, are constructed from the projection of the eigenvectors A^i on the original velocity field as:

$$\varphi^i = \sum_{n=1}^{N} A_n^i u^n \,/\left\|\sum_{n=1}^{N} A_n^i u^n\right\|, \quad i = 1, \ldots, N \tag{2.13}$$

where A_n^i is the nth component of the eigenvector corresponding to λ^i and $\| \cdot \|$ is the $L_{2\text{-norm}}$. The temporal POD coefficients a_i for the various modes are calculated by projecting the corresponding data set of the fluctuating velocity onto the POD modes: $a^n = \Psi^T u^n$, where $\Psi = [\phi^1\ \phi^2\ \ldots\ \phi^N]$. The expansion of the ensemble using an arbitrary number of modes m was performed using

$$u^n = \sum_{i=1}^{N} a_i^n \varphi^i = \psi a^n \tag{2.14}$$

The above equation yields the best approximation of the data ensemble in the sense that the average least-squares truncation error is a minimum for any given number $m \leq N$ basis functions over all sets of orthogonal basis functions. The instantaneous fields can be reconstructed using only a few modes to investigate the temporal evolution of structures. The ensemble-averaged energy of the fluctuating component is then given by the sum of all eigenvalues (Eqn. 2.15); while the fractional contribution of each eigenfunction to the total energy is given by the fractional contribution of its associated eigenvalue using Equation (2.16).

$$\mathrm{E} = \sum_{i=1}^{N} \lambda^i \tag{2.15}$$

$$E_n / E = \lambda_n / \sum_{n=1}^{N} \lambda_i \tag{2.16}$$

As previously stated, the POD technique has been applied to a wide range of turbulent flows. For instance, Kostas *et al*. (2002) used the POD technique to decompose both the fluctuating velocity and vorticity fields in order to investigate the structures within a backward facing step flow. They reported that the low-order modes (associated with the large-scale structures)

significantly contributed to the production of Reynolds stresses and turbulent kinetic energy. POD results presented by Shim *et al*. (2013) revealed symmetric counter-rotating vortices within the initial region of a free jet. These vortices were as a result of vortex merging at subharmonic sideband frequency. Further downstream, antisymmetric vortices dominated the flow with gradual displacement of the symmetric vortices. The dynamics of these vortices have been thoroughly investigated in the near-field region of turbulent free jets. For the 3D wall jet, Agelinchaab & Tachie (2011a) reported significant contribution of the low-order modes to the turbulence quantities within the self-similar region compared to the developing region. To date the POD technique has not been widely applied to 3D offset jets though it is useful in investigating the energy containing structures within the flow.

2.6 Summary of literature

In spite of the numerous investigations on turbulent reattached offset jets, many aspects of the flow remain unexplored due to the difficulty in accurately predicting/measuring the interaction of the flow structures within the shear layers. Previous studies on turbulent offset jets have shown that the flow field can be divided into recirculation, developing and self-similar regions. The development of the jet within the self-similar region has been investigated quite extensively, however, research on the flow characteristics within the recirculation and developing regions is scarce. Within the recirculation region, one of the main reasons why there is scarce data can be attributed to measurement techniques which are inappropriate in high turbulent zones. Although the self-similar region of the offset jet flow has been examined in great detail, there are still some inconsistencies in the results presented. For instance, results obtained for the mean velocity decay, wall-normal and lateral spread rates have shown varying conclusions for offset jets. There are inconsistent reports on the streamwise extent at which the offset jet attains self-similarity. Also,

the effect of the two shear layers on the turbulence statistics have to be investigated in detail. Studies have also shown that the lateral spread rate of the jet is greater than the wall-normal spread rate, however, different explanations have been given as reasons for this occurrence. Also, majority of previous studies utilized measuring techniques such as Prandtl tube, Pitot tube and planar PIV that did not allow simultaneous measurement of all three velocity components. As a result, only a subset of the Reynolds stress tensor was reported or not reported at all. There is therefore the need for direct measurements of all the Reynolds stresses and turbulent kinetic energy to adequately characterize the turbulence field, and provide a deeper insight into turbulent transport phenomena in these relatively complex shear flows.

The presence of large-scale coherent structures, generated by instability mechanisms, influences the flow dynamics of turbulent jets. Since these structures control the entrainment and mixing process in jets, it would be beneficial to investigate their interaction within the inner and outer shear layers of reattached offset jets. Also, the streamwise development of these structures (within the recirculation, developing and self-similar regions) would provide insight into their complex evolution.

CHAPTER THREE

3 EXPERIMENTATION

An overview of the offset jet facility, the particle image velocimetry (PIV) and acoustic Doppler velocimetry (ADV) system and measurement procedures are presented in this chapter.

3.1 Experimental setup

The experiments were performed in two stages. The first stage comprised the large scale testing in the Hydraulics Research & Testing Facility using a four-receiver acoustic Doppler velocimetry (ADV, which would be referred to as the Nortek Vectrino II). The second set of experiments was conducted in an open channel facility using a planar particle image velocimetry (PIV). In both cases, the x coordinate is aligned with the streamwise flow direction, with y coordinate in the wall-normal direction and z coordinate in the lateral direction. The origin of all three coordinates is as follows: $x = 0$ is at the nozzle exit, $y = 0$ on the bottom of the channel and $z = 0$ in the symmetry plane. The two water channel facilities are described next.

3.1.1 Large water channel

The large-scale experiments were conducted in a horizontal rectangular recirculating water channel at the Hydraulic Research and Testing Facility (HRTF), University of Manitoba, as shown in Figure 3.1. The channel is 1500 mm wide, 950 mm deep and 7000 mm long. The bottom channel was made of plywood overlaid with an acrylic sheet. One of the side walls was made of water resistant plywood, and the other wall made from a 25.4 mm thick acrylic sheet to facilitate flow visualization. Pressure taps of 3 mm diameter were made on the bottom of the channel and one side of the wall (acrylic side). The taps are 75 mm apart for the first 2000 mm length of the channel. The spacing is increased to 150 mm between 2000 mm to 5000 mm length of the channel. Flexible

(piezometric) tubes were fitted to the end of the pressure taps. The other end of the flexible tube is attached to a manometer board to allow pressure measurements in the streamwise direction, as shown in Figure 3.2.

The flow was driven by a fixed speed 65 hp centrifugal pump from a reservoir through 350 mm polyvinyl chloride (PVC) pipelines. The water flow into the head tank of the channel was regulated by a variable control valve and the discharge was measured by an ultra-sonic flow meter. The flow is conditioned by series of 200 mm long pipes with a diameter of 60 mm as shown in Figure 3.1. These pipes are held in place by stainless steel wire screens on both the upstream and downstream sections. The water (at room temperature) goes through a finite aspect ratio rectangular nozzle to form the 3D jets. The rectangular nozzles are made from stainless steel plates of thickness 25.4 mm as shown in Figure 3.3. The nozzle dimension is 60 mm high and 360 mm wide yielding an aspect ratio of 6. A schematic of the nozzle assembly plate (Figure 3.3) shows that the nozzles are offset at distances 0, 120, 240 and 360 mm yielding offset height ratios (h/b_o) of 0 (subsequently referred to as the wall jet), 2, 4 and 6, respectively.

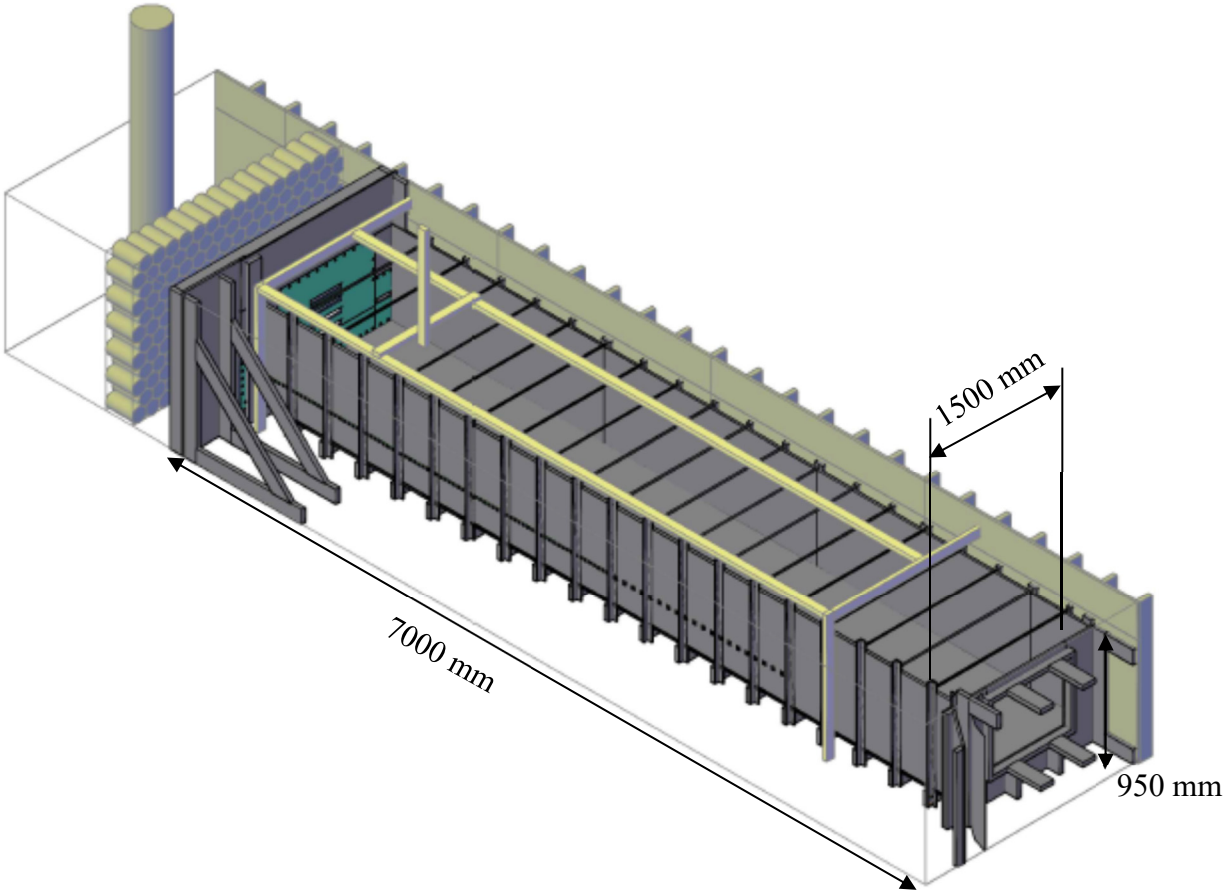

Figure 3.1 Model of the large water channel

Figure 3.2 Piezometric tubes aligned on a manometry board

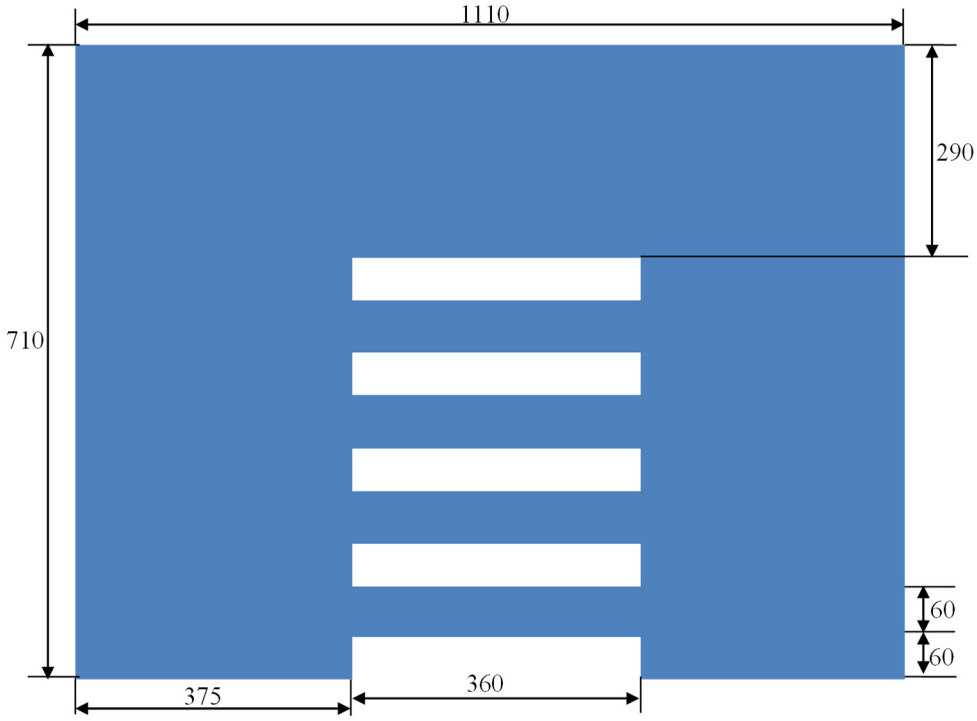

Figure 3.3 Schematic of nozzle plate (all dimensions in millimeters)

3.1.2 Small water channel

A scaled down experiment was conducted using a planar PIV to investigate the effect of h/b_o and rib location on the offset jet. The open channel was designed and constructed by Engineering Laboratory Design, Inc., Minnesota, USA. Figure 3.4 depicts the test facility for the small scale experiment, with Fig. 3.5 showing the complete setup. The dimensions of the open channel are 2500 mm long and a square cross section of 200 × 200 mm^2. The side walls as well as the bottom of the water channel were made from a smooth acrylic to facilitate optical access. Series of steel plates and honey combs are fitted within the settling chamber of the channel which is located upstream of the test section. This is to condition the flow before entering the contraction section prior the test section. The area contraction ratio for the contraction section of the channel is six–to–one. The presence of the contraction causes the flow to accelerate thereby reducing the turbulence level. Flow through the water channel is driven by a belt-driven pump. The

specification of the motor that drives the pump is as follows: 25 hp, 600 V A/C 3-phase 60 Hz. The speed of the motor is controlled by a Toshiba transistor inverter.

The nozzle assembly consists of an artificial floor, a dam assembly and nozzle plates as shown in Figure 3.4a. The artificial floor was first screwed unto the main floor of the open channel. The dam assembly is tight-fitted into the groove within the artificial floor and the sides of the open channel. In order to ensure the nozzle assembly was water-tight, a silicon-foam rubber gasket (7 mm wide and 1 mm thick) was placed within the groove along the dam assembly. Rectangular nozzles with dimensions 8 mm high, b_o, and 48 mm wide, b, used for the current studies were made from smooth acrylic plate of 6 mm thickness. Thus, an aspect ratio of 6 was maintained for both the large and small scale studies. The four nozzles used in the present studies were made on separate acrylic plates as shown in Figure 3.4a. The rectangular nozzles were positioned at offset heights, h, of 0, 16, 32 and 64 mm yielding offset h/b_o of 0, 2, 4 and 8, respectively. The nozzle assembly was mounted 150 mm from the inlet of the water channel.

3.2 Measurement procedure

3.2.1 ADV system

The type of ADV used for the present studies is the Nortek Vectrino II which is shown in Fig. 3.6a. The Nortek Vectrino II measures 3D velocity components of water by measuring the Doppler shift. This is attained by transmitting a short pulse of sound from the central excitation transmitter. The sound waves are then reflected and recorded by each of the four transducers surrounding the transmitter. The Nortek Vectrino II is a profiling ADV. There is not one sampling volume, as is typical of ADV's. The sampling volume is divided into several cells and the number and size of the cells are user-defined. The sampling volume is cylindrical with a

(a)

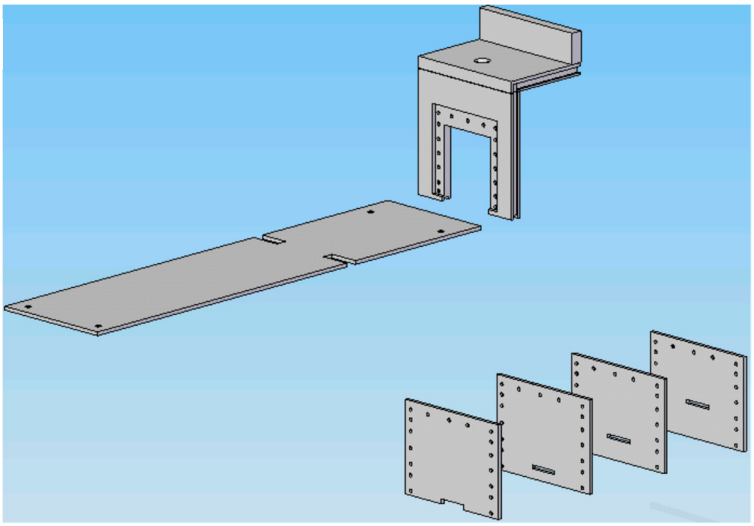

(b)

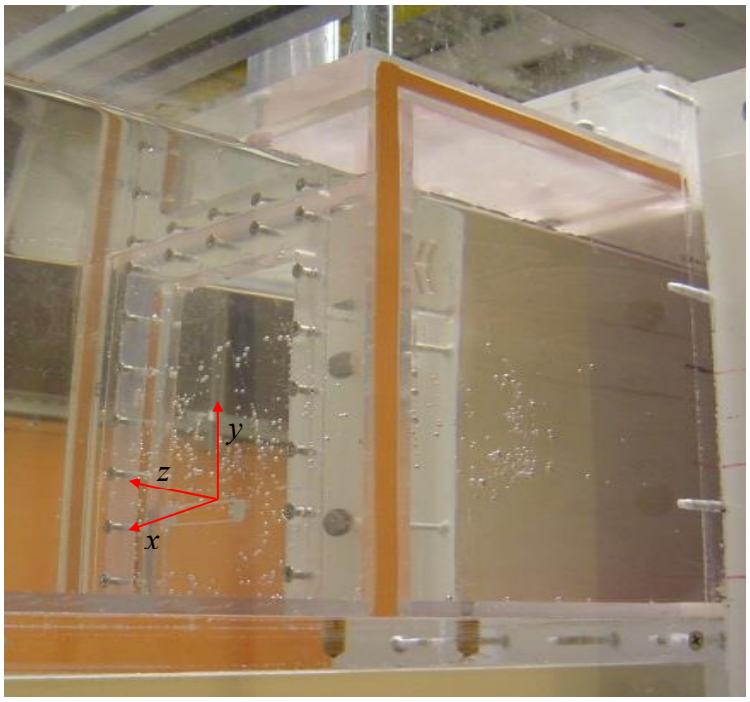

Figure 3.4 Setup for the small water channel experiment (a) nozzle assembly, and (b) complete facility

diameter of 6 mm and a user selectable total length between 3–30 mm. In the present investigation the sampling volume was divided into 21 cells of 1 mm length as indicated in Fig. 3.6b. Although the probe is immersed in the water, it does not interfere with the measured

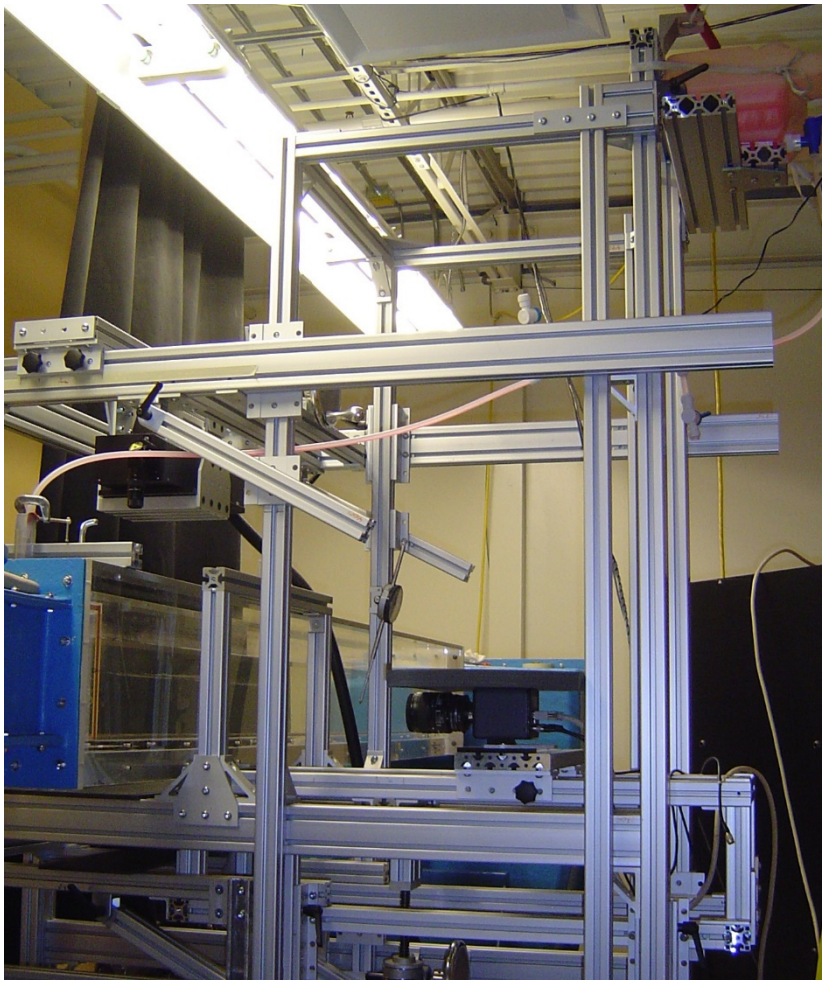

Figure 3.5 Complete setup in the small water channel with camera and laser mounted on a traversing mechanism

sampling volume. This makes the Nortek Vectrino II a quasi-noninvasive measuring device. The 3D component of velocities is then calculated based on the frequency shift between the transmitted and reflected signal. The shift in frequency can be determined from Eqn. (3.1)

$$F_{Doppler} = -F_{source}\frac{V}{C} \tag{3.1}$$

where $F_{Doppler}$ is the Doppler shift, F_{source} is the transmitted frequency, V is the source velocity relative to the receiver and C is the speed of sound in water.

The main components of the Nortek Vectrino II are the penetrator, signal conditioning module and the probe as shown in Fig. 3.6a. The probe consists of four receiving transducers, each mounted inside a receiver arm and a transmitting transducer in the center. The transducers are covered with a hard epoxy. The four receivers are equally spaced at 90° from each other. The four transducers are angled at 30° towards the center. The configurations of the transducers make them surround the central active transducer thereby creating an intersection point 50 mm beneath the central transducer as indicated in Fig. 3.6b. In order to measure the velocity, the ADV sends out sound pulses from the transmitter at a high pulse frequency f_p. Since the flow is particle laden, the transmitted pulses are reflected back to the four receivers by seeding particles within the flow. Seeding particles (10 μm diameter neutrally buoyant spherical hollow glass spheres with specific gravity of 1.07, settling velocity of 2.45×10^{-6} ms^{-1}, and Stokes number of 0.5) was used in the present investigation to ensure that an acceptable signal to noise ratio was achieved. The estimated Stokes number indicates that the seeding particles followed the fluid streamlines. In order to obtain converged time average velocities, the data was acquired at a sampling rate of 100 Hz for 5 minutes. The adopted sampling time was based on preliminary measurements acquired for 3, 5, 10, 15, 20 and 30 minutes. Two of the four transducers measure the wall-normal component of velocity with the remaining two measuring velocity components in the streamwise and lateral directions. The ultra sound signals are initially received as an analog signal and then subsequently digitized. Knowledge of the orientation of the bi-static axes for all four receivers allows calculation of the 3D water velocity. The bi-static velocities are converted to Cartesian coordinate velocities using a 3 × 3 transformational matrix which is defined by the probe geometry. Close to the bottom of the channel, the measured velocities can be contaminated with spikes, which could possibly be due to the interference between incident and reflected pulses. These spikes are as a result of

aliasing of the Doppler signal due to the phase shift between the incident and reflected pulses outside the range of ±180°. These spikes were filtered by spike removal algorithms (Islam & Zhu, 2013; Goring & Nikora, 2002).

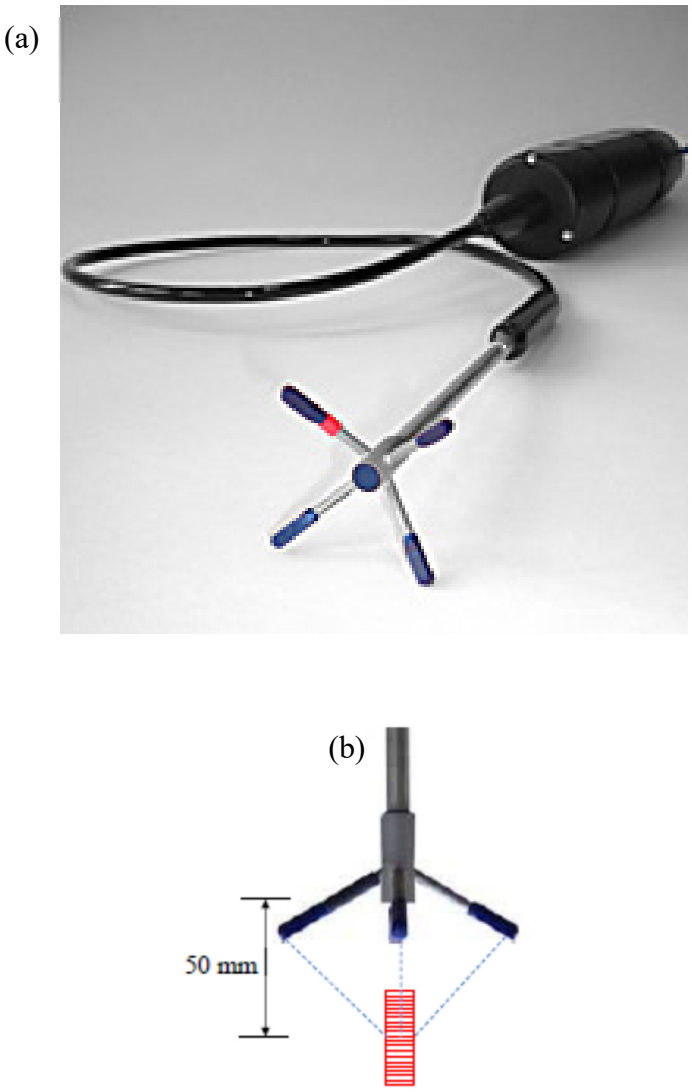

Figure 3.6 (a) An acoustic Doppler velocimeter used in the present investigation (b) sampling volume divided into 21 cells of 1 mm height

The ADV system was used to conduct velocity measurements within the large water flume located at the HRTF. Velocity measurements were conducted within the streamwise range $4 \leq x/b_o \leq 25$, which falls within the developing region of the jet as outlined by Padmanabham & Lakshmana Gowda (1991). Due to experimental constraints, velocity measurements could not be made close to the nozzle exit ($x/b_o < 4$).

3.2.2 PIV system

The velocity measurements in the small scale open channel were performed using a PIV technique. The PIV system comprises of three main components: the laser source, a charge-coupled device (CCD) camera and data acquisition system as shown in Figure 3.7. The laser source illuminates the flow field, while the camera images the flow field and the data acquisition system is used to acquire and process the captured images. The PIV is a non-intrusive optical velocity technique. The basic principles and components of the PIV are provided next and then followed by an overview of relevant information for the present study.

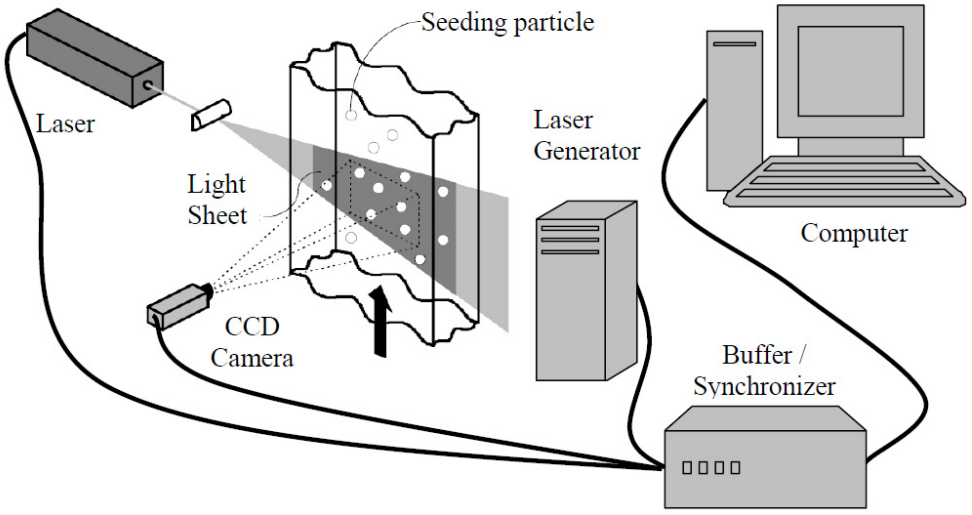

Figure 3.7 Typical experimental setup of a planar PIV system (Shah, 2009)

3.2.2.1 Basic PIV principles

The basic principle of the PIV system is as follows. The flow is seeded with small light scattering particles that follow the flow faithfully. The flow field is illuminated by a double pulsed laser sheet separated by a delay time, Δt. The light reflected by the seeding particles for the two images are captured. Once the two images are captured, they are divided into smaller subsections referred to interrogation areas (*IA*). A cross-correlation algorithm is applied to each *IA* to determine the displacement vector (Δs) between the first and second images. The corresponding velocity, V, for an *IA* is subsequently obtained from the expression $V = \Delta s/\Delta t$. The cross-correlation process is repeated for all interrogation areas within the flow field to determine the velocity vector map.

3.2.2.2 Laser source

The laser serves as a source of high intensity light that is required to freeze the motion of the flow during imaging. For most PIV systems, a double-pulsed neodymium-yttrium-aluminium-garnet (Nd:YAG) laser is used as the light source for illuminating the flow field. The Nd:YAG laser provide monochromatic light with high intensity illumination. The laser-emitted lights are passed through series of lenses thereby creating a plane sheet of light used to illuminate the flow field. Based on the field of view required, the length and width of the light sheet can then be adjusted.

3.2.2.3 Seeding particles

The required seeding particles should be small enough to faithfully follow the flow and should be large enough to scatter sufficient light to be captured by the camera. The seeding particles should also be homogeneously distributed within the flow (Westerweel *et al*. 1996). A rule of thumb is that about ten particles should be present in an *IA* for correlation. Some criteria

for selecting appropriate seeding particles should be upheld to since the PIV measures the particles velocity and not that of the fluid. In selecting the appropriate seeding particles, the following considerations must be ensured; the mean size, specific gravity, shape, width-to-size distribution and refractive index of the particle. These are all to ensure that the particles follow the flow faithfully. The seeding particles must have a desirable settling velocity, v_s, which can be estimated from Stokes law. The determination of the settling velocity was given by Mei *et al*. (1991) as;

$$v_s = \frac{\left(\rho_p - \rho_f\right) g d_p^2}{18\mu_f} \tag{3.2}$$

where ρ_p is the density of the particle, ρ_f is the fluid medium density, g is the acceleration due to gravity, d_p is the diameter of the particle and μ_f is the fluid viscosity. One other parameter of significance is the response time, τ_p, of the seeding particles, which is a measure of the tendency of the particles to attain velocity equilibrium within the flow. The response time can be estimated from Eqn. (3.3) as given by Raffel *et al*. (1998);

$$\tau_p = \rho_p \frac{d_p^2}{18\mu_f} \tag{3.3}$$

3.2.2.4 Recording device

The CCD camera is the most widely used recording device for PIV systems. This is because they offer high resolution, high frame rates and are also highly sensitive. However, photographic film cameras are a viable choice when very high resolutions are required. The CCD sensor is a significant component of the camera. The sensor is made up of an array of detectors known as pixels. The CCD camera uses high-performance progressive scan interline CCD chips that consist of an array of photosensitive cells as well as storage cells. During operation, the first captured image on the photosensitive cells is transferred to the storage cells. The second image is stored on

the photosensitive cells. Both images are then transferred sequentially from the camera to the storage device of the computer thereby maintaining an exposure interval Δt of less than 1 μs.

3.2.2.5 Image processing

In order to extract the displacement information from the recorded images by the camera, the images are sub-divided into interrogation areas. A correlation of the first and second images on the two frames for each interrogation area yields the average displacement vector. At the end of the correlation, a vector map of the average displacements for all the interrogation areas is generated. The image processing procedure is commonly done by either of these two correlation methods: an auto-correlation or cross-correlation.

3.2.2.6 Overview for current experiment

In the present study, the flow was seeded with 10 μm silver coated hollow glass spheres with a specific gravity of 1.4. The settling velocity and response time of the seeding particles were estimated to be 1.56×10^{-5} ms^{-1} and 7.78×10^{-6} s, respectively. The obtained settling velocity is insignificant compared to the measured streamwise velocities. In a similar manner, the response time obtained is very small compared to the sampling times employed in this study. This implies that the seeding particles indeed followed the flow faithfully. A New Wave Solo Nd:YAG double-pulsed laser with maximum energy of 120 mJ/pulse at 532 nm wavelength was used to illuminate the flow field. The laser sheet was aligned with the mid-span of the test section for measurements in the x–y plane, which coincided with the center of the nozzle, with the camera mounted perpendicular to the x–y plane. For measurements in the x–z plane, the laser sheet was aligned at y_m (which is the wall-normal location for the maximum streamwise velocity). Likewise for measurements in the lateral direction, the camera was mounted perpendicular to the lateral plane.

Scattered light from the tracer particles were captured with a 12-bit FlowSense EO 4M CCD camera that has a resolution of 2048 pixels × 2048 pixels and a pixel pitch of 7.4 μm. The CCD camera was fitted with a green bandpass filter of wavelength 530 nm. Dantec Dynamics commercial software (DynamicStudio version 3.4) was used to control the data acquisition. A camera field of view of 120 × 120 mm in the *x–y* plane and 118 × 118 mm in the *x–z* plane was used. The background noise was minimized by using a thin laser sheet with thickness of approximately 1 mm within the field of view of the camera. This has been observed to reduce the number of de-focused particles (Wang & Tan, 2007). The time interval between pulses was chosen such that the maximum particle displacement was smaller than 25% of the interrogation area size. This is recommended to ensure a good signal-to-noise ratio. The time interval was determined from Eqn. (3.4)

$$\Delta t = \frac{N \times d_{pitch}}{4 M_f U_m} \tag{3.4}$$

where N is the interrogation area window size, d_{pitch} is the pixel pitch, M_f is the magnification factor and U_m is the maximum velocity of the flow.

Measurements were performed in five planes spanning a streamwise extent of x/b_o = 0 to 80. In order to determine the appropriate number of instantaneous images required for this study, a convergence test was conducted. From the results obtained by analyzing the mean flow field and turbulent statistics using different sample sizes (500, 1000, 1500, 2000, 2500, 3000 and 4000 images), 2000 instantaneous images were determined to be sufficient to compute the mean velocities and turbulence statistics. Profiles of both mean velocities and turbulent intensities are indicated Figure 3.8 to illustrate the convergence of these quantities. In view of this, a sample size in excess of 4000 instantaneous image pairs was acquired in each measurement plane to calculate

the ensemble averaged statistics reported in this study. The instantaneous images were processed using the adaptive correlation option of DynamicStudio developed by Dantec Dynamics. The adaptive correlation utilizes a multi-pass fast Fourier transform cross-correlation algorithm to determine the average displacement of the particles within the interrogation area. The particle displacement was determined using a three-point Gaussian curve fit. An in-house MATLAB code was then used to calculate the mean velocities and higher order turbulence statistics.

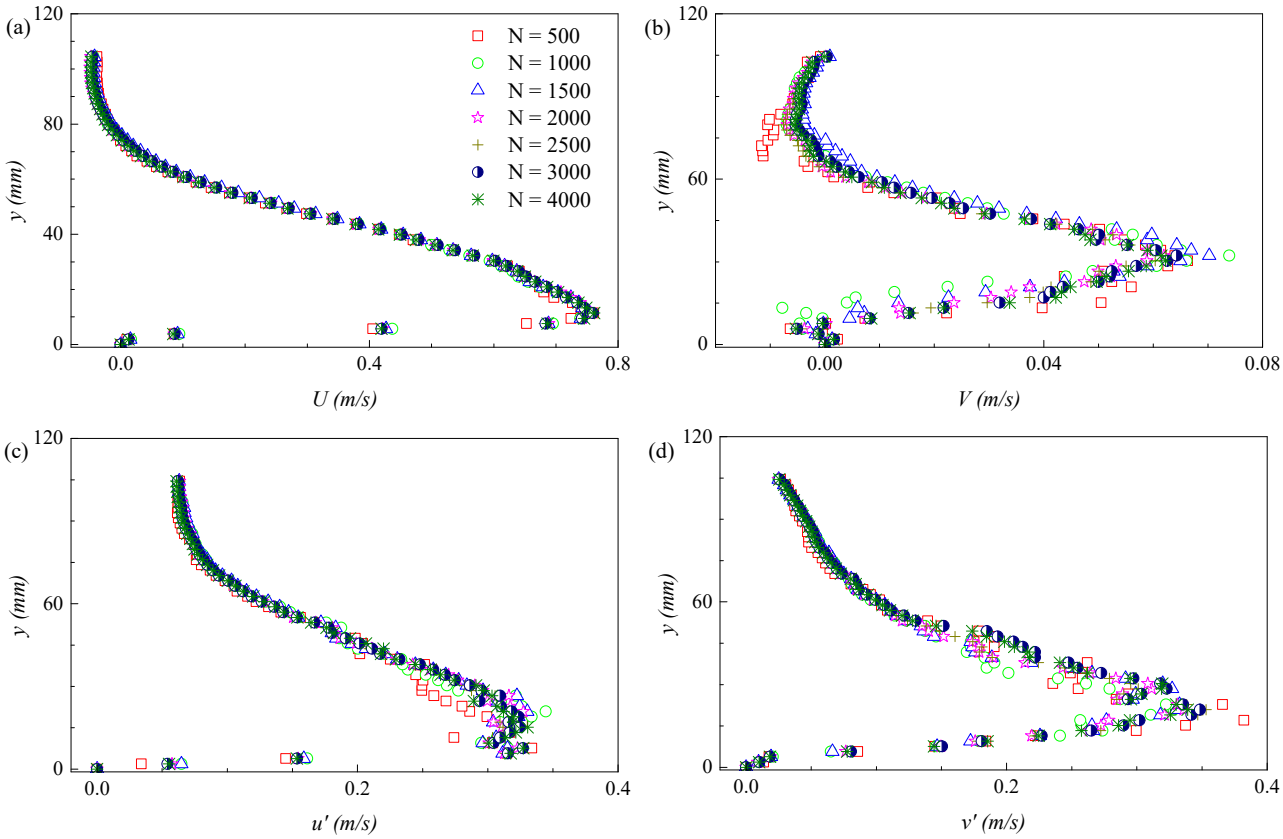

Figure 3.8 Profiles plots of the different sample sizes for (a) U, (b) V, (c) u' and (d) v'

3.3 Experimental conditions

3.3.1 Large water channel

Detailed velocity measurements were performed at several downstream locations with the ADV system. The various experimental conditions considered are summarized below.

Table 3.1 Experimental test condition for the offset height ratio configuration

Offset ratio (h/b_o)	b_o (mm)	b (mm)	Area (m^2)	U_o (ms^{-1})	Q (m^3s^{-1})	Re × 10^3	Tailwater (mm)
0	60	360	0.022	0.88	0.019	53	750
2	60	360	0.022	0.88	0.019	53	750
4	60	360	0.022	0.88	0.019	53	750
6	60	360	0.022	0.88	0.019	53	750

Table 3.2 Experimental test condition for the expansion ratio configuration

Expansion ratio	b_o (mm)	b (mm)	Area (m^2)	U_o (ms^{-1})	Q (m^3s^{-1})	Re × 10^3	Tailwater (mm)	h/b_o
0.24	60	360	0.022	0.88	0.019	53	750	4
0.49	60	735	0.044	0.88	0.039	53	750	4
0.75	60	1125	0.068	0.88	0.059	53	750	4
1	60	1500	0.090	0.88	0.079	53	750	4

Table 3.3 Experimental test condition for the surface roughness configuration

Roughness	b_o (mm)	b (mm)	Area (m^2)	U_o (ms^{-1})	Q (m^3s^{-1})	Re × 10^3	Tailwater (mm)	h/b_o
smooth	60	360	0.022	0.88	0.019	53	750	4
ribs: p/k=2, 4 & 8; k=12.7 mm	60	360	0.022	0.88	0.019	53	750	4
gravel (d=12.7mm)	60	360	0.022	0.88	0.019	53	750	4

3.3.2 Small water channel

Two experimental conditions were investigated in the small water channel. The first set of experiments was to investigate a scaled down version of the offset height ratio experiment conducted in the large channel. Experiments were conducted for nozzles offset height ratios of 0, 2, 4 and 8. The approach bulk velocity of the flow ranged from 0.75–1.51. This yielded Reynolds number ($\mathrm{Re} = (b_o U_o)/\nu$) and Froude number ($\mathrm{F} = U_o/(g b_o)^{0.5}$) based on the nozzle height (b_o) in the range of 6000–12080 and 2.7–5.4, respectively, where v is the kinematic viscosity of water and g is the acceleration due to gravity. The tailwater depth, y_t, of the flow was maintained constant at 116 mm throughout the experiment.

The second set of experiments was conducted at an offset height ratio of 2. As shown in Figure 3.9, a 2D acrylic rib of 10 × 10 mm square cross section spanning the entire channel width was used. Three sets of experiments corresponding to placement of the rib at x/b_o = 1.25, 3.45 and 6.25 from the nozzle exit (which are hereafter referred to as R1, R2 and R3, respectively, for brevity) were performed. Based on the first experimental run, the mean reattachment length for $h/b_o = 2$ jet was estimated as $4.4b_o$. Therefore, R1, R2 and R3 corresponded to streamwise locations within the recirculation, reattachment and developing regions, respectively. The tailwater depth, y_t, was maintained constant at 116 mm, which was sufficiently high to suppress the formation of a hydraulic jump. The bulk velocity, U_o, of the flow was 0.95 ms^{-1} yielding a Reynolds and Froude numbers of 7.6×10^3 and 3.4, respectively.

Detailed PIV measurements were performed at locations downstream of the nozzles, starting at the position where both the x and y coordinates are zero in the x–y plane. The streamwise extent of measurements in the x–y plane spanned $0 \leq x/b_o \leq 80$. Measurements in the x–z plane were conducted at y_m spanning a streamwise location within the range $15 \leq x/b_o \leq 60$.

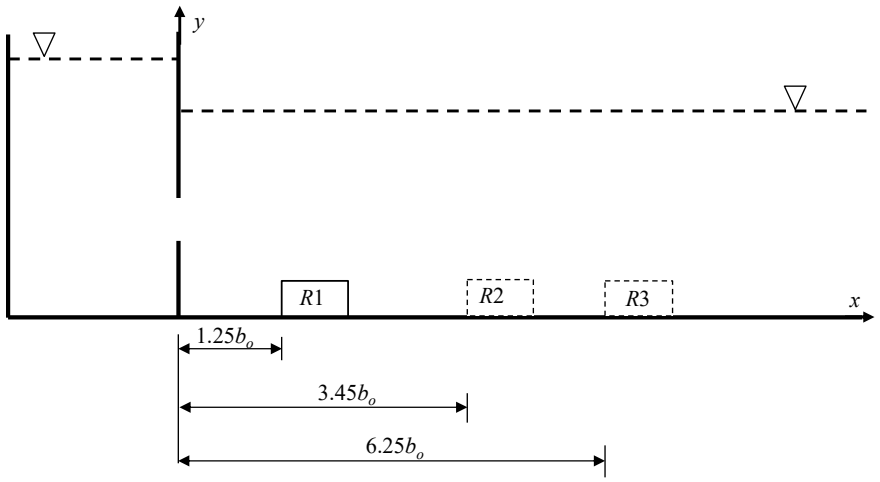

Figure 3.9 Side view of the rib experimental setup

Before proceeding to analyze the acquired experimental data, profiles of the streamwise mean velocity for the wall and offset jets were compared to empirical correlations for plane wall jets proposed by Verhoff (1963) and Schwarz & Cosart (1961). The proposed equations by Verhoff (1963) and Schwarz & Cosart (1961) are given in Eqns. (3.5) and (3.6), respectively. Data for the offset jets were extracted at $x/b_o = 50$ which was in the self-similar region of the flow. Figure 3.10 show that there was good agreement between the correlations and experimental data within the inner layer (except close to the wall) and part of the outer shear layer. The deviation of the experimental data from the correlations is as a result of the backflow region formed within the outer shear layer of the present configuration. The agreement between the experimental data and the empirical correlations reveals the accuracy of the present data.

$$\frac{U}{U_m} = 1.48\eta^{1/7}[1 - erf(0.68\eta)] \tag{3.5}$$

$$\frac{U}{U_m} = e^{[-0.937(\eta\text{-}0.14)^2]} \tag{3.6}$$

where η and erf are $y/y_{0.5}$ and error function, respectively.

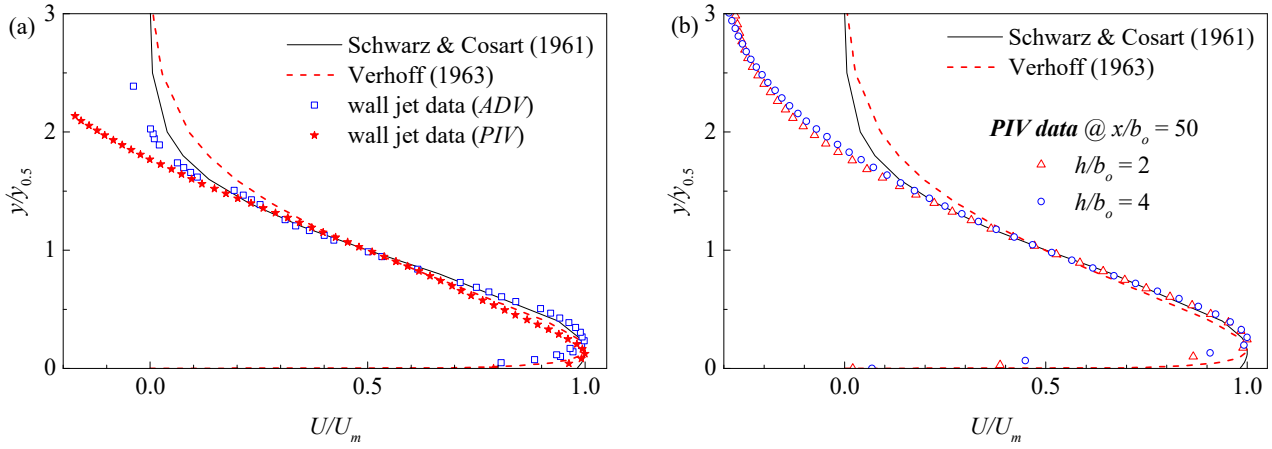

Figure 3.10 Comparison of present experimental data to proposed empirical correlations for wall jets (a) wall jet and (b) offset jets

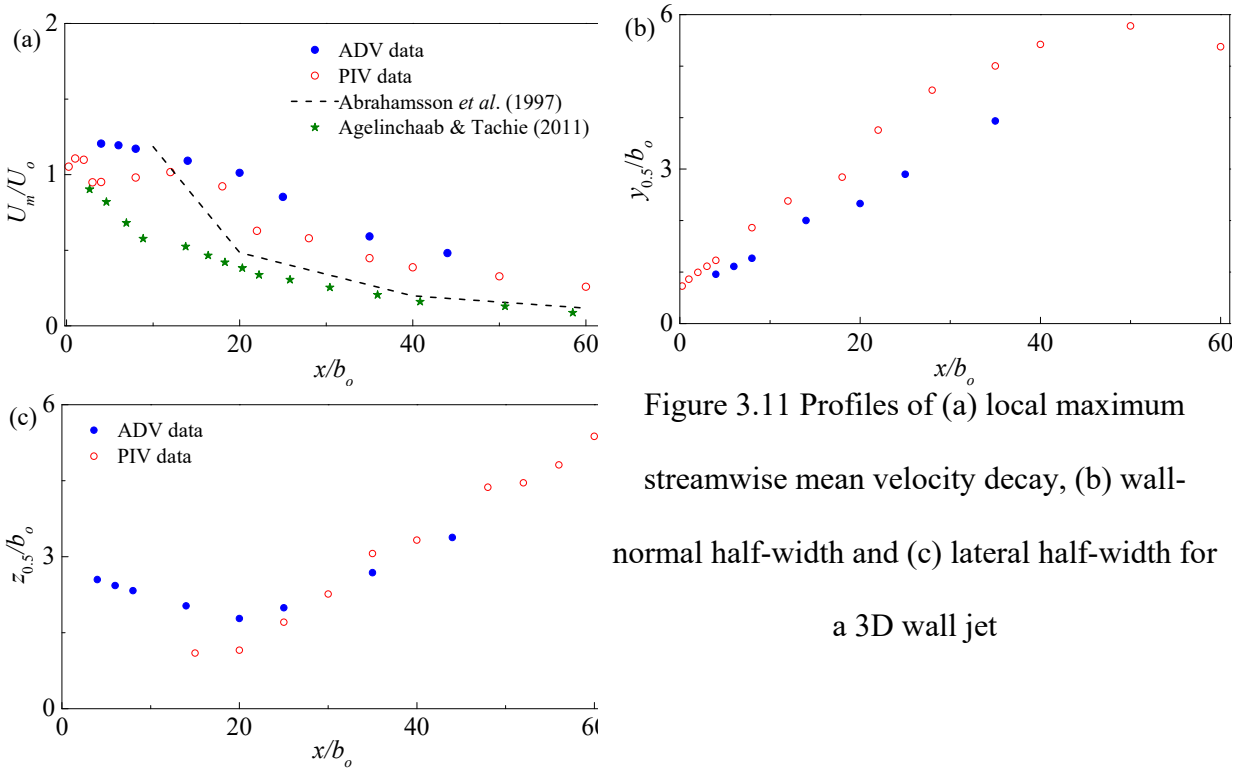

Figure 3.11 Profiles of (a) local maximum streamwise mean velocity decay, (b) wall-normal half-width and (c) lateral half-width for a 3D wall jet

Figure 3.11 depicts the decay of U_m, wall-normal half-width, $y_{0.5}$ and lateral half-width, $z_{0.5}$. For the estimated mean characteristics, there was a considerable agreement between the data for both the large and small water channels. The differences are within the uncertainty involved in

estimating these mean characteristics. The present results are compared to previous 3D wall jet results. Figure 3.11a indicates a slower decay of U_m compared to experimental results of Agelinchaab & Tachie (2011a) as well as correlation proposed by Abrahamsson *et al*. (1997). The discrepancy can be attributed in part to the different nozzle geometries utilized in the various studies as well as the free surface effect on the jet in the present configuration. Figures 3.11b and 3.11c reveal that the 3D wall jet spread at similar rates for both large and small water channels data. The initial decrease in the lateral half-width is attributed to the combined effects of the vena-contracta and deformation of elliptic vortical structures (Lee & Baek, 1994).

3.4 Experimental uncertainty

A detailed uncertainty analysis for the ADV measurements was conducted using the moving bootstrap technique reported by Garcia *et al*. (2006) and presented by Durand (2014) and would not be repeated herein. Based on the analysis, the uncertainty in the measurements in the streamwise and wall-normal mean velocities, lateral mean velocity and Reynolds stresses were ±3%, ±5% and ±15%, respectively.

The measurement uncertainty for the PIV measurements was determined using the approach outlined by Forliti *et al*. (2000), Prasad *et al*. (1992) and Keane & Adrian (1991). These uncertainties were estimated by taking into consideration both the bias and precision errors. The accuracy in the velocity measurements using the PIV technique is limited by the accuracy of sub-pixel interpolation of the displaced correlation peak. Based on the interrogation area and the algorithm used to estimate the mean velocity and turbulence quantities, the uncertainty in the mean velocities, Reynolds stresses and third order moments at 95% confidence level was estimated to be ±2.7% and ±12% and ±14% of the peak values, respectively. A complete uncertainty analyses have been provided in Appendix A.

The table below provides an overview of the objectives achieved with the different journal articles.

Table 3.4 Contributions from the different journal articles towards the overall research objectives

Paper title	***Achieved objective***
Flow characteristics within the recirculation region of three-dimensional turbulent offset jet **(Paper I)**	***h/b$_o$*** (PIV); Main contribution: The two-point correlation analysis has been applied to the recirculation region to investigate the large-scale structures and also quantify the integral length scales of these structures.
Experimental study of the flow structures of 3D turbulent offset jets **(Paper II)**	***h/b$_o$*** (PIV); Main Contribution: Both the two-point correlation analysis and proper orthogonal decomposition were applied to the developing and self-similar regions of the 3D offset jet to investigate the characteristics of the large-scale structures. The latter is the pioneer analysis conducted for 3D offset jets.
Flow characteristics of an offset jet over a surface mounted square rib **(Paper III)**	***Rib placement*** (PIV); Main contribution: Extended the quadrant analysis and probability density function to the flow field of a 3D offset jet.
Acoustic Doppler velocimeter measurements of a submerged three-dimensional offset jet flow over rough surfaces **(Paper IV)**	***Surface roughness*** (ADV); Main contribution: Presented all six Reynolds stress tensors measured simultaneously for a 3D offset jet within the symmetry and lateral planes.
Submerged turbulent offset jet issuing from a rectangular nozzle with varying expansion ratio **(Paper V)**	***h/b$_o$ and expansion ratio*** (ADV); Main contribution: Estimated the structure parameter without approximating the turbulent kinetic energy since all three normal stresses were measured. Since $\overline{w^2}$ was directly measured, a comparison was made with the widely used approximation in boundary layer flows within the flow domain of 3D offset jets.

CHAPTER FOUR

4 PAPER I

Flow Characteristics within the Recirculation Region of Three-dimensional Turbulent Offset Jet

4.1 Abstract

The preset study investigates the flow characteristics within the recirculation region of three-dimensional offset jets using a PIV technique. Measurements were performed for four nozzle offset height ratios (h/b_o) of 0, 2, 4 and 8. The discharged jet entrained the ambient fluid as depicted by streamlines superimposed on the mean velocity contours. Analysis of the flow field showed that the maximum streamwise mean velocity decay rate increased with increasing offset height ratio. Wall-normal spread rates of 0.066 and 0.016 were obtained for h/b_o = 0 and 2 offset jets, respectively, and lateral spread rates of 0.116, 0.114 and 0.096 for h/b_o = 0, 2 and 4 offset jets respectively. The reattachment lengths of the jets increased with increasing offset height ratio. Profiles of the mean velocities, Reynolds stresses and some of the budget terms (specifically, production, diffusion and convective terms) in the turbulent kinetic energy transport equation have been investigated. It was observed that increasing the offset height ratio influenced the distribution of these quantities within the recirculation region. A two-point velocity correlation analysis was performed to analyze the flow structures within the recirculation region. The two-point correlation revealed some large-scale structures and was observed to increase in size as the offset height ratio increased. The two-point correlation analysis also revealed that the integral length scales within the recirculation region of the flow increased with increasing offset height ratio.

4.2 Introduction

Jets can be classified into one of the following types: free, wall or offset jets. A free jet is formed when the origin of the discharged jet is sufficiently far from a boundary. The formation of a wall jet is established when the jet is issued at a boundary. An offset jet is formed when a jet discharges into an ambient medium above the surface of a boundary. Close to the nozzle exit, an offset jet possesses characteristic features similar to those of free jets and then further downstream after the reattachment point, has characteristics of wall jets. Therefore, the offset jet has characteristics of both free and wall jets, and is relatively more complex than a free jet and a wall jet.

A schematic diagram illustrating the features of an offset jet is depicted in Fig. 4.1. The streamwise, wall-normal and lateral directions are represented as x, y and z axis, respectively, as indicated in Figs. 4.1a and 4.1b. The origin in the $x - y$ plane of the jet is situated at the bottom wall and mid-span of the channel. The discharge bulk velocity, nozzle height and streamwise maximum mean velocity are represented by U_o, b_o and U_m respectively. As shown in Fig. 4.1a, the features of the offset jet include an offset height, h – which is the distance from the bottom of the channel ($y = 0$) to the origin of the discharged jet; wall-normal spread ($y_{0.5}$) – which is the wall-normal distance from the bottom of the channel to to the location where the local streamwise mean velocity is half the local maximum velocity (i.e., $U = 0.5U_m$); lateral spread ($z_{0.5}$) which is the lateral distance from the symmetry plane to the location where the local velocity is half the local maximum velocity (i.e., $U = 0.5U_m$). The wall-normal location of U_m, denoted by y_m distinguishes the inner layer ($y < y_m$) of the flow from the outer layer ($y > y_m$) while the reattachment length (L_e) gives an indication of the streamwise extent of the recirculation region of the flow. The wall-normal and lateral spreads give an indication of how

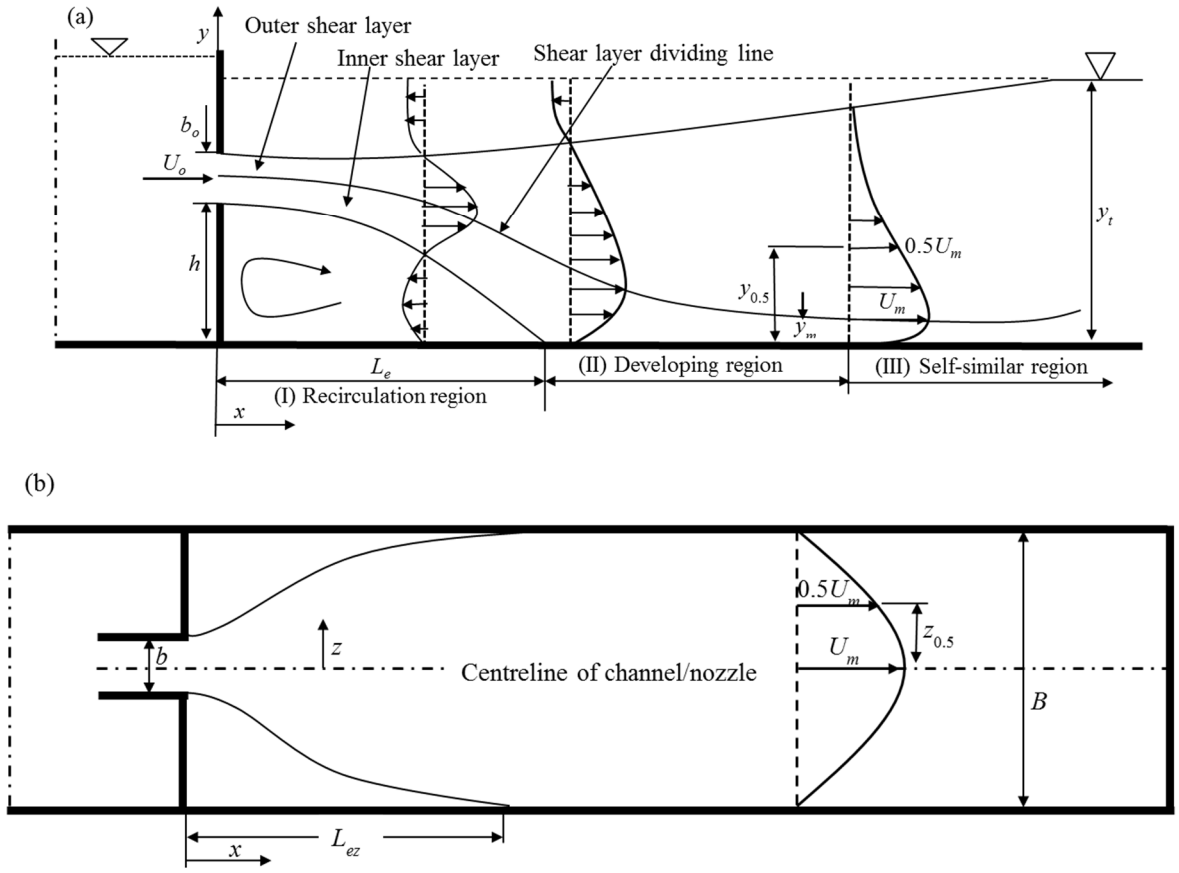

Figure 4.1 Schematic diagram of an offset jet discharged into tailwater (a) side view and (b) plan view

the jet spreads in the wall-normal and lateral directions, respectively, due to the entrainment of the ambient fluid by the discharged jet. The symbol y_t in Fig. 4.1a corresponds to the tailwater depth. The width of the channel is represented by B, nozzle width (b), and reattachment length in the lateral plane (L_{ez}) as indicated in Fig. 4.1b.

When a fluid jet is discharged from an offset nozzle into a channel, it entrains the surrounding fluid. During the entrainment, a low pressure region is created underneath the jet due to the presence of the wall. This causes the jet to deflect towards the wall and eventually reattaches to the wall to form a wall jet (Hoch & Jiji, 1981). The deflection of the jet towards the bottom wall

is referred to as the Coanda effect (Miozzi *et al*., 2010). The velocity of the deflected jet reduces as it approaches the wall causing a pressure rise within the jet. The pressure increases inside the jet until it reaches a maximum at the reattachment point. When the jet reattaches to the wall, it accelerates due to the formation of a favorable pressure gradient as a result of the reattachment. Turbulent wall jet conditions are established further downstream beyond the reattachment point. Figure 4.1a shows that offset jets have three distinct regions in the streamwise direction of the flow; the recirculation region, reattachment region and wall jet region. The mean velocity distribution evolves from the recirculation region through to the wall jet region where it recovers to that of a classical wall jet flow. The flow field of an offset jet is very complex, yet the characteristics of the flow within the recirculation region of an offset jet have not received considerable research attention. Offset jets are encountered in several engineering applications. Applications such as fuel injection system, combustion chambers of gas turbines, energy dissipation devices downstream of hydraulic structures (Mossa *et al*., 2003), environmental transport and mixing of effluent in lakes and rivers (Bhuyian *et al*., 2011; Tachie *et al*., 2004) are all controlled by the flow behavior of offset jets.

Given the numerous engineering applications of offset jets, several studies have been conducted in order to better understand the salient features of the flow field. There have been many experimental investigations on the flow field of two-dimensional (2D) offset jets which are formed when $b/B = 1$ (Bhuiyan *et al*., 2011; Gao & Ewing, 2007; Nasr & Lai, 1998, 1997; Yoon *et al*., 1995; Pelfry & Liburdy, 1986; Ayukawa & Shakouchi, 1976). Most of these studies focussed on the evolution of the mean velocity field, pressure distribution within the jet and the reattachment length of the offset jet by utilizing Pitot tubes, hot-wires, laser Doppler anemometry (LDA) and particle image velocimetry (PIV). Pelfrey & Liburdy (1986) reported the flow characteristics

within the recirculation region of an offset jet, but the investigations were restricted to the mean flow field. Some studies have also investigated the flow properties of three-dimensional (3D) offset jets which are formed when $b/B < 1$, (e.g., Agelinchaab & Tachie, 2011b; Davis & Winarto, 1980). Regarding information from the flow field of 3D offset jets, the measurements of Davis & Winarto (1980) for round offset jets were restricted to regions beyond the reattachment point ($x > L_e$). The authors reported only the mean velocity and Reynolds stresses. The most comprehensive study of 3D offset jets was reported by Agelinchaab & Tachie (2011b). They performed measurements for round offset jets with h/b_o of 0, 0.5, 1.5 and 3.5 at three different Reynolds numbers (Re): 5000, 10,000 and 20,000. The mean velocity, Reynolds stresses and higher order turbulence statistics ($\overline{u^3}$, $\overline{u^2v}$, $\overline{uv^2}$ and $\overline{v^3}$) were obtained to explain the flow behaviour. The flow charateristics (e.g., decay and spread rates, reattachment length, profiles of mean velocities, turbulence intensities and Reynolds shear streses) were observed to be nearly independent of Reynolds number (Agelinchaab & Tachie, 2011b). In the near field of the 3D offset jet flow, Agelinchaab & Tachie (2011b) observed that the flow charateristics were influenced by the offset height ratio. This is an indication that the flow characteristics within the recirculation region of 3D offset jets are significantly affected by offset height ratio. Moreover, the triple velocity correlations from the studies of Agelinchaab & Tachie (2011b) were obtained within the self-similar region (the region of the flow where the normalized streamwise mean velocity exhibit no variation with streamwise distance). Since majority of these studies concentrated mostly on the self-similar region of the flow, there is the need to investigate the flow behavior within the recirculation region, which is vital to the flow development of offset jets. Sailient quantities such as u', v', $\overline{uv}$ and the budget terms that have been reported within the self-similar region are also essential to understanding the flow behavior within the recirculation region.

Majority of the studies presented so far reported mainly one-point or point-wise statistics such as U, V, $\overline{u^2}$, $\overline{v^2}$. Although these measurements provide useful information about the turbulence field of offset jets, they cannot adequately describe the entire turbulence field. There is therefore the need to complement the one-point statistics with the two-point auto correlation which can be used to investigate the spatial extent over which the turbulence field is correlated (Agelinchaab & Tachie, 2011b). The two-point correlation analysis have been widely applied to boundary layer flows to investigate the spatial extent and inclination of hairpin-like structures (Volino *et al*., 2007). To date the only investigation to have applied the two-point correlation analysis to the flow field of 3D offset jets was that conducted by Agelinchaab & Tachie (2011b). The analysis, however, was limited to the self-similar region of the flow.

In view of this, the primary objective of the present study is to investigate the effects of offset height ratio (h/b_o) on the flow characteristics within the recirculation region of 3D offset jets. Comprehensive measurements of one-point and two-point turbulence statistics were carried out using a PIV for offset jets with four different offset heights. The results of the present study will provide information on the mean flow characteristics as well as higher order turbulence statistics.

4.3 Experimental setup and measurement procedure

4.3.1 Experimental facility

The experiments were conducted in a 2500 mm long open water channel with a square cross section of 200 × 200 mm^2. The side walls and channel bottom were made of smooth acrylic to facilitate optical access. The nozzle assembly was mounted 150 mm from the inlet of the water channel. Rectangular nozzles with dimensions 8 mm high (b_o) and 48 mm wide used for the current studies were made from smooth acrylic plate of 6 mm thickness.

4.3.2 PIV system and measurement procedure

The velocity measurements were performed using a planar PIV system. The flow was seeded with 10 μm silver coated hollow glass spheres having a specific gravity of 1.4. The settling velocity and response time of the seeding particles were estimated to be 1.56×10^{-5} ms^{-1} and 7.78×10^{-6} s, respectively. These values ensure that the seeding particle used in the present studies followed the flow faithfully. A New Wave Solo Nd:YAG double-pulsed laser with maximum energy of 120 $mJpulse^{-1}$ at 532 nm wavelength and 15 Hz repetition rate was used to illuminate the flow field. The laser sheet was aligned with the mid-span of the test section, which coincided with the center of the nozzle. Scattered light from the tracer particles were captured with a 12-bit FlowSenseEO 4M CCD camera that has a resolution of 2048 × 2048 pixels and a pixel pitch of 7.4 μm. The CCD camera was fitted with a green bandpass filter of wavelength 530 nm. Dantec Dynamics commercial software (DynamicStudio version 3.4) was used to control the data acquisition. A camera field of view of 120 × 120 mm in the $x - y$ plane and 118 mm × 118 mm in the $x - z$ plane was used. The background noise was minimized by using a thin laser sheet with thickness of approximately 1 mm within the field of view of the camera. This has been observed to reduce the number of de-focused particles (Wang & Tan, 2007). The interrogation area size was set to 64 pixels × 64 pixels with 50% overlap in both directions. The time interval between pulses was chosen such that the maximum particle displacement was smaller than 25% of the interrogation area size. Measurements were taken in four planes spanning a streamwise extent of $x/b_o = 0$ to 60. A sample size of 4000 instantaneous image pairs was acquired in each measurement plane to calculate the ensemble statistics reported in this study. The instantaneous images were processed using the adaptive correlation option of DynamicStudio developed by Dantec Dynamics. The adaptive correlation utilizes a multi-pass fast Fourier transform cross-correlation

algorithm to determine the average displacement of the particles within the interrogation area. The particle displacement was determined by using a three-point Gaussian curve fit. An in-house MATLAB code was then used to calculate the mean velocities and higher order turbulence statistics.

4.3.3 Test conditions and measurement uncertainties

Detailed measurements were taken from locations downstream of the nozzles, starting at the position where both the x and y coordinates are zero. Measurements in the lateral plane ($x - z$ plane) were taken at y_m. The tailwater depth, y_t, was maintained constant at 116 mm throughout the experiment. Four different runs were made for nozzles with offset height ratios (h/b_o) of 0 (subsequently referred to as the wall jet), 2, 4 and 8. The bulk velocity of the flow was between 1.09–1.30 ms^{-1} yielding a Reynolds and Froude numbers based on b_o in the range of 6000-12080 and 2.7–5.4 respectively. The experimental measurement uncertainties were determined using the approach outlined by Forliti *et al*. (2000), Prasad *et al*. (1992) and Keane & Adrian (1991). The uncertainties were estimated by taking into consideration both the bias and precision errors. The accuracy of velocity measurements using a PIV system is connected to the accuracy of the sub-pixel interpolation of the displacement correlation peak. The uncertainties in the mean velocities and turbulence statistics were calculated based on the interrogation area, curve fitting algorithm and filtering used in calculating the instantaneous vector maps, and number of instantaneous images. The uncertainty in the mean velocities, Reynolds stresses and third order moments at 95% confidence level was estimated to be ±2.7% and ±11% and ±15% of the peak values, respectively.

4.4 Results and discussion

In this section, the initial conditions, flow visualization and estimation of the reattachment lengths of the offset jets will be discussed. This will be followed by discussions on the streamwise development of the flow, mean velocities, Reynolds stresses and some budget terms of the turbulent kinetic energy in the recirculation region. The section will be concluded with presentation of two-point correlation analysis within the recirculation region of the flow.

4.4.1 Initial conditions

The streamwise bulk velocity (U_o) and the corresponding jet exit centerline velocity (U_j) were determined for each of the offset jets. The velocities at the jet exit ($x/b_o = 0$) could not be extracted due to reflection of the laser light on the upstream wall which distorted the velocities immediately at the jet exit. Therefore, the bulk velocity was estimated as the area average of the mean velocities close to the nozzle exit ($x/b_o \approx 1.0$). This was calculated from the following relation: $(1/b_o)\int_0^{b_o} U\partial y$. The ratios of U_j/U_o for all the test cases are shown in Table 4.1. The obtained U_j/U_o values increased from 1.15 to 1.69 as the offset height ratio increased from h/b_o = 0 to 8.

Table 4.1 Maximum exit centerline mean velocities (U_j) and bulk velocities (U_o) for the offset jets

h/b_o	U_j (ms^{-1})	U_o (ms^{-1})	U_j/U_o
0	1.74	1.51	1.15
2	1.31	1.01	1.30
4	1.47	1.09	1.35
8	1.27	0.75	1.69

4.4.2 Flow visualization and reattachment length

Iso-contours in the symmetry plane are shown to reveal some features of the offset jets (h/b_o = 2, 4 and 8). Figure 4.2 shows the contours of $U^* = U/U_o$, where U is the streamwise mean velocity, and the approximate turbulent kinetic energy, $k^* = 0.75(\overline{u^2}+\overline{v^2})/U_o^2$ with the superimposition of corresponding mean streamlines. The mean streamlines indicate that the jet entrains ambient fluid above and beneath it. Due to the entrainment of ambient fluid into the core region of the offset jet, the wall-normal extent of high U^* values was observed to decrease with streamwise distance. The deflected jet reattaches to the wall creating a recirculation region beneath the jet as depicted in Figs. 4.2a – 4.2c. The recirculation region is dominated by negative streamwise velocities. The sharp exit of the discharge nozzle caused the mean flow to accelerate resulting in the occurrence of the maximum mean velocity at a streamwise distance away from the nozzle exit. The acceleration of the mean flow at the nozzle exit can be attributed to the vena contracta effect. A backflow region (also characterized by the existence of negative streamwise mean velocities indicated by the color above the zero iso-contour line) was created above the offset jet. The maximum backflow velocity for three offset jets were estimated as ($-U/U_o$) = 5%, 6% and 4% for h/b_o = 2, 4 and 8 respectively. The contour plots of the turbulent kinetic energy for the three offset jets, shown in Figs. 4.2d through to 4.2f, revealed that the peak value of k^* occurred close to the nozzle exit ($x/b_o \sim 1$) for h/b_o = 4 offset jet but shifted farther downstream, to about x/b_o = 5, for h/b_o = 2 and 8 offset jets.

The mean reattachment length (L_e) is an important characteristic of offset jets due to its relevance in determining the development of the flow downstream of the nozzle, as well as the

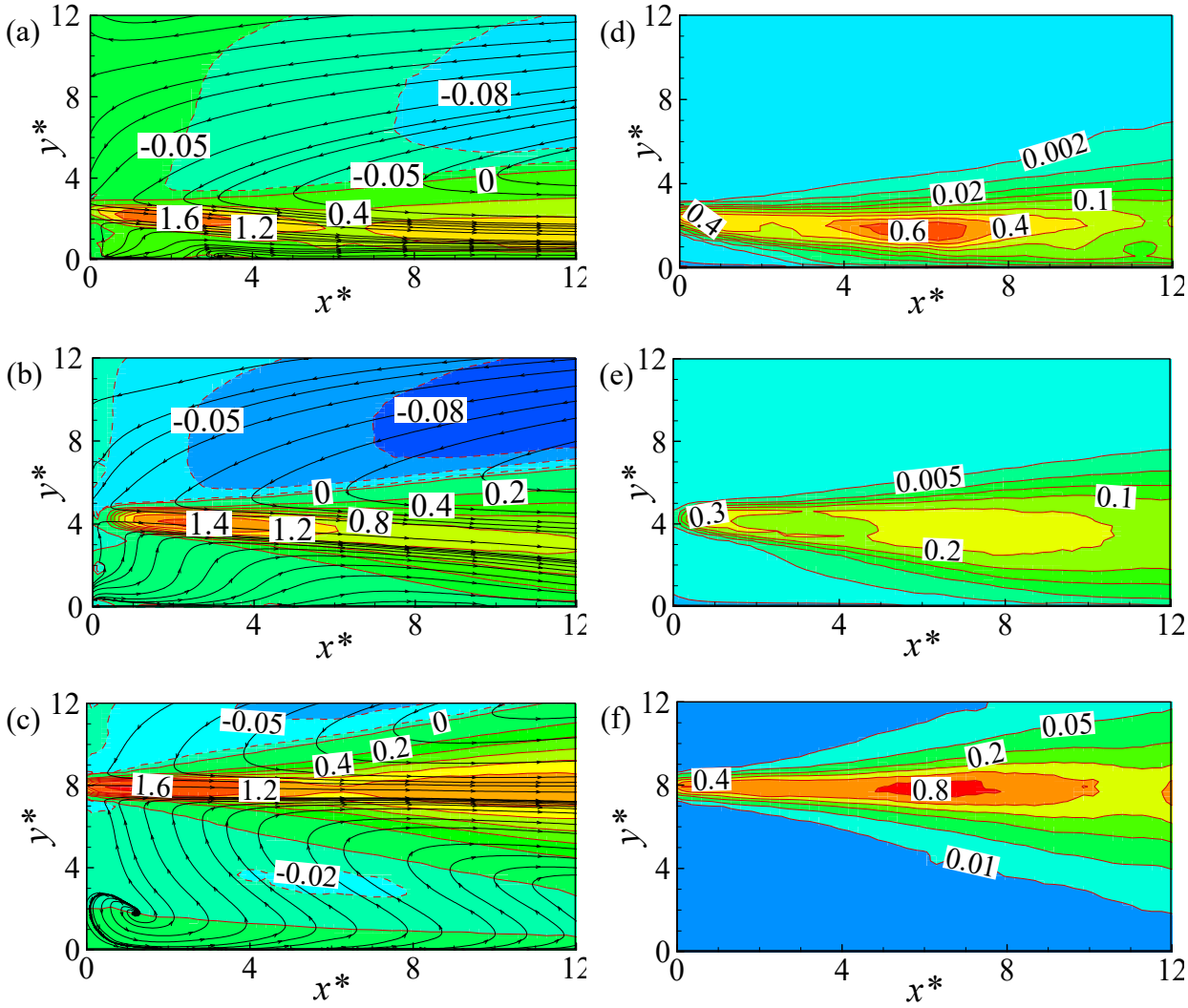

Figure 4.2 Mean Streamlines and iso-contours of ((a) – (c)) mean velocities and ((d) – (f)) turbulent kinetic energy, for h/b_o of 2, 4 and 8, respectively ($x^*=x/b_o$; $y^*=y/b_o$)

recirculation region. The reattachment length was defined as the streamwise distance from the jet origin to the point where the jet reattached to the bottom of the channel. Three different techniques were used to estimate the reattachment point; 1) mean streamlines, 2) stream function technique and 3) forward-flow technique. The mean streamline technique defines the reattachment point as the point where the mean streamline intersects the bottom of the channel. Using the stream function technique, the reattachment point is determined as the point where the zero stream function

intersects the bottom of the channel. Ra *et al*. (1990) defined the forward-flow fraction, γ_p, as the fraction of time for which a separated flow is directed in the downstream direction. For $\gamma_p = 1$ the flow is considered to be in the downstream direction all the time whereas $\gamma_p = 0$ means a reverse flow at all times. The reattachment point is estimated as the location where $\gamma_p = 0.5$. The uncertainty in the estimation of the reattachment length was about ± $0.5b_o$. The differences in estimating L_e from the three methods were within the uncertainty obtained for the estimation of L_e. Reattachment length (L_e/b_o) values, obtained from the average of the three approaches, for $h/b_o = 2$, 4 and 8 were 4.4, 6.2 and 16.3 respectively. The reattachment length was observed to increase with h/b_o. The reported value of $L_e/b_o = 6.2$ for $h/b_o = 4$ in the present investigation is comparable to 6.4 reported by Agelinchaab & Tachie (2011b) for an offset jet with h/b_o of 3.5. Bhuiyan *et al*. (2011) developed a L_e correlation for a 2D offset jet: $L_e/b_o = 2.786(h/b_o)^{0.86}$. The correlation predicted larger values of L_e/b_o compared to values obtained from the current studies which is explained by the fact that the initial momentum flux for a 2D nozzle is higher than for the 3D rectangular nozzle used in the present study. The difference in estimated values (from the correlation) of L_e/b_o and those obtained in the present study was 11%, 33% and 2% for $h/b_o = 2$, 4 and 8 respectively.

4.4.3 Development of the streamwise mean flow

The development of the mean flow in the streamwise direction was characterized using the decay of the maximum streamwise mean velocity (U_m), the wall-normal location of maximum velocity (y_m), and the spread of the jet in the wall-normal ($y_{0.5}$) and spanwise ($z_{0.5}$) directions. Previous results from contoured nozzles have indicated that U_m is constant within the potential core region, followed by a monotonic decay with streamwise distance. The decay of U_m is expected since there is entrainment of ambient fluid into the core region of the jet. However, the present results obtained from sharp edged nozzles indicated different trend in the region close to

the nozzle than observed in previous results for contoured nozzles. It should be noted that no prominent potential core region was observed close to the nozzle exit in the present study. It can be seen from Fig. 4.3a that U_m/U_o increases very close to the nozzle exit. The value of U_m increased by about 40%, 44% and 69% for offset jets with h/b_o = 2, 4 and 8, respectively from the nozzle exit before eventually decaying. The peaks of U_m occurred at x/b_o = 1, 2.5, 2 and 1 for offset jets with h/b_o = 0, 2, 4 and 8, respectively. Using the equivalent diameter (d_e) of the current nozzles, the specified peak locations correspond to x/d_e = 0.05, 0.11, 0.09 and 0.05, respectively for nozzles with h/b_o = 0, 2, 4 and 8. The obtained values are less than x/d_e = 0.25 reported by Quinn (2006) for a free jet produced from a sharp-edged round orifice. As indicated in previous section, the observed increase in U_m close to the nozzle exit can be attributed to the vena contracta effect generated by the sharp edge of the nozzles used. The vena contracta effect causes unsteadiness within the jet due to the separation of the jet upstream. The unsteadiness leads to enhanced mixing and entrainment of the ambient fluid in the present study. A similar observation was reported by Quinn & Militzer (1988) for turbulent jets exiting a sharp-square orifice and by Essel *et al*. (2013) for turbulent jets produced from rectangular slots with sharp edges. The normalized values of U_m decayed sharply within the region $x/b_o < 10$ to a local minimum which was 47%, 61% and 59% less than U_j at about x/b_o = 6 for h/b_o of 0, 2 and 8 respectively. This was not observed for offset jet with h/b_o = 4. The values of U_m then increased by 12% within the region $10 < x/b_o < 16$ before finally decreasing monotonically further downstream.

In order to estimate the decay rates of the jets, datasets within the region $28 \leq x/b_o \leq 60$ was used for offset jets with h/b_o = 0 and 2 and $32 \leq x/b_o \leq 60$ for offset jet with h/b_o = 4. These regions corresponded to the self-similar region of the flow. The decay rate for the offset jet with h/b_o = 8 could not be estimated due to the flow dynamics within the estimation region used. That

is, the self-similar region could not be determined for the $h/b_o = 8$ offset jet due to the challenge in estimating $y_{0.5}$ values of the jet beyond $x/b_o > 25$. Previous studies estimated the decay rate of the maximum velocity using a power law fit of the form: $U_m \, \alpha \, (x/b_o)^{-n}$, where n is the decay rate and α is a proportionality symbol. Using the power law fit, the decay rate for the wall jet was observed to be accurately estimated with a decay rate of 0.996 and an R^2 value of 0.99 as shown in Fig. 4.3b. As can be seen in Fig. 4.3b, the distributions of U_m for the offset jets are not accurately described by the power law. Therefore, a linear fit was used to estimate the decay rates for the two offset jets. Decay rate values of 0.017 and 0.011 with $R^2 = 0.99$ were obtained for $h/b_o = 2$ and 4 offset jets respectively as indicated in Fig. 4.3c.

The variation of y_m with x/b_o (Fig. 4.3d) can be used to examine the effect of offset height on the growth of the inner layer as shown in Fig. 4.1a. The y_m results for $h/b_o = 8$ will not be examined due to its proximity to the free surface. For the case of the wall jet, y_m was observed to increase linearly with x/b_o in the region $x/b_o < 5$. Beyond $x/b_o > 5$, fairly constant values of y_m were obtained except within the region $20 \leq x/b_o \leq 30$ where there was a slight increase. It can be seen from Fig. 4.3d that the development of y_m for offset jet with $h/b_o = 2$ and 4 does not occur in a similar trend to that of the wall jet. Rather the development of y_m for the two offset jets occurred in two stages. For stage I, which corresponds to $x/b_o \leq 10$ for $h/b_o = 2$ jet and $x/b_o \leq 25$ for the $h/b_o = 4$ jet, y_m decreases sharply with streamwise distance. The values of y_m remained fairly constant in stage II which occur downstream of stage I. That is, within the recirculation and reattachment regions of the flow, y_m occurred farther away from the wall for the offset jets, but after redevelopment of the jet into a wall jet, y_m moved closer to the wall. The values of y_m for $h/b_o = 0$, 2 and 4 collapsed beyond the region $x/b_o \geq 32$. Previous studies by Agelinchaab & Tachie (2011) reported four stages in the development of y_m. The stage with constant y_m values adjacent to the

nozzle was not observed in the present study. The difference may be partly attributed to initial conditions such as nozzle geometry, Froude number as well as intense backflow and the presence of tailwater.

The half widths $y_{0.5}$ and $z_{0.5}$ of the jet are a measure of the spread of the jet in the wall-normal and lateral directions, respectively. Figure 4.3e shows the distributions of the wall-normal jet half width. The spread of the wall jet increased with x/b_o immediately downstream of the nozzle exit. The wall jet exhibited a noticeable increase in the values of $y_{0.5}$ with streamwise distance in the region $0.5 \leq x/b_o \leq 50$. Beyond $x/b_o > 50$, the effect of intense backflow suppressed the spread of the jet in the wall-normal plane. In the near regions of the offset jets, $x/b_o < 5$, the jet was observed to contract slightly with x/b_o. This gives an indication of the formation of the vena-contracta close to the nozzle exit. This effect was not noticeable in the near region of the wall jet though there was an increase in the jets exit velocity. Beyond the region $x/b_o > 5$, the jet spread linearly with streamwise distance for the jet with $h/b_o = 2$. The trend in $y_{0.5}$ is consistent with those reported in previous studies by Agelinchaab & Tachie 2011b). Figure 4.3e shows a considerable increase in $y_{0.5}$ with x/b_o compared to y_m. It is also observed that the spread of the $h/b_o = 4$ offset jet was suppressed with streamwise distance, which was as a result of intense backflow. In the case of the $h/b_o = 8$ offset jet, the wall-normal spread could only be estimated up to $x/b_o = 25$. The spread in the lateral direction however increased consistently with streamwise distance as shown in Fig. 4.3f. Measurements within the

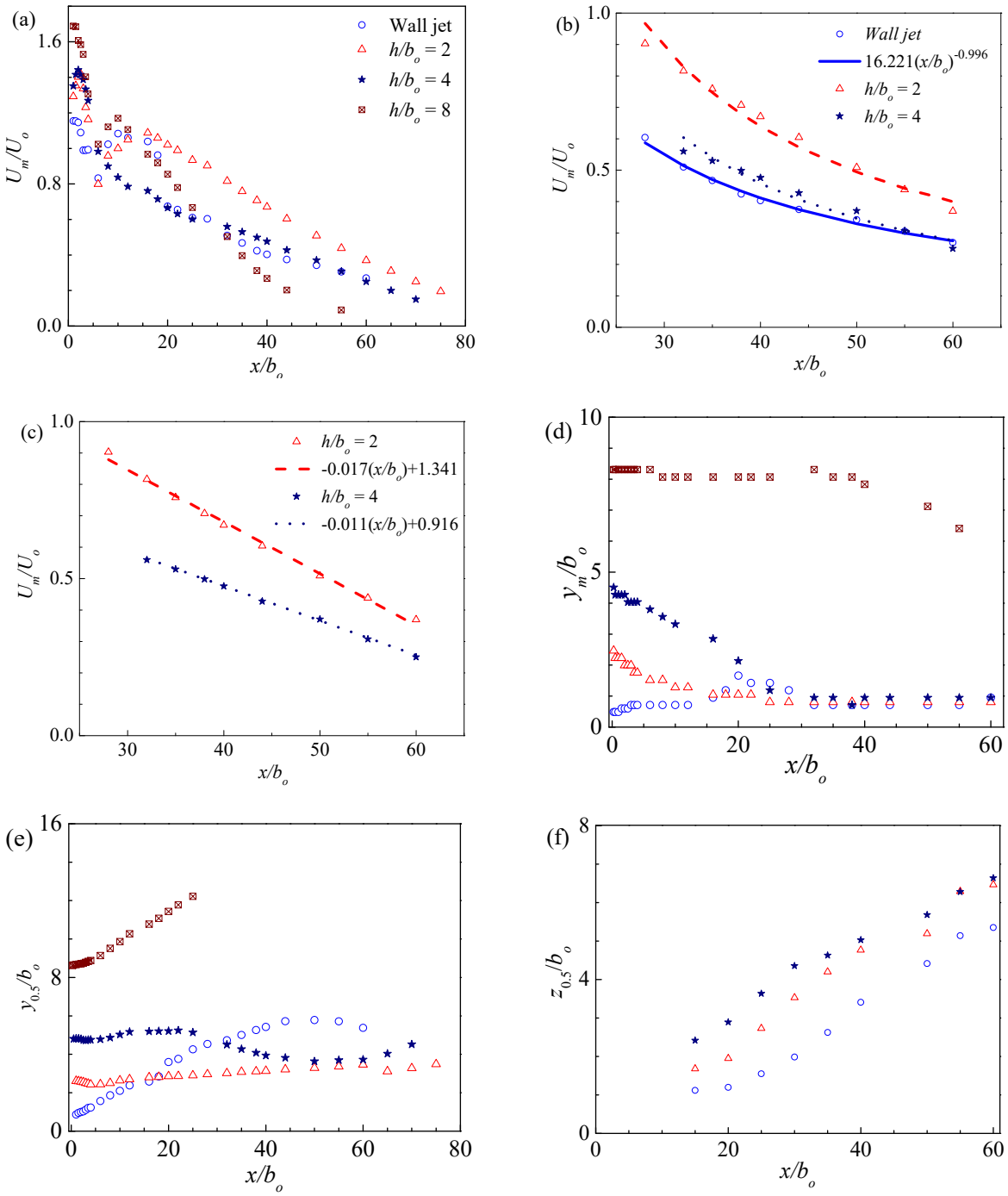

Figure 4.3 Variation of (a) local maximum mean velocity, U_m, (b) power law fit to U_m, (c) linear fit to U_m, (d) wall-normal location of U_m, y_m, (e) wall-normal jet half-width, $y_{0.5}$, and (f) lateral jet half-width, $z_{0.5}$

lateral plane for h/b_o = 8 offset jet was not presented in this subplot since the flow dynamics inhibited accurate measurements in this plane. The current experiment reveals that $z_{0.5}$ increased with increasing h/b_o.

In order to establish the growth rate of the offset jets, the spread rates were estimated for the jets. The spread rate was determined as the gradient ($dy_{0.5}/dx$ and $dz_{0.5}/dx$) of the linear fit to the measured data. The wall-normal spread rate for offset jet with h/b_o = 4 and 8 could not be determined due to the relatively narrow linear region as shown in Fig. 4.3e. The wall-normal spread of the h/b_o = 4 offset jet was suppressed by intense backflow beyond $x/b_o > 30$ as shown in Fig. 4.3e. It can be seen from Fig. 4.3e that in the region $x/b_o > 50$, the spread of the wall jet was impeded by the presence of the backflow. Since the backflow intensifies with x/b_o, the wall-normal spread rate for h/b_o = 0 and 2 jets were estimated within the regions $28 \leq x/b_o \leq 50$ and $28 \leq x/b_o \leq 60$, respectively. With this approach, only the linear region was utilized in estimating the spread rate. This was done in order to eliminate the suppressing effect of the backflow on the jet growth. The lateral spread rate was obtained within the regions $28 \leq x/b_o \leq 60$ for offset jets h/b_o = 0, 2 and 4. Wall-normal spread rates of 0.066 and 0.016 were obtained for the wall jet and h/b_o = 2 offset jet, respectively. The value of $dy_{0.5}/dx$ for h/b_o = 2 is however 70% less than value reported by Agelinchaab & Tachie (2011b) for an offset jet with h/b_o = 1.5. The lower wall-normal spread rates in the present study may be attributed, in part, to the presence of the backflow. In the lateral direction, the spread rate ($dz_{0.5}/dx$) was estimated to be 0.116, 0.114 and 0.096 for jets with h/b_o = 0, 2 and 4 respectively. The present results revealed one of the salient features of 3D turbulent jets (i.e., larger values of $dz_{0.5}/dx$ compared to $dy_{0.5}/dx$). The larger values may be attributed to the presence of secondary mean motion which causes a significant lateral outflow (Newman *et al*. 1972). Davis & Winarto (1980) attributed the larger lateral spread rate to enhanced turbulent

diffusion parallel to the wall, while Craft & Launder (2001) and Launder & Rodi (1983) attributed it to the creation of streamwise vorticity by the anisotropy of the Reynolds stresses. Values of $dz_{0.5}/dx$ were observed to decrease with increasing h/b_o. The decreasing trend is in agreement with $dz_{0.5}/dx$ values of 0.33, 0.29 and 0.23 reported by Davis & Winarto (1980) for h/b_o = 0.5, 1.5 and 3.5 respectively. The present findings (decrease in $dz_{0.5}/dx$ with h/b_o within the self-similar region) are also consistent with reports by Agelinchaab & Tachie (2011). The anisotropy of the spread rate of the jets was examined in the present study. The ratio of ($dz_{0.5}/dx$)/ ($dy_{0.5}/dx$) in the present study was 1.8 and 7.1 for h/b_o = 0 and 2 respectively. The obtained value for the wall jet was less than values in the range of 3.7–8.6 reported for generic jets (Davis & Winarto, 1980; Abrahamsson *et al*. 1997) and that of the offset jet is comparable to 5.0–9.2 reported by Davis & Winarto (1980).

4.4.4 Mean velocities and turbulence statistics

Subsequent discussions will be limited to flow characteristics within the recirculation region of the three offset jets (h/b_o = 2, 4 and 8). The local maximum mean velocity, U_m, and nozzle height, b_o, were used as the appropriate velocity and length scales, respectively, for the quantities presented in this section.

4.4.4.1 Mean velocity profiles

Figure 4.4 shows the profiles of the streamwise mean velocity (U) and wall-normal mean velocity (V) at selected streamwise locations for the offset jets. The streamwise locations, x, were normalized by L_e. This enabled the extraction of the data at similar geometrical locations. In order to characterize the mean flow within the recirculation region, profiles of U and V were extracted at x/L_e = 0.2, 0.5 and 1. The streamwise velocity distribution at these three streamwise locations have been presented in Fig. 4.4a. The plots were offset at intervals of one with the dashed lines

representing the zero mark as indicated on top of the axis. Figure 4.4a demonstrates the effect of the presence of the ambient fluid on the jet, which is in relation to the spreading of the jet. The streamwise velocity distributions shown in Fig. 4.4a exibit profiles with off-center peaks downstream of the nozzle. Off-center peaks have been observed in previous studies for jets produced by sharp edged nozzles (Quinn & Militzer, 1988; Deo *et al*., 2007; Hsiao *et al*., 2010; Essel *et al*., 2013). This feature is largerly attributed to the effect of secondary flows which are caused by the streamline curvature as the jet exits the sharp nozzle and its accompanying centrifugal effect (Quinn & Militzer, 1988). Figure 4.4a shows the evolution of the streamwise mean velocity of the offset jets within the recirculation region. At $x/L_e = 0.2$, the U profiles of the different offset jets collapsed fairly well. Further downstream ($x/L_e = 0.5$), U profiles for $h/b_o = 2$ and 4 collapsed while that of $h/b_o = 8$ was obserevd to increase in width. At the reattachment point, the profiles for $h/b_o = 2$ and 4 offset jets collapsed in the outer region of the flow. The U profile for the $h/b_o = 8$ offset jet at $x/L_e = 1$ exhibited considerable spread and did not collapse on the profiles for the other two offset jets. This highlights the fact that b_o is not the appropriate length scale to allow complete collapse of the profiles.

Insight into the wall-normal mean velocity component, V, is of great interest, since secondary mean motion prevails in turbulent 3D jets. Within the recirculation region, there were positive V values for all the jets close to the wall as shown in Fig. 4.4b. This is an indication of fluid entrainment from the wall region upward into the jet. There were, however, negative V values within the outer region of the jet. This is attributed to entrainment of the ambient fluid from the outer region into the core region of the jet. At the reattachment point, negative values of V were obtained for the various offset jets close to the wall. The distribution of V supports the notion that secondary motions carry fluid down towards the wall and away from the symmetry plane along

the wall (Launder & Rodi, 1983). The results presented in Fig. 4.4b show that the entrainment of ambient fluid was inhibited once the jet reattached. The gradient $\partial V/\partial y$ from analysis is not negligible and as a result cannot be overlooked when considering the transport of momentum and turbulence. This implies that the gradient $\partial V/\partial y$ contribute significantly to momentum transport, the production of $\overline{v^2}$ and turbulence kinetic energy.

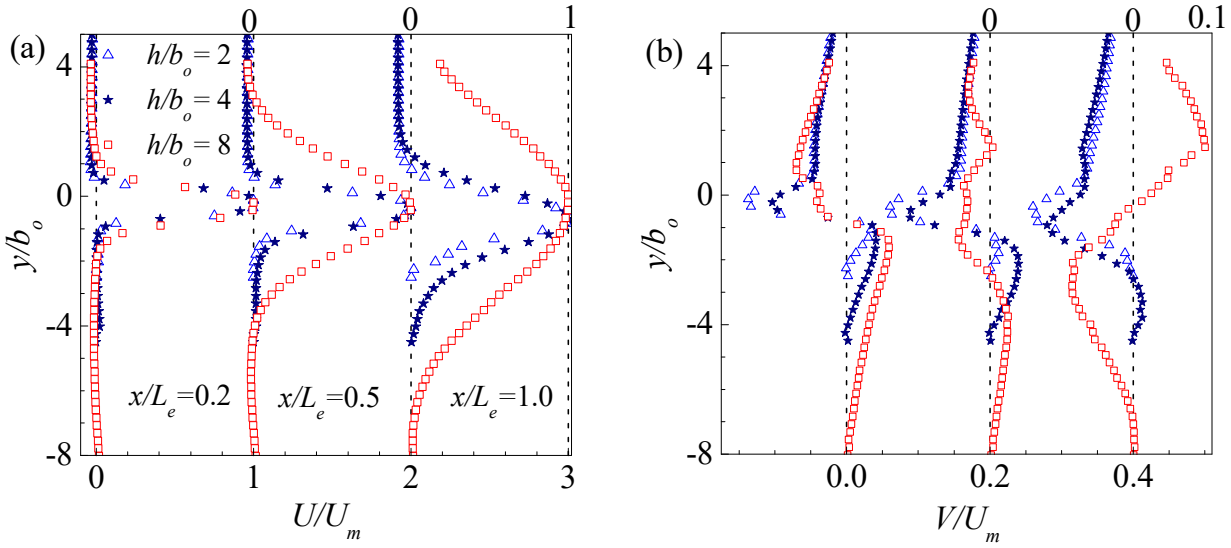

Figure 4.4 Mean velocity distribution (a) streamwise and (b) wall-normal; origin located at the center of the nozzle

4.4.4.2 Reynolds stresses

Figure 4.5 shows the distribution of the Reynolds stresses ($\overline{u^2}$, $\overline{v^2}$ and $-\overline{uv}$) in the $x - y$ plane at five selected streamwise locations within the recirculation region. As the jet approaches the reattachment point, the lower shear layer separates into forward and reverse flow. This process has been observed to cause an increase in the relative strength of the larger eddies before the jet's reattachment (Pelfrey & Liburdy, 1986) and affects the Reynolds stresses prior to and after the reattachment of the jet. The peak values of $\overline{u^2}$ were observed to be greater than those of $\overline{v^2}$ (from

Figs. 4.5a-f). The peak values of $\overline{u^2}$ were observed to increase with streamwise distance for h/b_o = 2 and 4, but with h/b_o = 8, there was an initial increase and then a reduction until the reattachment point. The trends observed here for h/b_o = 2 and 4 are similar to those reported by Agelinchaab & Tachie (2011). The trend of $\overline{v^2}$ for all the jets are similar to their corresponding $\overline{u^2}$ but were of lower magnitude. Since $\overline{u^2}$ is not equal to $\overline{v^2}$, isotropic turbulence models cannot accurately reproduce the turbulence statistics within the recirculation region of offset jets.

Figures 4.5g-4.5i, show that the profiles of $-\overline{uv}$ for each of the offset jets exhibited an asymmetric behavior due to the nature of the shear layers. Positive values were observed close to the wall and became negative further away from the wall. The wall-normal location (y_{uv}), where $-\overline{uv}$ changes sign was compared to y_m at various streamwise locations, x/L_e. It was observed that within the recirculation region, the two points did not coincide. For h/b_o = 2 and 4 offset jets, values of y_m predominantly occurred closer to the wall than the wall-normal location where $-\overline{uv}$ = 0. This was different within the recirculation region of h/b_o = 8 offset jet, where y_{uv} occurred closer to the wall than y_m. The difference between these two locations were estimated to be 30%, 35% and 4% of the offset height for h/b_o = 2, 4 and 8, respectively. Since these two points do not coincide, it suggests that the flow characteristics within the recirculation region cannot be accurately reproduced by eddy viscosity based turbulence models.

Comparing the effect of offset height on the Reynolds stresses, profiles of $\overline{u^2}$, $\overline{v^2}$ and $-\overline{uv}$ are shown in Fig. 4.6 at x/L_e of 0.2, 0.5 and 1. For the Reynolds normal stresses, increasing h/b_o enhanced their corresponding peak values. However, within the recirculation region, there was no significant effect of h/b_o on $-\overline{uv}$.

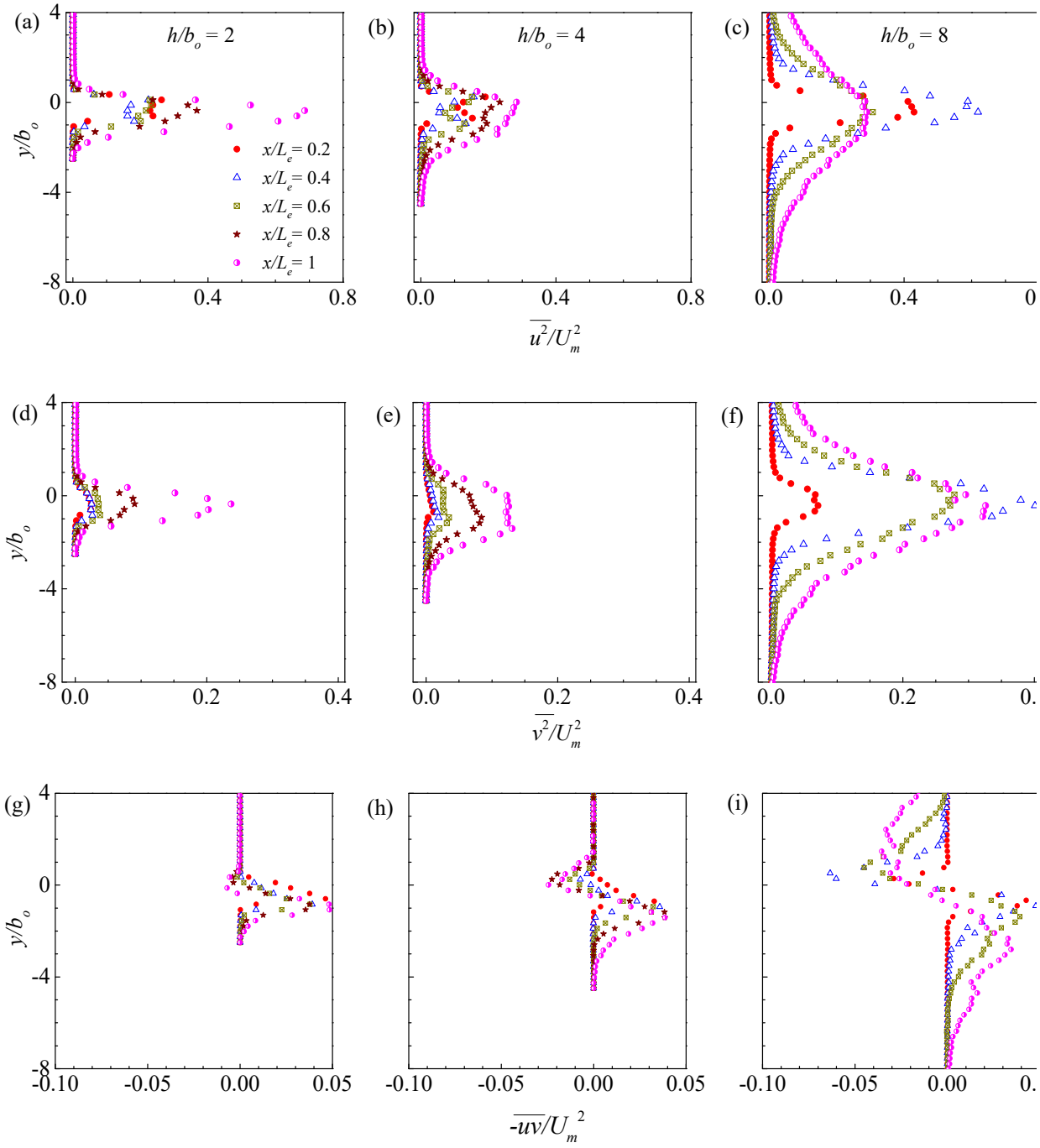

Figure 4.5 Reynolds stress distribution within the recirculation region of the flow (a)-(c) $\overline{u^2}$, (d)-(f) $\overline{v^2}$ and (g)-(i) $-\overline{uv}$ for the offset jets

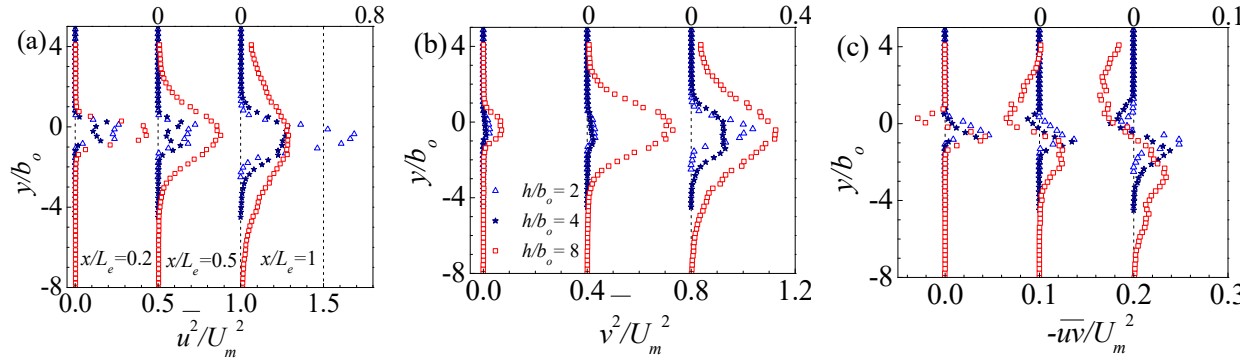

Figure 4.6 Comparison of the Reynolds stress distribution for the various offset jets (a) $\overline{u^2}$, (b) $\overline{v^2}$ and (c) $-\overline{uv}$

4.4.5 Budget terms of the turbulent kinetic energy (TKE)

This section presents analysis of some of the budget terms of the turbulent kinetic energy transport equation. The budget terms of the turbulent kinetic energy reported in the present study are the production (P_k), convection (C_k) and diffusion (D_k) terms. These terms were estimated as follows: $P_k = -(\overline{uv}\partial U/\partial y+\overline{uv}\partial V/\partial x+\overline{u^2}\partial U/\partial x+\overline{v^2}\partial V/\partial y)$, $D_k = -0.5[\partial(\overline{u^3}+\overline{uv^2})/\partial x + \partial(\overline{u^2v}+\overline{v^3})/\partial y]$ and $C_k = U\partial k/\partial x+V\partial k/\partial y$ respectively. These three terms (normalized and represented as P_k^*, C_k^* and D_k^*) are shown in Figure 4.7. Within the recirculation region, the peak value of the production term for the h/b_o = 2 and 4 offset jets increases with streamwise distance. Increasing h/b_o resulted in a decrease in turbulence production within the recirculation region with streamwise distance. Figure 4.7a indicates sections of negative turbulence kinetic energy production (drain of energy from the turbulence field), for streamwise locations x/L_e = 0.2 and 0.5. From the analysis of the individual terms, the major contributors to the turbulence production are $-\overline{uv}\partial U/\partial y$, $-\overline{u^2}\partial U/\partial x$ and $-\overline{v^2}\partial V/\partial y$ terms. The $-\overline{uv}\partial V/\partial x$ term was observed to be negligible and did not contribute significantly to the production of turbulence. This highlights the significant contribution of the

Reynolds normal stresses to turbulence production within the flow fields of 3D offset jets. Profiles of the convective and diffusion terms are shown in Figure 4.7b and 4.7c respectively. Analysis of the two convective terms revealed that peak values of the streamwise convection term ($U\partial k/\partial x$) were larger than the corresponding wall-normal component ($V\partial k/\partial y$) for the offset jets. Upon careful analysis of the turbulence diffusion, it was observed that the peak value of the streamwise component was larger than that of the wall-normal component. The scatter in the data is a result of the streamwise turbulence diffusion component.

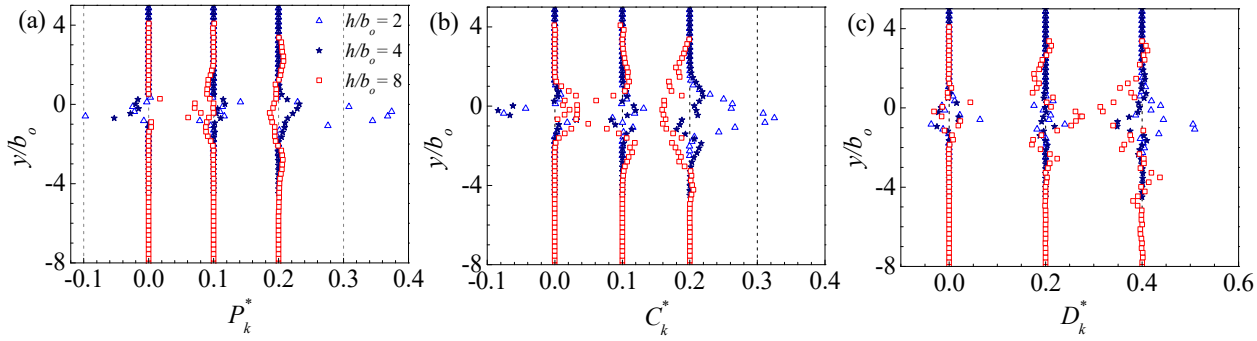

Figure 4.7 (a) Production of turbulence kinetic energy, P_k^*, (b) convection of turbulence, C_k^*, and (c) diffusion of turbulence, D_k^*

4.4.6 Two-Point Auto Correlation

Two-point correlation is a useful statistical technique for investigating features of coherent structures and integral length scales. The two-point correlation was employed in the present study to investigate the effect of h/b_o on how the turbulence structures within the recirculation region of the jet are correlated as well as estimate the integral length scales of the large-scale structures that enhance turbulent mixing and entrainment. The two-point correlation functions in the $x - y$ plane at a reference point (x_r, y_r) for the streamwise (u) and wall-normal (v) fluctuating velocities and streamwise (u') and wall-normal (v') turbulence intensities separated by Δx and Δy are defined as:

$R_{uu} = \{u(x_r, y_r)u(x_r + \Delta x, y_r + \Delta y)\}/\ \{u'(x_r, y_r)u'(x_r + \Delta x, y_r + \Delta y)\}$ and $R_{vv} = \{v(x_r, y_r)v(x_r + \Delta x, y_r + \Delta y)\}/\ \{v'(x_r, y_r)v'(x_r + \Delta x, y_r + \Delta y)\}$. The correlation functions were calculated for each PIV realization and then ensemble-averaged point-by-point. The analysis was performed at x/L_e = 0.2, 0.4, 0.5 and 0.6 for all of the offset jets. Subsequently, only results at x/L_e = 0.2 will be presented in this section due to similarities in the trends at the various streamwise locations. Figure 4.8 shows contours of the two-point correlations of the streamwise fluctuating velocity (R_{uu}) and wall-normal fluctuating velocity (R_{vv}) for the offset jets centered at y_{ref}/y_m = 0.5 within the recirculation region of the flow. Contour levels used in the present study for R_{uu} and R_{vv} were from 0.6 to 1.0 at intervals of 0.1. The origins of the R_{uu} and R_{vv} contours were set at the auto-correlation peak.

The contours of R_{uu} are relatively rounded and increase in size with h/b_o. Similar to the R_{uu} contours, the R_{vv} contours were also observed to increase in size with h/b_o as shown in Fig. 4.8. A slice through the contours (not shown), revealed that R_{uu} profiles in the wall-normal direction decay more rapidly than in the streamwise direction. In contrast, profiles of R_{vv} in the streamwise direction decayed rapidly than in the wall-normal direction. The results indicate that the streamwise and wall-normal turbulence structures are respectively correlated in the streamwise and wall-normal directions.

The streamwise extent of R_{uu} (Lx_{uu}), which can be used to estimate the integral length scales within the flow, was estimated as twice the distance from the self-correlation peak to the point farthest away on the 0.6 contour levels an approach previously adapted by Agelinchaab & Tachie (2011). The streamwise extent of R_{vv} (Lx_{vv}) was estimated as the distance between most upstream and downstream points on the 0.6 contour levels of R_{vv}. The wall-normal extents of R_{uu} (Ly_{uu}) and R_{vv} (Ly_{vv}) were estimated as the wall-normal distance between the farthest and closest points on

the 0.6 contour levels for R_{uu} and R_{vv}. A more precise approach in estimating the integral length scales of the turbulent structures within the recirculation region of the flow is to integrate the profiles of $R_{uu}(x)$ for the offset jets. Profiles were extracted at four streamwise locations (x/L_e = 0.2, 0.4, 0.5 and 0.6) and five wall-normal locations within the inner region of the flow at y/y_m = 0.3, 0.4, 0.7, 0.8 and 0.9. Analyses were done for offset jets with h/b_o of 2 and 4, and the results compared to the streamwise extent, Lx_{uu}, obtained from their corresponding $R_{uu}(x)$ contour levels. The percentage difference between the results for the two estimations of the integral length scales was 2% and 11% for h/b_o of 2 and 4 respectively. It should be noted that not all the profiles of $R_{uu}(x)$ (including those for h/b_o = 8) decayed to zero. This made it challenging to estimate the integral length scale using the integration approach. Nonetheless due to the comparable nature of the results obtained from the two methods, the extents for the various offset jets were estimated from the 0.6 contour levels shown in Fig. 4.8. The values of Lx_{uu}, Ly_{uu}, Lx_{vv} and Ly_{vv} are presented in Table 4.2 and are normalized with b_o. It was observed that within the recirculation region, all the extents, Lx_{uu}, Ly_{uu}, Lx_{vv} and Ly_{vv} increased with increasing h/b_o. It is obvious from the results that the large scale structures within the recirculation region increase in size with h/b_o. Comparing the results obtained within the recirculation region to that of boundary layer results, the ratios of Lx_{uu} to Ly_{uu} and Lx_{vv} to Ly_{vv} were estimated. Within this region, the ratio of Lx_{uu}/Ly_{uu} = 1.81 ±0.37 obtained is less than 4.2 ±0.2 reported by Agelinchaab & Tachie (2011) within the self-similar region of 3D offset jets. The ratio of Lx_{vv}/Ly_{vv} = 0.75 ±0.15 obtained in the present studies was however comparable to 0.87 ±0.05 and 0.80 reported by Agelinchaab & Tachie (2011) and Volino *et al*. (2007) respectively. This is indicative of the fact that the structures within the recirculation region of the offset jets are less stretched in the streamwise direction compared to boundary layer flows.

Table 4.2 Spatial extents of the contours normalized by b_o

Extents	$h/b_o = 2$	$h/b_o = 4$	$h/b_o = 8$
Lx_{uu}	1.08	2.60	4.80
Ly_{uu}	0.86	1.18	2.45
Lx_{vv}	0.70	1.17	1.63
Ly_{vv}	0.72	1.75	2.64

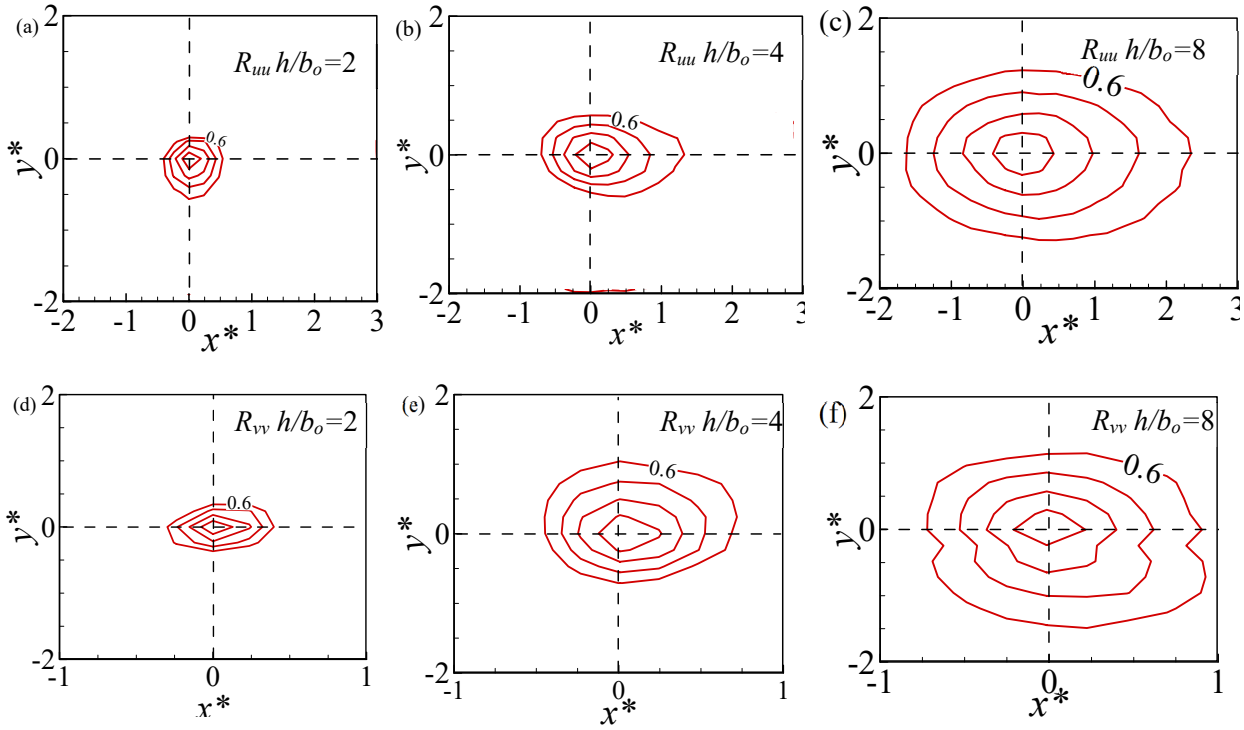

Figure 4.8 Contours of streamwise auto-correlation, R_{uu}, and wall-normal auto-correlation, R_{vv}, for the offset jets at $x/L_e = 0.2$ and $y/y_m = 0.5$

4.5 Conclusions

The flow characteristics within the recirculation region of a three-dimensional offset jet discharged into a tailwater has been investigated experimentally using a PIV system. The development of the flow is greatly dependent on h/b_o of the nozzle. Streamlines of the mean velocities indicated entrainment of tailwater both beneath and above the jet. The reattachment

length was observed to increase with increasing h/b_o. The maximum mean velocity decay rate was observed to increase with increasing h/b_o. The wall-normal and lateral spread rates of the jets decreased with h/b_o. Analysis of the Reynolds stresses revealed that the Reynolds shear stress was independent of offset height within the recirculation region of the flow. Two-point velocity correlation was also presented to illustrate how the turbulence structures are correlated within the recirculation region of the flow. The results from the contours revealed that the turbulence structures grow in both streamwise and wall-normal directions with offset distance, and the integral length scales increased with h/b_o. Overall, the results provide insight into the effect of h/b_o on the flow characteristics within the recirculation region of an offset jet, which is a region that has received relatively little attention in the literature due in part to the complex flow dynamics and associated measurement difficulties.

CHAPTER FIVE

5 PAPER II

Experimental Study of the Flow Structures of 3D Turbulent Offset Jets

5.1 Abstract

Three-dimensional turbulent offset jets were investigated using a particle image velocimetry technique. Detailed measurements were performed for offset height ratios of 0, 2 and 4. The presence of backflow influenced the distribution of the mean velocity and Reynolds stresses. A two-point correlation analysis was used to investigate the spatial distribution of large-scale structures within the inner shear layer of the flow domain. The results revealed that large-scale structures dominate the inner layer of the self-similarity region. Proper orthogonal decomposition was performed on the fluctuating velocity field within the symmetry and lateral planes using the snapshot approach. Results from the reconstructed field provided insight into the contributions of the most energetic structures to the turbulence statistics. The energetic structures contributed more to the Reynolds shear stress and streamwise turbulence intensity, while contributing less to the wall-normal turbulence intensity.

5.2 Introduction

A three-dimesional (3D) offset jet is formed when a fluid jet is discharged from a nozzle of a finite aspect ratio at a certain offset height from the channel bottom. Offset jets are encountered in diverse engineering and technological applications, such as energy dissipation devices downstream of hydraulic structures (Mossa *et al*., 2003), and in environmental transport and mixing of effluent in lakes and rivers (Bhuyian *et al*., 2011; Tachie *et al*., 2004). Investigating the flow field of offset jets will help explain the physics of complex separated and reattached flows.

Moreover, the complex flow field of offset jets makes them ideal test cases for assesing the perfomance of different turbulence models. Figure 5.1 shows the flow field of an offset jet with some salient features. The Cartesian coordinate system is used with x, y and z representing the streamwise, wall-normal, and lateral directions, respectively. The jet exit is at $x = 0$, the channel bottom is at $y = 0$, and the symmetry plane is at $z = 0$. The recirculation region was defined as the streamwise distance from the nozzle exit to the reattachment point of the discharged offset jet. The developing region spanned from the reattachment point to the streamwise distance where the self-similarity region commences. The self-similarity region was defined as the region where the flow quantities did not vary with streamwise distance when the appropriate scaling is applied. The symbols h, b_o, U_o, L_e and y_t represent the offset height, nozzle height, bulk velocity, mean reattachment length and tailwater depth, respectively. Likewise, the symbols U_m, y_m and $y_{0.5}$ represent the local streamwise maximum mean velocity, wall-normal location of U_m and the jet half-width (defined as wall-normal location where $U = 0.5U_m$ and $\partial U/\partial y < 0$), respectively. The offset jet can be divided into two shear layers, the inner and outer layers, separated by a shear layer dividing line. The inner shear layer spans from the bottom of the channel to y_m, with the outer shear layer spanning from y_m to the upper edge of the jet.

A considerable number of studies have been conducted to investigate the flow characteristics of 3D wall jets (e.g., Sforza & Herbst, 1970; Newman *et al*., 1972; Koso & Ohashi, 1981; Padmanabham & Lakshmana Gowda, 1991; Abrahamsson *et al*., 1997; Agelinchaab & Tachie, 2011a). Initial studies by Sforza & Herbst (1970) considered 3D wall jets generated from rectangular orifices with varying aspect ratios of 0.025, 0.05, 0.1 and 1. The decay of U_m was used to divide the flow field into three regions; (a) the potential core region, defined as the region where U_m was equal or close to the jet exit velocity, U_j, (b) characteristic

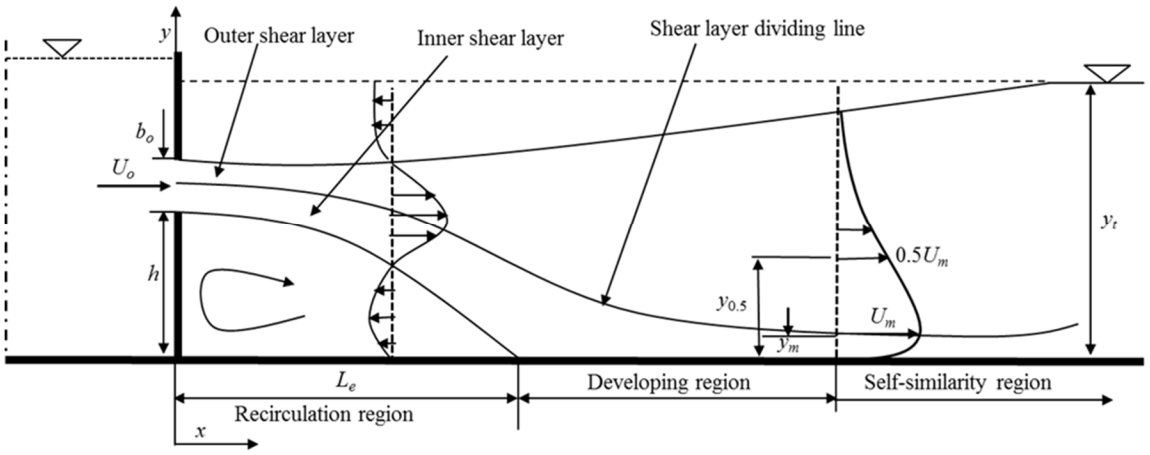

Figure 5.1 Schematic diagram of a discharged submerged offset jet

decay region, where the decay of U_m was observed to depend on the nozzle geometry and (c) the radial decay region, where the decay of U_m and flow characteristics became independent of nozzle geometry. Recent studies by Agelinchaab & Tachie (2011a) on a 3D round wall jet, performed at three different Re = 5000, 10000 and 20000 revealed that the early development of the flow depended on Re. The decay of U_m for a 3D wall jet was observed to increase with Re within the developing region of the flow. However, the decay of U_m and the jet half-width were observed to be independent of Re beyond 50d, which was within the estimated self-similarity region.

To date, the most comprehensive studies on 3D offset jets are those reported by Davis & Winarto (1980), Agelinchaab & Tachie (2011b) and Nyantekyi-Kwakye *et al*., (2015a). The investigation by Davis & Winarto (1980) utilized hot-wire annemometry to characterize the mean velocities and Reynolds stresses. A greater mixing rate within the lateral plane was observed compared to the wall-normal plane, which was consistent with higher spread rates (defined as $dy_{0.5}/dx$ and $dz_{0.5}/dx$ within the symmetry and lateral planes, respectively, where $z_{0.5}$ is the lateral half-width and it is defined as the lateral location where $U = 0.5U_m$), of 0.32, 0.33, 0.29 and 0.23 in the lateral plane compared to 0.037, 0.036, 0.039 and 0.046 obtained within the symmetry plane

for h/b_o of 0, 0.5, 1.5 and 3.5, respectively. Agelinchaab & Tachie (2011b) provided detailed studies on 3D round offset jets (with h/b_o ranging from 0 – 3.5) using a planar PIV system with a Re range of 5000 – 20000. The results indicated that both the decay of U_m and growth of the shear layer were influenced by h/b_o within the developing region. Their results also included two-point correlation analysis which together with the one-point statistics improved our understanding of the turbulence field of 3D offset jets.

Majority of the studies conducted on 3D offset jets relied on one-point statistics measurements. Multipoint statistics such as the two-point correlation and proper orthogonal decomposition (POD) have been used for wall-bounded and free shear flows to complement one-point statistic measurements. These techniques are used to investigate the large-scale and energetic structures which contribute immensly to turbulence production, mixing and entrainment of ambient fluid. The two-point correlation technique has been used to estimate the integral length scales and average inclination of hairpin-like vortex packets within the flow field of turbulent boundary layers (Volino *et al*., 2007), free jets (Wygnanski & Fiedler, 1969) and more recently in 3D wall and offset jets (Agelinchaab & Tachie, 2011a, b). The 3D offset jet results presented by Agelinchaab & Tachie (2011b) showed that the integral length scale increased with increasing h/b_o. However, the average inclination of the hairpin-like vortex packet within the inner shear layer was found to be 11° ± 3°, and independent of h/b_o. This inclination angle is similar to values of 13.2 ± 2.5°, 11° and 12° reported for canonical turbulent boundary layers (Volino *et al*., 2007; Christensen & Wu, 2005; Adrian *et al*., 2000).

The POD technique is used to extract the most energetic modes which are normally associated with the large-scale structures within the flow. This is achieved by decomposing series

of data sets into orthogonal functions (Holmes *et al*., 1996). The data from the POD technique can be used to reconstruct tubulence statistics such as streamwise turbulence intensity u' (defined as $(\overline{u^2})^{0.5}$, where u is the streamwise fluctuating velocity), wall-normal turbulence intensity v' (defined as $(\overline{v^2})^{0.5}$, where v is the wall-normal fluctuating velocity) and Reynolds shear stress, $\overline{uv}$. For flow dynamics dominated by large-scale strucutres, the turbulence statistics can be reconstructed satisfactorily with the first few modes obtained from the POD technique. The POD technique has been applied to a wide range of flows including bar racks in open channel (Tsikata *et al*., 2014), free jets (Meyer *et al*., 2007; Shim *et al*., 2013) and 3D wall jets (Agelinchaab & Tachie, 2011a). The results by Shim *et al*. (2013) revealed symmetric counter-rotating vortices within the initial region of the jet. These vortices were as a result of vortex merging at subharmonic sideband frequency. Further downstream, antisymmetric vortices dominated the flow with gradual displacement of the symmetric vortices. For the 3D wall jet, Agelinchaab & Tachie (2011a) reported significant contribution of the low-order modes to the turbulence quantities within the self-similarity region compared to the developing region. To date the POD technique has not been applied to the flow field of 3D offset jets though it is useful in quantifying the energy containing scales within the flow. Incorporating the two-point correlation analysis and POD technique will aid in providing an insightful interpretation of the dynamics of large-scale structures in 3D offset jets.

Previous studies were limited to the flow characteristics within the recirculation region of 3D offset jets. The flow dynamics were investigated using one-point statistics and two-point correlation analyses. The objective of the present study is to examine the effect of offset height ratio on the flow structures of 3D offset jets within the developing and self-similarity regions of

the flow. Analyses of the flow field will include investigating the spatial distribution of vortex structures using multipoint statistics such as the two-point correlation and proper orthogonal decomposition.

5.3 Experimental setup

5.3.1 Experimental facility

The experiments were conducted in a 2500 mm long open water channel with a square cross section of 200 mm × 200 mm. The side walls and channel bottom were made of smooth acrylic to facilitate optical access. Figure 5.2 shows a schematic of the experimental setup. The nozzle assembly was mounted 150 mm from the inlet of the water channel. Rectangular nozzles with dimensions 8 mm high (b_o) and 48 mm wide (b) used for the current studies were made from smooth acrylic plate of 6 mm thickness.

5.3.2 PIV system and measurement procedure

The velocity measurements were performed using a planar PIV system. Details of the PIV system and measurement procedure were presented by Nyantekyi-Kwakye *et al*. (2015a), so only an overview is presented herein. The flow was seeded with 10 μm silver coated hollow glass spheres having a specific gravity of 1.4. A New Wave Solo Nd:YAG double-pulsed laser with maximum energy of 120 mJ per pulse at 532 nm wavelength was used to illuminate the flow. The laser sheet was aligned with the mid-span of the test section for measurements in the symmetry (x–y) plane, which coincided with the center of the nozzle. Within the lateral (x–z) plane, the laser sheet was aligned at y_m. Scattered light from the tracer particles were captured with a 12-bit FlowSenseEO 4M charge-coupled device camera with a resolution of 2048 pixels × 2048 pixels

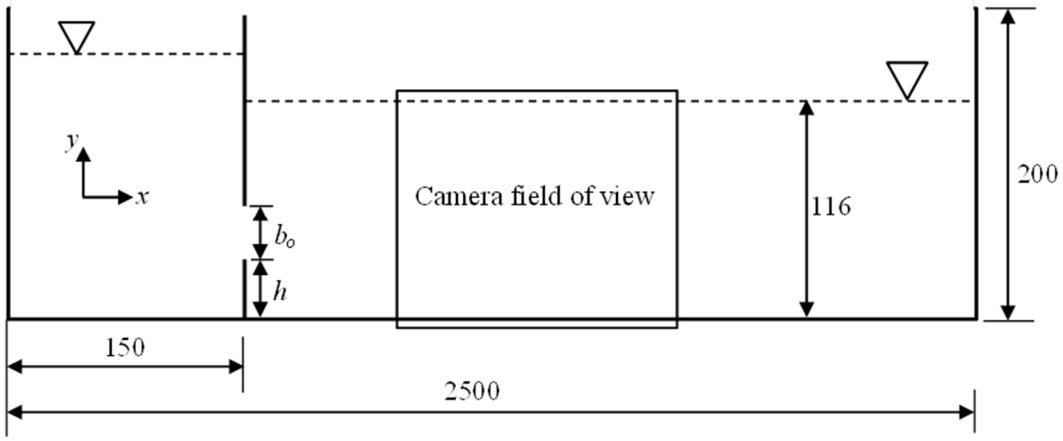

Figure 5.2 Schematic diagram of the experimental setup (side view; all dimensions in millimeters)

and a pixel pitch of 7.4 μm. A camera field of view of 120 × 120 mm^2 in the *x–y* plane and 118 × 118 mm^2 in the *x–z* plane was used and images were captured at an acquisition rate of 4 Hz. The interrogation area size was set to 64 pixels × 64 pixels with 50% overlap in both directions within the *x–y* plane and *x–z* plane. The instantaneous images were post-processed using the adaptive correlation option of DynamicStudio developed by Dantec Dynamics. An in-house MATLAB code was then used to calculate the mean velocities and higher order turbulence statistics. Based on initial convergence test, the mean velocities and turbulence statistics were calculated using 4000 instantaneous image pairs.

5.3.3 Test conditions and measurement uncertainties

Detailed measurements were taken at locations downstream of the nozzle. Measurements in the lateral plane were taken at y_m. The tailwater depth was maintained constant at 116 mm throughout the experiments as shown in Fig. 5.2. Experiments were conducted for nozzles with offset height ratios (h/b_o) of 0 (which corresponds to the wall jet), 2 and 4. The bulk velocity (U_o), which is defined as the area average of the velocity at the nozzle exit, was between 1.01-1.51 ms^{-1} yielding

a Reynolds and Froude numbers in the range of 8080–12080 and 3.6–5.4, respectively. The measurement uncertainty in the mean velocities and Reynolds stresses at 95% confidence level was estimated to be ±2.7% and ±11%, respectively, using the approach outlined by Forliti *et al*. (2000), Prasad *et al*. (1992) and Keane & Adrian (1991).

5.4 Results and discussion

Results are presented within the region $0 \leq x/b_o \leq 60$. The present results are also compared with previous studies on 3D wall and offset jets. The initial conditions and development of the 3D wall and offset jets (i.e., distribution of U_m, y_m, $y_{0.5}$ and $z_{0.5}$) have been thoroughly discussed and presented by Nyantekyi-Kwakye *et al*. (2015a) and as such will not be reported herein.

5.4.1 Flow visualization

Figure 5.3 shows contours of $U^* = U/U_o$ for the offset jets, with x^* and y^* denoting x/b_o and y/b_o, respectively. The maximum mean velocity of the discharged jet increased with streamwise distance close to the nozzle exit. This was as a result of the vena-contracta effect due to the sharp edge nature of the nozzle. The level of acceleration increased from $U^* = 1.1$ for the wall jet to 1.4 for both $h/b_o = 2$ and 4 offset jets. The low level of acceleration for the 3D wall jet is likely due to the wall resistance on the flow. The streamwise extent of the vena-contracta was estimated to be around $x/b_o = 1.0$, 2.5 and 2.5 for $h/b_o = 0$, 2 and 4, respectively. The smaller streamwise extent observed for the wall jet is due to the direct interaction between the jet and the bottom wall, and the similarity in the streamwise extent for $h/b_o = 2$ and 4 suggests that the interaction between the bottom wall and the jet for these two offset height is not significantly different. Beyond these streamwise locations, U was observed to decay with streamwise distance due to enhanced entrainment of the ambient fluid. A backflow region was formed above the jets.

Increasing the h/b_o resulted in a more intense backflow farther downstream. The maximum backflow velocity ($-U/U_o$) was estimated to be about 5%, 14% and 12% for h/b_o = 0, 2 and 4, respectively. The presence of the backflow subdued the wall-normal spread of the 3D jets as reported by Nyantekyi-Kwakye *et al.* (2015a). The mean reattachment length which is an important feature of offset jets was estimated to be $4.4b_o$ and $6.2b_o$ for h/b_o = 2 and 4 offset jets, respectively.

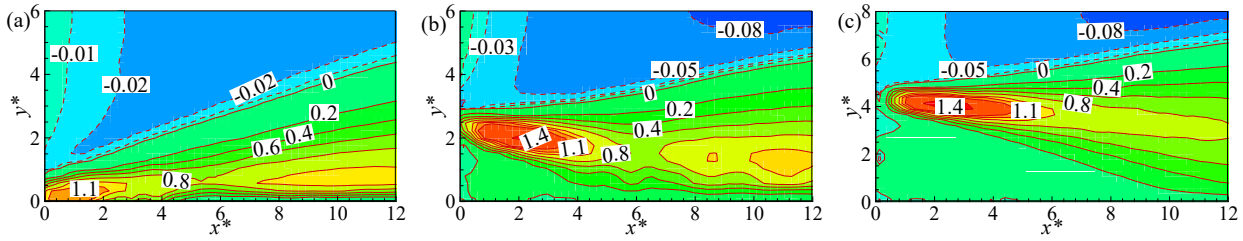

Figure 5.3 Contours of normalized streamwise mean velocities for (a) wall jet, (b) h/b_o = 2 and (c) h/b_o = 4 ($x^* = x/b_o$ and $y^* = y/b_o$)

5.4.2 Mean velocities and turbulence statistics

5.4.2.1 Mean velocity profiles

Profiles of the streamwise mean velocities extracted at x/b_o = 4, 10, 15, 20, 30, 50 and 60 are shown in Fig. 5.4. The velocity and length scale used was U_m and $y_{0.5}$, respectively. Different flow patterns were observed within the recirculation and developing regions, giving an indication of dependence of the mean flow on h/b_o in the early regions of the flow. The profiles change sign within the outer shear layer due to the intense backflow. Figure 5.4 also shows that the mean velocity distribution for the various jets was independent of h/b_o beyond $x/b_o \geq 30$. Profiles for the jets develop and attain self-similarity with streamwise distance (not shown). The profiles for the wall jet attained self-similarity at $x/b_o \geq 28$, which is further downstream compared to x/b_o = 20

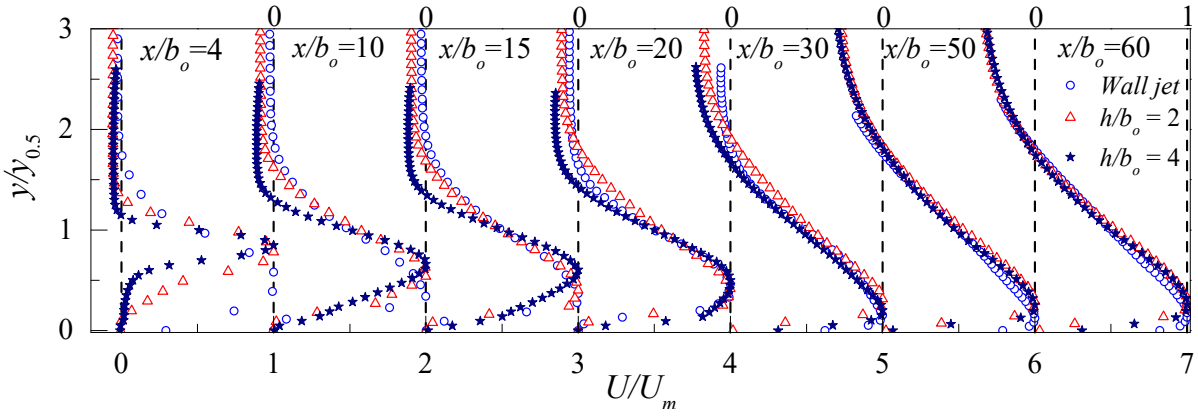

Figure 5.4 Streamwise mean velocity distribution of the offset jets

reported by Agelinchaab & Tachie (2011a) for a 3D wall jet. The longer streamwise extent for the wall jet can be attributed to the presence of the backflow within the outer shear layer as well as the turbulent free surface. The profiles for both offset jets (h/b_o = 2 and 4) attained self-similarity at approximately $x/b_o \geq 38$. This is similar to $x_l/b_o \geq 40$ reported by Agelinchaab & Tachie (2011b) for h/b_o = 1.5 and 3.5 (where $x_l = x - L_e$). It is to be noted that the profiles did not collapse entirely within the backflow region. Within the self-similarity region, the wall-normal location for the onset of the backflow occurred at $y = 1.78y_{0.5}$ for all test cases. It was observed that y_m moved closer to the bottom of the channel with increasing streamwise distance; for the wall jet, the value of y_m moved from about $y_m \approx 0.60y_{0.5}$ at x/b_o = 2 to a constant value of about $0.17y_{0.5}$ (within the self-similarity region). These values are consistent with previous studies on 3D wall jet by Abrahamsson *et al*. (1997). The location of y_m was observed to shift from $0.77y_{0.5}$ and $0.89y_{0.5}$ to $y_m \approx 0.23y_{0.5}$ and $0.24y_{0.5}$ for offset jets with h/b_o = 2 and 4, respectively.

5.4.2.2 Reynolds stresses

Figure 5.5 shows the distribution of the Reynolds stresses ($\overline{u^2}$, $\overline{v^2}$ and $-\overline{uv}$) in the $x - y$ plane at selected x/b_o. The profiles for all the jets did not attain self-similarity for the streamwise

range covered in this study unlike previous studies by Agelinchaab & Tachie (2011c). This can be partly explained by the backflow and associated high turbulence level in the outer shear layer. This also suggests that there is a strong interaction between the inner and outer shear layer of the turbulence field compared to the streamwise mean velocity. Double peaks were observed close to the nozzle exit until x/b_o = 2.2, 2.0 and 4.0 for h/b_o = 0, 2 and 4 offset jets, respectively. Changing h/b_o resulted in a reduction of $\overline{u^2}$ levels at x/b_o = 4. The reduction in $\overline{u^2}$ levels with increasing h/b_o at the initial stages of the jets development may be as a result of enhanced lateral stretching of eddies within the wall jet. Within the region $52 \leq x/b_o \leq 60$, the peak value of the normalized $\overline{u^2}$ was approximately 0.11 for the wall jet but increased to 0.13 and 0.22 for h/b_o = 2 and 4, respectively. It may be concluded that differences in the levels of $\overline{u^2}/U_m^2$ downstream of the flow with h/b_o are as a result of enhanced mixing due to the jet impingement.

The trend of $\overline{v^2}$ profiles for the 3D offset jets are qualitatively similar to their corresponding $\overline{u^2}$ profiles, except that the peak values are smaller in magnitude as shown in Fig. 5.5b. This is a clear indication of large-scale anisotropy in the turbulence field. The anisotropy level increased consistently with streamwise distance for the wall jet. For the offset jets, the level of anisotropy was observed to increase within the developing region of the flow and gradually decreased farther downstream. The level of anisotropy was observed to depend on h/b_o with estimated $\overline{v^2}/\overline{u^2}$ values of 0.40 ± 0.03 and 0.34 ± 0.02 for the wall jet and h/b_o = 4 offset jet, respectively, which are the two extreme cases estimated within the region $52 \leq x/b_o \leq 60$. These results demonstrate the limitation of turbulence models based on the isotropic assumption.

The Reynolds shear stress profiles are shown in Fig. 5.5c. The profiles are anti-symmetric at some streamwise locations. Positive values were obtained close to the wall, with negative values

occurring farther away from the wall. The wall normal location y_{uv}, where $-\overline{uv}$ changed sign was compared to the wall-normal location where the mean shear ($\partial U/\partial y + \partial V/\partial x$, where V is the wall-normal mean velocity) also changed sign. The results indicate that these two locations do not always coincide within the flow domain, thereby highlighting the limitation of turbulence models based on the eddy viscosity concept. Beyond $x/b_o > 20$, profiles of $-\overline{uv}$ are predominantly negative with peak values of $-\overline{uv}/U_m^2$ = 2.6%, 4.7% and 5.6% at x/b_o = 60 for wall jet and h/b_o = 2 and 4 offset jets, respectively.

5.4.3 Flow characteristics in the lateral plane

In order to examine the flow characteristics in the lateral plane, both streamwise and lateral mean velocities, and Reynolds stresses ($\overline{u^2}$, $\overline{w^2}$ and $-\overline{uw}$) are reported in Figs. 5.6 and 5.7. Measurements within the lateral plane were conducted on one side of the channel after initial measurements on both sides revealed the flow to be symmetric. The results are reported for five streamwise locations (x/b_o = 15, 30, 40, 50 and 60). The velocity and length scales used to normalize quantities in the lateral plane were U_m and $z_{0.5}$, respectively. The U profiles shown in Fig. 5.6a exhibited a reasonable collapse for the various jets. Profiles of U attained self-similarity earlier in the lateral plane compared to the symmetry plane (not shown). This observation suggests that the presence of the channel bottom had an impact on the rate at which the profiles evolved to the self-similar state within the symmetry plane. Profiles of the lateral mean velocity, W, for the various jets are presented in Fig. 5.6b and did not attain self-similarity. The distribution of W at x/b_o of 15 for the wall jet was predominantly positive. Increasing h/b_o to 2 and 4 at the same x/b_o = 15, caused the W profiles to switch to predominantly negative values as

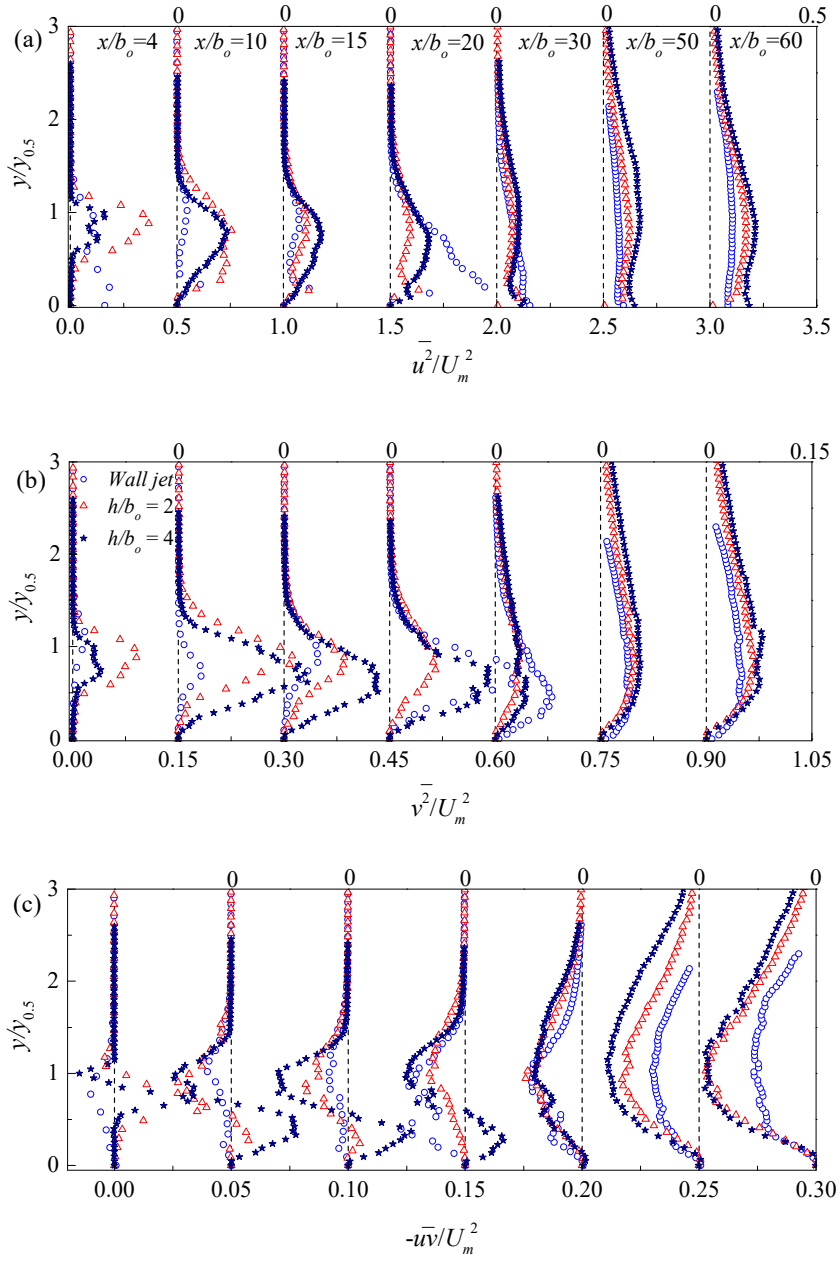

Figure 5.5 Distribution of the Reynolds stresses (a) $\overline{u^2}$, (b) $\overline{v^2}$ and (c) $-\overline{uv}$

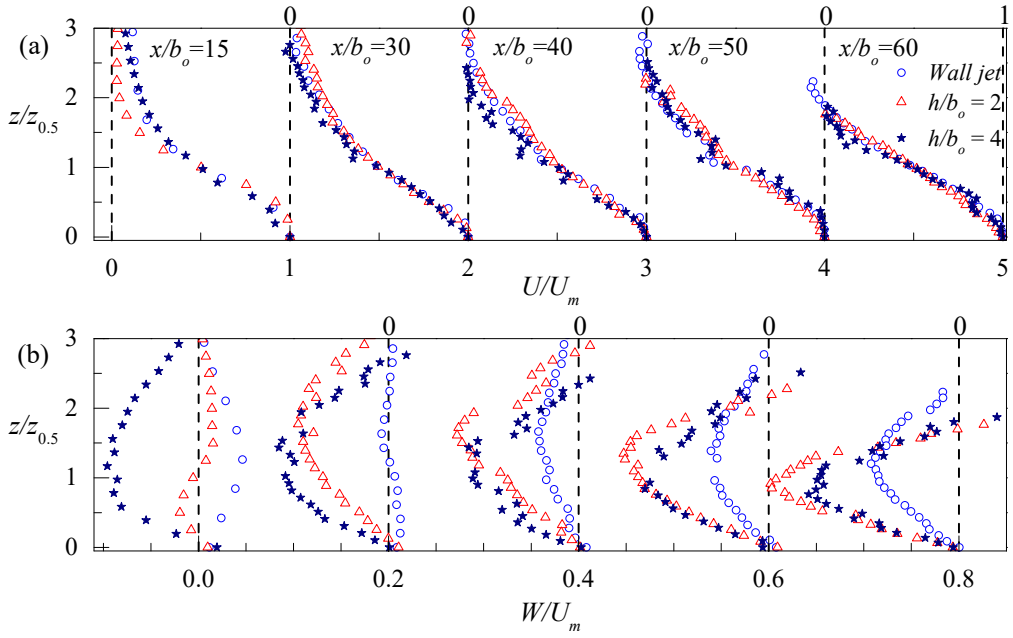

Figure 5.6 Profiles of (a) streamwise mean velocity and (b) lateral mean velocity for the offset jets

a result of entrainment of the ambient fluid into the core regions of the jet. Larger values of W were obtained compared to V at similar measurement planes. This in part, explains the observed larger lateral spread rates (0.116 and 0.114 for h/b_o = 0 and 2, respectively) of the jet compared to the wall-normal spread rates (0.066 and 0.016 for h/b_o = 0 and 2, respectively), reported by Nyantekyi-Kwakye *et al*. (2015a).

The profiles of $\overline{u^2}$, $\overline{w^2}$ and $-\overline{uw}$ are presented in Fig. 5.7 for the 3D offset jets. For the streamwise locations considered the profiles of $\overline{u^2}$, $\overline{w^2}$ and $-\overline{uw}$ did not attain self-similarity. The profiles of $\overline{u^2}$ shown in Fig. 5.7a were nearly independent of h/b_o when h/b_o was increased from0 to 2. However, the normalized peak of $\overline{u^2}$ increased by 53% when h/b_o was further increased to 4. The present $\overline{u^2}$ data for h/b_o of 0 and 2 were estimated to be 34% and 25% greater than corresponding values reported by Agelinchaab & Tachie (2011a) at x/b_o = 60 for h/b_o = 0 and

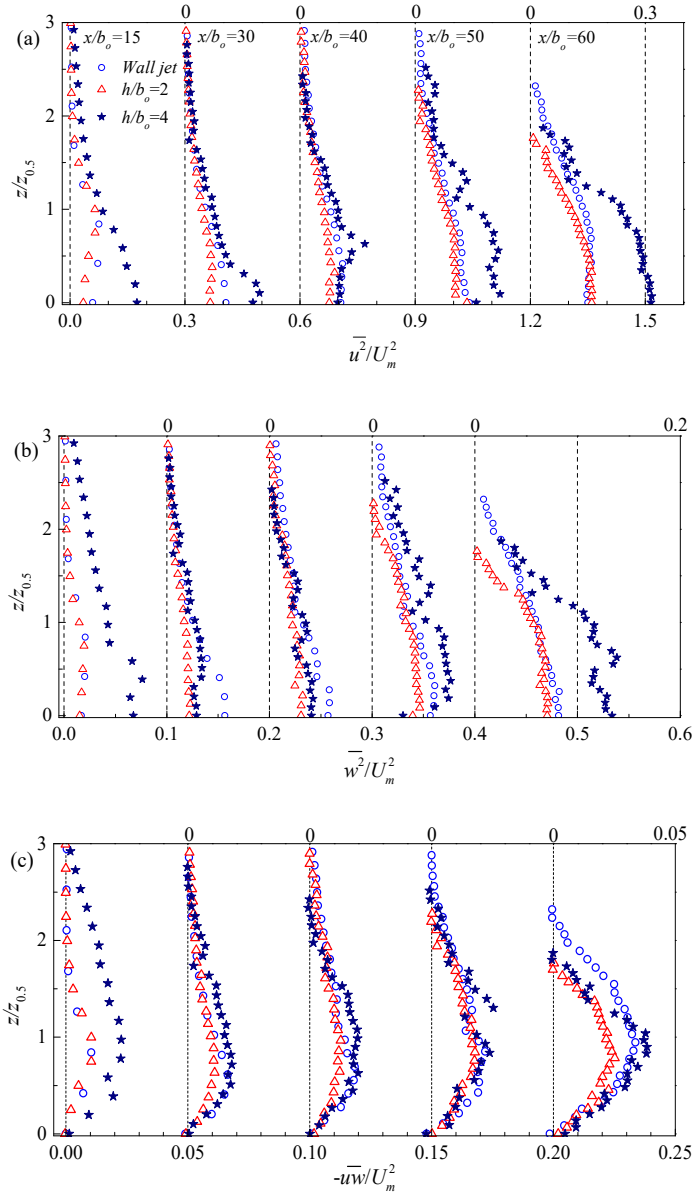

Figure 5.7 Reynolds stress distribution in the lateral plane (a) $\overline{u^2}$, (b) $\overline{w^2}$ and (c) $-\overline{uw}$ for the offset jets

1.5, respectively. The profiles of $\overline{w^2}$ are shown in Fig. 5.7b with the peaks for $h/b_o = 0$ and 2 being 20% less than those reported by Agelinchaab & Tachie (2011a). The peak values of $\overline{w^2}$ are less than $\overline{u^2}$ values, highlighting the anisotropic nature of the flow, but are larger than $\overline{v^2}$ at similar x/b_o

locations. The anisotropy of the normal stresses has been reported to contribute to the generation of stress-induced streamwise vorticity by Abrahamsson *et al.* (1997). This mechanism causes a lateral movement of fluid away from the symmetry plane thereby contributing to the larger lateral spreading of 3D jets. The profiles of $-\overline{uw}$ (shown in Fig. 5.7c) showed similar trends to those of $\overline{u^2}$ and $\overline{w^2}$. The present data for $-\overline{uw}$ are similar to those reported in previous study by Agelinchaab & Tachie (2011a). For the same streamwise location, the peak values of $\overline{uv}$ are larger than $\overline{uw}$ and this may be attributed to a lower correlation between u and w compared to that between u and v.

5.4.4 Two-point auto correlation

The two-point correlation was employed to investigate the effect of h/b_o on the correlation of turbulence structures within the developing and self-similarity regions of the flow. Comprehensive two-point correlation analysis has been presented within the recirculation region by Nyantekyi-Kwakye *et al*. (2015a) and as such will not be repeated herein. The two-point correlation functions in the $x - y$ plane at a reference point (x_r, y_r) for u and v separated by Δx and Δy are defined as

$$R_{uu}= \overline{(u(x_r, y_r)u(x_r + \Delta x, y_r + \Delta y))}/u'(x_r,y_r)u'(x_r+\Delta x, y_r+\Delta y) \tag{5.1}$$

$$R_{vv}= \overline{(v(x_r, y_r)v(x_r + \Delta x, y_r + \Delta y))}/v'(x_r,y_r)v'(x_r+\Delta x, y_r+\Delta y) \tag{5.2}$$

The analysis was performed at two x/b_o locations, 10 and 50, representing the developing and self-similarity regions, respectively. The wall-normal locations were restricted to within the inner shear layer of the flow with y/y_m ranging from 0.1 to 0.9 at 0.1 intervals. From these analyses, contours of R_{uu} were used to estimate the average inclination of the hairpin-like structures within the flow.

Figures 5.8 and 5.9 show contours of the two-point correlation functions for the streamwise fluctuating velocity (R_{uu}) and wall-normal fluctuating velocity (R_{vv}), respectively at $y_r/y_m = 0.5$ for $x/b_o = 10$ and 50. Contour levels used in the present study for R_{uu} and R_{vv} were from 0.6 to 1.0 at intervals of 0.1. Within the developing region, the R_{uu} contours were more rounded and smaller in size compared to the self-similarity region. The relatively smaller size of R_{uu} contours in the developing region can be attributed to the breakdown of the large-scale structures after reattachment of the jet. This was evident from the analyses of the flow structures within the recirculation region, reported by Nyantekyi-Kwakye *et al.* (2015a), where larger contours were obtained compared to the developing region. As the jet develops farther downstream, the structures merge and become larger within the self-similarity region. The R_{uu} contours also increase in size with x/b_o as well as h/b_o. Similarly, the R_{vv} contours (Fig. 5.9) increase in size with x/b_o and h/b_o, implying that the structures increase in size with h/b_o.

The angle of inclination ($\beta°$) of the R_{uu} contours within the inner shear layer of the flow indicates the average inclination of the hairpin-like structures. Values of $\beta°$ were estimated by fitting least-squares through the farthest points away from the peak of the self-correlation at different contour levels. In order to minimize estimation errors, ellipses of different sizes were fitted to the various contour levels (e.g., shown in Fig. 5.8) to estimate the inclinations. The obtained values for β within the self-similarity region are summarized in Table 5.1. The values of β for the various jets are independent of h/b_o. These values are in good agreement with 11.2° ± 0.6° reported by Agelinchaab & Tachie (2011b) for 3D jets and are also comparable to 13.2° ± 2.5° reported for boundary layer flow by Volino *et al*. (2007).

The turbulent length scales within the self-similarity region at $y_r/y_m = 0.5$ were estimated from streamwise and wall-normal extents of the 0.6 contour levels. This approach has been described in detail by Nyantekyi-Kwakye *et al*. (2015a). Values of Lx_{uu}, (streamwise extent of R_{uu}), Ly_{uu}, (wall-normal extent of R_{uu}), Lx_{vv} (streamwise extent of R_{vv}) and Ly_{vv} (wall-normal extent of R_{vv}) normalized by b_o are presented in Table 5.1. The estimated integral length scale (Lx_{uu}) increased with increasing h/b_o. It should also be remarked that within the inner layer, the extents increased with wall-normal distance. It can be seen from Table 5.1 that larger values of Lx_{uu} were obtained compared to Lx_{vv}. The larger values of Lx_{uu} can be attributed to the fact that R_{uu} is linked to the convection velocity of the various hairpin-like packets as suggested by Volino *et al*. (2007). Likewise, the observed larger values of Lx_{uu} in comparison with the other turbulent length scales may be attributed to a stronger coherence of streamwise fluctuating velocity signal (Tachie *et al*., 2009). For instance, values of Lx_{uu}/Ly_{uu} of 2.3, 4.2 and 4.6 were obtained for $h/b_o = 0$, 2 and 4 offset jets, respectively. The obtained values for the offset jets are comparable to 4.2 ± 0.2 reported by Agelinchaab & Tachie (2011c) for offset jets with h/b_o ranging from 0 to 3.5, but are larger than 2.5 reported by Volino *et al*. (2007) in a turbulent boundary layer.

Slices through the streamwise and wall-normal R_{uu} contours at $x/b_o = 10$ and 50 within the symmetry plane are plotted in Fig. 5.10. These profiles provide an indication of the decay of the auto-correlations in the streamwise and wall-normal directions. Figure 5.10 revealed that R_{uu}

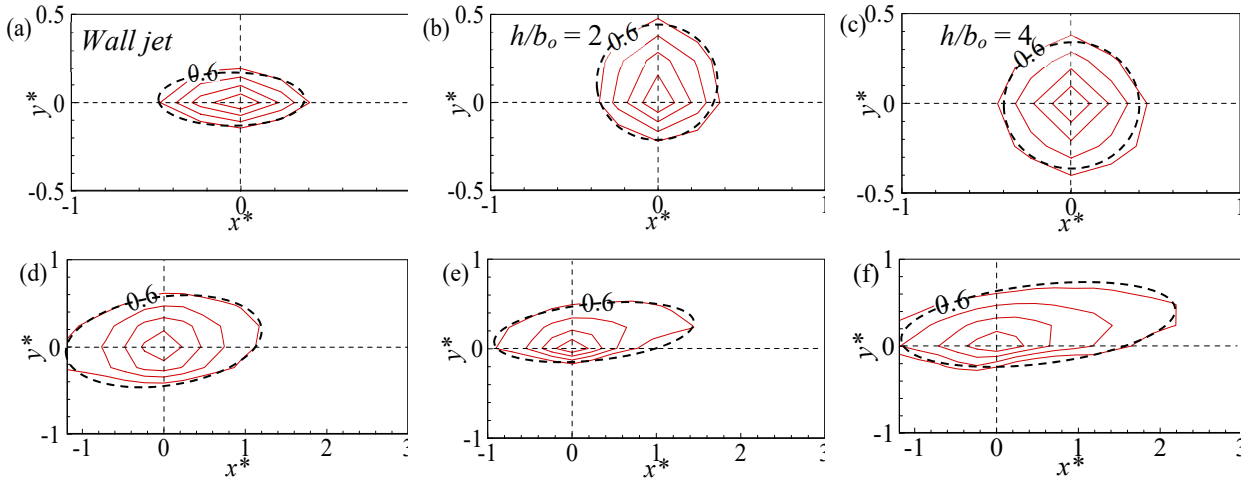

Figure 5.8 Contours of R_{uu} at x/b_o of 10 (a to c) and 50 (d to f): at $y/y_m = 0.5$ for $h/b_o = 0$, 2 and 4

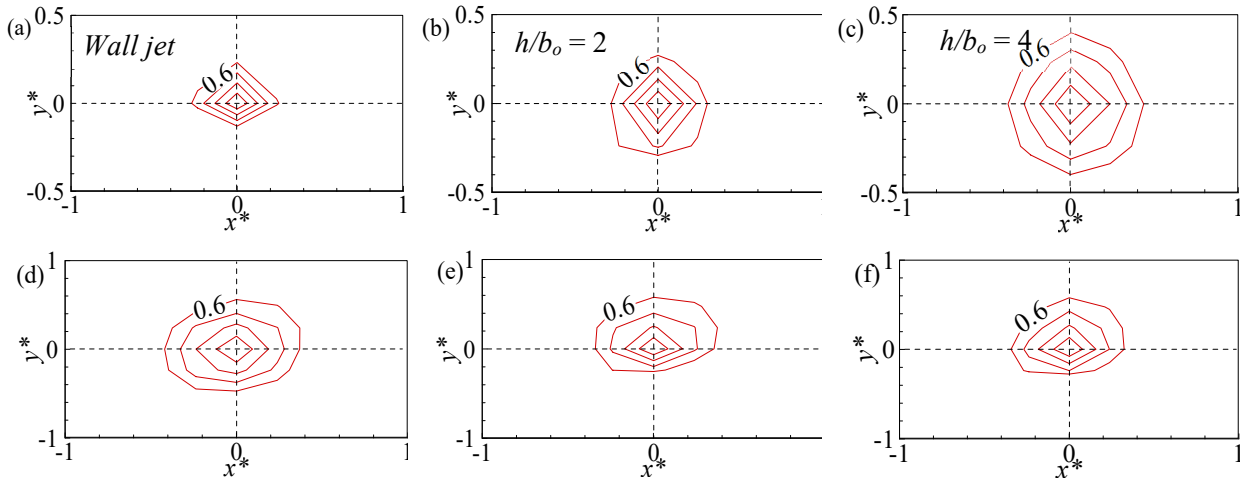

Figure 5.9 Contours of R_{vv} at x/b_o of 10 (a to c) and 50 (d to f): at $y/y_m = 0.5$ for $h/b_o = 0$, 2 and 4

Table 5.1 Inclination and normalized spatial extents of the contours estimated at $x/b_o = 50$ and $y_r/y_m = 0.5$

Quantities	*Wall jet*	$h/b_o = 2$	$h/b_o = 4$
Angle of inclination, β°	12.3	11.8	11.8
Lx_{uu}	2.30	2.86	4.40
Ly_{uu}	1.02	0.68	0.96
Lx_{vv}	0.78	0.72	0.66
Ly_{vv}	1.03	0.89	0.86

profiles decayed faster in the developing region compared to the self-similarity region of the flow. This is a direct inference from the fact that the large-scale structures are more organized and correlated within the self-similarity region compared to the developing region. It was also observed that R_{uu} profiles in the wall-normal direction (shown in Fig. 5.10b) decay more rapidly than in the streamwise direction. Figure 5.10a shows that increasing h/b_o resulted in a slower decay of $R_{uu}(x)$.

Contour plots of R_{uu} and R_{ww} in the lateral plane at $x/b_o = 50$, $y = y_m$ and $z/b_o = 0.7$ are presented in Fig. 5.11. The R_{uu} contours within the lateral plane were observed to increase in size when h/b_o was increased from 0 to 2. However, a subsequent increase to $h/b_o = 4$ resulted in a smaller size of the R_{uu} contour. The smaller size of the contours for the $h/b_o = 4$ offset jet may have been a result of the wavy surface of the flow due to intense backflow. Within the lateral plane the R_{uu} contours were more rounded than in the symmetry plane. The smaller sizes of the contours are consistent with the low levels of Reynolds stresses in the lateral plane compared to the symmetry plane. Contours of R_{ww} also exhibited dependence on h/b_o with a larger contour when h/b_o was increased from 0 to 2.

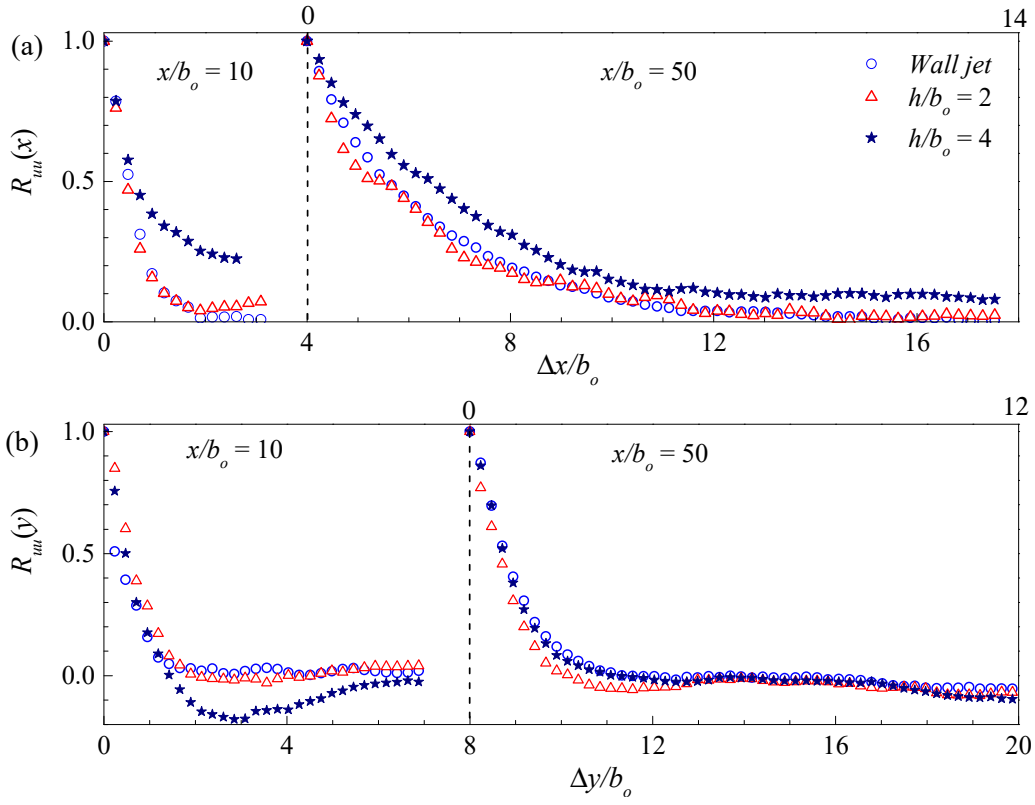

Figure 5.10 Streamwise and (b) transverse slices through self-correlation points at $y/y_m = 0.5$ for the jets at x/b_o of 10 and 50

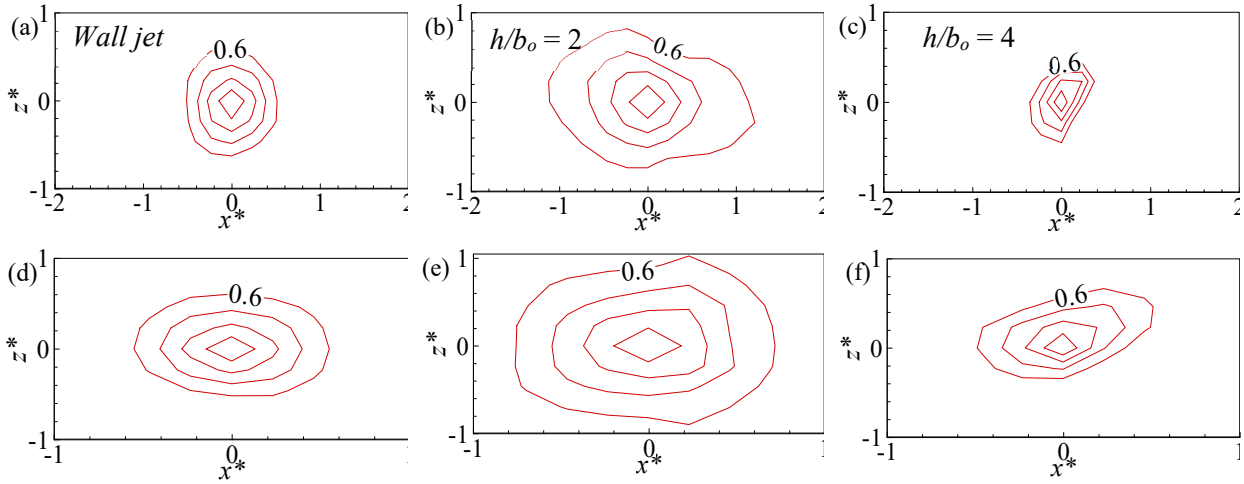

Figure 5.11 Contours of R_{uu} (a to c) and R_{ww} (d to f): at $x/b_o = 50$ and $z/b_o = 0.7$ within the lateral plane for $h/b_o = 0$, 2 and 4 ($z^* = z/b_o$)

5.4.5 Proper orthogonal decomposition (POD) analysis

The *POD* analysis was used in the present study to extract the dominant features within the flow fields of the offset jets. The snapshot approach proposed by Sirovich (1987) was adopted in the present investigation. The snapshot POD method was described in detail by Meyer *et al*. (2007) and an overview presented in Chapter 2 and as such would not be repeated herein. The energy convergence, spectra analysis and reconstructed profiles of the u', v' and $-\overline{u}\overline{v}$ are reported in this section. The results are presented within the symmetry plane for recirculation region (P1), developing region (P2) and self-similar region (P4) which correspond to $0 \leq x/b_o \leq 12$, $14 \leq x/b_o \leq 26$ and $51 \leq x/b_o \leq 63$, respectively. Results for the lateral plane are presented for P2 only since the results from the other planes are qualitatively similar.

5.4.5.1 Convergence test

A convergence of the POD was performed to confirm that the sample size of 4000 was sufficient to achieve converged results. This was achieved by computing the fractional turbulent kinetic energy ($\lambda_i/\Sigma\lambda$) associated with the most energetic mode (which is mode 1) for increasing N. Results on the convergence are presented only for P1 and P2 within the symmetry and lateral plane, respectively (Table 5.2). The convergence for P2 and P4 (within the symmetry plane) was not presented since a qualitatively similar conclusion can be drawn as per analysis for P1. It can be seen from Table 5.2 that the contribution of mode 1 to the total energy ($\lambda_1/\Sigma\lambda$) decreased significantly when N was increased from 10 to 20. The energy level decreased with increasing N until a threshold value was attained, beyond which there was no significant difference. The 4000 snapshots used for the present analysis were therefore sufficient for convergence of the POD results.

Table 5.2 Convergence test for POD snapshots for the offset jets in the symmetry and lateral planes

N	Eigenvalues, λ					
	Symmetry plane			Lateral plane		
	P1			P2		
	Wall jet	h/b_o = 2	h/b_o = 4	*Wall jet*	h/b_o = 2	h/b_o = 4
10	19.1	31.9	28.8	17.6	17.9	19.3
20	11.3	20.6	18.5	19.9	12.6	13.6
100	7.7	9.0	11.3	9.5	11.8	9.3
500	7.0	8.0	7.0	8.3	9.2	10.5
1000	7.1	7.3	6.7	8.2	9.8	14.4
2000	7.2	7.3	7.9	7.0	9.8	14.4
3000	7.2	7.6	8.7	7.4	9.6	13.9
4000	7.1	7.6	8.6	7.2	9.7	14.1

Energy spectra

The distributions of fractional and cumulative energy associated with the first 50 modes are shown in Fig. 5.12 within the symmetry and lateral planes. As expected, the fractional energy associated with the modes decreased monotonically with increasing number of modes. The rate of decay of the fractional energy within P4 is faster than for P1 and P2. The fractional energy was larger within P4 compared to P1 and P2. That is, the dominant structures within the self-similarity region are more organized and energetic compared to the developing region. This observation supports the results obtained from the two-point analysis where larger turbulent length scales were estimated within the self-similarity region compared to the developing region. For P2, measurements in the lateral plane depict more energetic features compared to the symmetry plane as shown in Figs. 5.12b and 5.12d.

The cumulative contribution of the modes to the total turbulent kinetic energy is also shown in Fig. 5.12. Within the symmetry plane, the first mode respectively captured about 7.1%, 7.6% and 8.6% of the total turbulent kinetic energy in P1 for h/b_o = 0, 2 and 4 jets as illustrated in Table 5.2. In the lateral plane, the wall jet converged at a slower rate compared to the offset jets. The slower convergence can be attributed to an increase in range of turbulent length scales. The modes required to capture 50% and 90% of the total turbulent kinetic energy for the 3D jets are summarized in Table 5.3. Within the developing regions of the jets, increasing h/b_o resulted in a slower convergence of the total turbulent kinetic energy. Since the low-order modes in the self-similarity region are more energetic and organized than in the developing region, fewer modes were required to capture 50% and 90% of the total energy for the offset jets in P4.

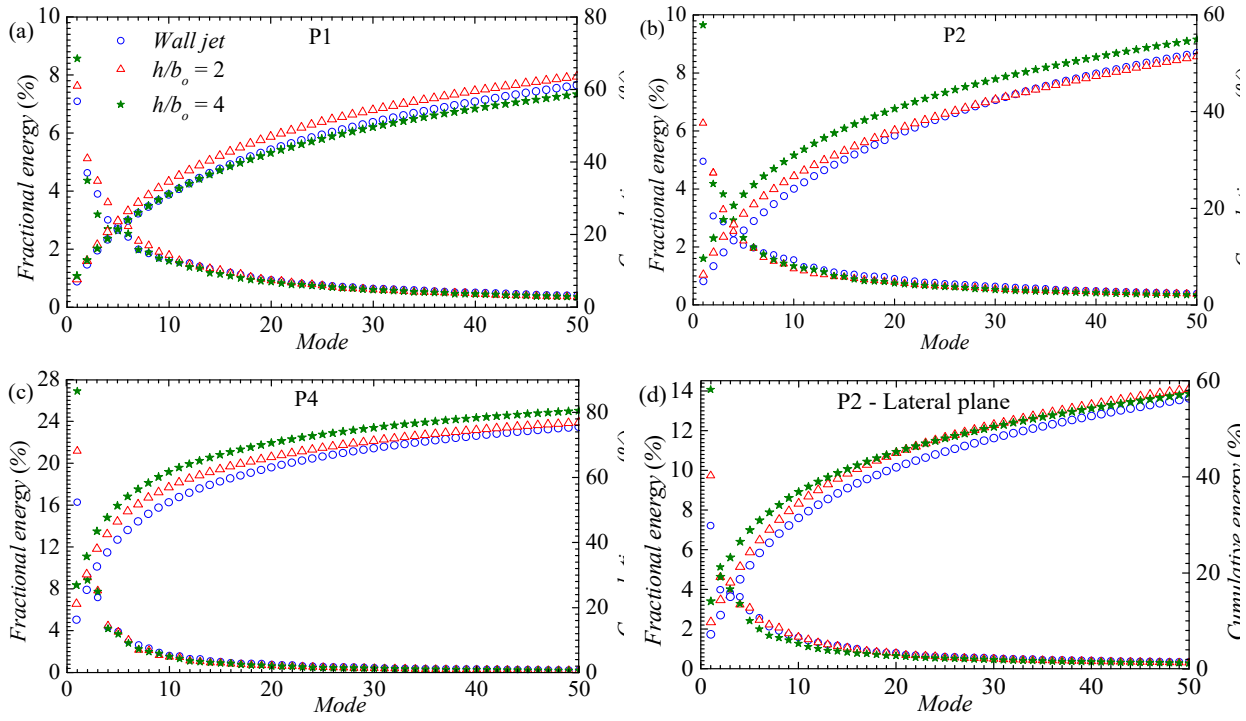

Figure 5.12 Distribution of fractional and cumulative kinetic energy for the first 50 modes for the offset jets

Table 5.3 Number of modes required to contribute 50% and 90% of the total energy within the flow field

Condition	Symmetry plane						Lateral plane	
	P1		P2		P4		P2	
	50%	90%	50%	90%	50%	90%	50%	90%
Wall jet	29	263	45	455	9	238	34	470
$h/b_o = 2$	24	281	47	468	6	235	29	521
$h/b_o = 4$	31	368	37	483	5	167	30	602

5.4.5.2 Reconstruction of turbulence quantities

The reconstructed velocity field is used to quantify the contribution of the coherent structures to the turbulence statistics. The reconstructed turbulence statistics are presented in the form of contours and one-dimensional profile plots. A low-order representation of u', v' and $-\overline{u}\overline{v}$ within the symmetry plane was reconstructed using modes 1 and 2, and the results are compared to the corresponding ensemble-averaged PIV data. The velocity scale employed for normalizing the contours was U_o. Due to space limitation, contours are only presented for the wall jet; however, the results for all test cases will be discussed. Reconstructed contours for the offset jets have been presented in Appendix C. Contribution from the low-order modes are shown in Fig. 5.13. The first mode contributed about 59%, 10%, 10% and 19% towards the maximum values of u', v', as well as the positive and negative peaks of $-\overline{u}\overline{v}$, respectively. Increasing the number of modes to 2 contributed an additional 9%, 5%, 2% and 17% to the maximum values of u', v' and the positive and negative peaks of $-\overline{u}\overline{v}$, respectively. Overall, the first 10 modes contributed about 78%, 25%, 55% and 69% to the total maximum values of u', v' and negative peak of $-\overline{u}\overline{v}$, respectively. This implies that the low-order modes contributed more significantly to u' within the developing region

compared to both $-\overline{uv}$, and v'. Likewise within the self-similarity region (not shown), the first mode contributed 70%, 29% and 53% towards u', v' and the negative peak of $-\overline{uv}$, respectively. However, the first 10 modes contributed about 81%, 49% and 82% towards the maximum values of u', v' and the negative peak of $-\overline{uv}$, respectively. Analyzing the modal contribution towards u', v' and $-\overline{uv}$ for the offset jets in the self-similarity region revealed that the low-order modes contributed proportionately towards u' and $-\overline{uv}$ compared to v'. Increasing h/b_o resulted in a decrease in the contribution of the low-order modes to the turbulence quantities within the developing region. This was however not the case within the self-similarity region, where it was observed that the flow was characterized by more energetic structures when h/b_o was increased. For example, the first 10 modes contributed about 12% more towards the maximum negative value of $-\overline{uv}$ for the offset jets compared to the wall jet. This explains the low level of Reynolds shear stress obtained in the self-similarity region for the wall jet compared to the offset jets.

The distribution of the reconstructed u', v' and $-\overline{uv}$ are presented at two streamwise locations x/b_o = 10 and 60 representing the developing and self-similarity regions, respectively and are shown in Fig. 5.14 for the wall jet. The reconstructed fields were obtained from modes 1, 2 and 5, together with modes that contributed 50% and 90% of the total turbulent kinetic energy. This was done in order to quantitatively investigate the cumulative effect of using more modes for reconstructing the turbulence statistics. For each streamwise distance, the corresponding ensemble-average obtained from the PIV data is included for comparison. Both U_m and $y_{0.5}$ were used as the velocity and length scales, respectively. It can be seen from Fig. 5.14 that increasing the number of modes caused the reconstructed profiles to gradually approach the ensemble-averaged PIV data. Within the self-similarity region, the low-order modes revealed significant

peaks for $-\overline{uv}$ and u'. The contribution of the low-order modes to the peak of v' was observed to be the least. This is an indication that the less energetic structures contribute significantly to the formation of the peak of v'. Figure 5.14 clearly depicts that the energetic structures contribute more to $-\overline{uv}$ and u' than v'. For instance at x/b_o = 60 for the wall jet case, the first 5 modes contributed about 86% and 81% towards $-\overline{uv}$ and u', respectively, compared to 48% towards v'. The present results are consistent with previous measurements by Agelinchaab & Tachie (2011b) for a 3D wall jet.

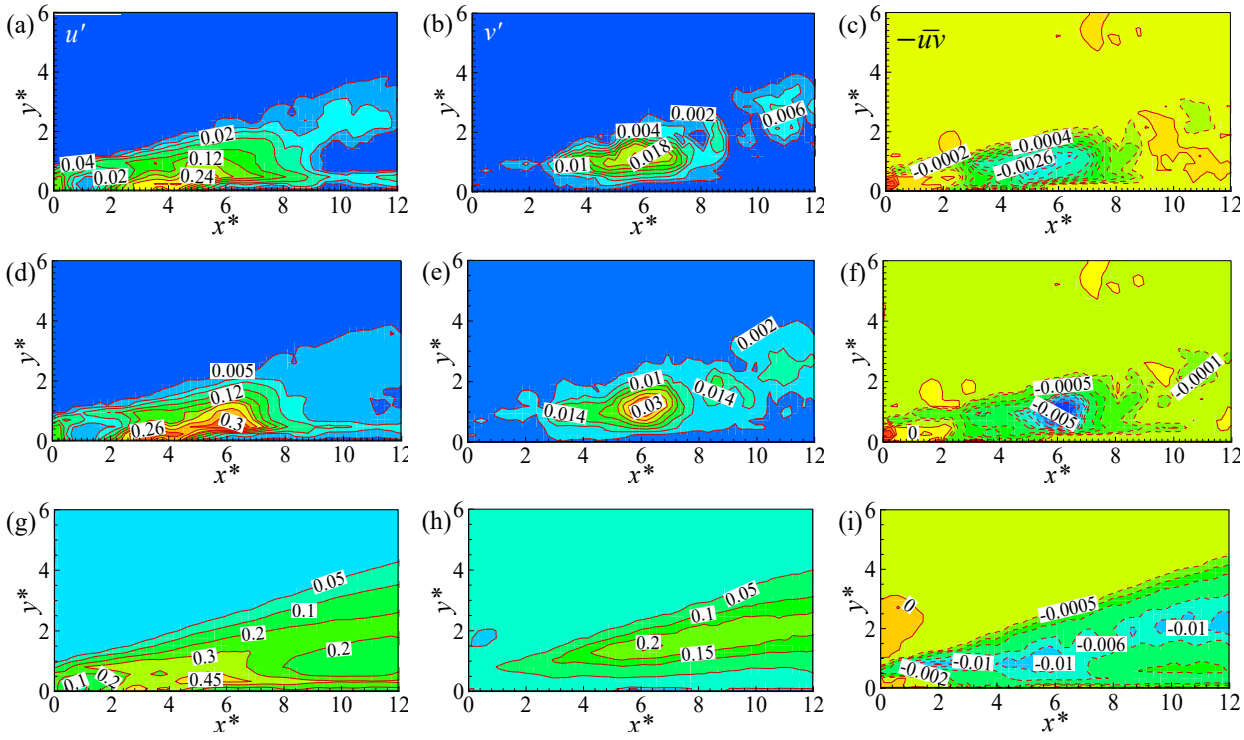

Figure 5.13 Contour plots of u', v' and $-\overline{uv}$ for mode 1 (a - c), mode 2 (d - f) and PIV data (g - i)

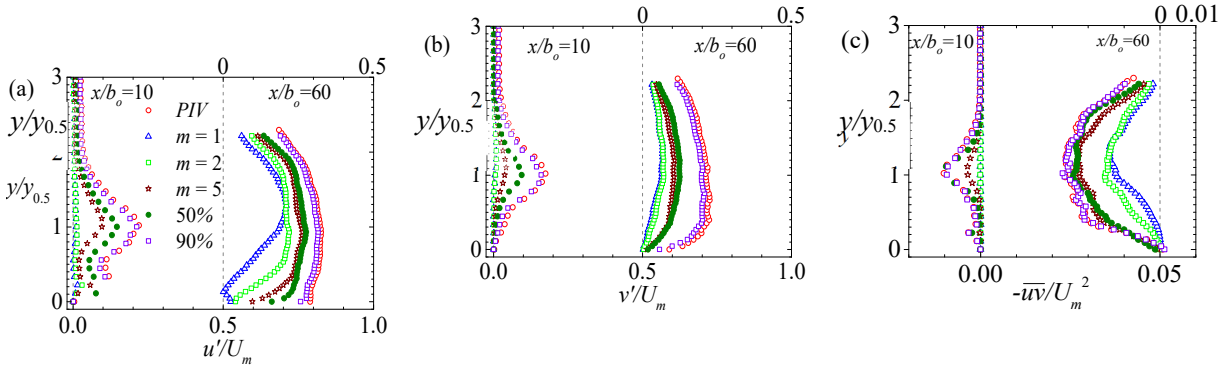

Figure 5.14 Reconstructed profiles of (a) u', (b) v' and (c) $-\overline{uv}$ for the wall jet

5.5 Conclusions

Investigations of 3D turbulent offset jets were conducted using a PIV technique. The offset jets were generated from sharp-edged rectangular nozzles. Both one-point and multi-point statistics were used to provide insight into the salient features of 3D offset jets. The development of the flow within the developing region was observed to be dependent on h/b_o. The formation of a backflow region within the outer shear layer influenced the development of the mean flow and Reynolds stresses. Profiles of the streamwise mean velocity attained self-similarity beyond $x/b_o \geq 28$ for the wall jet, which was farther downstream compared to previous studies. For the two offset jets, U profiles attained self-similarity at $x/b_o \geq 38$. Due to the presence of the backflow, the distribution of Reynolds stresses did not attain self-similarity for the x/b_o range considered in the present investigation. Analysis of the Reynolds stresses revealed that turbulence models based on eddy viscosity concept and isotropic turbulence assumption will likely be unsuccessful in predicting the flow field of 3D offset jets.

Contours of the two-point analysis revealed that the large-scale structures within the inner layer increase with wall-normal distance from the channel bottom. The contours also increased in size with increasing h/b_o within the self-similarity region. Within the self-similarity region, the

integral length scale increased with increasing h/b_o. The average inclination of the hairpin-like structures within the self-similarity region was estimated to be $12° \pm 0.2°$, and this was independent of h/b_o. The POD analysis revealed the dominance of energetic structures in the self-similarity region compared to the developing regions. A low-order representation of the u', v' and $-\overline{u}\overline{v}$ terms suggest that the less energetic structures are responsible for the formation of the peak values. The energetic structures contributed more towards u' and $-\overline{u}\overline{v}$ compared to v'.

CHAPTER SIX

6 PAPER III

Flow Characteristics of an Offset Jet over a Surface Mounted Square Rib

6.1 Abstract

A three-dimensional offset jet flow over a surface mounted square rib was investigated using particle image velocimetry at Reynolds number of 7600. The square rib was mounted at three different locations downstream of the nozzle exit. Contour and profile plots in the symmetry plane were used to investigate the effect of the rib on the mean flow distribution and turbulence statistics. Changing the rib location enhanced the mixing and entrainment characteristics of the jet thereby leading to larger wall-normal spread rates. The quadrant analysis revealed a significant contribution of all events towards the Reynolds shear stress. The joint probability density function analysis showed that the structures within the outer shear layer of the jet differed from those of boundary layers. Results from the two-point correlation analysis indicated that the introduction of a surface mounted rib modified the flow structures within the developing region. However, there was no significant structural difference between the flow with mounted rib and the no rib case within the self-similar region. The proper orthogonal decomposition was used to examine how changes in rib location modified the dynamics of the energetic modes towards the turbulent kinetic energy and Reynolds shear stress within the developing and self-similar regions.

6.2 Introduction

Three-dimensional (3D) offset jets are encountered in many engineering applications such as environmental discharges for communal or industrial wastewater, fluid injection system, defrosting in automobiles and thrust-augmenting ejectors for vertical takeoff and landing aircrafts.

Likewise, 3D offset jet flow over surface mounted ribs are encountered in engineering applications such as baffle blocks in stilling basins for energy dissipation. The shear layer of 3D offset jets is significantly distorted when the jet reattaches to the solid boundary, making it impossible to use the thin shear layer approximations. In this regard, detailed studies of offset jet flows can be used as prototypical flows to investigate the flow fields of complex separated and reattached flows. The flow characteristics of 3D offset jets over surface mounted ribs can also be used to model practical flow phenomena such as discharge of submerged jets in stilling basin applications. Also, understanding the flow characteristics of 3D offset jets over a surface mounted rib can help improve the design and performance of hydraulic structures.

The flow fields of an offset jet over a surface mounted rib can be divided into three main regions: (i) recirculation region, (ii) developing or recovery region, and (iii) self-similar region as shown in Figure 6.1(a). The recirculation region spans from the nozzle exit to the location where the jet reattaches to the bottom of the channel. The developing region spans from the mean reattachment point to the start of the self-similar region. The self-similar region is the streamwise range where the flow characteristics do not vary with streamwise distance when appropriate scaling is applied. The reattachment of the jet is an unsteady process and may occur within a streamwise range denoted in Figure 6.1a as the reattachment region. The reattached offset jet consists of an inner shear layer (which exhibits structural similarities to a turbulent boundary layer) and an outer shear layer (with characteristics similar to half of a free jet). The inner and outer shear layers are separated by a shear layer dividing line. The inner shear layer extends from the channel bottom to y_m (which is the wall-normal location of the local maximum streamwise mean velocity, U_m) while the outer shear layer extends from y_m to the edge of the jet. Since these two shear layers have different turbulent characteristics, they strongly interact making the reattached offset jet an

interesting flow to investigate. Figure 6.1a also shows the wall-normal half-width, $y_{0.5}$, which is the wall-normal location where the local velocity is equal to $0.5U_m$.

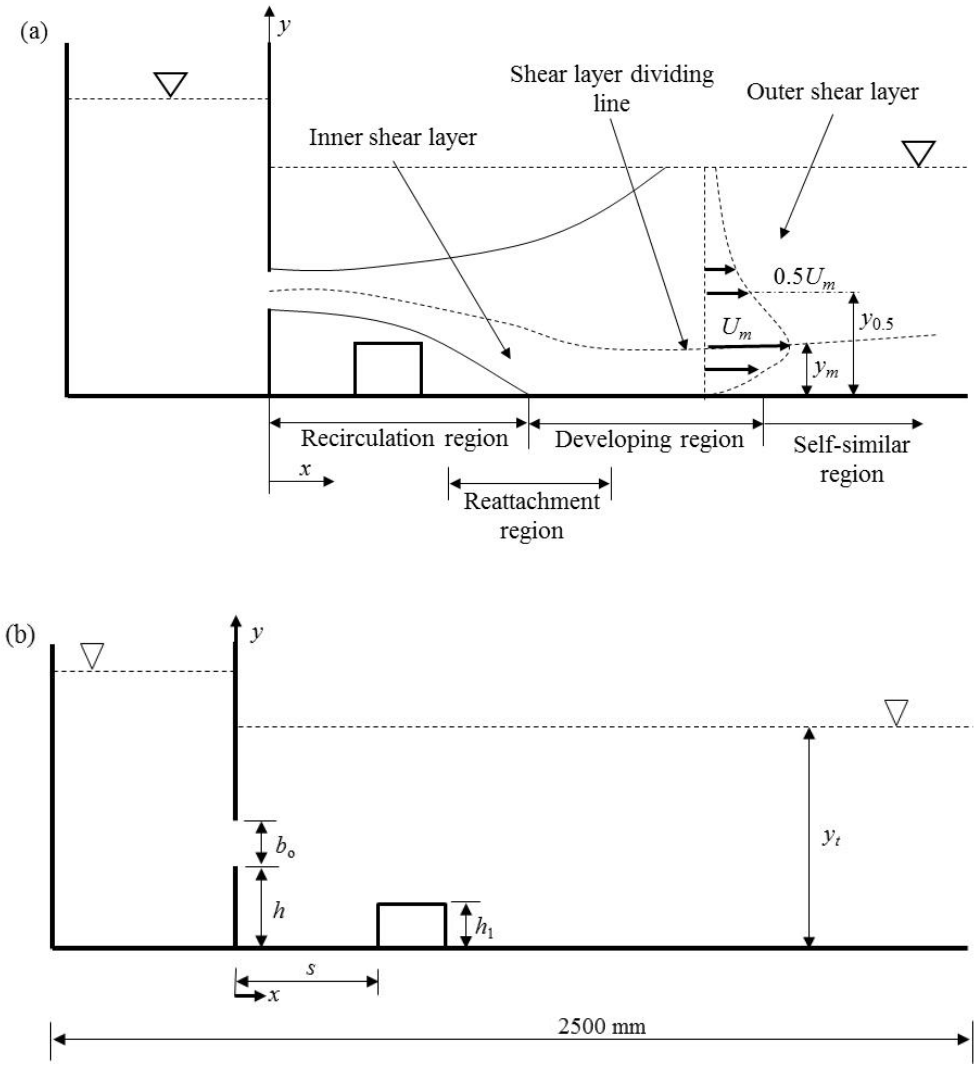

Figure 6.1 Schematic of (a) an offset jet flow over a square mounted rib and (b) experimental setup (side view)

The turbulent flow characteristics over surface mounted ribs have been studied extensively (Shah & Tachie, 2009b; Agelinchaab & Tachie, 2008; Hwang *et al*., 1999; Martinuzzi & Tropea, 1993; Antoniou & Bergeles, 1985; Bergeles & Athanassiadis, 1983; Castro, 1979). Martinuzzi &

Tropea (1993) investigated flow characteristics over surface-mounted ribs with 11 different aspect ratios (*AR*, defined as the ratio of rib width to rib height) ranging from 1 to 24. The effect of the ribs on the flow patterns was classified to be either two-dimensional (2D) or 3D depending on *AR*. It was found that when $AR > 10$, 2D regions existed upstream of the recirculation region formed in front of the rib. The results by Martinuzzi & Tropea (1993) showed that the flow in the vicinity of ribs with small *AR* was characterized by the interaction of the horseshoe-vortex with the recirculation vortex and the reattaching shear layer. Increasing *AR* caused the effect of the horseshoe vortex to be observed along the wake edges. Bergeles & Athanassiadis (1983) studied the effect of square and rectangular ribs of varying lengths on the extent of the recirculation region. Their results revealed that the length of the recirculation region formed in front of the ribs was independent of the aspect ratio. However, the length of the recirculation region downstream was observed to decrease with increasing rib aspect ratio. Similar conclusions were reported by Hwang *et al*. (1999).

Recent studies by Shah & Tachie (2009b) considered flow over a surface mounted square rib in the presence of adverse and favorable pressure gradients. In the vicinity of the rib, the separated shear layer dominated the dynamics of the flow. Both Reynolds stresses and turbulence production were significantly enhanced within the separated shear layer. The mean velocity and turbulent quantities across a larger portion of the channel were greatly enhanced by the adverse pressure gradient (APG) compared to a favorable pressure gradient (FPG). The effect of rib geometry (square, rectangular and semi-circular rib) on flow separation in an open channel was investigated by Agelinchaab & Tachie (2008). It was observed that the separated shear layer reattached on top of the rectangular rib before subsequently reattaching to the bottom of the channel. However, the separated shear layer completely enclosed the square and semi-circular ribs

and reattached to the channel bottom. Since the separated shear layer reattached on top of the rectangular rib, it affected the downstream development of the boundary layer. Within the reattachment region of the separated shear layer, variations in the Reynolds stresses were attributed to the dominant wall damping effect compared to vortex stretching and the strain rate. The flow characteristics within the recirculation and reattachment regions were strongly dependent on rib geometry. A new shear layer developed downstream of the reattachment point. A distance of approximately 90 rib heights downstream of the rib was required for boundary layer parameters (such as the Clauser parameter) to attain values measured upstream of the rib. This development rate was strongly dependent on rib geometry within the reattachment region of the flow.

Most previous experimental studies on surface mounted ribs were conducted in either zero pressure gradient boundary layers, APG, FPG, closed channels and open channels. The flow characteristics of 3D offset jets over ribs have not been researched in detail. The 3D offset jet flow is significantly different in configuration to previous experimental studies reviewed since there is a primary recirculation region due to the elevation of the jet from the bottom of the channel. Investigations by Nyantekyi-Kwakye *et al*. (2015a) and Agelinchaab & Tachie (2011c) revealed that large scale structures responsible for mixing and entrainment of the jet increased in size with increasing offset height ratio of the 3D jet. These structures were observed to be more dynamically dominant in the outer shear layer than in the inner shear layer of the flow (Agelinchaab & Tachie, 2011c). In an earlier study, Nyantekyi-Kwakye *et al*. (2015b) investigated the flow characteristics of 3D offset jets in the absence of a surface mounted rib in both the symmetry and lateral planes. Their results showed drastic flow variations in the symmetry plane compared to the lateral plane. To date, the dynamics of the complex interaction between the inner and outer shear layers of the reattached jet is not fully understood. The 3D offset jet over a smooth surface is quite complex,

and the introduction of a surface mounted rib within the inner shear layer creates an even more complicated flow configuration. For example, the introduction of the rib causes an interaction with the inner shear layer and this interaction can be diffused farther away from the channel bottom and nozzle exit. The objective of this study is therefore to investigate the effect of rib location on the flow structures of a 3D offset jet. The present experiment was performed at Reynolds number and flow condition similar to previous studies by Nyantekyi-Kwakye *et al*. (2015a, b). Detailed velocity measurements were performed in the symmetry plane (where the interaction of the inner and outer shear layers can be modified in the presence of a surface mounted rib) using planar particle image velocimetry. Both one-point and multi-point statistics were used to investigate the flow dynamics of the turbulent offset jet over the surface-mounted rib. Results from the present study would be useful to assess the ability of turbulence models to predict the flow characteristics of 3D offset jets.

6.3 Experimental setup and measurement procedure

The experiments were performed in an open channel with dimensions 2500 mm long and a square cross section of 200 × 200 mm^2. The side walls as well as the bottom of the test section were made from smooth acrylic to facilitate optical access. A Cartesian coordinate system was used, with x and y representing the streamwise and wall-normal directions, respectively. The 3D offset jet was generated from a sharp-edged rectangular nozzle with dimensions 8 mm high (b_o) and 48 mm wide. The experiments were conducted for an offset height ratio (h/b_o) of 2. As shown in Figure 6.1b, a two dimensional acrylic rib of 10 × 10 mm square cross section spanning the entire channel width was used. Three sets of experiments corresponding to placement of the rib at streamwise locations of x/b_o = 1.25, 3.45 and 6.25 from the nozzle exit (which are hereafter referred to as R1, R2 and R3, respectively, for brevity) were performed. From the reference experiment

with no mounted rib (Nyantekyi-Kwakye *et al*., 2015a), the mean reattachment length was estimated to be $4.4b_o$. Therefore, R1, R2 and R3 corresponded to streamwise locations within the recirculation, reattachment and developing regions, respectively. The tailwater depth, y_t, was maintained constant at $14.5b_o$, which was sufficiently high to suppress the formation of a hydraulic jump. The bulk velocity, U_o, of the flow was 0.95 ms^{-1} yielding a Reynolds number ($Re = (b_oU_o)/\nu$) and Froude number ($F = U_o/(gb_o)^{0.5}$) of 7.6×10^3 and 3.4, respectively, where ν is the kinematic viscosity of water and g is the acceleration due to gravity. Measurements were conducted in the symmetry plane (x–y), over a streamwise range of $0 \leq x/b_o \leq 80$.

The velocity measurements were performed using a planar particle image velocimetry system. The flow was seeded with 10 μm silver coated hollow glass spheres having a specific gravity of 1.4. A New Wave Solo Nd:YAG double-pulsed laser with maximum energy of 120 mJ per pulse at 532 nm wavelength was used to illuminate the flow field. The laser sheet was aligned with the mid-span of the test section for measurements in the symmetry plane. A thin laser sheet of approximately 1 mm was used within the camera field of view in order to reduce the number of de-focused particles. Scattered light from the tracer particles were captured with a 12-bit charge-coupled device (CCD) camera that has a resolution of 2048 × 2048 pixels, and a pixel pitch of 7.4 μm. The CCD camera was fitted with a green band-pass filter of wavelength 530 nm. Dantec Dynamics commercial software (DynamicStudio version 3.4) was used to control the data acquisition. A camera field of view of 120 × 120 mm^2 was used. Measurements were acquired in five planes, with the first plane capturing the reattachment of the discharged offset jet. The interrogation area size was set to 32 pixels × 32 pixels with 50% overlap in both directions within the symmetry plane. The time interval between pulses was chosen such that the maximum particle displacement was smaller than 25% of the interrogation area size. The instantaneous images were

post-processed using the adaptive correlation option of DynamicStudio developed by Dantec Dynamics. An in-house MATLAB code was then used to calculate the mean velocities and higher order turbulence statistics. Based on a convergence test, the mean velocities and turbulence statistics were calculated using 4000 instantaneous image pairs captured at a rate of 4 Hz. The uncertainty in the mean velocities and Reynolds stresses at 95% confidence level was estimated to be ±2.7% and ±11% of the peak values, respectively, following the procedure outlined by Nyantekyi-Kwakye *et al*. (2015a)

6.4 Results and discussion

6.4.1 Mean velocity structure

Streamlines are used to visualize the mean flow structure within the x–y plane as shown in Figure 6.2. The red line underneath the streamlines is the zero streamwise mean velocity contour level. Entrainment of the ambient fluid into the core region of the jet created a pressure drop between the discharged jet and the bottom of the channel. This led to the deflection of the discharged jet towards the bottom of the channel where it eventually attached. The attached jet enclosed a recirculation region which is clearly visible underneath the discharged jet. In the case of R1 (Figure 6.2a), only the primary recirculation due to the offset of the jet from the channel bottom was observed. For both R2 and R3, two recirculation regions were observed as can be seen from Figure 6.2b to Figure 6.2c. Prior to the leading edge of the rib, the center of the recirculation bubble occurred at $x/b_o = 2.1$ and $y/b_o = 1$ for R2 and $x/b_o = 1.8$ and $y/b_o = 0.9$ for R3. Beyond the trailing edge of the rib, the center of the recirculation bubble was observed to be at $x/b_o = 5.2$ and $y/b_o = 0.5$ for R2 and $x/b_o = 8.4$ and $y/b_o = 0.58$ for R3. Changing the rib location also increased the magnitude of negative U within the recirculation region by about 50% and 29% when the rib

location was changed from R1 to R2 and from R1 to R3, respectively. This is attributed to the deflection of the jet by the rib when it was mounted at the reattachment point and beyond. An important feature of an offset jet is the streamwise extent of the recirculation region, which is referred to as the reattachment length (L_e). The mean L_e was estimated using the 50% forward-flow fraction technique. Mean L_e values of $4.75b_o$, $7.05b_o$ and $8.60b_o$ were obtained for R1, R2 and R3, respectively. The value for R1 was similar to $4.4b_o$ obtained for the reference case with no surface mounted rib reported by Nyantekyi-Kwakye *et al.* (2015a). The L_e prior to the leading edge of the rib for R2 and R3 was $3.05b_o$ and $6.0b_o$, respectively. The relatively longer mean reattachment length for R2 and R3 were as a result of the rib placement and its corresponding interaction with the discharged offset jet.

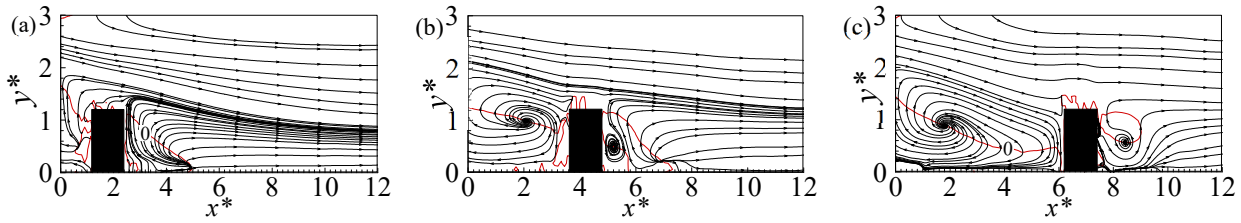

Figure 6.2 Streamlines of the mean velocity for experiment (a) R1, (b) R2, (c) R3 (where $x^* = x/b_o$ and $y^* = y/b_o$)

6.4.2 Jet decay and spread

The decay of the local maximum streamwise mean velocity, U_m, and wall-normal jet half width, $y_{0.5}$, were used to investigate the influence of rib location on the streamwise development of the 3D offset jet and are illustrated in Figure 6.3. Values of U_m increased close to the nozzle exit for all the jets due to the vena-contracta effect. The extent of increase spanned a streamwise distance of x/b_o = 4.5, 2.5 and 3.0 for R1, R2 and R3, respectively. After the initial increment, U_m

decayed rapidly until x/b_o = 4.3 and 6.0 for R2 and R3, respectively due to the presence of the rib. As the jet flow past the rib, U_m increased again until x/b_o = 6.0 and 9.6 for R2 and R3, respectively. Beyond these locations, U_m gradually reduced with streamwise distance due to enhanced mixing and entrainment of ambient fluid. As the jet developed farther downstream, lower values of U_m were observed for both R2 and R3 compared to R1. This was expected since the rib was positioned within the recirculation region in the case of R1 and as such had minimal effect on U_m. Changing the rib location in the case of R2 and R3 caused an interaction of the rib with the jet, thereby creating extra recirculation regions which enhanced entrainment of ambient fluid thereby reducing U_m levels. It should be remarked that entrainment of the ambient fluid is enhanced as separation is approached. Therefore, the greater the number of recirculation zones, the higher the level of entrainment by the offset jet. The decay rates for the jets were estimated as the gradient of the linear fit (of the form $U_m/U_o = B(x/b_o + c_u)$; where B is the decay rate and c_u is the kinematic virtual origin), to the experimental data within the region $25 \leq x/b_o \leq 80$. Decay rate values of 0.015, 0.012 and 0.011 were estimated for R1, R2 and R3, respectively. The estimated values confirm a slightly faster decay for both R2 and R3 compared to R1 due to the enhanced mixing and entrainment. The present decay rate for R1 is comparable to 0.017 reported for the reference case Nyantekyi-Kwakye *et al*. (2015a).

The wall-normal jet half-width ($y_{0.5}$), which is a measure of the wall-normal growth of the 3D offset jet is illustrated in Figure 6.3b. The wall-normal half-width varied linearly with streamwise distance except close to the nozzle exit, i.e., at $x/b_o \leq$ 4.7, 3.0 and 4.2 for R1, R2 and R3, respectively, where values of $y_{0.5}$ reduced with streamwise distance. The observed decrease in $y_{0.5}$ gives credence to the presence of the vena-contracta effect due to the sharp-edged nature of the rectangular nozzle which leads to the generation of horseshoe vortices close to the nozzle exit.

Sforza & Herbst (1970) observed that the presence of these horseshoe vortices close to the nozzle exit cause some irregularities within the velocity field. Changing the rib location enhanced the levels of $y_{0.5}$ due to the higher levels of U_m decay discussed previously. The spread rate of the jet was estimated as the gradient ($dy_{0.5}/dx$) of the linear fit to the measured data and occurred in two stages as a result of the backflow formed in the jet outer shear layer. The first stage was estimated within the region $25 \leq x/b_o < 60$ with spread rate values of 0.018, 0.014 and 0.011 for R1, R2 and R3, respectively. The second stage occurred within the region $60 \leq x/b_o \leq 80$ and was characterized by intense backflow within the outer shear layer of the jet. Spread rate values of 0.049, 0.066 and 0.052 were obtained for R1, R2 and R3, respectively within the second stage. The present results indicate larger wall-normal spreading of the discharged jet in the second stage compared to the first stage. The slightly larger wall-normal spread rates for R2 and R3 compared to R1 can be linked to their enhanced U_m decay. The present $dy_{0.5}/dx$ value of 0.056 ±0.007 is in agreement with 0.055 ±0.001 reported by Agelinchaab & Tachie (2011c) and slightly less than 0.041 ±0.005 obtained by Davis & Winarto (1980) for 3D offset jets with $h/b_o = 0 – 3.5$.

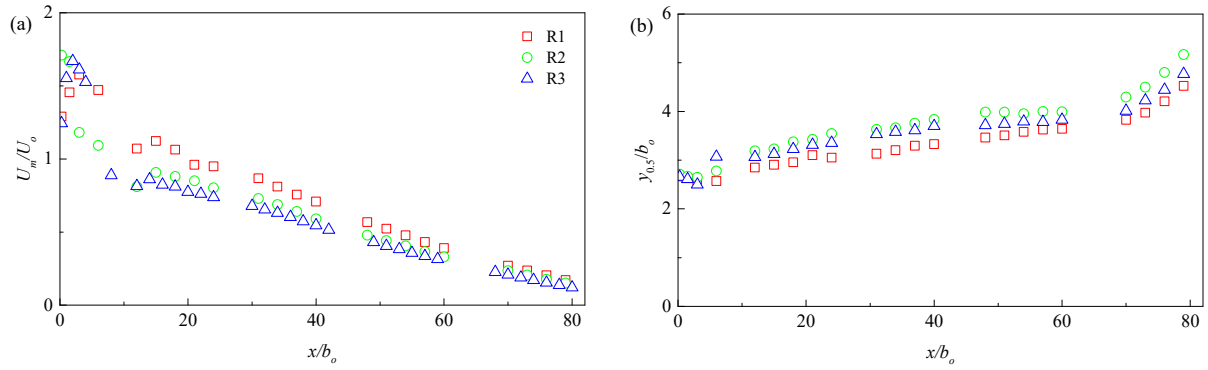

Figure 6.3 Profiles of (a) local maximum streamwise mean velocity decay and (b) wall-normal jet half-width

6.4.3 Mean velocity profiles and Reynolds stresses

Profile plots of the streamwise mean velocity, U, and Reynolds stresses are presented in Figure 6.4 at selected streamwise locations ($x/b_o = l_r$, L_e, 10, 15, 20 and 30) in order to investigate the flow characteristics within the different flow regions. Streamwise location l_r corresponds to midway between the trailing edge of the rib and the reattachment point. The velocity and length scales used were U_m, and $y_{0.5}$, respectively. The distribution of U was observed to be modified by the rib placement within the developing region of the flow as can be seen in Figure 6.4a. The recovery process is slowest in the case of R3. However, beyond $x/b_o \geq 30$, the rib placement did not affect the distribution of U for all test conditions. Negative values of U within the outer shear layer were as a result of the backflow region created above the jet, with an estimated magnitude of $0.3U_m$ for all test conditions. The streamwise mean velocity of the 3D offset jet attained self-similarity beyond $x/b_o \geq 20$ for both R1 and R2 and $x/b_o \geq 25$ for R3. The farther downstream extent of the rib in the case of R3 was as a result of slow relaxation of the flow after reattachment. It is to be noted that complete collapse of U profiles was not attained within the backflow region. The streamwise extent for the onset of self-similarity of the 3D offset jets are less than $x/b_o \geq 38$ for the no rib case reported by Nyantekyi-Kwakye *et al*. (2015b).

Figures 6.4b-6.4d show the distribution of the Reynolds stresses ($\overline{u^2}$, $\overline{v^2}$ and $-\overline{uv}$) for all test conditions at the same streamwise locations previously specified. The normalized profiles of the Reynolds stresses did not attain self-similarity within the streamwise range considered. It should be emphasized that within the recirculation and reattachment region, the distribution of the streamwise Reynolds normal stress ($\overline{u^2}$) was observed to be similar at l_r and L_e for R1, with the profiles showing distinct double peaks. Beyond L_e, there was a slight increase in $\overline{u^2}$ before

subsequently reducing due to enhanced mixing. Changing the rib location to R2 and R3 resulted in high levels of $\overline{u^2}$ at L_e and beyond, until $x/b_o = 30$ where the effect of rib on the flow diminished just as observed in the distribution of U. At L_e, $\overline{u^2}$ increased by 76% and 83% when the rib location was changed to R2 and R3, respectively. Likewise, changing the rib location to R2 and R3 at $x/b_o = 10$ resulted in an increase of over 70% in $\overline{u^2}$. It should be noted that $\overline{u^2}$ was relatively high for R2 at l_r compared to R1 and R3 test cases. This occurrence suggests that the flow dynamics within the recirculation and reattachment regions are largely controlled by the structures generated by the reattachment process and not the high turbulence levels within the outer shear layer. A similar distribution was observed for the wall-normal Reynolds normal stress ($\overline{v^2}$). The levels of $\overline{v^2}$ increased by 74% and 64%, respectively, when the rib location was changed to R2 and R3 at $x/b_o = 10$. These results show that changing the rib location influenced the dynamics of the flow within the developing region more than in the self-similar region. The enhanced levels of the normal stresses can be attributed to the breakdown of larger structures after reattachment of the jet, an event which controls the dynamics of the normal stresses (Etheridge & Kemp, 1978), and can also be associated with the strong shear within these regions as was reported by Shah & Tachie (2009b). The normal stresses became independent of rib location beyond $x/b_o \geq 30$. As a result of mixing and spreading of the 3D offset jet, the levels of the Reynolds normal stresses decreased monotonically and the normalized profiles became more uniform with streamwise distance. These findings are in agreement with results by Kostas *et al*. (2005) for flow over a backward facing step.

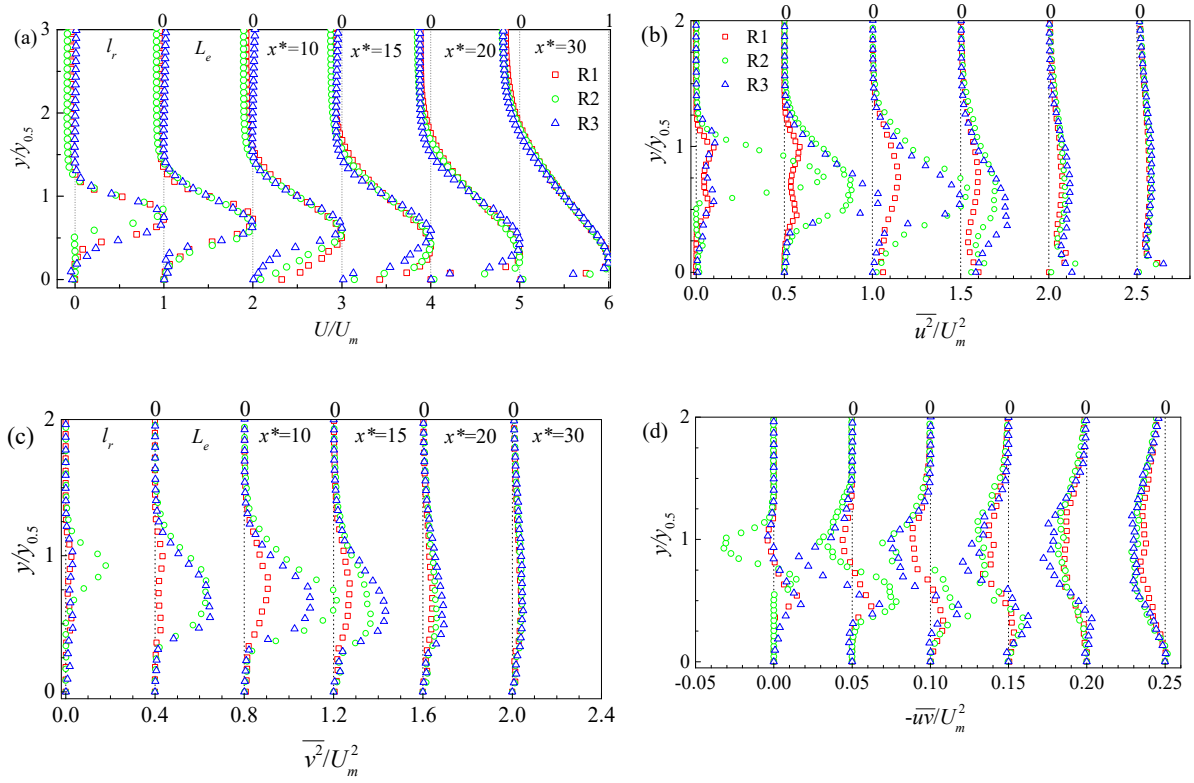

Figure 6.4 Profiles of streamwise mean velocity and Reynolds stresses at selected x/b_o locations

The effect of rib placement on the Reynolds shear stress, $-\overline{uv}$, is examined in Figure 6.4d. The antisymmetric distribution of $-\overline{uv}$ persisted for all test conditions for x/b_o considered. For both R1 and R3, the magnitude of the maximum positive $-\overline{uv}$ is larger than the maximum negative $-\overline{uv}$ at l_r and L_e. However, the magnitude of the maximum negative $-\overline{uv}$ for R2 is larger than the maximum positive $-\overline{uv}$ within the recirculation region and vice versa at L_e. The larger values of Reynolds shear stress at l_r and L_e can be associated with the prevalence of large turbulence structures generated within the recirculation region. Since the recirculation region is characterized by large vortical structures, they largely control the Reynolds shear stress producing events within this region. For a backward facing step flow, Etheridge & Kemp (1978) attributed the enhanced

levels of the Reynolds shear stress at l_r to the rotation and stretching of the vortex line along the dividing streamline by the mean strain rate. Beyond L_e, the large structures are broken down thereby causing a shift of energy to higher wavenumbers which again modified the Reynolds shear stress distribution within the developing regions of the jet. Since $-\overline{uv}$ proportionately resides in the larger structures, there is a reduction in the Reynolds shear stress due to the reduction in eddy size beyond L_e. The present result at l_r is qualitatively similar to that reported by Bradshaw & Wong (1972) who attributed the decrease in $-\overline{uv}$ downstream of reattachment to the reduction in turbulent length scale. As a result of mixing and spreading of the 3D offset jet, the level of $-\overline{uv}$ decreased with x/b_o. In a forward facing step flow, Ren & Wu (2011) also attributed low levels of Reynolds shear stress downstream of the flow reattachment on top of the step to high levels of turbulent mixing resulting in entrainment of high momentum freestream fluid. Changing the rib location did not significantly enhance the peak values of $-\overline{uv}$ farther downstream.

An interesting feature of turbulent wall jet flows is the occurrence of the counter-gradient diffusion phenomenon (CGDP) due to the anti-symmetric distribution of the Reynolds shear stress and the mean shear gradient. The CGDP occurs when the sign of the Reynolds shear stress, $-\overline{uv}$, and the mean shear gradient, $S_{ij} = \partial U/\partial y + \partial V/\partial x$ are different as defined by Lykossov (1992). The presence of the CGDP leads to negative values of the eddy viscosity, ν_τ, when using the gradient diffusion hypothesis; $-\overline{uv} = 2\nu_\tau S_{ij}$. This has implications for the momentum transport. In order to investigate the occurrence of CGDP, profiles of the Reynolds shear stress and the mean shear gradient are shown in Figure 6.5 at x/b_o = 10, 15 and 30. The profiles show that both the Reynolds shear stress and the mean shear gradient do not change sign at the same wall-normal location within the reattached regions of the offset jet. The present observation is similar to previous studies

by Nyantekyi-Kwakye *et al*. (2015b) for the no rib case and Agelinchaab & Tachie (2011c) for 3D offset jets, as well as plane wall jets over both smooth (Azim, 2013; Abrahamsson *et al*., 1994) and rough surfaces (Banyassady & Piomelli, 2015; Dey & Sarkar, 2008). Mounting a rib within the inner shear layer of the jet deflected the location of $-\overline{u}\overline{v} = 0$ into the outer shear layer in the developing region. Thus, within the developing region, the CGDP occurred within the outer shear layer of the jet but as the jet developed further downstream through the self-similar region, the CGDP occurred in the inner shear layer of the jet. As the jet developed, the high turbulence levels within the outer shear layer displaced negative $-\overline{u}\overline{v}$ towards the bottom of the channel similar to reports by Azim (2013) and Abrahamsson *et al*. (1994) for a plane wall jet. The present observations indicate an interaction between the inner and outer shear layers of the discharged offset jet similar to reports by Banyassady & Piomelli (2015) for a plane wall jet. The occurrence of the CGDP has significant implications for the ability of turbulence models based on the eddy viscosity concept (which assumes the point of zero shear stress to coincide with y_m) to accurately reproduce the mean flow properties.

6.4.4 Turbulence structure

Turbulent flows are characterized by organized motions, which are also referred to as coherent structures. These structures play important dynamic role in the mixing, entrainment as well as momentum turbulent transport. Therefore, understanding the dynamics of these structures is fundamentally important for improving our knowledge on turbulent shear flows. The quadrant analysis, probability density function, two-point correlation and proper orthogonal decomposition techniques were used in the present study to investigate these structures.

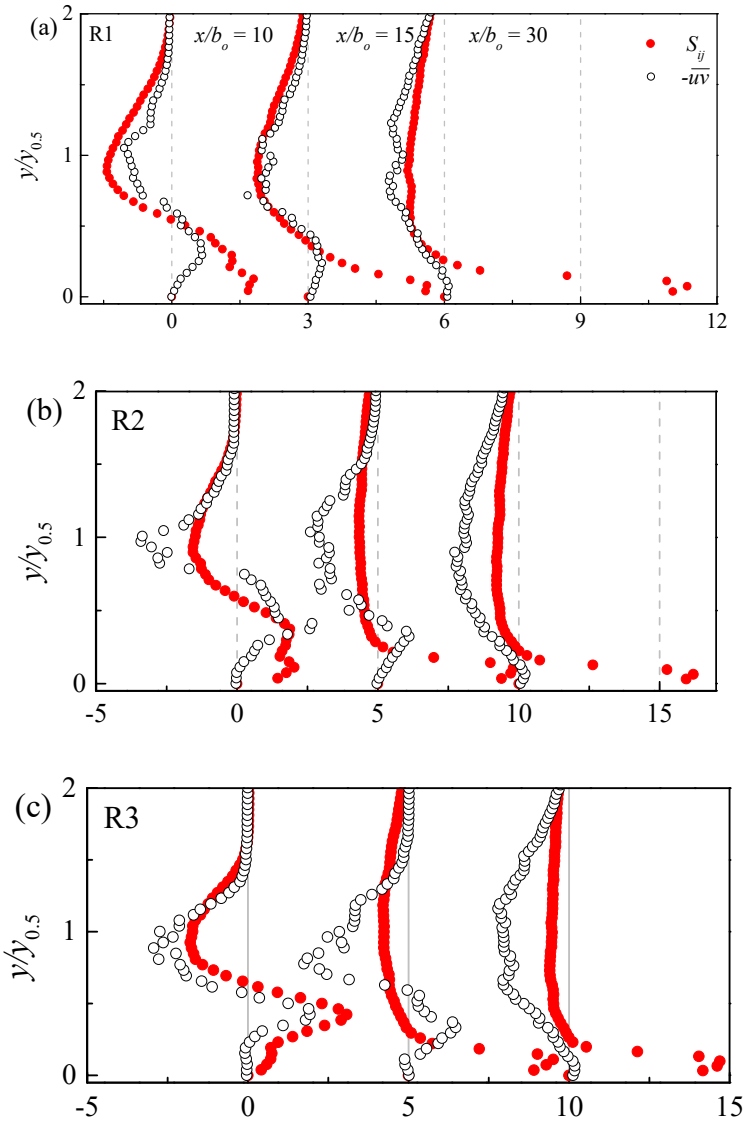

Figure 6.5 Relation between the mean shear gradient and the Reynolds shear stress within the reattachment region of the offset jet for (a) R1, (b) R2 and (c) R3

6.4.4.1 Quadrant analysis

Quadrant analysis was used to decompose the active motions that contribute to the Reynolds shear stress. This involves investigating the relationship between the fluctuating velocity components, u and v and sorting them into four different quadrants: first quadrant, $Q1$ (where $u >$

0, $v > 0$), second quadrant, $Q2$ ($u < 0$, $v > 0$), third quadrant, $Q3$ ($u < 0$, $v < 0$) and fourth quadrant, $Q4$ ($u > 0$, $v < 0$). Following the methodology proposed by Lu & Willmarth (1973), the Reynolds shear stress at each grid point was decomposed into contributions from the four quadrants as follows:

$$\overline{uv}_Q(x,y) = \frac{1}{N}\sum_{i=1}^{N} u_i(x,y)v_i(x,y) \tag{6.1}$$

where N is the total number of instantaneous velocity vectors (which is the total number of PIV snapshots) at each grid point.

Contour plots of $Q1$, $Q2$, $Q3$ and $Q4$ are presented for only R1 and R3 in Figure 6.6 and Figure 6.7, respectively. It should be noted that the dominant contributors to the Reynolds shear stress in turbulent boundary layers are the $Q2$ and $Q4$ events (Alfredsson & Johansson, 1984). However, the present contours provide evidence of significant contribution from all quadrant events. In the case of R1, the relative peaks of the different quadrant events were -0.03, 0.05, -0.03 and 0.03 for $Q1$, $Q2$, $Q3$ and $Q4$, respectively. This means that the peaks of both $Q2$ and $Q4$ events contributed 62.5% and 37.5% towards the peak positive Reynolds shear stress. Although both $Q1$ and $Q3$ events are also principal shear stress producing events, the $Q3$ events contributed more than the $Q1$ events for R3 (similar to reports by Hattori & Nagano (2010) for a forward facing step flow). It is interesting to note from Figures 6.6 and 6.7 that the contributions from both $Q2$ and $Q4$ events to the total Reynolds shear stress close to the nozzle exit was not affected by changing the rib location. However, beyond L_e, a more pronounced contribution was observed for $Q2$ events compared to $Q4$ events. The $Q2$ events contributed about 50% more towards the Reynolds shear stress compared to $Q4$ events beyond L_e when the rib location was changed from R1 to R3. A contour representation of the quadrant events within the self-similar region is illustrated in Figure

6.8 for R3. Similar to the developing region, contributions of both $Q1$ and $Q3$ events towards $-\overline{u}\overline{v}$ are relevant within the self-similar region. The dominance of the various quadrant events will enhance mass transfer between the offset jet and ambient fluid. Results from the space fraction for R1 and R3 are shown in Figure 6.9. For R1, both $Q1$ and $Q3$ events occur up to 30% of the time beyond the trailing edge of the rib within the outer shear layer of the jet. However, the frequency for the $Q2$ and $Q4$ events was about 50% and occurred at the leading edge of the rib (which corresponds to the region of high positive $-\overline{u}\overline{v}$). The space fraction for both $Q1$ and $Q3$ events within the outer shear layer beyond the trailing edge of the rib was not affected by changing the rib location. However, the rate of occurrence of $Q1$ event in the recirculation region was 40% for R3, which was larger than 10% for R1. Similar to R1, regions of positive $-\overline{u}\overline{v}$ were characterized by high occurrence of both $Q2$ and $Q4$ events up to about 40% to 60% for R3. The present results indicate that the space fraction for $Q4$ event increased up to 10% when the rib location was changed from R1 to R3.

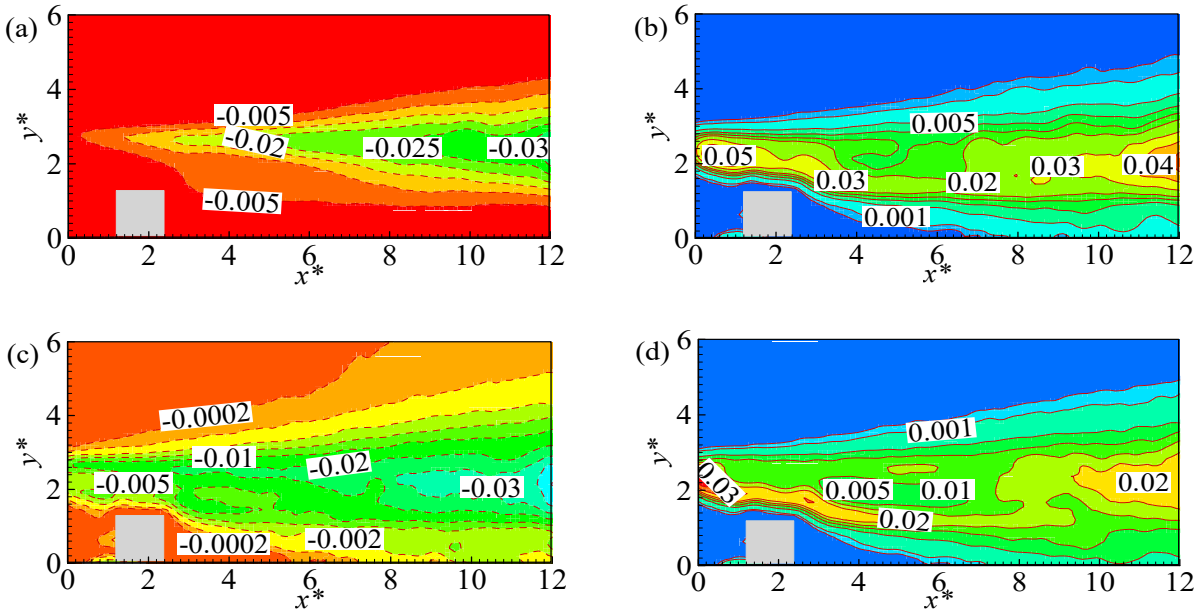

Figure 6.6 Contours of (a) $Q1$, (b) $Q2$, (c) $Q3$ and (d) $Q4$ for R1 within the recirculation and developing region

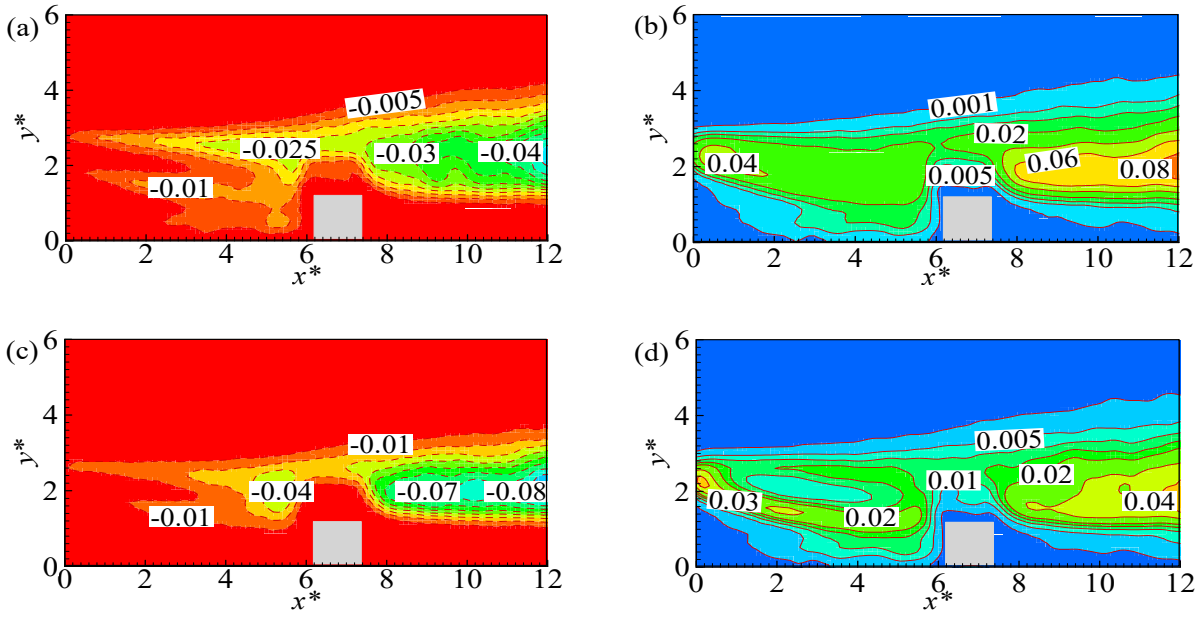

Figure 6.7 Contours of (a) $Q1$, (b) $Q2$, (c) $Q3$ and (d) $Q4$ for R3 within the recirculation and developing region

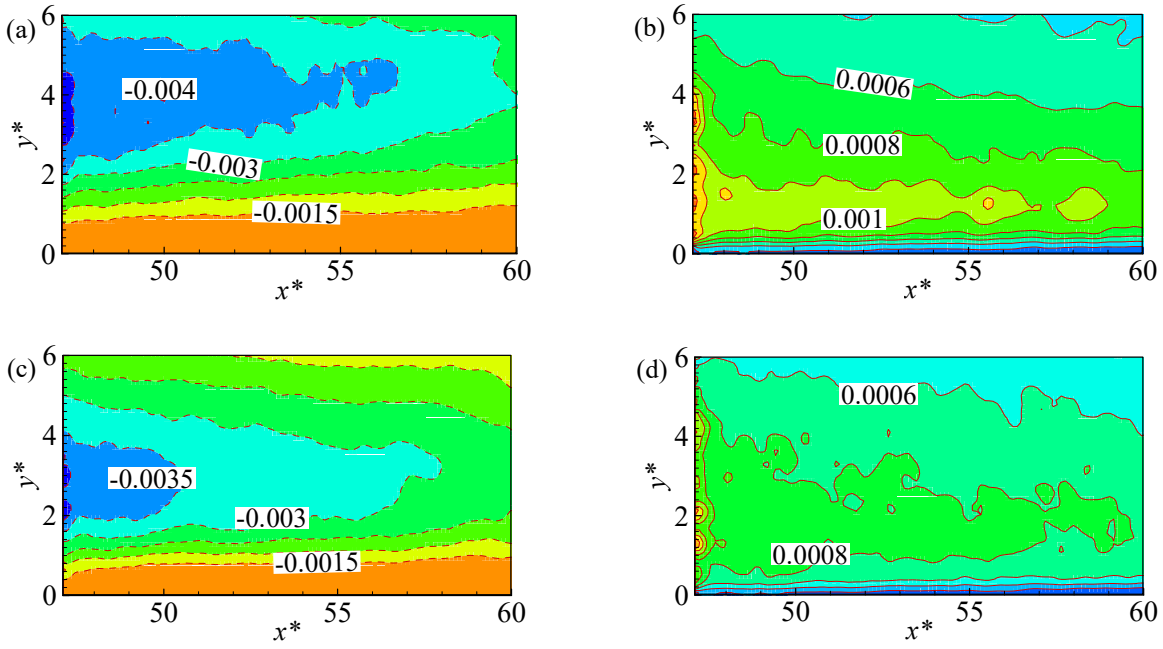

Figure 6.8 Contour plots of (a) $Q1$, (b) $Q2$, (c) $Q3$ and (d) $Q4$ for R3 within the self-similar region

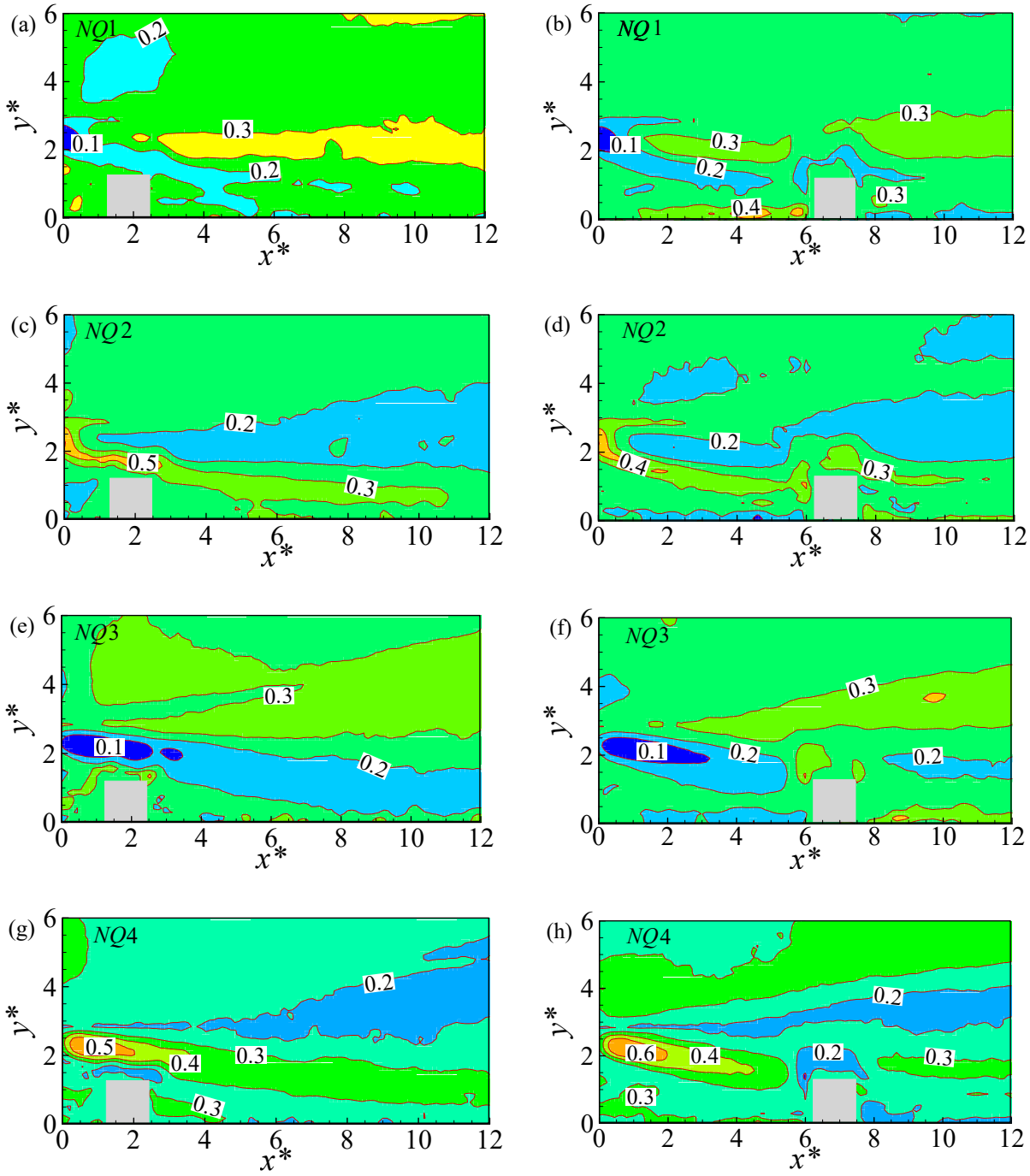

Figure 6.9 Contours of space fraction; *NQ*1, *NQ*2, *NQ*3 and *NQ*4 for R1 (a, c, e and g) and R3 (b, d, f and h)

6.4.4.2 Joint and weighted joint probability density function analysis

The joint probability density function (JPDF), $P(u, v)$ of the fluctuating velocities, and weighted JPDF (WJPDF), $uvP(u, v)$ were used to investigate the contributions of the coherent structures towards the turbulence statistics of the offset jet flow. The WJPDF gives a measure of the contribution of the sign and magnitude of the fluctuating velocities to the Reynolds shear stress (Ong & Wallace, 1998). Contour plots of JPDF and WJPDF are shown in Figure 6.10 and Figure 6.11 for R1 and R2, respectively. The contours were extracted at $x/b_o = 55$ and at three different wall-normal locations of $0.25y_m$, $0.5y_m$ and $4y_m$ representing locations within the inner and outer shear layers of the jet. Similar to turbulent boundary layers, the shape of the JPDF contours show that both $Q2$ and $Q4$ events dominated the inner shear layer ($0.25y_m$ and $0.5y_m$) as was reported from the quadrant analysis. This resulted in the elongated shape of the JPDF contours with the major axis in line with the opposite sign quadrants and no significant inclination. The contours show that the fluctuations are not evenly distributed suggesting the anisotropic nature of the turbulence field. The present shape of the JPDF contour is similar to those reported by Banyassady & Piomelli (2015, 2014) within the inner shear layer of a plane wall jet over smooth and rough surfaces. The WJPDF contours within the inner shear layer show the nearly equal distribution of the various quadrant events and this is not affected by rib position. Within the outer shear layer, although $Q2$ and $Q4$ contributed to the Reynolds shear stress, the JPDF contours were inclined towards the like-sign quadrants. Since the positive mean shear gradient ($\partial U/\partial y > 0$) is directed towards the bottom of the channel in the outer shear layer, it resulted in rearrangement of the quadrant events as indicated in Figures 6.10d and 6.11d, as was reported by Banyassady & Piomelli (2014) for plane wall jets. The shape of the contours within the outer shear layer differs from those obtained in the outer region of turbulent boundary

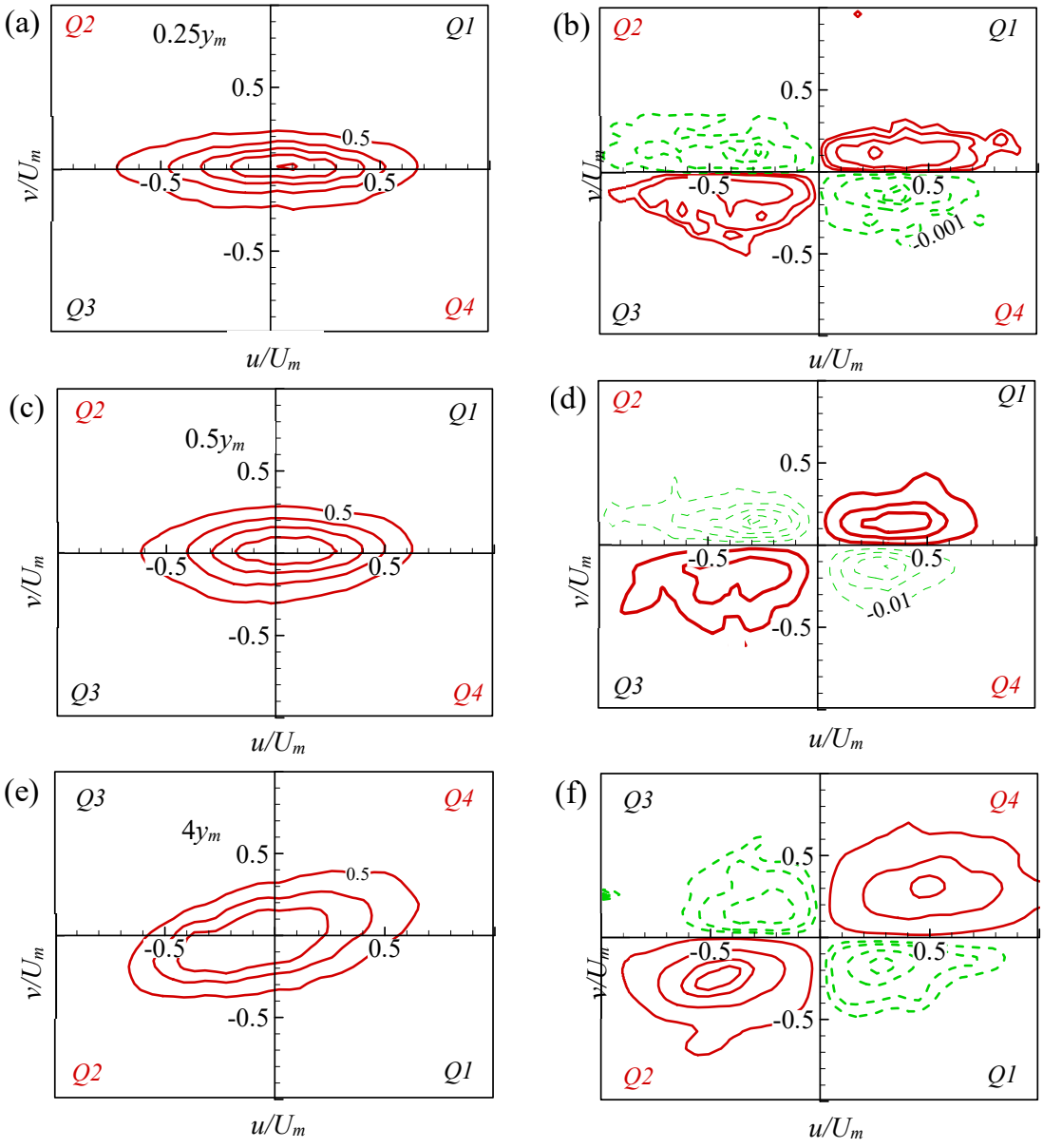

Figure 6.10 (a, c and e) JPDF and (b, d and f) WJPDF contours of *u* and *v* for R1. Dashed lines represent negative contour levels

layer flow (Nolan *et al*., 2010); the JPDF contours in their study were more rounded (implying an isotropic turbulence field) in the outer region. The present results suggest that there is an ejection

of low momentum fluid by the outer layer structures towards the wall ($Q2$ event) and a sweep of high momentum jet towards the outer shear layer ($Q4$ events). This observation is an

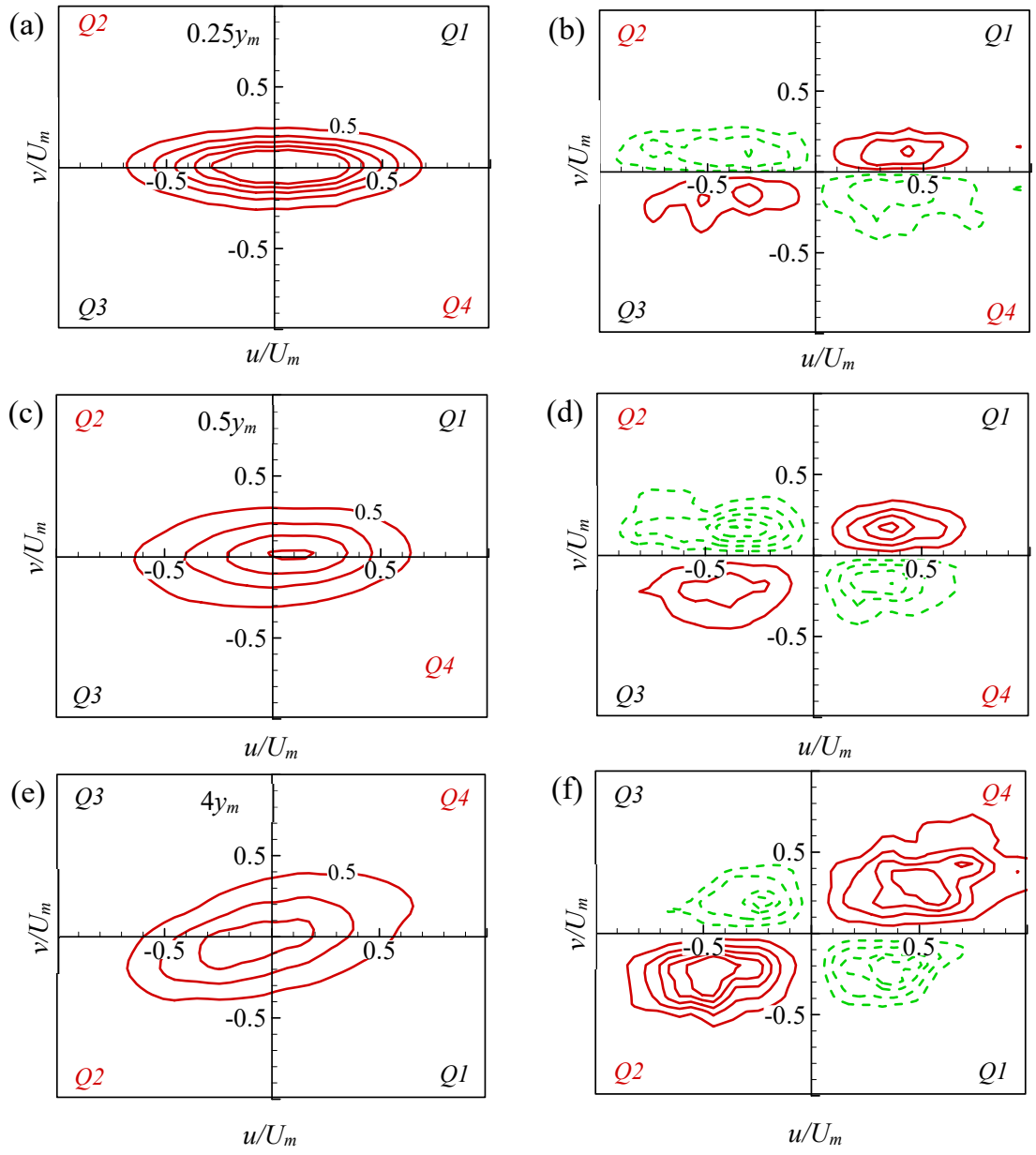

Figure 6.11 (a, c and e) JPDF and (b, d and f) WJPDF contours of u and v for R2. Dashed lines represent negative contour levels

indication of interaction of the outer layer with the inner shear layer of the turbulent jet flow supporting observations made by Banyassady & Piomelli (2015). This interaction transports positive Reynolds shear stress from the outer shear layer towards the inner shear layer. Changing the rib location (as can be seen from Figure 6.11) did not alter the shape and inclination of the JPDF and WJPDF contours within both the inner and outer shear layers.

6.4.4.3 Two-point correlation

The two-point correlation is a useful multi-point technique for investigating features of coherent structures and integral length scales. The two-point correlation was employed to investigate the effect of rib location on the correlation of turbulence structures within the developing and self-similar region of the flow. The two-point correlation function, R_{ab}, was defined at a reference point (x_r, y_r) between two arbitrary quantities; a and b separated in the streamwise and wall-normal directions by Δx and Δy as:

$$R_{ab} = \overline{a(x_r,y_r)b(x_r+\Delta x,\, y_r+\Delta y)} \big/ a'(x_r,y_r)b'(x_r+\Delta x,y_r+\Delta y) \tag{6.2}$$

where a' and b' are the root mean square values of a and b, respectively. The arbitrary quantities a and b can either be the streamwise or wall-normal fluctuating velocity components. The analysis was performed at two streamwise locations, x/b_o = 10 and 55 representing the developing and self-similar regions of the flow, respectively. Several wall-normal locations, y/y_m = 0.5, 1, 1.5, 2, 3 and 4, ranging from the inner through to the outer shear layer were examined. From these analyses, contours of R_{uu} were used to estimate the average inclination of the hairpin-like vortices within the flow, and turbulent length scales were estimated from the auto-correlation functions of the streamwise velocity fluctuation (R_{uu}) and wall-normal velocity fluctuations (R_{vv}).

Iso-contours of R_{uu} at y/y_m = 0.5, 1 and 4 within the developing region (x/b_o = 10) and self-similar region (x/b_o = 55) are shown in Figures 6.12 and 6.13, respectively. The R_{uu} contour levels used in the present studies varied from 0.5 – 1.0 at 0.1 intervals. Within the developing region, the R_{uu} contours (Figure 6.12) are rounded in both the inner and outer shear layers of the flow. The inner shear layer is characterized by smaller structures as shown by the small physical size of the R_{uu} contours, while the outer shear layer is dominated by large scale structures. The present distribution of small and large structures within the inner and outer shear layer support previous experimental work by Nyantekyi-Kwakye *et al*. (2015b) and Agelinchaab & Tachie (2011c) for 3D offset jets as well as large eddy simulations of a plane wall jet over smooth and rough surfaces by Banyassady & Piomelli (2014). The R_{uu} contours decreased in size with increasing rib distance from the nozzle exit within the inner shear layer, an observation linked to the breakdown of the larger structures after the jets reattachment. Since the offset jet reattached to the channel bottom earliest for R1 compared to R2 and R3, the structures began to reorganize sooner in the case of R1 compared to R2 and R3. The turbulent structures in the inner shear layer of the developing region for R1 was similar to that of the no rib case. The longer mean L_e for both R2 and R3 modified the flow structures within the inner shear layer in the developing region. The size of the R_{uu} contours increased with rib location within the outer shear layer of the 3D offset jet, signifying the generation of larger structures within the outer shear layer of the jet when the rib location was changed. Figure 6.13 shows R_{uu} contours within the self-similar region of the offset jet flow. The contours were more elliptic and positively inclined within the inner shear layer of the flow where the mean shear gradient is positive $(\partial U/\partial y > 0)$. Within the outer shear layer, since the positive $\partial U/\partial y > 0$ is directed towards the channel bottom, the R_{uu} contours had negative inclinations. This observation is consistent with results obtained from the JPDF analysis. The flow topology suggests

a strong spatial coherence of the turbulence structures within the self-similar region compared to the developing region. The spatial extent of the R_{uu} contours is larger within the self-similar region compared to the developing regions of the flow. This highlights the differences in turbulent length scales within the developing and self-similar regions of the 3D offset flow. The varied turbulent length scales within the developing region is responsible for the variations observed in the flow dynamics. The shape of the R_{uu} contours within the inner shear layer of the self-similar region resemble those reported for 3D offset jets with no mounted rib (Nyantekyi-Kwakye *et al*., 2015b), plane wall jets (Banyassady & Piomelli, 2015, 2014) and boundary layers (Volino *et al*., 2007). A similar analysis was done for the spatial distribution of the R_{vv} contours (not shown). The key finding was that the R_{vv} contours were more rounded within the developing and self-similar regions of the flow.

Slices through the auto-correlation peak of the R_{uu} contours (at $y/y_m = 1$) in both streamwise and wall-normal directions at x/b_o = 10 and 55 are shown in Figure 6.14. These profiles provide an indication of the spatial coherence and size of the turbulent structures in the streamwise and wall-normal directions. The profiles show that within the developing region the turbulence structures were more spatially coherent for R2 and R3 compared to R1 and the no rib case. This observation can be attributed to the smaller size of the turbulent structure at $y = y_m$ for R1 and the no rib case compared to both R2 and R3 as shown in Figure 6.12. The spatial coherence of the turbulent structures in the developing region for R1 was similar to the flow configuration without a surface mounted rib. This was because for R1, the rib was positioned within the recirculation region and this limited its interaction with the discharged jet. Within the self-similar region, the introduction of the rib played a minimal role in the spatial coherence and length of the turbulent structures as can be seen from Figure 6.14.

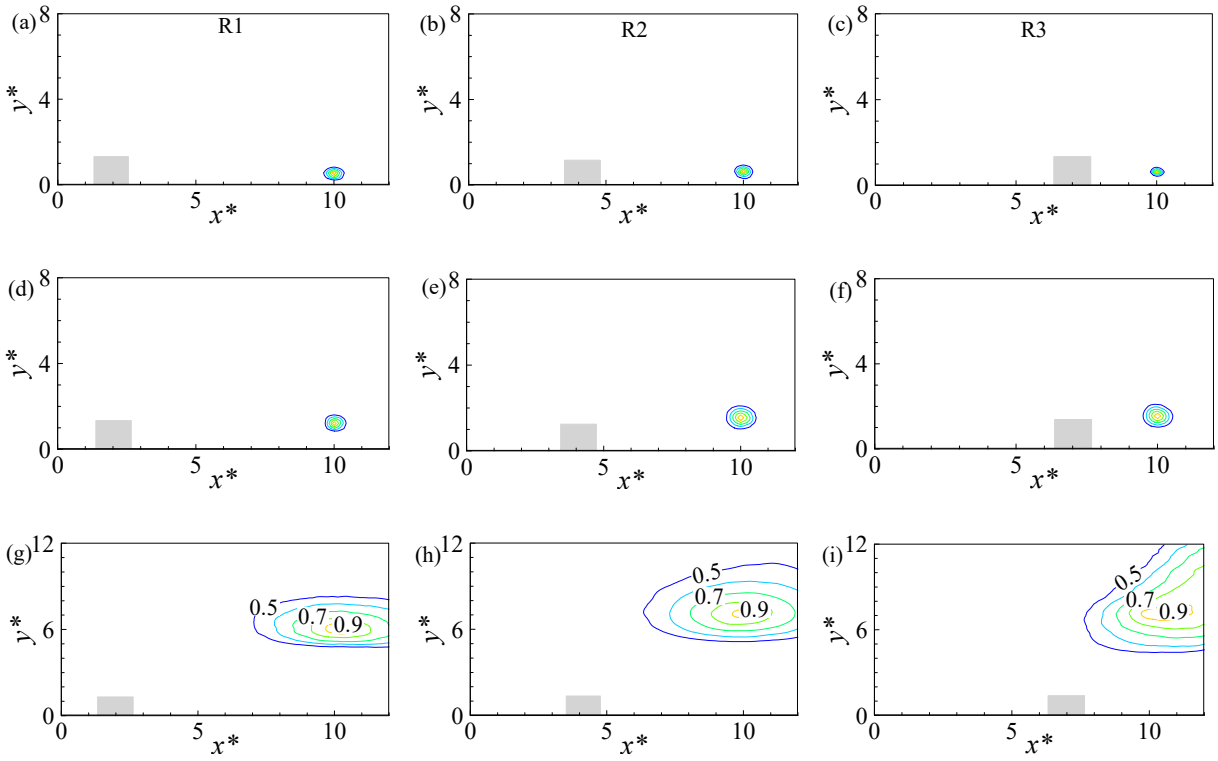

Figure 6.12 Contours of R_{uu} correlation at (a) – (c) y/y_m = 0.5, (d) – (f) y/y_m = 1 and (g) – (i) y/y_m = 4 within the developing region at x/b_o = 10

6.4.4.3.1 Inclination and integral length scales of the vortices:

The angle of inclination of R_{uu} correlation contours (denoted by β) within the inner and outer shear layers of the flow represent the average inclination of the hairpin-like vortex structures. Values of β were obtained by fitting a line through the farthest points of the different contour levels from the self-correlation peak. The inclinations were estimated at selected y/y_m locations within the self-similar region and shown in Table 6.1. Larger inclination angles were obtained within the inner shear layer. Further away from the channel bottom, the values of β decrease since the wall effect diminishes. Farther out into the outer shear layer, the structures changed orientation having negative inclination as has been previously discussed. Changing the rib location did not

significantly affect the inclination of the hairpin-like vortices. The estimated values of β within the inner shear layer (10.9°–11.8°) are in good agreement with β = 11.8° obtained for the generic case where there was no surface mounted rib, β = 11.2° ± 0.6° reported by Agelinchaab & Tachie (2011c) for 3D offset jets and 11°± 3° reported by Agelinchaab & Tachie (2011a) for 3D wall jet. The values also compare well with reported values for boundary layer investigations; β = 10–20° (Adrian *et al*., 2000) and β = 10° (Krogstad & Antonia, 1994).

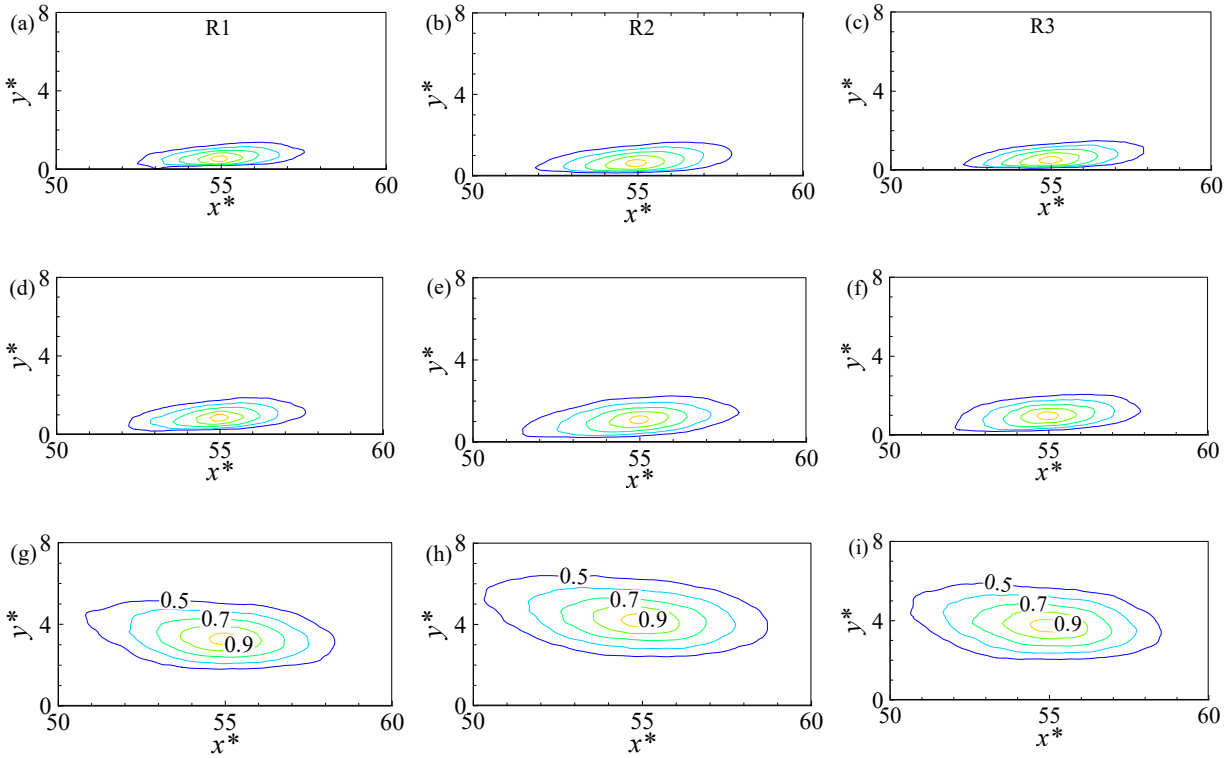

Figure 6.13 Contours of R_{uu} correlation at (a) – (c) y/y_m = 0.5, (d) – (f) y/y_m = 1 and (g) – (i) y/y_m = 4 within the self-similar region at x/b_o = 55

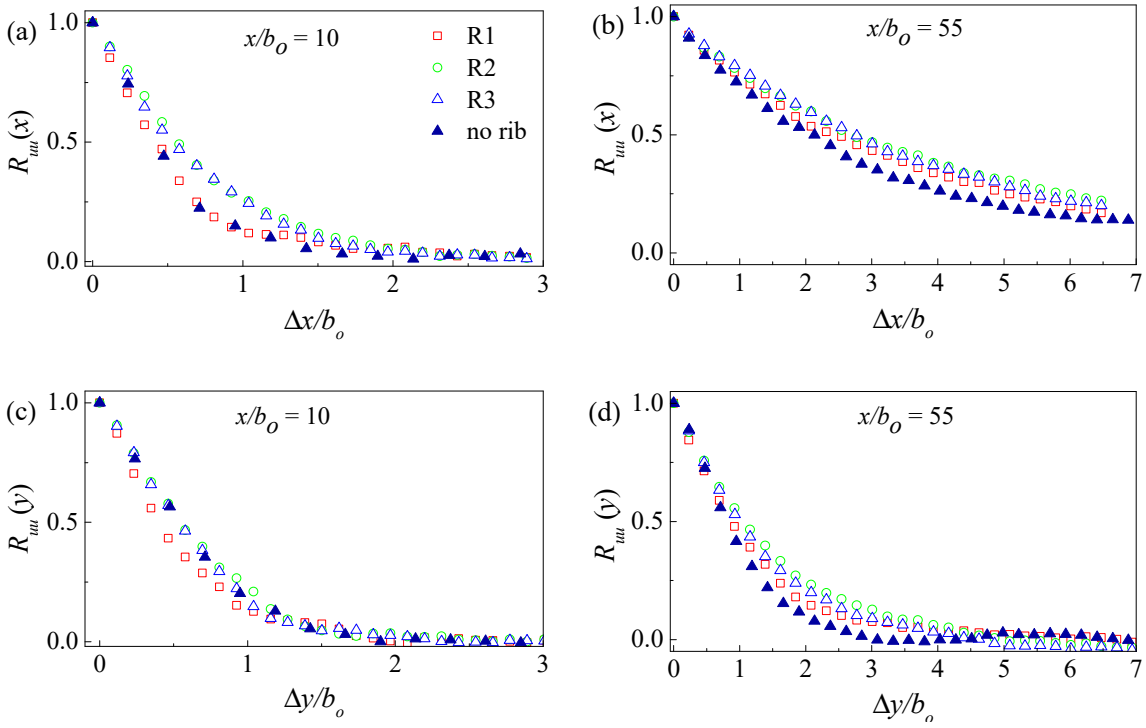

Figure 6.14 One-dimensional profiles of the R_{uu} correlation function

Table 6.1 Inclination of R_{uu} contours within the self-similar region at selected wall-normal locations

y/y_m	Inclination angle, β [°]		
	R1	**R2**	**R3**
0.5	11.8	10.9	11.7
1.0	10.7	7.0	8.1
1.5	8.9	7.7	7.0
2.0	5.6	0	-0.4
3.0	-5.3	-5.7	-1.1
4.0	-3.2	-5.7	-7.1

In order to quantify the size of the energy containing structures, the integral length scales were determined. The streamwise and wall-normal integral length scales were estimated from the one-dimensional profiles of the R_{uu} and R_{vv} correlation functions (e.g., shown in Figure 6.14 for

R_{uu}). The streamwise extents of R_{uu} (Lx_{uu}), R_{vv} (Lx_{vv}), wall-normal extents of R_{uu} (Ly_{uu}) and R_{vv} (Ly_{vv}) were estimated by integrating their corresponding profiles for the auto-correlation functions. The estimated values of Lx_{uu}, Ly_{uu}, Lx_{vv} and Ly_{vv} normalized by b_o within the developing and self-similar regions of the flow at y/y_m = 0.5, 1.0, 1.5, 2.0, 3.0 and 4.0 are plotted in Figure 6.15 and Figure 6.16, respectively. Within the developing region, the length scales increased with wall-normal distance. For instance, Lx_{uu} increased by about 73% from y/y_m = 0.5 to y/y_m = 4. The turbulent length scales within the developing regions of the flow were smaller compared to the self-similar region. This is attributed to the breakdown of the large scale structures due to the reattachment of the discharged jet to the channel bottom. The values of the integral length scales within the developing region are sensitive to the specific rib location whereas those in the self-similar region weakly depend on the rib location. The distribution of normalized Lx_{uu}, Ly_{uu} and Ly_{vv} estimated at y_m at different streamwise distances are examined in Figure 6.17. For all test conditions, the integral length scales predominantly increase with increasing x/b_o. The distribution of Lx_{uu} initially decreased within the regions $6 \leq x/b_o \leq 10$, $4 \leq x/b_o \leq 16$ and $4 \leq x/b_o \leq 16$ for R1, R2 and R3, respectively. This occurrence gives credence to the breakdown of larger structures due to the reattachment process. As previously noted, the placement of the rib changed the flow dynamics within the developing region compared to the self-similar region. The relatively larger values of the integral length scales for R2 and R3 with x/b_o, are responsible for the efficient mixing and entrainment mechanisms that caused higher decay of the R2 and R3 configurations compared to R1 and no rib case.

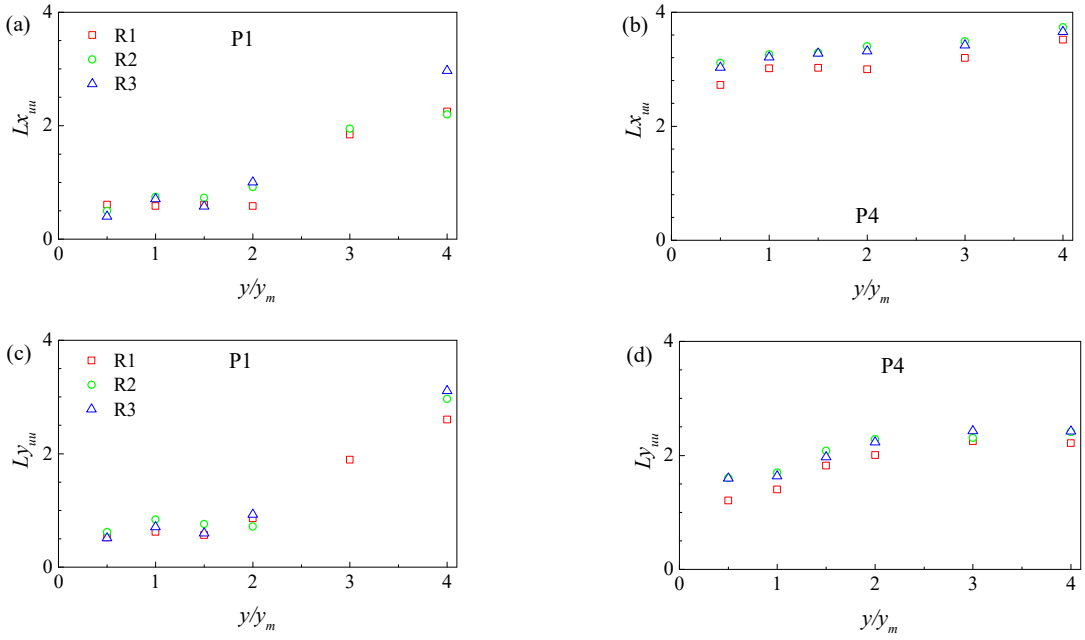

Figure 6.15 Variation of estimated integral length scales with wall-normal distance from R_{uu} correlation functions in the developing region (a & c) and self-similar region (b & d)

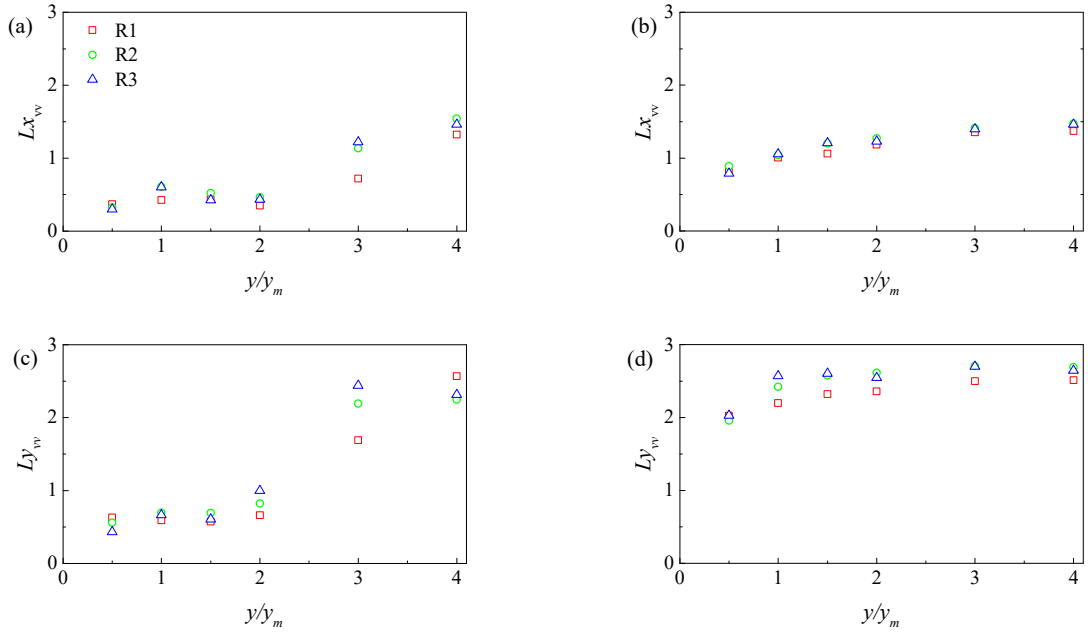

Figure 6.16 Variation of estimated integral length scales with wall-normal distance from R_{vv} correlation functions in the developing region (a & c) and self-similar region (b & d)

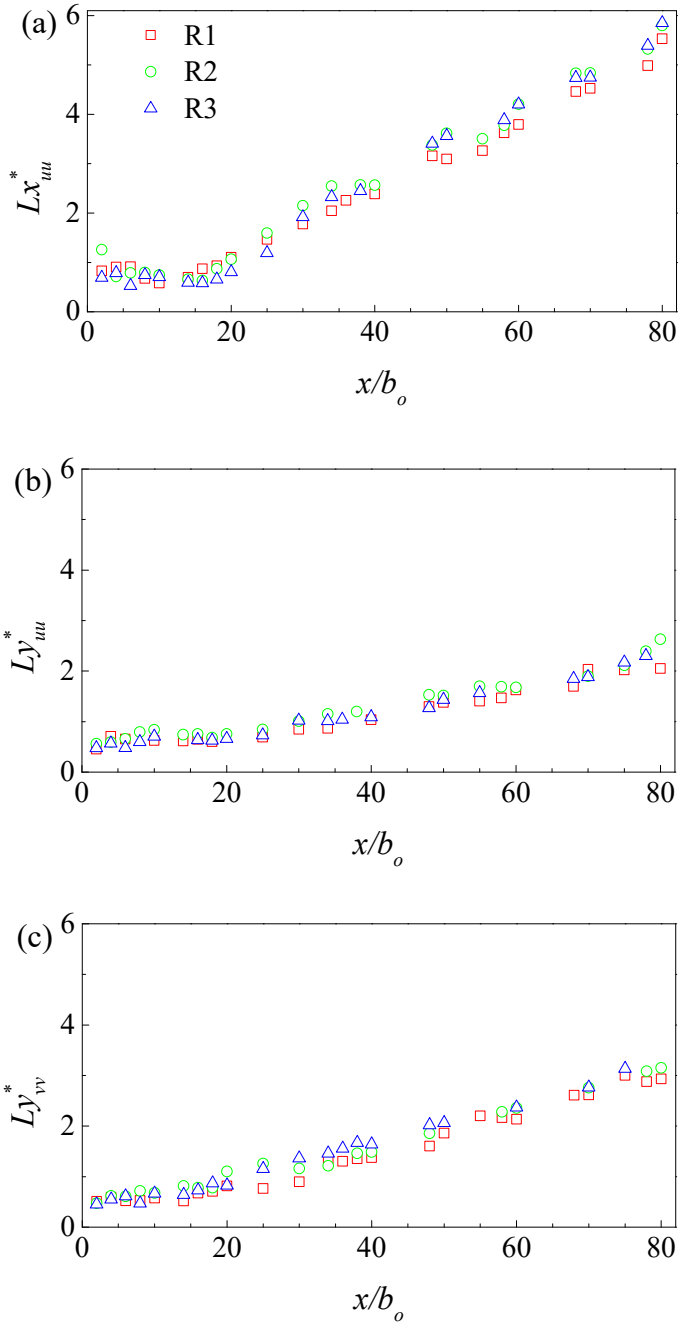

Figure 6.17 Distribution of integral length sales with streamwise distance

6.4.4.4 Proper orthogonal decomposition

The POD technique was used to extract the dominant features and identify coherent structures within the flow fields. The uniqueness of the POD technique is its ability to decompose

the flow field into a set of basis functions which are optimal in terms of energy. That is, the dominant structures of the flow can be satisfactorily captured within the first few modes. Since its introduction, the POD technique has been applied to investigate coherent structures in boundary layers (Volino *et al*., 2007), separated flows (Shah & Tachie, 2009a) and turbulent offset jets (Nyantekyi-Kwakye *et al*., 2015b). An overview of the snapshot approach proposed by Sirovich (1987) has been presented in Chapter 2 and as such will not be presented herein.

6.4.4.4.1 Convergence and energy spectra

The number of snapshots required for the convergence of the POD results was evaluated by computing the fractional turbulent kinetic energy associated with the first mode for increasing *N*. Results of the energy convergence for all measurement planes were qualitatively similar. The energy fraction for the first mode decreased with increasing *N* until a threshold value was attained where the fractional energy became independent of *N*. For instance, in the case of R1, increasing *N* from 2000 to 3000 resulted in 2.2% and 1.5% difference in the fractional turbulent kinetic energy within P1 and P4 (developing and self-similar regions), respectively. Based on these observations, it was determined that $N = 4000$ was sufficient to perform the POD analysis.

Figure 6.18 shows the fractional and cumulative energy distributions for the first 50 modes within the developing and self-similar regions. Included in Figure 6.18 is the data for the no rib condition. The lower modes from the POD are associated with the large scale energy containing structures, while the higher modes are linked to the small scale energy containing structures. Figure 6.18a shows that within the developing region the first mode contributed 4.3%, 4.9% and 5.6% of the total energy for R1, R2 and R3, respectively. These values are less than 7.6% obtained for the no rib condition. This is an indication that the introduction of a surface mounted rib resulted in a

wider range of energy containing scales in the developing region. However, Figure 6.18b revealed that the first mode contributed 27%, 20.1%, 21.3% and 22.0% of the total energy for the no rib condition, R1, R2 and R3, respectively, within the self-similar region. The significantly higher fractional energy content of the first mode within the self-similar region signifies the existence of larger structures within this region compared to the developing region from the two-point correlation analysis. This observation is consistent with the larger integral length scales estimated within the self-similar region compared to the developing region of the flow. The fractional energy decays with increasing number of modes. It can be seen from Figure 6.18 that the fractional energy decayed by 93% and 99% within the developing and self-similar regions, respectively, for the first 50 modes in the case of R2. For all test conditions, the fractional energy decayed exponentially with increasing number of modes, with the rate of decay being very significant within the self-similar region. Figure 6.18a also shows that within the developing region, the first 50 modes contributed 64.6% 48.8%, 54.8% and 53.7% cumulatively to the total kinetic energy for the no rib condition, R1, R2 and R3, respectively. The smaller energy contents for the rib cases give credence to the fact that a wider range of turbulent scales were present within the developing region of the jet compared to the no rib case. Likewise, the first 50 modes cumulatively contributed 76.9%, 75.1%, 77.5% and 78.1% towards the total kinetic energy within the self-similar region for the no rib case, R1, R2 and R3, respectively. These results indicate that the convergence of the modes is slower within the developing region compared to the self-similar region. The slower convergence can be attributed to a wider range of energy containing scales due to the separation and reattachment process.

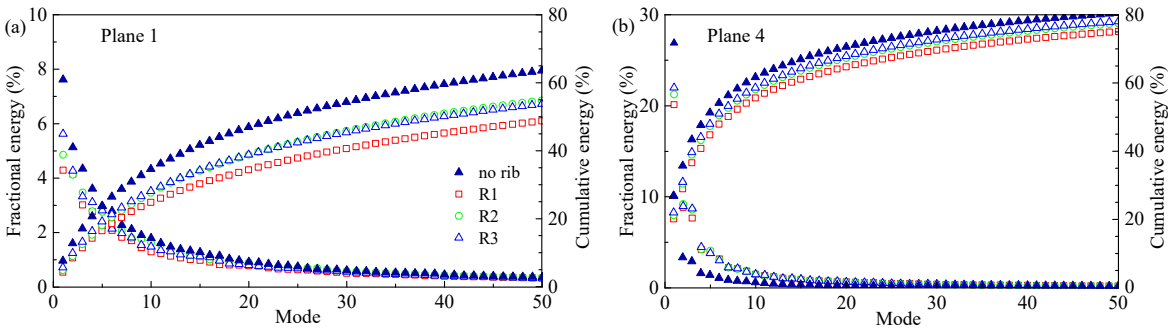

Figure 6.18 Fractional and cumulative energy distribution of the first 50 modes

6.4.4.4.2 Reconstructed turbulence quantities

The POD modes were used to reconstruct the turbulent kinetic energy (TKE) and $-\overline{uv}$ in order to quantitatively investigate the contribution of the coherent structures. Contour plots of normalized TKE (represented as k^*) and $-\overline{uv}$ for R2 were reconstructed using modes m = 1, 2, 3, 5 and 10. These were compared with the contours obtained from the ensemble PIV data. The results for R1 and R3 are not shown since the conclusions are qualitatively similar to those presented for R2. Figures 6.19 – 6.22 show plots in the developing and self-similar regions of the flow. The corresponding vector plots of the eigenfunctions are superimposed on these contours. This approach facilitates visualization of the direction of the vectors. Compared to the ensemble PIV data, the first mode contributed 12% and 24% of the TKE in P1 and P4, respectively. Within P1 and P4, the first 10 modes contributed 46% and 39%, respectively, towards the maximum value of the TKE. The results obtained for $-\overline{uv}$ also exhibit a similar pattern with the first mode capturing a significant portion of the Reynolds shear stress as shown in Figures 6.21 and 6.22. Comparing the results of the different POD modes to the ensemble PIV data, the maximum value of negative $-\overline{uv}$ after the reattachment (in P1) of the jet captured by the first mode was about 35% while the positive peak was only about 9%. Similarly, within P4 the first mode captured 50% and 3% of the

maximum negative and positive $-\overline{u}\overline{v}$, respectively. Within both P1 and P4, the maximum value of the negative $-\overline{u}\overline{v}$ for the first 10 modes was already similar to that of the ensemble PIV data. The present results give an indication that the large scale structures contributed more significantly towards negative $-\overline{u}\overline{v}$ than to the TKE.

The distribution of the eigenvectors can be used to examine the presence of turbulent structures and contributions of the various quadrant events by the POD modes. The first POD mode shows that large turbulent structures are generated within the outer shear layer of the jet and are transported downstream of the flow as can be seen from Figure 6.19. Further downstream, the number of vortices decreased whereas the vortices present in the flow increase in size. This observation suggests the occurrence of vortex pairing and merging. A similar observation was made in the far-field of a free jet by Shinneeb *et al.* (2008). Within P1, the first mode shows that the inward interaction event, $Q3$, dominated the outer shear layer of the jet. When the number of modes was increased to two, $Q3$ events are evident close to the nozzle exit (thus above the recirculation region) and $Q1$ events are dominant beyond the reattachment point. All these events occurred within the outer shear layer where $-\overline{u}\overline{v}$ was predominantly negative. The present results within the outer shear layer of the jet are consistent with the quadrant analysis previously discussed. Increasing the number of modes to 10 revealed the sweep event, $Q4$ and ejection event, $Q2$, dominate the inner shear layer of the jet.

A two-point correlation analysis was conducted for modes ranging from 1 to 3500 within the self-similar region (at $x/b_o = 49$) of the flow but only contours generated from mode 1, 2, 5, 10 and 50 are presented. The results are compared to the ensemble averaged PIV data. The results for R1, R2 and R3 were qualitatively similar and as such only plots for R2 are presented. Figure 6.23

shows the spatial distribution of the streamwise two-point correlation function contour (R_{uu}) for the selected POD modes and ensemble-averaged PIV data. The structures presented in Figure 6.23 were extracted at y/y_m = 0.5. The results demonstrate that the more energetic modes are indeed associated with the larger structures within the flow. For example, the largest structure was contained by the first mode which happens to be the most energetic. The first and second mode exhibited significant structural differences. However, there were no significant structural differences when the number of modes was increased further. Increasing the number of modes resulted in a decrease in the spatial extents of the structures and also a more distinct inclination of the structures. As the number of modes increased, the structures tended to take the exact shape and orientation of the ensemble PIV data as indicated in Figure 6.23(c-f). The dynamic role of the less energetic modes in shaping the size of the structures is apparent from Figure 6.23.

The values of β estimated from the R_{uu} contours for mode 4 to mode 50 ranged between 9.3° – 9.9° which are in close agreement with β = 10.9° estimated from the ensemble averaged PIV data. The obtained results show that the dynamics of the turbulent structures (size and inclination) can be captured using very few POD modes. Values of normalized Lx_{uu} at wall-normal locations, y/y_m = 0.5, 1 and 2 from the PIV modes are shown in Figure 6.24. As expected, larger values of Lx_{uu} were obtained from the energetic modes and this was consistent at all three wall-normal locations. Increasing the number of modes resulted in a decrease in the estimated length scale. For example at y/y_m = 0.5, increasing the number of modes from 4 to 5 resulted in a 20% decrease of the estimated length scale. Beyond mode 200, normalized values of Lx_{uu} approached that obtained from the PIV data.

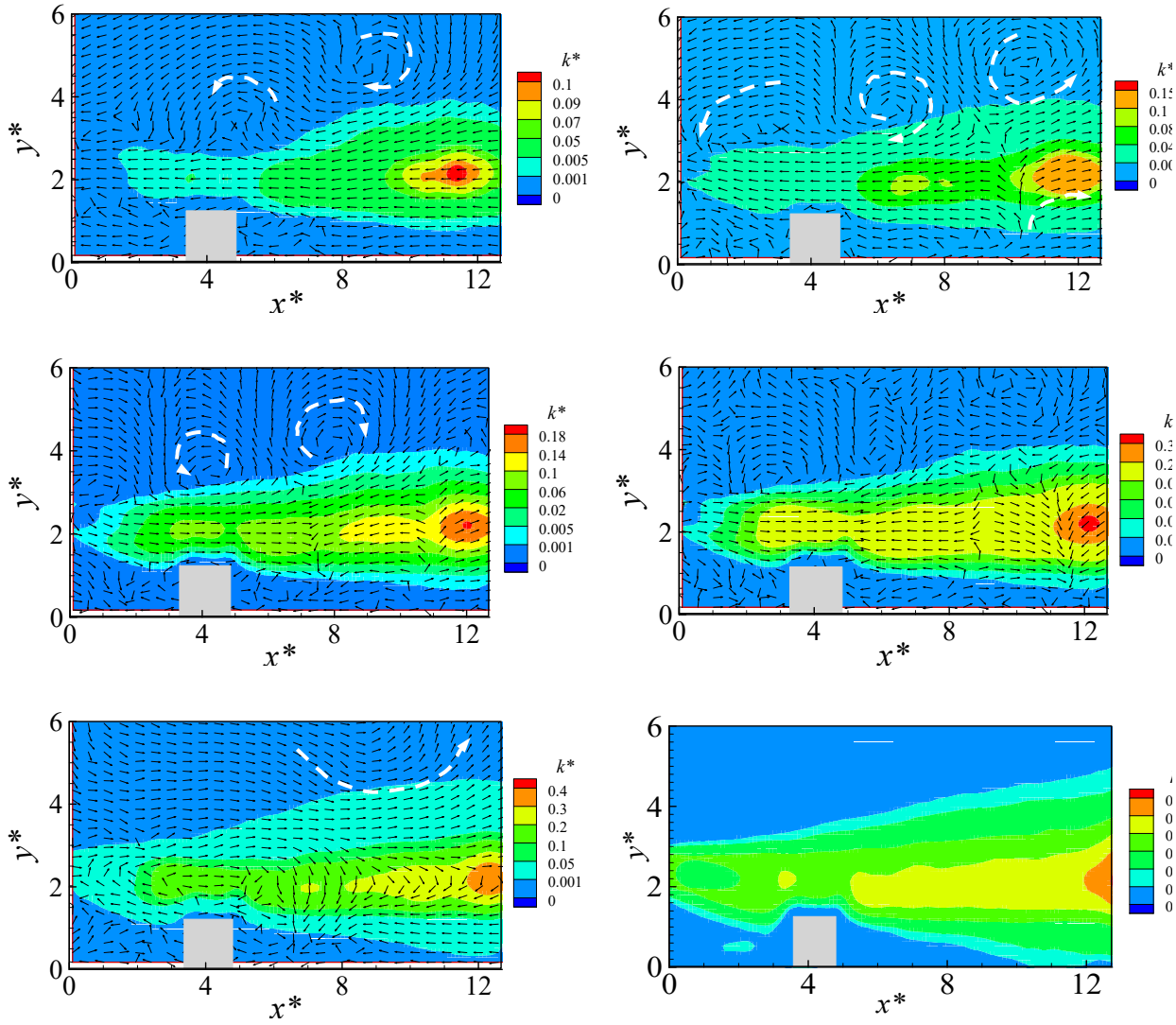

Figure 6.19 Contour plots of reconstructed normalized turbulent kinetic energy for R2 for modes (a) 1, (b) 2, (c) 3, (d) 5, (e) 10 and (f) ensemble PIV data within the developing region

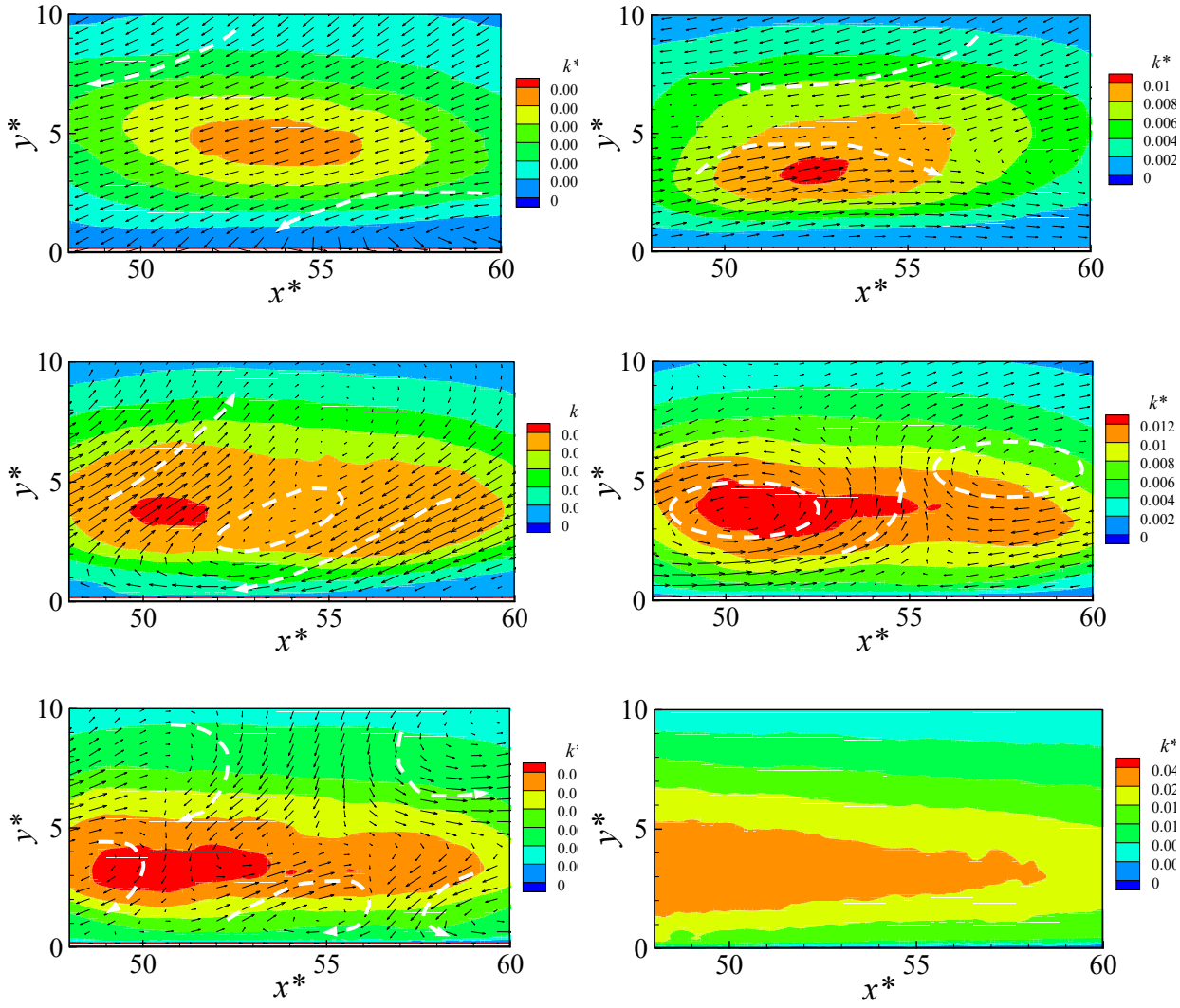

Figure 6.20 Contour plots of reconstructed normalized turbulent kinetic energy for R2 for modes (a) 1, (b) 2, (c) 3, (d) 5, (e) 10 and (f) ensemble PIV data within the self-similar region

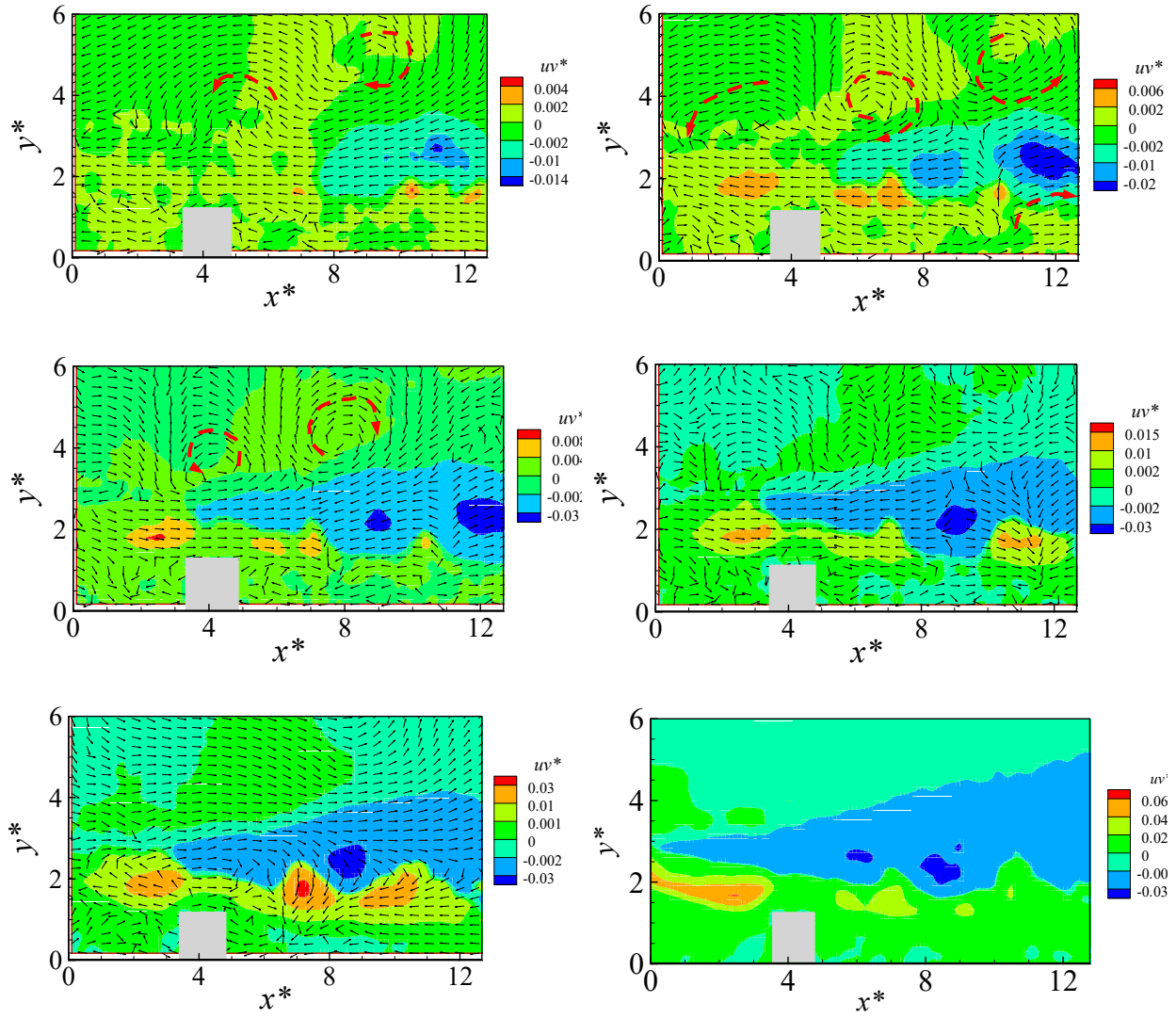

Figure 6.21 Contour plots of reconstructed Reynolds shear stress for R2 for modes (a) 1, (b) 2, (c) 3, (d) 5, (e) 10 and (f) ensemble PIV data within the developing region

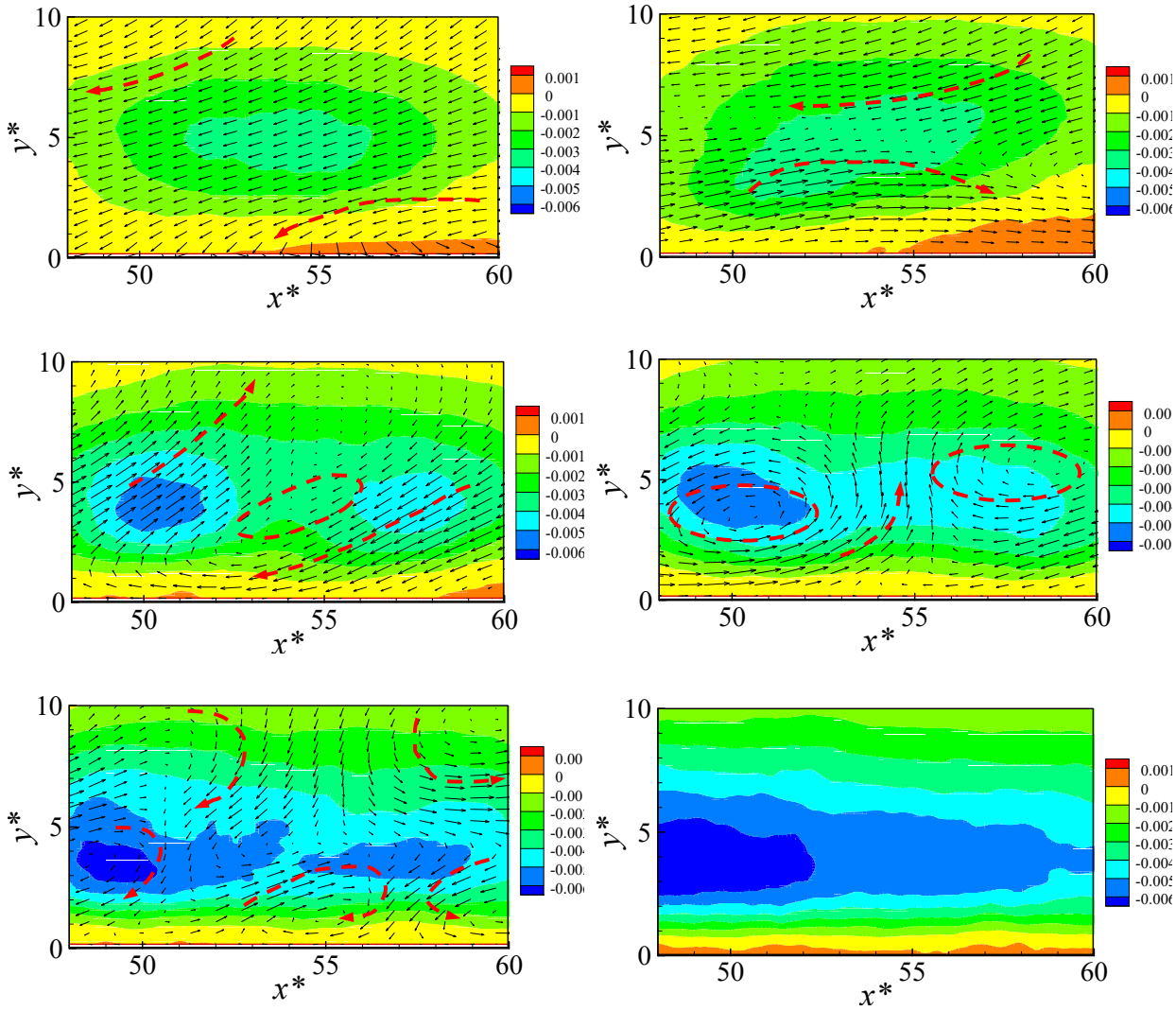

Figure 6.22 Contour plots of reconstructed Reynolds shear stress for R2 for modes (a) 1, (b) 2, (c) 3, (d) 5, (e) 10 and (f) ensemble PIV data within the self-similar region

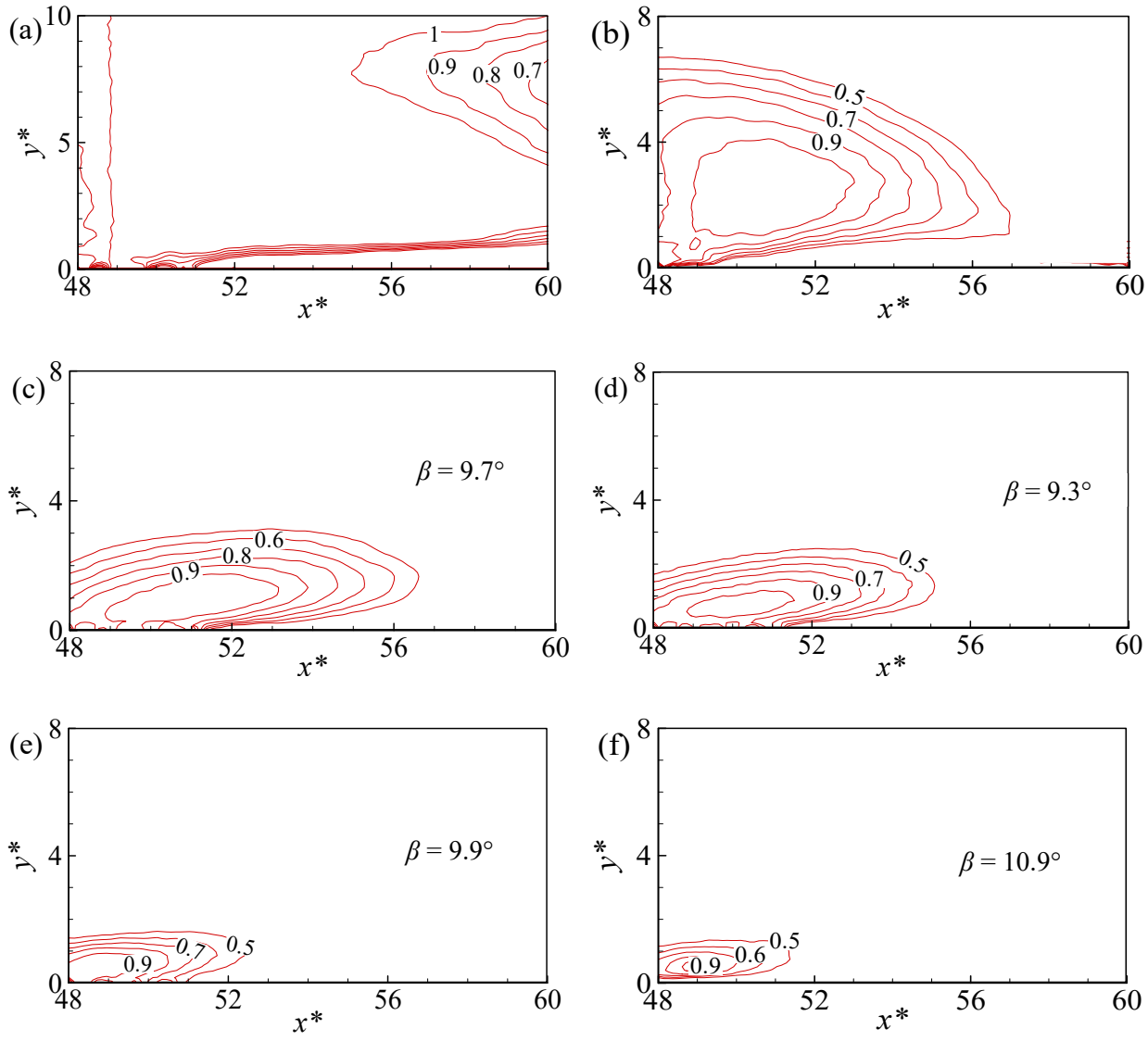

Figure 6.23 Contour plots of the R_{uu} correlation function for (a) mode 1, (b) mode 2, (c) mode 5, (d) mode 10, (e) mode 50 and (f) ensemble averaged PIV data for R2 configuration

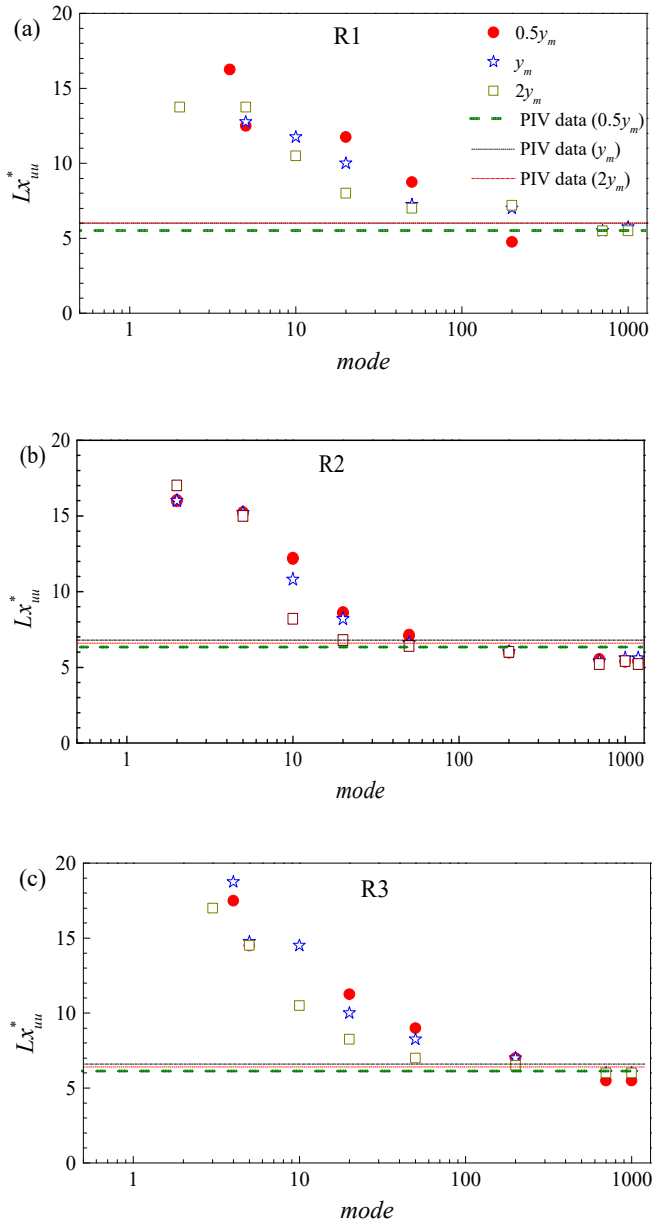

Figure 6.24 Estimation of integral length scale from the POD modes at selected wall-normal locations

6.5 Conclusions

An experimental study was conducted to investigate the effect of rib location on a three-dimensional offset jet flow using particle image velocimetry. A two-dimensional square rib was

mounted at x/b_o = 1.25, 3.45 and 6.25 from the nozzle exit, denoted herein as R1, R2 and R3, respectively. Both one-point and two-point statistics were used to investigate the flow development within the developing and self-similar regions of the offset jet flow. The mean reattachment length increased with increasing rib distance from the nozzle exit with values of $4.75b_o$, $7.05b_o$ and $8.60b_o$ for R1, R2 and R3, respectively. Estimated decay rates illustrate that changing the rib location from R1 to R2 and R3 enhanced mixing and entrainment of the ambient fluid. The wall-normal spread of the jet occurred in two stages due to intense backflow within the jet outer shear layer.

The streamwise mean velocity profiles attained self-similarity beyond $x/b_o \geq 20$ for both R1 and R2, and $x/b_o \geq 25$ for R3. The distribution of the Reynolds stresses showed that the flow dynamics were significantly modified by changing the rib distance from the nozzle exit within the developing region. For instance, changing the rib location from R1 to R2 or R3 resulted in over 70% increase in $\overline{u^2}$ levels within the developing region. The present results show that the flow dynamics within the recirculation and developing regions were largely controlled by the structures generated within the recirculation zone, whereas the flow dynamics in the self-similar region were controlled by the high turbulent outer shear layer. Within the developing region, the introduction of the rib deflected the wall-normal location of zero shear stress into the outer shear layer. This observation differed from the occurrence within the self-similar region and the no rib case. The present results illustrate the interaction between the inner and outer shear layers of the 3D offset jet. The JPDF contours show that the turbulence structure in the outer shear layer of the offset jet differed from that of turbulent boundary layers due to the significant mean shear gradient. The direction of the positive mean shear gradient in the outer shear layer resulted in rearrangement of the various quadrant events.

Analysis from the two-point correlation showed that for offset jets larger structures dominated the self-similar region compared to the developing region. Thus, a strong spatial correlation existed between the structures within the self-similar region compared to the developing region. Similarly, the outer shear layer is characterized by larger structures compared to the inner shear layer. The effect of the large structures generated in the outer shear layer is transported into the inner shear layer as the jet evolves downstream, thereby resulting in an interaction of the outer shear layer on the inner shear layer. The average inclination of these structures within the inner shear layer of the self-similar region was independent of the presence and location of the rib and was similar to canonical near-wall turbulent flows. Within the outer shear layer however, the inclination of these structures was solely controlled by mean shear gradient, and this translated into rearrangement of the various quadrant events. The integral length scales estimated from the auto-correlation functions revealed significant merging of large-scale structures as the jet evolved through the developing to the self-similar region. The integral length scales within the self-similar region were weakly dependent of rib location.

Results from the POD analysis showed that the dominant modes were more energetic within the self-similar region than the developing region. Similar to the quadrant analysis, the eigenvectors showed that both $Q1$ and $Q3$ events dominated the outer shear layer of the jet. The two-point correlation analysis on the POD modes revealed that the size of the turbulent structures contained by the energetic mode was larger than the less energetic modes. This observation gave credence to the fact that indeed large-scale structures are associated with the energetic modes.

PS: *An article presented at the 9th Turbulence and Shear Flow Phenomenon Conference which investigated the flow characteristics in the vicinity of the rib is presented in Appendix B.*

CHAPTER SEVEN

7 PAPER IV

Acoustic Doppler Velocimeter Measurements of a Submerged Three-Dimensional Offset Jet Flow over Rough Surfaces

7.1 Abstract

The flow characteristics of a submerged three-dimensional offset jet over transverse square ribs and gravel are experimentally investigated using an acoustic Doppler velocimeter. The pitch-to-height ratio of the ribs was varied to achieve *d*-type, intermediate and *k*-type roughness. The Reynolds number based on the nozzle height and jet exit bulk velocity was 53000. The mean flow properties and turbulent statistics are compared to those obtained over a smooth surface. Both decay and wall-normal spread rates were independent of surface roughness with estimated values of 0.66 ±0.03 and 0.138 ±0.01, respectively, with these values influenced by the presence of lateral confinement on the flow. The distribution of the mean flow, within the inner shear layer, revealed a dependence on surface roughness after reattachment. A representation of the Reynolds normal stresses within the symmetry and lateral planes revealed the highly anisotropic nature of the turbulence field of offset jets.

7.2 Introduction

Three-dimensional offset jet flows over rough surfaces occur in many engineering applications. The presence of surface roughness increases momentum transport and flow resistance. Roughness elements also promote near-wall turbulence, skin friction as well as convective heat transfer (Nagano *et al*., 2004; Jimenez, 2004). Due to the significance of roughness in engineering designs, different roughness elements (such as sand grain, gravel, transverse ribs

and wire mesh) have been used in the past to investigate roughness effects on turbulent flows. While results from previous investigations have advanced our understanding of rough wall turbulent flow structures, the vast majority of these measurements were obtained in boundary layer flows (Schultz & Flack, 2005; Krogstad & Antonia, 1999; Krogstad *et al*., 1992) and plane wall jets (Banyassady & Piomelli, 2014; Rostamy *et al*., 2011a; Tachie *et al*., 2004). Thus, our knowledge of the characteristics of turbulent 3D offset jet flow over rough surfaces is deficient.

Figure 7.1 shows a schematic of an offset jet flow over a rough surface. The Cartesian coordinate system is adopted with x, y and z representing the streamwise, wall-normal and lateral directions, respectively. The exit of the jet is at $x = 0$, the bottom of the channel is at $y = 0$ and $z = 0$ is on the symmetry plane. The discharged jet deflects towards the bottom of the channel due to its proximity to the wall, resulting in the creation of a low pressure region underneath the jet and subsequently reattach to the wall. The flow field of the offset jet can be divided into the recirculation, developing and self-similar regions. The recirculation region is characterized by large-scale mixing. The jet is divided into the inner and outer shear layers separated by a dividing streamline. The inner shear layer extends from the bottom of the channel to the inflexion point where $\partial U/\partial y = 0$, where U is the streamwise mean velocity. The flow characteristics within the inner shear layer resemble that of a classical boundary layer, while the outer shear layer has structures that resemble a free jet. The interaction between the inner and outer shear layers results in some unique flow features which can lead to significant flow modification. The wall-normal half-width, $y_{0.5}$, is defined as the wall-normal distance from the bottom of the channel to the location where $U = 0.5U_m$ and $\partial U/\partial y < 0$ and lateral half-width, $z_{0.5}$, (not indicated on Fig. 7.1), is defined as the lateral distance from the symmetry plane (where $z = 0$) to the lateral location where $U = 0.5U_m$. The symbols U_m, y_m, h and b_o represent the local maximum streamwise mean velocity,

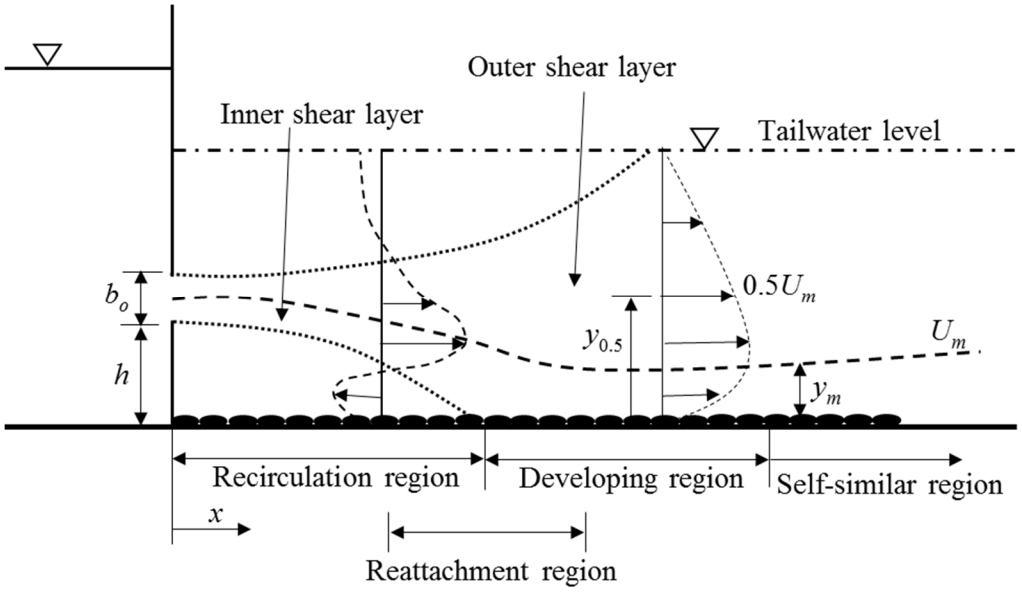

Figure 7.1 Schematic diagram of discharged offset jet with an overlaid roughness

the wall-normal location of U_m, offset distance and nozzle height, respectively. Due to its distinctive features, submerged 3D offset jets are prototypical flows for investigating interaction between wall-bounded and free shear flow such as those encountered in flow under sluice gates, spillways and energy dissipaters downstream of hydraulic structures.

Early studies by Perry *et al*. (1969) classified surface roughness as either *d*-type or *k*-type roughness. The *k*-type roughness is used to describe flow configurations where the roughness function depends on the Reynolds number based on the roughness height, *k*, and friction velocity, U_τ, (i.e., $k^+ = kU_\tau/\nu$, where ν is the kinematic viscosity). In cases where narrow spaces exist between the roughness elements, the *k*-type scaling is not valid. In these instances, outer variables (such as boundary layer thickness, δ, or pipe/nozzle diameter, *d*) are used and are therefore referred to as *d*-type. For flow over two-dimensional (2D) transverse ribs, the classification of roughness is based on the pitch (*p*) to height (*k*) ratio, *p/k*. Both *d*-type and *k*-type roughness configurations are attained when $p/k < 4$ and $p/k > 4$, respectively. An intermediate roughness is obtained when $p/k = 4$.

While measurements on rough surfaces have advanced our understanding of turbulence characteristics, the majority of these studies focused on turbulent boundary layers (Akinlade *et al*., 2004; Nagano *et al*., 2004; Cui *et al*., 2003; Tachie *et al*., 2003; Miyake *et al*., 2001; Grass *et al*., 1993), and wall jets (Rostamy *et al*., 2011a; Dey & Sarkar, 2008; Tachie *et al*., 2004). Agelinchaab & Tachie (2006) used particle image velocimetry (PIV) to investigate open channel turbulent flow over hemispherical ribs. Three p/k configurations of 2, 4 and 8 corresponding to the *d*-type, intermediate and *k*-type roughness, respectively, were used. For both *d*-type and intermediate roughness regimes, stable vortices were formed within the cavities generated by the attached ribs. This to some extent prevented the flow from reattaching to the channel bottom. Their results indicated that a larger vortex size was created within the cavity for the intermediate roughness compared to both the *d*-type and *k*-type roughness, with the vortex formed in the case of the *k*-type being the smallest in size. That is, for the *k*-type roughness, the vortices only occupy a fraction of the cavity with the separated flow more likely to reattach to the channel bottom. The turbulence levels were enhanced when p/k was increased from 2 to 8 due to the strong interaction between the shear layers. The turbulence level peaked at the crest of the ribs for both *d*-type and intermediate roughness. This was not the case for the *k*-type roughness where the turbulence level peaked within the cavity. Based on these observations, Agelinchaab & Tachie (2006) concluded that the interaction between the outer layer of the flow and cavities formed between the ribs varied with both roughness type and p/k. Studies conducted by Okomato *et al*. (1993) utilized transverse square rods which were arranged to yield a wide range of pitch-to-height ratios: $2 \leq p/k \leq 17$. Within the shear layer, the turbulence intensities increased with p/k when $p/k \leq 9$ but decreased for $p/k > 9$. This occurrence was attributed to the interaction between the ribs, which reached a maximum at $p/k = 9$.

Tachie *et al*. (2004) experimentally studied the effects of smooth and transitionally rough beds on the flow characteristics of a plane wall jet. For both smooth and rough wall, the mean velocity distribution collapsed within the outer shear layer of the flow, however, there was a significant modification to the velocity distribution within the inner shear layer. This suggests that roughness effects were confined to the inner shear layer of the wall jet flow. Their results also revealed that the presence of roughness increased the inner layer thickness of the jet and the skin friction coefficient. The results presented by Dey & Sarkar (2008) showed that for a submerged plane wall jet flow over different sand grain roughness of size 0.49 mm, 0.8 mm, 1.86 mm and 3 mm, the decay rate of U_m increased over the rough surface compared to the smooth surface. A faster decay of a jet flow should in part result in larger jet half-width. However, according to Tachie *et al*. (2004) the introduction of roughness did not affect the jet half-width. The findings of both Rostamy *et al*. (2011a) and Dey & Sarkar (2008) in recent studies on the effect of roughness on the jet half-width support observation made by Tachie *et al*. (2004). Rostamy *et al*. (2011b) also revealed that the introduction of roughness resulted in low peak levels of the streamwise Reynolds normal stress; for example, they reported that roughness reduced values of $\overline{u^2}$ at $y/y_{0.5}$ = 0.5 and 1.5 by 15% and 25%, respectively, compared to the corresponding smooth wall values (where u is the streamwise fluctuating velocity). The turbulence intensity distribution presented in inner variables for a plane wall jet over a rough surface failed to collapse with data obtained over a smooth surface outside the roughness sublayer (Rostamy *et al*., 2011b).

It has been demonstrated that the presence of roughness elements modifies both the mean flow characteristics and higher order turbulent statistics in boundary layer and wall jet flows. It is therefore essential to extend these investigations to offset jets since they occur in many practical

engineering applications. In view of this, Yoon *et al*. (1995) investigated the effect of roughness on a 2D offset jet using a split film probe and p/k configurations of 1, 2 and 3. Values of the local maximum streamwise mean velocity, after the jet's reattachment, reduced with increasing p/k due to enhanced momentum loss. Increasing the p/k resulted in an increment in the wall-normal jet half-width. Investigations by Bhuiyan *et al*. (2011) on 2D offset jet flow over different roughness elements (wire mesh, corrugated bed, gravel and marble) also revealed that the decay of U_m was not significantly dependent on surface roughness. Similarly, the mean L_e of the offset jet was also independent of surface roughness. The 3D turbulent jet differs from plane jets with the former exhibiting lateral spread. In view of this, several studies have been conducted to investigate the flow properties of 3D wall jets (Abrahamsson *et al*., 1997; Launder & Rodi, 1983), and offset jets (Nyantekyi-Kwakye *et al*., 2015a, b; Agelinchaab & Tachie, 2011). The review by Launder & Rodi (1983) revealed a significantly larger lateral spread rate compared to the wall-normal spread rate, yielding a ratio of about 5.5:1. The driving force behind this mechanism is not fully understood and attempts have been made to explain this feature using secondary mean motions (Davis & Winarto, 1980) and generation of streamwise vorticity as analyzed by Launder & Rodi (1983). Agelinchaab & Tachie (2011) observed that increasing h/b_o from 0 – 3.5 resulted in a more rapid decay of U_m. At a specific h/b_o, L_e was independent of Reynolds number (Re = dU_j/ν; where d and U_j are the nozzle diameter and jet exit velocity, respectively) beyond 5000. More recently, Nyantekyi-Kwakye *et al*. (2015a, b) extensively investigated the flow characteristics of 3D offset jets over a smooth surface using a PIV system. For an offset height ratio of 4, the Reynolds number based on the jet exit bulk velocity was 8720 with an estimated mean L_e of $6.2b_o$. The presence of a backflow region within the outer shear layer of the jet modified the distribution of the mean and turbulence statistics.

Although the effects of wall roughness on generic wall jets have been investigated over the past decades, only a few measurements have been made to understand how wall roughness changes the flow characteristics of offset jets. The few investigations of roughness effects on offset jets pertained to 2D offset jet configuration. It is apparent that more complex mechanisms control the evolution of 3D offset jets compared to 2D offset jets. Given the paucity of experimental data on the turbulent characteristics of 3D offset jet flow over rough surfaces and its importance to engineering applications, further studies are required to elucidate the effects of surface roughness on such flow configurations. Therefore, the present experimental investigation focuses on the effect of surface roughness on a submerged 3D offset jet. Four different roughness configurations (made from acrylic square rib and gravel) were used. The flow velocity was measured using a four receiver acoustic Doppler velocimeter which allows simultaneous measurement of all three velocity components.

7.3 Experimentation

The experiments were conducted in a recirculating channel with dimensions 1500 mm wide, 950 mm deep and 7000 mm long. The bottom of the channel was made of plywood and overlaid with an acrylic sheet. One of the side walls was made from smooth water resistant plywood and the other side made from a 25.4 mm thick acrylic sheet to facilitate flow visualization. The flow was driven by a fixed speed 65 hp centrifugal pump from a reservoir through 350 mm PVC pipelines. The water flow into the head tank of the channel was regulated by a variable control valve and the discharge was measured using an ultra-sonic flow meter. The discharge was monitored to ensure it remained constant during the experiments. The flow was conditioned by series of 200 mm long, 60 mm diameter pipes held in place by stainless steel wire screens on both the upstream and downstream sections. The water at room temperature was discharged through a

60 mm high (b_o) and 360 mm wide rectangular nozzle made from stainless steel plates of thickness 25.4 mm. The channel to nozzle width ratio is 4.2, which is not infinitely wide and can confine the jet in the lateral direction. The nozzle was offset at a height, h of 240 mm from the bottom of the channel yielding an offset height ratio, $h/b_o = 4$. The bulk velocity (U_o), measured from the flow discharge determined with an ultra-sonic flow meter, was 0.88 ms^{-1} yielding Reynolds number of approximately 53000. The tailwater depth was controlled by a vertical tailgate located at the downstream end of the flume and was maintained constant at 750 mm throughout the experimental runs. The present configuration led to the formation of a backflow which resulted in high turbulence levels within the outer shear layer of the jet. It is to be noted that the current setup is geometrically similar to the work done by Nyantekyi-Kwakye *et al*. (2015a, b). Square acrylic ribs with height, k, of 12.7 mm, spanning the entire channel width, was used as roughness element to investigate 2D roughness on the flow as shown in Figure 7.2. Three different values of the pitch, p, were chosen to achieve different types of roughness configurations. Specifically, values of p = 25.4 mm, 50.8 mm and 101.6 mm were chosen to yield p/k = 2, 4 and 8 corresponding to d-type, intermediate and k-type roughness, respectively. Gravel with equivalent diameter of 12.7 mm (selected using calibrated sieve) was also used to investigate the effect of 3D roughness on a 3D offset jet flow. The gravel was attached to the channel bottom using cement.

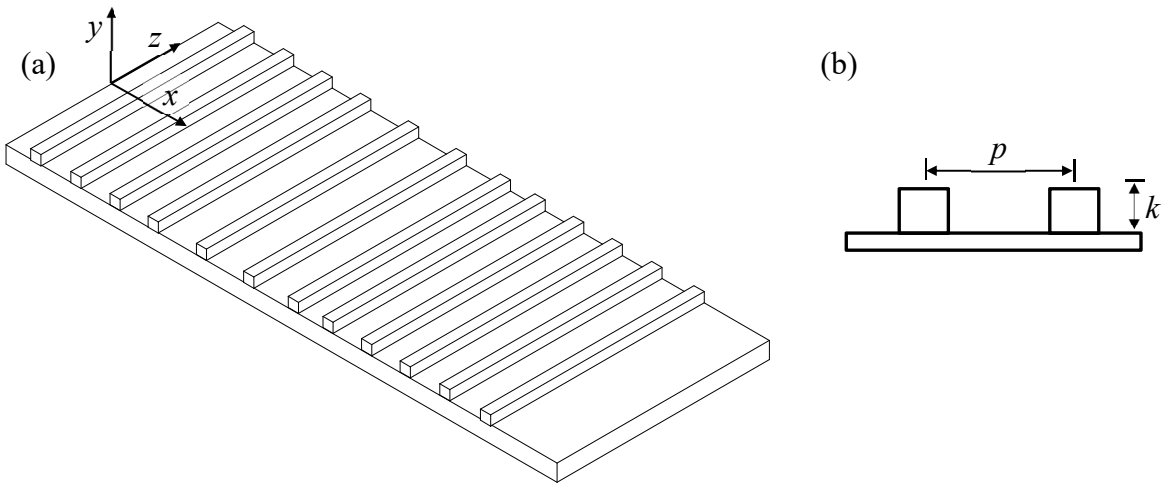

Figure 7.2 Schematic of the bottom of the flume overlaid with transverse square rib roughness

A downward facing Nortek Vectrino II (RUD, Norway) was used to measure the instantaneous velocity field within the symmetry and lateral planes. Measurements in the lateral plane were conducted at y_m. The Nortek Vectrino II like any other acoustic Doppler velocimeter operates on the Doppler shift principle. The instrument consists of a transducer, four sound receivers and a signal conditioning electronic module. The sampling volume of the Nortek Vectrino II is centered at a distance of 50 mm from the probe. The sampling volume is cylindrical with a diameter of 6 mm and a user selectable total length between 3–30 mm. In the present investigation the sampling volume was divided into 21 cells of 1 mm length. Seeding particles (10 μm diameter neutrally buoyant spherical hollow glass spheres with specific gravity of 1.07, settling velocity of 2.45×10^{-6} ms^{-1}, and Stokes number of 0.5) were placed within the flow to ensure that an acceptable signal to noise ratio was achieved. The estimated Stokes number indicates that the seeding particles followed the fluid streamlines. In order to obtain converged time average velocities, the data was acquired at a sampling rate of 100 Hz for 5 minutes. The adopted sampling time was based on preliminary measurements acquired for 3, 5, 10, 15, 20 and 30 minutes. Since

the sampling volume was located 50 mm below the Nortek Vectrino II, the captured data was largely free from the disturbance induced by the probe. Close to the channel bottom, the measured velocities can be contaminated with spikes, which could possibly be due to the interference between incident and reflected pulses. These spikes are as a result of aliasing of the Doppler signal due to the phase shift between the incident and reflected pulses outside the range of ±180°. These spikes were filtered by spike removal algorithms (Islam & Zhu, 2013; Goring & Nikora, 2002). Knowledge of the orientation of the bi-static axes for all four receivers allows calculation of the 3D water velocity. The bi-static velocities are converted to Cartesian coordinate velocities using a 3 × 3 transformational matrix which is defined by the probe geometry. The Nortek Vectrino II can measure velocities in the range ±0.01–4 ms^{-1} with accuracy of ±0.5% of the measurement range. Velocity measurements were conducted within the streamwise range $4 \leq x/b_o \leq 25$, which falls within the developing region of the jet as outlined by Padmanabham & Lakshmana Gowda (1991). Due to experimental constraints, velocity measurements could not be made close to the nozzle exit ($x/b_o < 4$). A detailed uncertainty analysis was conducted using the moving bootstrap technique reported by Garcia *et al*. (2006). Based on the analysis, the uncertainty in the measurements in the streamwise and wall-normal mean velocities, lateral mean velocity and Reynolds stresses were ±3%, ±5% and ±15%, respectively.

7.4 Results and Discussion

7.4.1 Jet development

The reattachment length is defined as the streamwise distance from the nozzle exit to the point where the discharged jet attaches to the bottom of the flume. A dye was injected into the flow domain to estimate the mean L_e. This technique could not yield accurate estimations due

quick diffusion of the dye. Therefore, the mean L_e was estimated from the distribution of U (since the recirculation region is characterized by negative U values, the reattachment point was defined as the streamwise location where there were no negative values of U within the inner shear layer of the jet) and the results compared with the scaled down studies by Nyantekyi-Kwakye *et al*. (2015b). The distributions of the streamwise mean velocity showed that the jet reattached to the bottom of the flume beyond $x/b_o > 6$, which can be compared to $L_e = 6.2b_o$ obtained from the scaled down experiment by Nyantekyi-Kwakye *et al*. (2015b) for an offset jet with $h/b_o = 4$. Previous studies have shown that both Re (beyond 5000, Agelinchaab & Tachie, 2011) and surface roughness (Bhuiyan *et al*., 2011) have no significant effect on the reattachment length of offset jets.

The jet development was investigated using the decay of U_m, wall-normal half-width, $y_{0.5}$ and lateral half-width, $z_{0.5}$. Figure 7.3a shows the distribution of U_m normalized by the jet exit bulk velocity, U_o. As a result of entrainment of ambient fluid, U_m decreases with increasing x/b_o. The decay rate of U_m can be used to characterize the mixing characteristics of the jet and ambient fluid. The decay rate was estimated from a power law fit described by $U_m/U_o = C(x/b_o)^{-n}$ (where, C and n are a coefficient and the decay rate, respectively) within the region $12 \leq x/b_o \geq 25$. The streamwise range was chosen in order to focus on the reattached section of the jet. The estimated

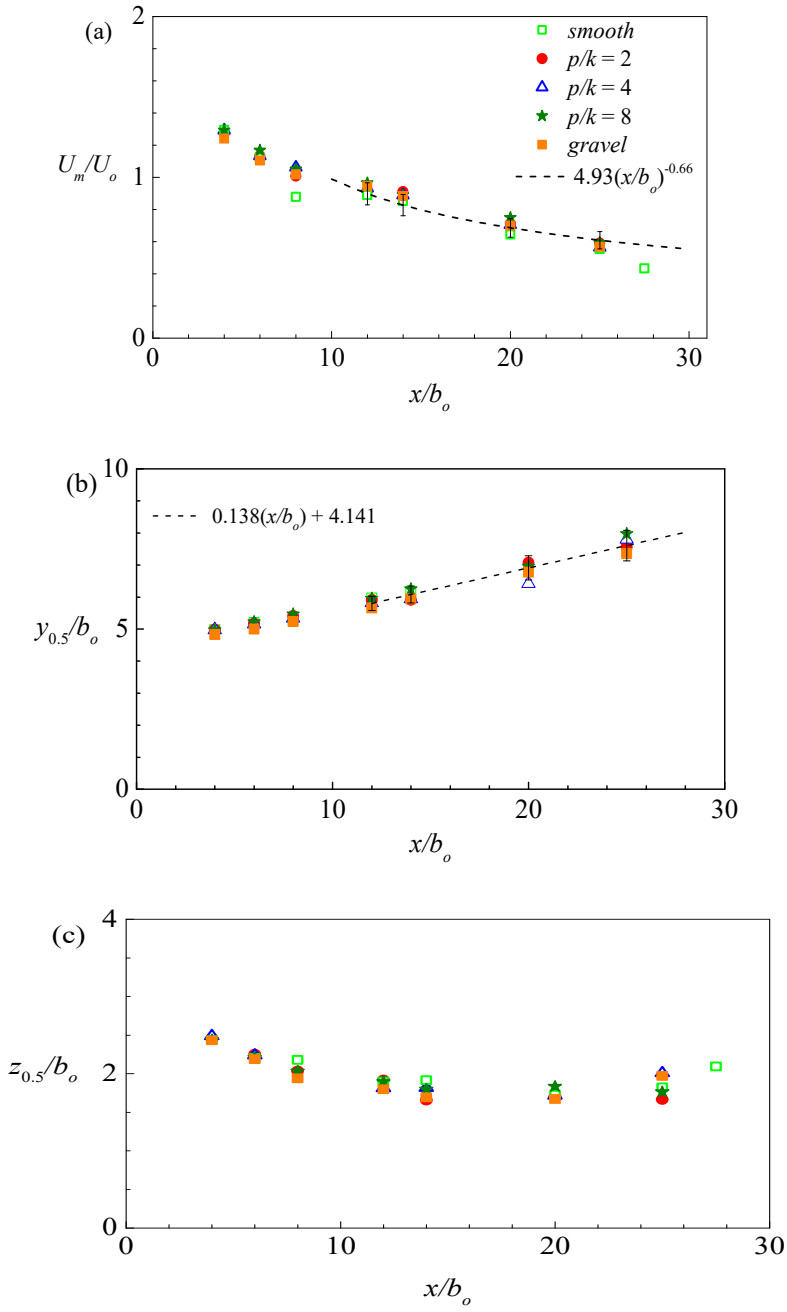

Figure 7.3 Development of the 3D offset jet flow (a) decay of U_m, (b) wall-normal half-width, $y_{0.5}/b_o$ and (c) lateral half-width, $z_{0.5}$

decay rate was 0.66 ±0.03 for all test conditions which falls in the range 0.63 – 0.85 reported by Padmanabham & Lakshmana Gowda (1991) within the developing region of 3D wall jets. The

present results are in qualitative agreement with previous studies by Bhuiyan *et al*. (2011) which showed that the decay of U_m for plane offset jet was insensitive to surface roughness. The present decay rate value is less than 1.29 (obtained within the self-similar region) reported by Abrahamsson *et al*. (1997) for a 3D wall jet within. The difference between results by Abrahamsson *et al*. (1997) and the present value can be attributed to experimental setup which highlights lateral confinement of the jet by the side walls. Side walls affect the relative entrainment of ambient fluid, both in the near and far field of the jet. The presence of the side walls reduced the level of lateral entrainment of ambient fluid by the jet. It is worth pointing out that the investigation by Abrahamsson *et al*. (1997) was conducted in an 'infinite' basin with channel width to nozzle diameter ratio in the order of 160 which is far greater than 4.2 in the present investigation, highlighting the confinement of the jet in the lateral direction hence the reduced decay rate.

The jet half-width is an important length scale for turbulent jets since it provides a measure of the growth rate of the jet. Figure 7.3b shows variation of the wall-normal half width, $y_{0.5}/b_o$, with streamwise distance. The wall-normal half-width increased with increasing x/b_o and was almost independent of surface roughness similar to the U_m decay. In order to estimate the spread rate, $dy_{0.5}/dx$, a linear fit of the form $y_{0.5}/b_o = m(x/b_o) + c$ was applied to the experimental data (where m is the spread rate and c is the intercept) within the region $12 \leq x/b_o \leq 25$. A spread rate of 0.138 ±0.01 was obtained for the different test conditions. The estimated wall-normal spread rate for the 3D offset jet is higher than of 0.048 reported by Launder & Rodi (1981) and 0.065 obtained by Abrahamsson *et al*. (1997) for 3D wall jets. The difference in spread rates can be attributed to the influence tailwater depth, which was not present in the previous studies (for e.g., that of Abrahamsson *et al*., 1997). It is interesting to note that the investigation by Ead & Rajaratnam (2004) on a plane wall jet over a rough surface with limited tailwater depth yielded a

wall-normal spread rate of 0.125, which is similar to the current estimated wall-normal spread rate. The lack of distinct roughness effects on the wall-normal spread rate supports findings of Rostamy *et al*. (2011a), Dey & Sarkar (2008) and Tachie *et al*. (2004). Unlike the wall-normal half-width, Fig. 7.3c shows that the lateral half-width decreased with streamwise distance until $x/b_o = 14$. This can be attributed to swirling motions or vortical structures that were generated on the sides of the jet within the lateral plane. The dynamics of these structures can largely be controlled by the presence of a lateral confinement especially if there is a tendency of the jet reattaching to it. The presence of these structures also signifies the occurrence of the axis-switching phenomenon which is prevalent in aspect ratio nozzles (Quinn, 1992). The axis-switching tends to reduce the spread of the jet in the major axis (or lateral plane) while increasing the spread in the minor axis (or vertical plane). These structures formed in the major axis therefore suppressed the spread of the jet in the lateral direction, hence the observed decrease in $z_{0.5}$ within the region $x/b_o \leq 14$. Reports by Lee & Baek (1994) attributed the observed initial decrease in $z_{0.5}$ to the combined effects of the vena-contracta and deformation of elliptic vortical structures. Beyond $x/b_o = 14$, values of $z_{0.5}$ start to slightly increase with streamwise distance. Similarly, the distribution of $z_{0.5}$ was not dependent on surface roughness. Due to the lack of a substantive linear section in the distribution of $z_{0.5}$, the lateral spread rate was not determined.

7.4.2 Streamwise mean velocity

Within the symmetry plane, the streamwise and wall-normal mean velocities were normalized by U_m (the velocity scale) and wall-normal distance by $y_{0.5}$ (length scale). Figure 7.4a shows the development of the streamwise mean velocity, U, of the offset jet at selected streamwise locations (x/b_o = 4, 6, 8, 12, 14 and 20). It should be noted that some of the streamwise distances occurred on top of the 2D ribs. The effect of roughness on the offset jet flow was not evident within

the region x/b_o < 20, even though results from the scaled down experiment conducted by Nyantekyi-Kwakye *et al*. (2015b) and the present mean velocity distribution suggest that the offset jet already reattached to the bottom of the flume beyond x/b_o > 6. This observation reveals that the present roughness configuration did not greatly alter the flow within the recirculation and early developing regions of the 3D offset jet. However, at x/b_o = 20, values of U/U_m are lower for the rough surfaces compared to the smooth surface within the inner shear layer of the jet. For instance at x/b_o = 20 and $y/y_{0.5}$ = 0.3, values of U/U_m decreased by 10%, 16%, 14% and 20% for the *d*-type, intermediate, *k*-type and gravel roughness, respectively, compared to the smooth surface. Figure 7.4a indicates that the effect of roughness was confined to the inner shear layer and did not extend into the outer shear layer of the offset jet flow. Similarity in the distribution of U for 3D offset jet flows on smooth surface has been reported from previous studies (Nyantekyi-Kwakye *et al*., 2015a; Agelinchaab & Tachie, 2011). Profiles of U/U_m for the smooth surface attained self-similarity beyond $x/b_o \geq 20$. This occurred earlier than $x/b_o \geq 38$ reported by Nyantekyi-Kwakye *et al*. (2015a) for an offset jet with h/b_o = 4. In contrast, profiles of U for the *d*-type, intermediate, *k*-type and gravel roughness did not attain self-similarity within the x/b_o range considered. This observation highlights the difference in turbulent scales for flow over the rough surfaces compared to the smooth surface.

The wall-normal mean velocity, V, distribution in Fig. 7.4b shows that positive values prevail within the inner shear layer in the region x/b_o < 8. The positive value within the inner shear layer is indicative of the presence of recirculation flow within which ambient fluid is entrained from the wall region into the core jet. Downstream of the reattachment, negative values of V dominated the inner shear layer whereas positive V values were observed in the outer shear layer, with the current roughness configurations having a minimal influence on this distribution. The

positive values of V correspond to expansion of the jet while negative V values represent entrainment of ambient fluid into the core jet. The present distribution of V would suggest that the gradient $\partial V/\partial y$ would contribute to the production of turbulent kinetic energy.

7.4.3 Reynolds stresses

The distributions of the Reynolds normal stresses ($\overline{u^2}$, $\overline{v^2}$, and $\overline{w^2}$, where u, v and w are the fluctuating velocities in the streamwise, wall-normal and lateral directions, respectively) in the symmetry plane are shown in Fig. 7.5. The Reynolds normal stresses did not attain self-similarity within the streamwise range considered. The Reynolds normal stresses ($\overline{u^2}$, $\overline{v^2}$ and $\overline{w^2}$) exhibited

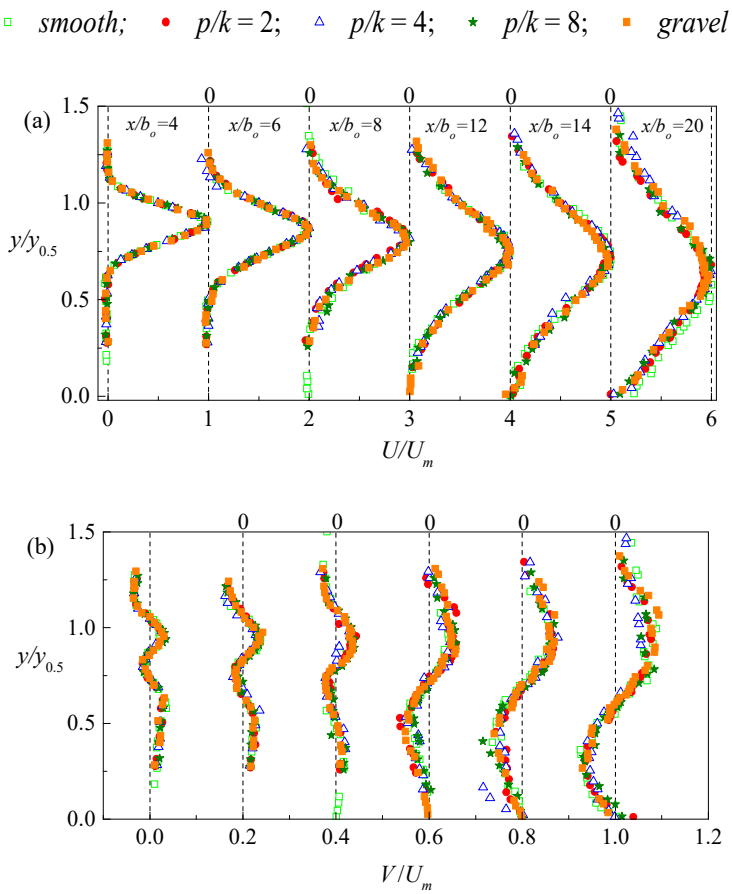

Figure 7.4 Profiles of (a) streamwise and (b) wall-normal mean velocities

double peaks close to the nozzle exit. The presence of the double peak is an indication of high turbulence at the edges of the jet where there exist high mean velocity gradient. The lower and upper peak values of the normal stresses at $x/b_o = 4$, which falls within the recirculation region of the flow, were of equal magnitude for each test condition. Thus the presence of the recirculation region and roughness did not influence both peak values. The normalized peak values of $\overline{u^2}$, $\overline{v^2}$ and $\overline{w^2}$ were 0.037, 0.013 and 0.026, respectively. Due to the high turbulence levels within the outer shear layer as a result of the backflow, higher peak levels of the normal stresses were obtained in the present investigation compared to previous studies by Abrahamsson *et al*. (1997). The distribution of the Reynolds normal stresses reveals the anisotropic nature of the turbulence field of 3D offset jets. The anisotropy in the turbulence field has been widely viewed to contribute to the generation of streamwise vortices. After reattachment of the jet, larger values of $\overline{w^2}$ occurred close to the wall compared to $\overline{v^2}$. The near wall peaks of $\overline{v^2}$ decreased slightly over the roughness elements. The low levels of $\overline{v^2}$ were as a result of the wall damping effect on the wall-normal velocity fluctuation component (Launder & Rodi, 1983). As the jet spreads, the double peaks diminish downstream of the nozzle exit. Changing the roughness configuration from *d*-type through intermediate to the *k*-type roughness did not alter the distribution of $\overline{u^2}$ and $\overline{w^2}$.

Figure 7.6 shows the distribution of the Reynolds shear stresses, ($\overline{uv}$. $\overline{uw}$ and $\overline{vw}$, within the symmetry plane). Similarly, the Reynolds shear stresses for the different test conditions did not attain self-similarity within the present streamwise extent. Figure 7.6a shows that negative values of $\overline{uv}$ dominated the inner shear layer, becoming positive in the outer shear layer of the 3D offset jet. This distribution persisted for the streamwise range considered in the present investigation. The profiles indicate that the Reynolds shear stress ($\overline{uv}$) distribution is independent of surface

roughness within the region $4 \leq x/b_o \leq 12$. That is, the structures within the recirculation region control the dynamics of the flow within the early stages of the jet. Beyond $x/b_o = 12$, there were some scattered data for the flow over rough surface within the inner shear layer. Similarly, Banyassady & Piomelli (2014) reported that the distribution of $\overline{uv}$ for a 2D wall jet was not affected by surface roughness within the outer shear layer when normalized by U_m and $y_{0.5}$. This suggests that the effect of roughness was largely restricted to the inner shear layer of the jet. For a generic wall jet flow, the strong influence of the turbulent outer shear layer on the inner shear layer resulted in the displacement of the wall-normal position of zero shear stress from the position of the local maximum streamwise mean velocity. These two wall-normal locations did not coincide in the present investigations for flow over both smooth and rough surfaces. For instance, with the *d*-type roughness configuration, the wall-normal location of $\overline{uv}$ occurred closer to the channel bottom than the wall-normal location of U_m. This signifies a strong interaction of the turbulent outer shear layer and the inner shear layer of the offset jet flow. This interaction transports positive Reynolds shear stress from outer shear layer into the inner shear layer. This observation agrees with those made by Abrahamsson *et al*. (1997) for a 3D wall jet flow where the change in sign of $\overline{uv}$ occurred closer to the wall than the position where the mean velocity gradient was zero at 80*d*. Figures 7.6b and 7.6c show the distribution of $\overline{uw}$ and $\overline{vw}$, respectively. It is to be noticed that $\overline{uv}$ is much larger than both $\overline{uw}$ and $\overline{vw}$, rendering inhomogeneity in the Reynolds shear stress. The shear stress component, $\overline{vw}$, is the smallest and closer to zero within the symmetry plane. This goes to show that the contribution by $\overline{vw}$ to the generation of streamwise vorticity is small.

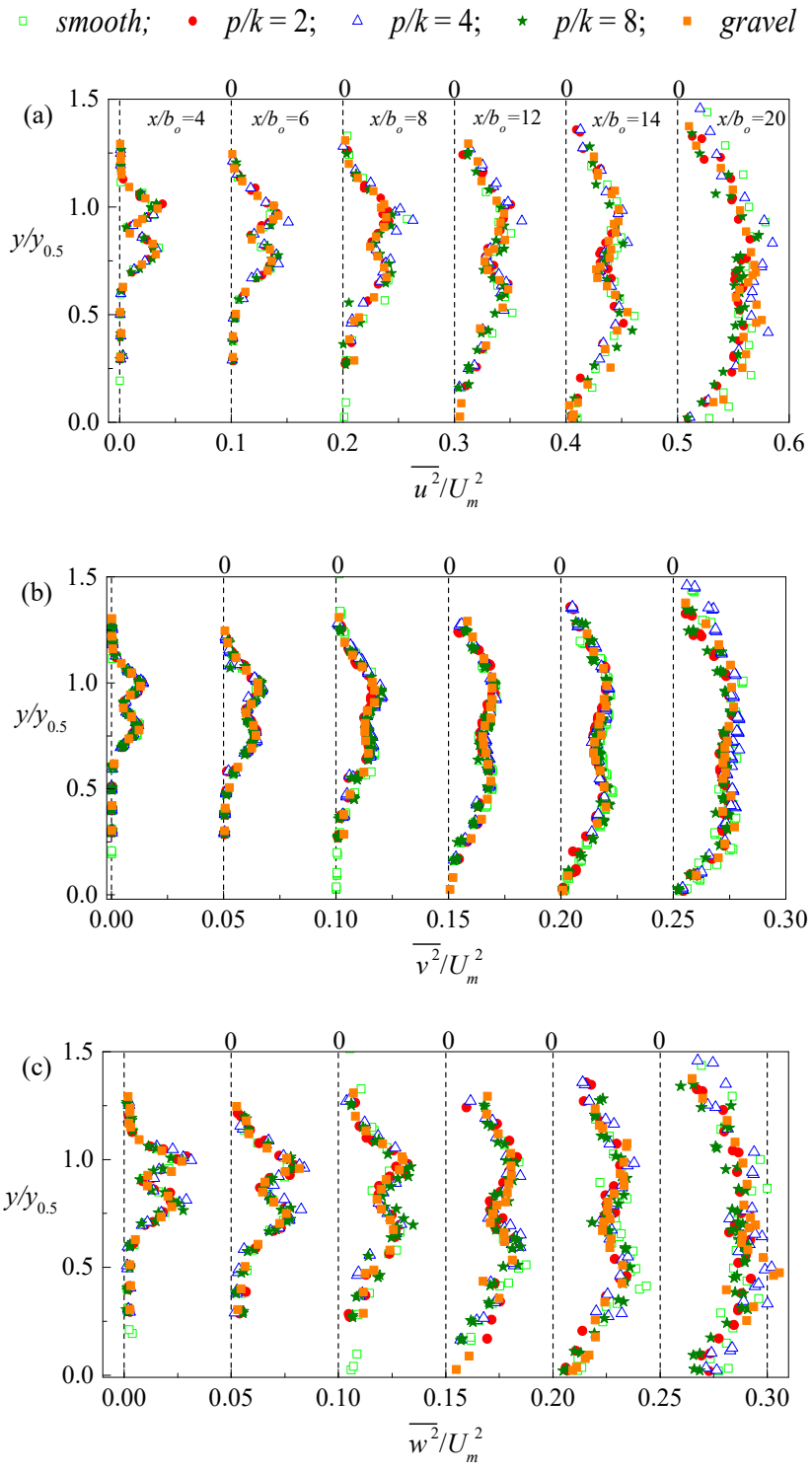

Figure 7.5 Reynolds normal stress distribution within the symmetry plane

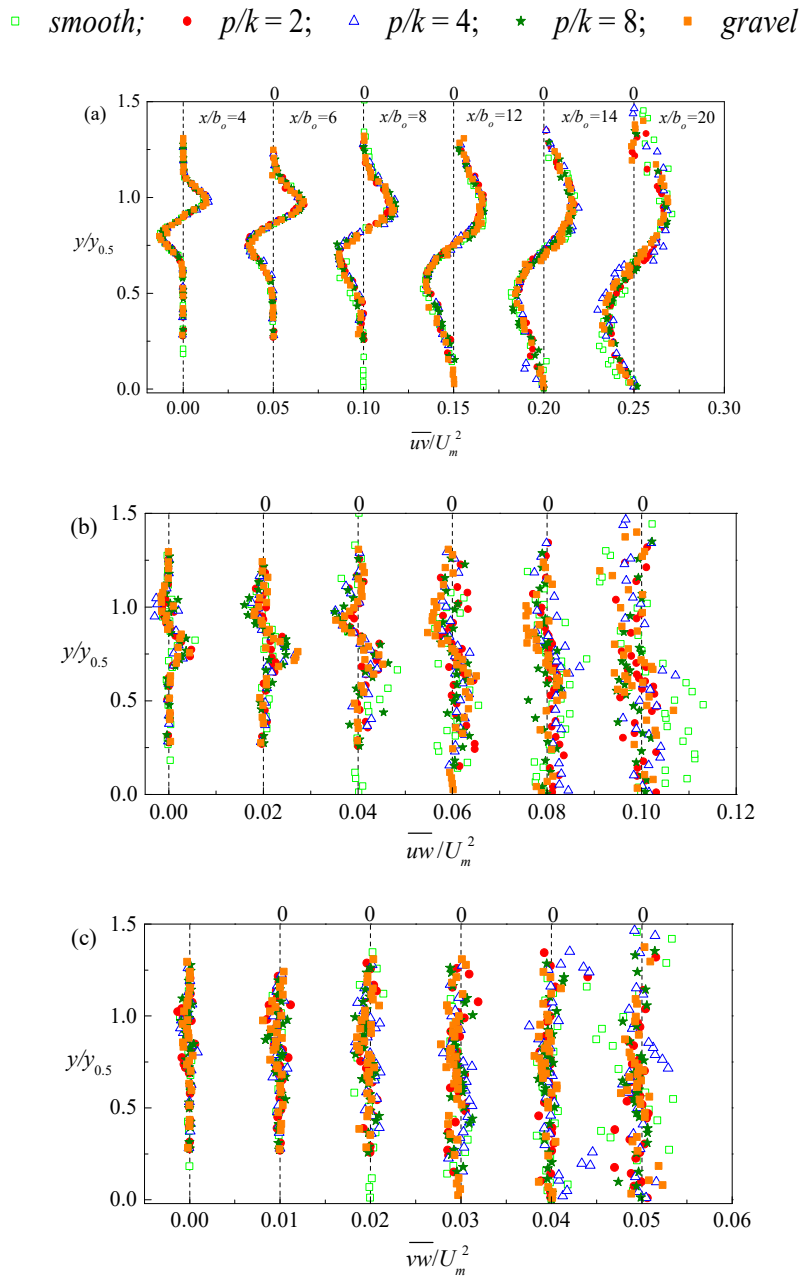

Figure 7.6 Reynolds shear stress distribution within the symmetry plane

7.4.4 Measurements in the lateral plane

Measurements within the lateral plane were taken at y_m and conducted on one side of the channel. This was because initial measurements across the entire width of the channel revealed

flow symmetry. The velocity and length scales used are U_m and $z_{0.5}$, respectively. Profiles of the streamwise and lateral mean velocities are shown in Fig. 7.7. The profiles of U at the various streamwise locations were independent of surface roughness (Fig. 7.7a). This may be attributed to the extent of the wall-normal location where measurements in the lateral plane were taken. That is, it has been established from previous sections that the effect of roughness, if present, was confined to the inner shear layer. Knowledge of the lateral mean velocity component, W, is of great interest since the presence of secondary mean motions influence the dynamics of the 3D jet flow. Figure 7.7b shows that W attained values close to zero within the symmetry plane and increased towards a maximum within the vicinity of the lateral jet half-width. Farther downstream, the levels of W compared to V reveal that there was a significant lateral motion of the discharged offset jet. From continuity, it is expected that the wall-normal mean velocity should be directed towards the core region of the jet. These secondary mean motions, when present, coupled to the anisotropy in the turbulence field contributes to the generation of streamwise vortices. Unlike the distribution of U in the lateral plane, the lateral mean velocity was dependent on surface roughness at some streamwise locations. The distribution of W at $x/b_o = 8$ and $x/b_o = 20$ were predominantly positive over the smooth surface compared to the predominantly negative values over the *d*-type, intermediate, *k*-type and gravel roughness profiles.

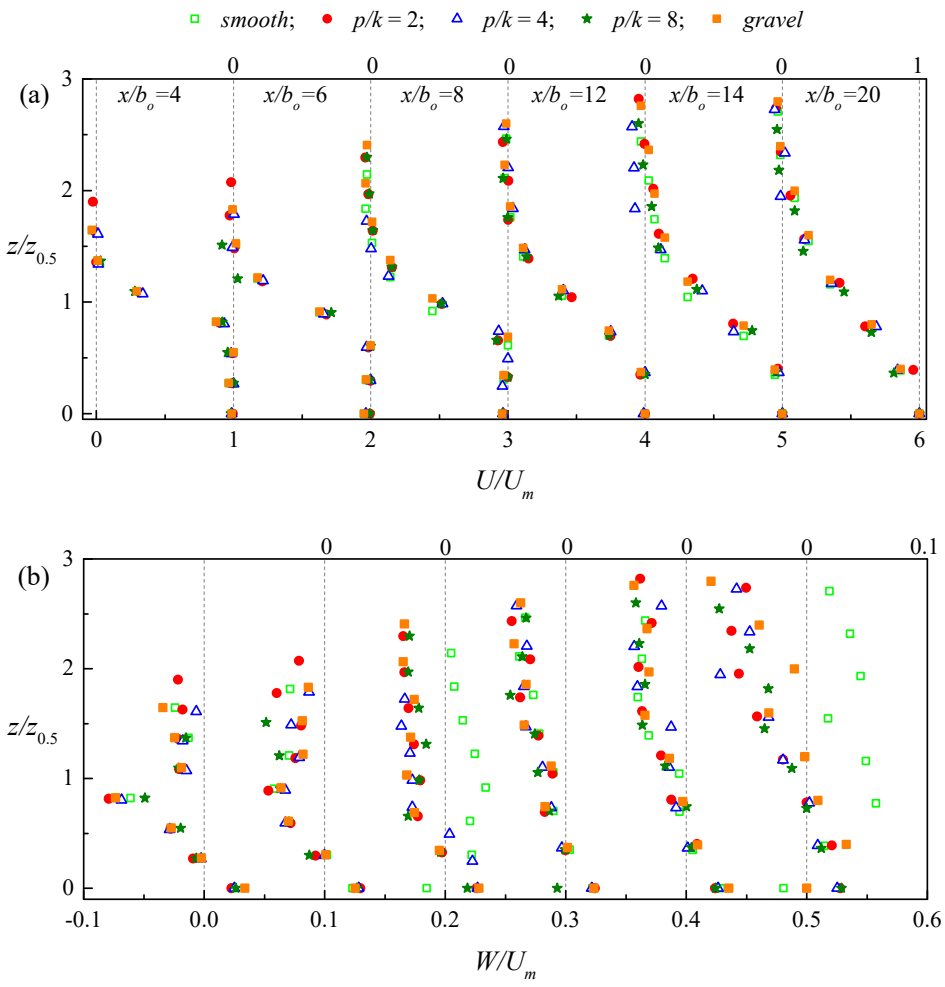

Figure 7.7 Profiles of (a) streamwise mean velocity, U, and (b) lateral mean velocity, W, within the lateral plane

The distributions of Reynolds stresses in the lateral plane are shown in Fig. 7.8. Similar to observations made within the symmetry plane, larger peak values occurred for $\overline{u^2}$ compared to both $\overline{v^2}$ and $\overline{w^2}$. After reattachment of the offset jet, larger values of $\overline{u^2}$ were obtained in the lateral plane compared to the symmetry plane. For example, the peak value of $\overline{u^2}$ within the lateral plane for the gravel roughness was 21% larger than that obtained within the symmetry plane at x/b_o = 20. For all test conditions, values of $\overline{w^2}$ were larger than corresponding $\overline{v^2}$ at the same x/b_o

locations. For instance, the peak of $\overline{w^2}$ for the *d*-type roughness was 75% and 31% greater than $\overline{v^2}$ at x/b_o locations of 4 and 20, respectively. Again, it should be noted that the levels of $\overline{v^2}$ and $\overline{w^2}$ would enhance the generation of streamwise vortices. Profiles of the normal stresses suggest that the introduction of roughness did not have a major impact on its distributions. Similarly, the Reynolds shear stress, $\overline{uw}$, was not affected by the surface roughness. The shear stress approaches zero in the symmetry plane. Values of $\overline{uv}$ in the symmetry plane were much higher than $\overline{uw}$ within the lateral plane (about 43%) at x/b_o = 20. The lateral shear stress increases with streamwise distance for all test conditions.

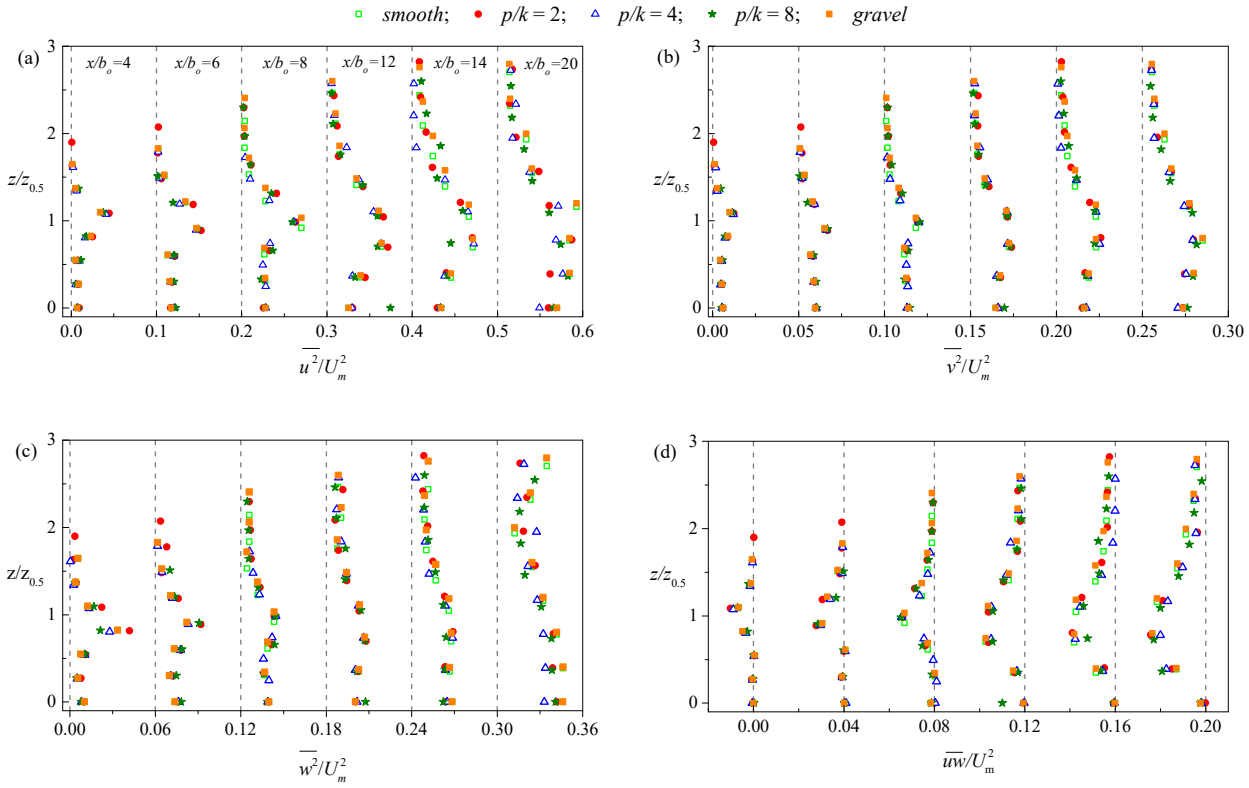

Figure 7.8 Reynolds stress distribution within the lateral plane

7.5 Conclusions

The present investigation sought to elucidate the flow behavior of a submerged 3D offset jet flow over both smooth and rough surfaces using an acoustic Doppler velocimeter. The roughness elements were made from transverse square ribs and gravels. The square ribs were arranged to yield p/k values corresponding to the d-type, intermediate and k-type roughness configurations. Measurements were performed within a streamwise range of $4 \leq x/b_o \leq 25$. The development of the 3D offset jet was independent of surface conditions within the recirculation and early reattachment regions highlighting control of the flow dynamics by large structures dominating these regions. The decay of the local maximum streamwise mean velocity was independent of surface roughness with a decay rate of 0.66 ±0.03. That is, the decay of U_m in the present study was largely controlled by entrainment of the ambient fluid by the offset jet. Due to the 3D nature of the jet, the discharged jet spread in both the symmetry and lateral planes. The estimated wall-normal spread rate 0.138 ±0.01 was independent of surface roughness, and could have been enhanced by vortical structures formed on each side of the discharged jet within the lateral plane. The presence of the side walls coupled with the aspect ratio of the discharged nozzle contributed to the formation of these vortical structures which led to an initial decrease in $z_{0.5}$. The mean flow distribution was independent of surface roughness within the recirculation and early developing regions of the flow but the effect of surface roughness was evident beyond $x/b_o = 20$. The streamwise mean velocity over the smooth surface attained self-similarity beyond $x/b_o = 20$. Since the present measurement technique allowed simultaneous measurements of all three velocity components, the distribution of all three Reynolds normal stresses within the symmetry and lateral planes depicted strong anisotropy in the turbulence field of the 3D offset jet. The high anisotropic

nature of the offset jet flow coupled with the dominant secondary mean motions, would contribute to the generation of streamwise vortices.

CHAPTER EIGHT

8 PAPER V

Submerged Turbulent Offset Jet issuing from a Rectangular Nozzle with varying Expansion Ratio

8.1 Abstract

The mean and turbulence characteristics of an offset jet issuing from nozzles of various offset heights and expansion ratios were experimentally investigated using a four receiver acoustic Doppler velocimeter. The jet was discharged from sharp-edged rectangular nozzles at offset height ratios of 0, 2, 4 and 6; and expansion ratios of 0.24, 0.49, 0.75 and 1.00 at an exit Reynolds number based on the nozzle height of 5.3×10^4. The results indicated that the decay rate of the streamwise mean velocity increased with increasing offset height ratio. However, increasing the expansion ratio decreased the decay rate of the discharged jet with values of 0.914, 0.371, 0.379 and 0.358 for expansion ratio 0.24, 0.49, 0.75 and 1.00, respectively. The highly anisotropic turbulence field for the offset height and expansion ratios highlights the drawback of using isotropic turbulence models to predict the present flow characteristics.

8.2 Introduction

Turbulent jets occur in diverse environmental and engineering applications, some of which include the disposal of communal and industrial waste, spillway applications, film cooling, fuel injection systems and combustion chambers of gas turbines. Turbulent jets can be either two or three-dimensional (3D) in nature. Two-dimensional jets (hereafter referred to as plane jets) are formed when the discharged jet has an infinite width whereas 3D jets are formed from nozzles of finite width. Turbulent jets can be grouped into one of the following broad categories: free, wall,

surface and offset jets. A free jet is formed when a discharged jet is sufficiently far from a boundary that would restrict its development. A wall jet is established when a discharged jet is confined on one side by a solid boundary. For a surface jet, the discharged jet is confined on one side by the free surface of the flow. An offset jet is formed when a jet is discharged into a medium at a certain distance from the boundary, which may be a solid wall or a free surface. The offset jet possesses characteristic features of both free jet (close to the nozzle exit) and a wall jet (after reattachment of the discharged jet to the bottom of the channel). This makes the turbulence characteristics of an offset jet relatively more complex than observed in the two limiting cases. The present study focuses on an experimental investigation of 3D offset jet reattaching to a solid wall.

Figure 8.1 shows a typical flow field of a 3D offset jet. The streamwise, wall-normal and lateral directions are represented by x, y and z axis, respectively. The exit of the jet is at $x = 0$, the bottom of the channel is at $y = 0$, and $z = 0$ is located on the line of symmetry. The streamwise, wall-normal and lateral components of the mean velocities are denoted by U, V and W with their corresponding fluctuating components by u, v and w, respectively. The reattachment length of the offset jet (defined as the streamwise distance from the nozzle exit to the point where the jet reattaches to the bottom of the channel) is denoted by L_e. The notations U_o, b_o and h denote the exit bulk velocity, nozzle height and offset distance, respectively. The submerged offset jet entrains ambient fluid, resulting in the creation of a low pressure region underneath the jet, causing it to deflect and reattach to the channel bottom. Turbulent wall jet conditions are established beyond the reattachment point. A schematic of the mean velocity profiles in the symmetry (x-y) and lateral (x-z) planes for a 3D wall jet are depicted in Fig. 8.1b. The symbols U_m, y_m, $y_{0.5}$ and $z_{0.5}$ correspond to the local maximum streamwise mean velocity, wall-normal location of U_m, wall-normal half-width (defined as the wall-normal location where $U = 0.5U_m$ and $\partial U/\partial y < 0$) and lateral

half-width (lateral location where $U = 0.5U_m$), respectively. The wall jet is generally regarded as a two-layer shear flow. The inner layer, which extends from the bottom of the channel to y_m exhibits flow characteristics similar to a turbulent boundary layer, while the outer layer (which spans from y_m to the edge of the jet) shows flow characteristics that resemble those of a free jet. Due to their unique characteristics, turbulent 3D jets are used as prototypical flows for investigating the physics of near wall and free shear turbulent flows.

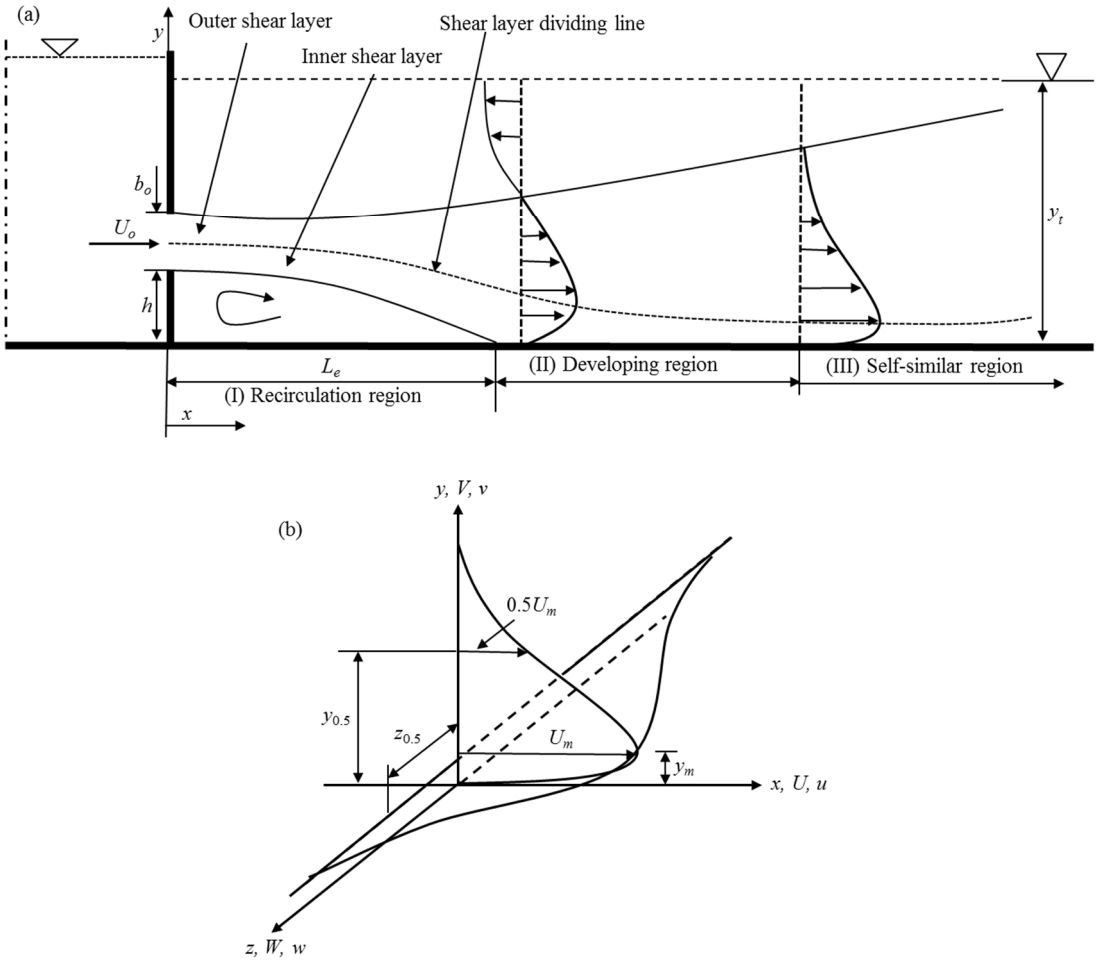

Figure 8.1 Schematic diagram of (a) discharged turbulent offset jet into tailwater and (b) velocity characteristics of 3D turbulent jet

Moreover, the complex flow field of offset jets makes them well suited test cases for assessing the performance of different turbulence models (Kumar, 2015; Pramanik & Das, 2013; Rathore & Das, 2013; Nasr & Lai, 1998).

Early studies on turbulent jets concentrated on the flow characteristics of free jets perhaps due to their relatively simpler flow physics which is partly explained by the absence of any confinement effects (Quinn, 2006; Quinn & Militzer, 1988; Lee & Baek, 1994; Hussain & Clark, 1977; Wygnanski & Fiedler, 1969; Bradshaw, 1966). Similarly, characteristics of plane and 3D wall jets have been studied extensively (e.g., Agelinchaab & Tachie 2011a; Ead & Rajaratnam, 2004 & 2002; Abrahamsson *et al*. 1997; Padmanabham & Gowda 1991). Ead & Rajaratnam (2002) investigated the effect of shallow tailwater depth on the mean flow characteristics of a plane wall jet using a Prandtl tube. Their results showed that for a finite tailwater depth, the wall jet decayed appreciably faster with streamwise distance. The wall-normal spread rate occurred in two stages (which were controlled by tailwater depth) with values of 0.076 and 0.20–0.35 in the first and second stages, respectively. Abrahamsson *et al*. (1997) used a hot-wire anemometry technique to investigate the flow field of a fully developed 3D round wall jet. The wall-normal and lateral spread rates were estimated to be 0.065 and 0.320, respectively. The larger lateral spread rate, which is a characteristic feature of 3D wall jets, was attributed to secondary mean motions. Their results also revealed the highly anisotropic nature in the turbulence field of 3D wall jets, which according to Launder & Rodi (1983) contributed to the generation of streamwise vortices.

In recent years, both plane offset jets (Bhuiyan *et al*., 2011; Gao & Ewing 2007; Nasr & Lai, 1998) and 3D offset jets (Nyantekyi-Kwakye *et al*., 2015a,b; Agelinchaab & Tachie, 2011b) have recieived considerable research attention. Agelinchaab & Tachie (2011b) conducted velocity

measurements for a 3D round offset jet with h/b_o ranging from 0 – 3.5 using planar particle image velocimetry (PIV). They reported that the mean L_e was independent of Reynolds number beyond 5000. As expected, the lateral spread rate was 4.5 times larger than the wall-normal spread rate. Recent planar PIV measurements by Nyantekyi-Kwakye *et al*. (2015a,b) in submerged 3D offset jets with h/b_o ranging from 0–4 issuing from sharp-edged rectangular nozzles at an exit Reynolds number range of $6 \times 10^3 – 12 \times 10^3$, showed that the decay rate of U_m depended on h/b_o.

Although several studies have been conducted to elucidate mixing and turbulence characteritcs of offset jets, most of these studies (Agelinchaab & Tachie, 2011b; Bhuiyan *et al*., 2011) utilized measuring techniques such as Prandtl tube, Pitot tube and planar PIV that did not allow simultaneous measurement of all three velocity components. As a result, only a subset of the Reynolds stress tensor was reported (Nyantekyi-Kwakye *et al*., 2015b; Agelinchaab & Tachie, 2011b), or not reported at all (Bhuiyan *et al*., 2011). More often than not, the turbulent kinetic energy was approximated based on the one or two Reynolds normal stresses that were directly measured (Agelinchaab & Tachie, 2011b). Given the highly anisotropic nature of 3D offset jets, there is a need for direct measurements of all the Reynolds stresses and turbulent kinetic energy to adequately characterize the turbulence field, and provide a deeper insight into turbulent transport phenomena in these relatively complex shear flows. Measurements of all the three components of the mean velocity and complete Reynolds stress tensor are also essential for providing complete datasets needed to realistically assess the predictive capability of turbulence models and to provide a guide to calibrating some of the constants used in turbulence models. Also, a systematic investigation of the effect of offset height ratio and nozzle expansion ratio (defined here as the ratio of the nozzle width to channel width) on the characteristics of submerged 3D offset is yet to be undertaken. Based on the above-mentioned gaps in the literature, the goal of the present study

was to provide complete sets of refined velocity measurements to better understand the effect of offset height and nozzle expansion ratios on the mixing and turbulence characteristics of submerged 3D offset jets. The velocity measurements were performed using an acoustic Doppler velocimeter (ADV) which allowed simultaneous measurements of all the three components of mean velocities and six Reynolds stresses.

8.3 Experimental setup and measurement procedure

The experiments were conducted in a recirculating water channel with dimensions 1500 mm wide (B), 950 mm deep and 7000 mm long as shown in Fig. 8.2. The flow was driven by a fixed speed 65 hp centrifugal pump from a reservoir to a constant head tank, and then travelled through 350 mm diameter PVC pipelines. The water flow from the reservoir into the head box of the channel was regulated by a control valve and the discharge was measured using an ultra-sonic flow meter. The discharge was monitored to ensure that it remained constant during the experiments. The water was discharged through a sharp-edged rectangular nozzle with dimensions 60 mm high (b_o) and 360 mm wide (b), made from stainless steel plates of thickness 25.4 mm. The exit bulk velocity (U_o), measured from the flow discharge was 0.88 ms^{-1} yielding a Reynolds number of 5.3×10^4. The tailwater depth was controlled by a vertical louver tailgate located downstream of the channel and was maintained constant at 750 mm throughout the experiments. In order to achieve the first objective, the nozzle was set to offset heights, h, of 0, 120, 240 and 360 mm from the bottom of the channel yielding an offset height ratio, $h/b_o = 0$ (hereafter referred to as wall jet), 2, 4 and 6, respectively. It should be remarked that given the proximity of the $h/b_o = 6$ offset jet to the bottom of the channel and free surface, the discharged jet at this test condition may have tendencies of a free jet. The present experimental setup for the h/b_o investigation is geometrically similar to the scaled down model used by Nyantekyi-Kwakye *et al*. (2015a, b) to

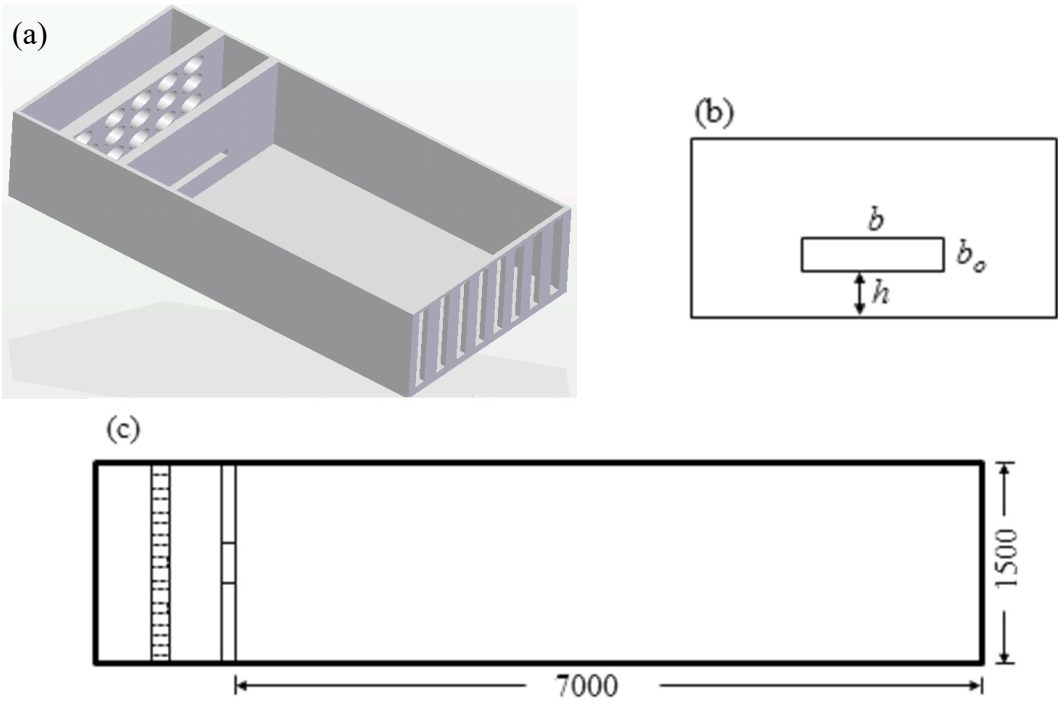

Figure 8.2 Sketch of (a) experimental test section, (b) nozzle plate and (c) plan view of the test section (all dimensions in millimeters, sketch not to scale)

investigate the flow field of 3D offset jets. Similar to the scaled down model, there was a formation of a backflow region within the outer layer of the discharged jet. The second objective was achieved by fixing the h/b_o at 4, maintaining the nozzle height as 60 mm and varying the width of the nozzle, b. The different values of b used were 360 mm, 735 mm, 1125 mm and 1500 mm yielding an expansion ratio ($ER = b/B$) of 0.24, 0.49, 0.75 and 1.00 (hereafter referred to as plane jet), respectively. In order to conduct measurements at the same exit Reynolds number, the exit bulk velocity was maintained constant (0.88 ms^{-1}) for the different ER experiments.

A downward facing Nortek Vectrino II was used to measure all three instantaneous velocities downstream of the nozzle within the symmetry and lateral planes. Measurements in the lateral plane (with the exception of ER = 1.00 where no measurements were made in the lateral

plane) were performed at y_m for half of the channel, since initial measurements on both sides of the symmetry plane had shown the flow to be symmetric. The Nortek Vectrino II, like any other ADV, operates on the Doppler shift principle. The instrument consists of a transducer, four sound receivers and a signal conditioning electronic module. The sampling volume of the Nortek Vectrino II is centered at a distance of 50 mm from the probe. The sampling volume is cylindrical with a diameter of 6 mm and a user selectable length between 3 – 30 mm. In the present investigation the sampling volume was divided into 21 cells of 1 mm length. Seeding particles (10 μm diameter neutrally buoyant spherical hollow glass spheres with specific gravity of 1.07 and settling velocity of 2.45×10^{-6} ms^{-1}) were placed within the flow to ensure that an acceptable signal to noise ratio was achieved. The estimated settling velocity indicates that the seeding particles followed the flow faithfully. In order to obtain converged time-averaged velocities, the data was acquired at a sampling rate of 100 Hz for 5 minutes. Since the center of the sampling volume was located 50 mm below the Nortek Vectrino II, the acquired data was largely free from the disturbance induced by the probe. Close to the bottom of the channel, the measured velocities can be contaminated with spikes, which could possibly be due to the interference between incident and reflected pulses. These spikes are as a result of aliasing of the Doppler signal due to the phase shift between the incident and reflected pulses outside the range of ±180°. These spikes were filtered by the spike removal algorithm proposed by Islam & Zhu (2013). Knowledge of the orientation of the bi-static axes for all four receivers allowed calculation of the 3D water velocity. The bi-static velocities were converted to Cartesian coordinate velocities using a 3 × 3 transformational matrix which is defined by the probe geometry. The Nortek Vectrino II can measure velocities in the range ± 0.01 – 4 ms^{-1} with accuracy of ± 0.5% of the measurement range. Velocity measurements were conducted in a streamwise range of $4 \leq x/b_o \leq 45$. Due to constraints in the experimental

setup, measurements could not be made within the region $0 \leq x/b_o < 4$. Detailed uncertainty analysis was conducted using the moving bootstrap technique reported by Garcia *et al*. (2006). The uncertainty in both the streamwise and wall-normal mean velocities (U and V) was ±3%, lateral mean velocity was 5% and Reynolds stresses as well as turbulent kinetic energy was ±15%.

8.4 Results and discussion

8.4.1 Offset height ratio

8.4.1.1 Reattachment length, streamwise velocity decay and jet spread

The mean reattachment length, L_e, which is an important characteristic of offset jets, was estimated from the distribution of U. It was estimated as the distance from the nozzle exit to the location where there were no negative values of U in the inner shear layer. The discharged offset jet reattached to the bottom of the channel beyond $x/b_o > 4$ and 6 for the $h/b_o = 2$ and 4 offset jets, respectively. It is to be remarked that the previous investigation by Agelinchaab & Tachie (2011b) reported that the mean L_e was independent of Reynolds number beyond 5000. Since L_e is independent of Re, the present values can be compared to $4.4b_o$ and $6.2b_o$ for offset jets with $h/b_o = 2$ and 4, respectively, from the scaled down model by Nyantekyi-Kwakye *et al*. (2015b) which was conducted at $\mathrm{Re} = 5.3 \times 10^4$. For the $h/b_o = 6$ offset jet, the upper edge of the jet was located $5.5b_o$ from the surface of the tailwater, which was close to the offset distance $6b_o$ from the bottom of the channel. Unlike the smaller h/b_o configurations, the effect of wall confinement on the $h/b_o = 6$ offset jet was negligible in the near-field regions making the jet behave like a turbulent free jet.

Some of the salient features of the offset jet and its mixing characteristics can be investigated using the evolution of the local maximum streamwise mean velocity, U_m, wall-normal and lateral half-widths with streamwise distance. Due to entrainment of ambient fluid by the jet, U_m decays with x/b_o as shown in Fig. 8.3a. The rate of U_m decay was estimated from a power law fit described by $U_m/U_o = C(x/b_o)^{-n}$ (where, C and n are a coefficient and the decay rate, respectively). Decay rates for the different h/b_o offset jets were estimated in the region $x/b_o \geq 14$ and the values shown in Table 8.1. A more pronounced decay of U_m occurred for the offset jets compared to the wall jet due to rapid mixing and enhanced entrainment of the ambient fluid except in the case of $h/b_o = 2$ offset jet. The estimated decay rate values are less than those reported by other investigators. For example, Agelinchaab & Tachie (2011b) reported a decay rate of 1.17 ±0.03 for 3D offset jets with h/b_o ranging from 0 – 3.5 issuing from a long pipe. The difference in decay rate values can be attributed to lateral confinement (which restricted lateral entrainment by the jet) in the present investigation.

As the 3D offset jet entrains ambient fluid, it spreads in both the wall-normal and lateral directions. The spread of the jet is characterized by the wall-normal and lateral half widths. Normalized values of wall-normal half-width are shown in Fig. 8.3b for the different test conditions. In order to collapse the data obtained for the different offset jets and also develop a single correlation, the offset height was subtracted from the $y_{0.5}$ values. The wall-normal spread rate was estimated as the gradient, $\mathrm{d}(y_{0.5}–h)/\mathrm{d}x$, of the linear fit to the experimental data in Fig. 8.3b within the region $4 \leq x/b_o \leq 35$. An estimated spread rate of 0.085 was obtained for the jets.

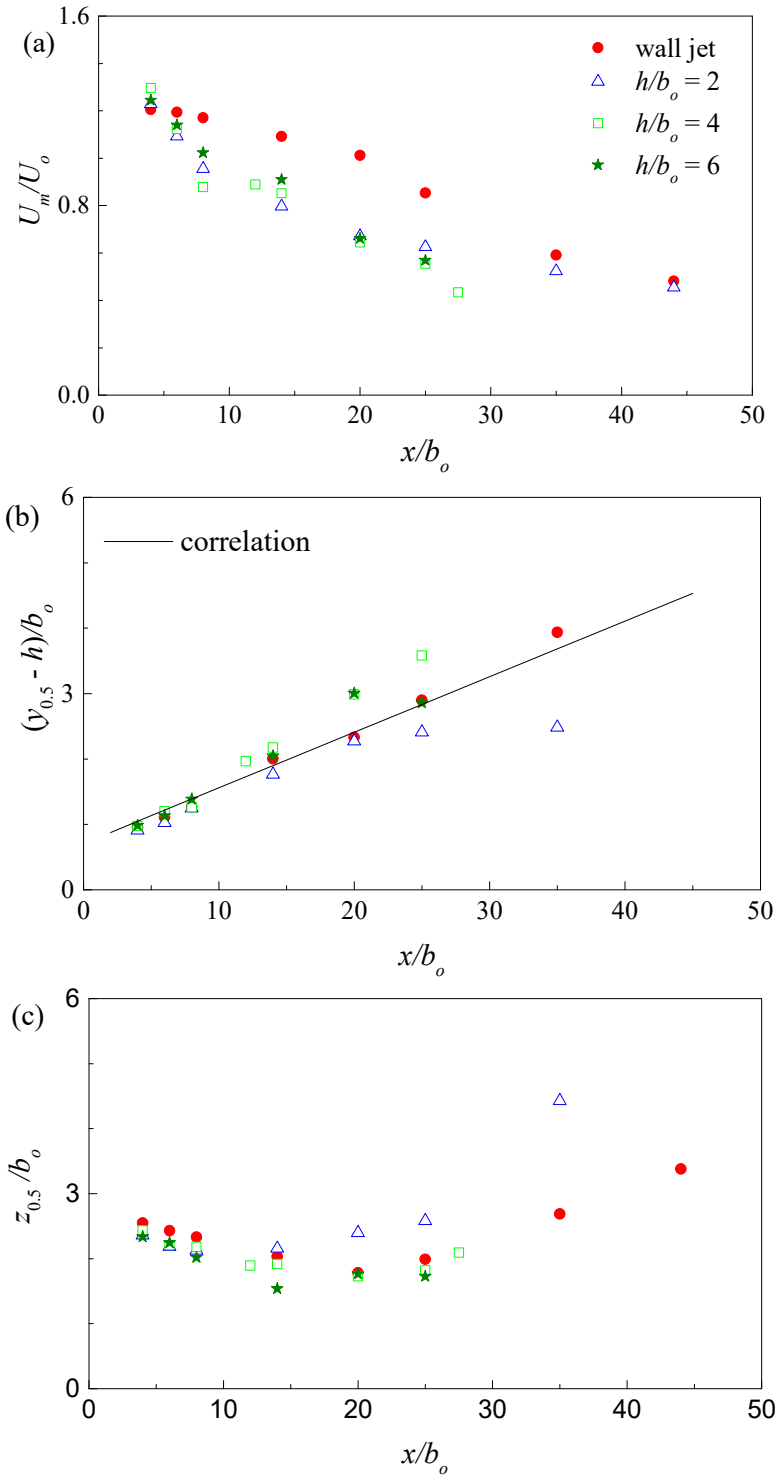

Figure 8.3 Variation of (a) local maximum streamwise mean velocity decay, (b) wall-normal half-width and (c) lateral half-width, for the different offset height ratios

The solid line represents the correlation obtained from the combined dataset. Whereas $y_{0.5}$ values of the wall jet followed the correlation line, those of the offset jet deviated from the line at x/b_o = 20 and 14 for h/b_o = 2 and h/b_o = 4 and 6 offset jets, respectively. Beyond x/b_o = 20 the h/b_o = 2 offset jet spread at a rate of 0.013 while the h/b_o = 4 and 6 offset jets spread at a rate of 0.126 and 0.077, respectively beyond x/b_o = 14. The lower spread rate for the h/b_o = 2 offset jet is reflective of the slower decay rate compared to the other offset jets. The present spread rate value is greater than 0.065 and 0.055 ±0.001 reported by Abrahamsson *et al*. (1997) for a 3D round wall jet and Agelinchaab & Tachie (2011b) for 3D offset jets, respectively. This disparity can be connected to entrainment of negative momentum fluid as a result of the backflow region caused by the limited tailwater depth in the present investigation.

The lateral jet half-width for the different offset jets is illustrated in Fig. 8.3c. Values of $z_{0.5}$ decreased with streamwise distance until x/b_o = 14, beyond which it began to increase. The initial decrease can be attributed to the combined effects of the vena-contracta and deformation of elliptic vortical structures (Lee & Baek, 1994). A common phenomenon that occurs in aspect ratio (*AR*) nozzles is axis switching which is caused by the difference in induced velocities caused by the different segments of azimuthal vortical structures as well as streamwise vortex pairs. As a result, the orientation of the jet cross-section switches at some downstream distance from the nozzle exit. The azimuthal deformation of these structures leads to a much greater initial spread of the jet in the minor axis than the major axis, hence the observed initial decrease in $z_{0.5}$ values. For h/b_o = 0, 2, 4 and 6 offset jets, the axis switching occurred at x/b_o = 14, 20, 12 and 12, respectively. These locations were farther downstream than the normalized streamwise location of 5 reported by Quinn (1992) for a free jet issuing from a rectangular nozzle with an *AR* of 5. The presence of the channel bottom in the present investigation could have influenced the flow dynamics of the jet.

8.4.1.2 Streamwise mean velocity distribution in the symmetry and lateral planes

Profiles of the streamwise mean velocity at different streamwise locations (x/b_o = 4, 6, 14, 20 and 25) within the symmetry plane are presented in Fig. 8.4. The velocity scale used for normalization was U_m. For the length scale, y^* ($y^* = y/y_{0.5}$) and y^{**} (also referred to as the mixed scaling, $y^{**} = (y–y_m)/(y_{0.5}–y_m)$) were used for the wall and offset jets, respectively. The mixed scaling was used for the offset jets since y^* failed to effectively collapse profiles of U for the x/b_o range considered. The dashed line represents an empirical correlation proposed by Verhoff (1963) for a similarity profile of a plane wall jet. The plots for the jets were staggered with the dotted lines in Fig. 8.4 representing the starting point of the superseding plot. It is clear that the mean velocity exhibited similarity using the conventional and mixed scaling for the wall and offset jets, respectively. Due to the formation of a backflow region, the data for the 3D wall jet deviated from the empirical correlation proposed by Verhoff (1963) within the outer shear layer. The mean velocity profiles of the 3D wall jet became self-similar at $x/b_o \geq 14$, which is close to 20 reported by Abrahamsson *et al*. (1997). Using the conventional scaling for the offset jets revealed that the jets required a longer x/b_o extent (than what was presently considered) in order to attain self-similarity. However, using the mixed scaling for the offset jets collapsed profiles of U beyond $x/b_o \geq 6$ within both the inner and outer shear layers similar to reports by Agelinchaab & Tachie (2011b).

Profiles of U, V and W within the lateral plane are illustrated in Fig. 8.5. The velocity and length scales employed were U_m and $z_{0.5}$, respectively. The profiles of U collapsed for the different h/b_o configurations, suggesting that the profiles of U are independent of h/b_o in the lateral plane. However, profiles of both V and W within the lateral plane did not collapse for the different h/b_o configurations. The profiles of W provide an indication of inward entrainment of ambient fluid

Table 8.1 Estimates of the decay and spread rates for the various experiments

Rates	Offset height ratio, h/b_o				Expansion ratio, ER			
	0	2	4	6	0.24	0.49	0.75	1.00
n	0.756	0.480	0.914	0.816	0.914	0.371	0.379	0.358
$dy_{0.5}/dx$	---	---	---	---	0.126	---	0.030	0.046
$dz_{0.5}/dx$	---	---	---	---	---	0.201	0.152	---

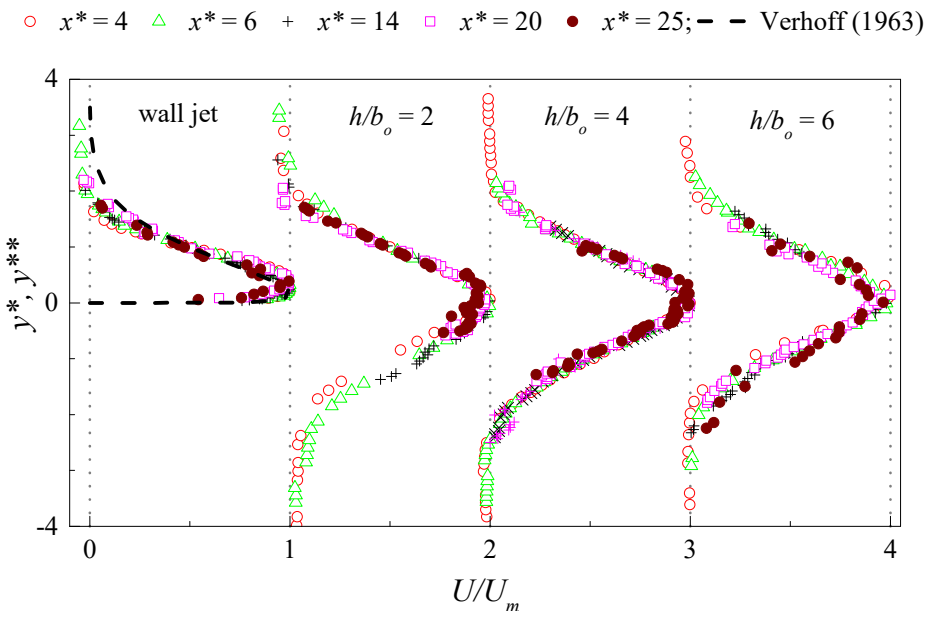

Figure 8.4 Streamwise mean velocity distributions at selected locations the offset jets (where $y^* = y/y_{0.5}$ and $y^{**} = (y–y_m)/(y_{0.5}–y_m)$)

into the core region of the jet. This also signifies high levels of near field mixing of the discharged jet. The present distribution of the secondary mean velocities suggests that their gradients would contribute to the generation of vortices within the flow field.

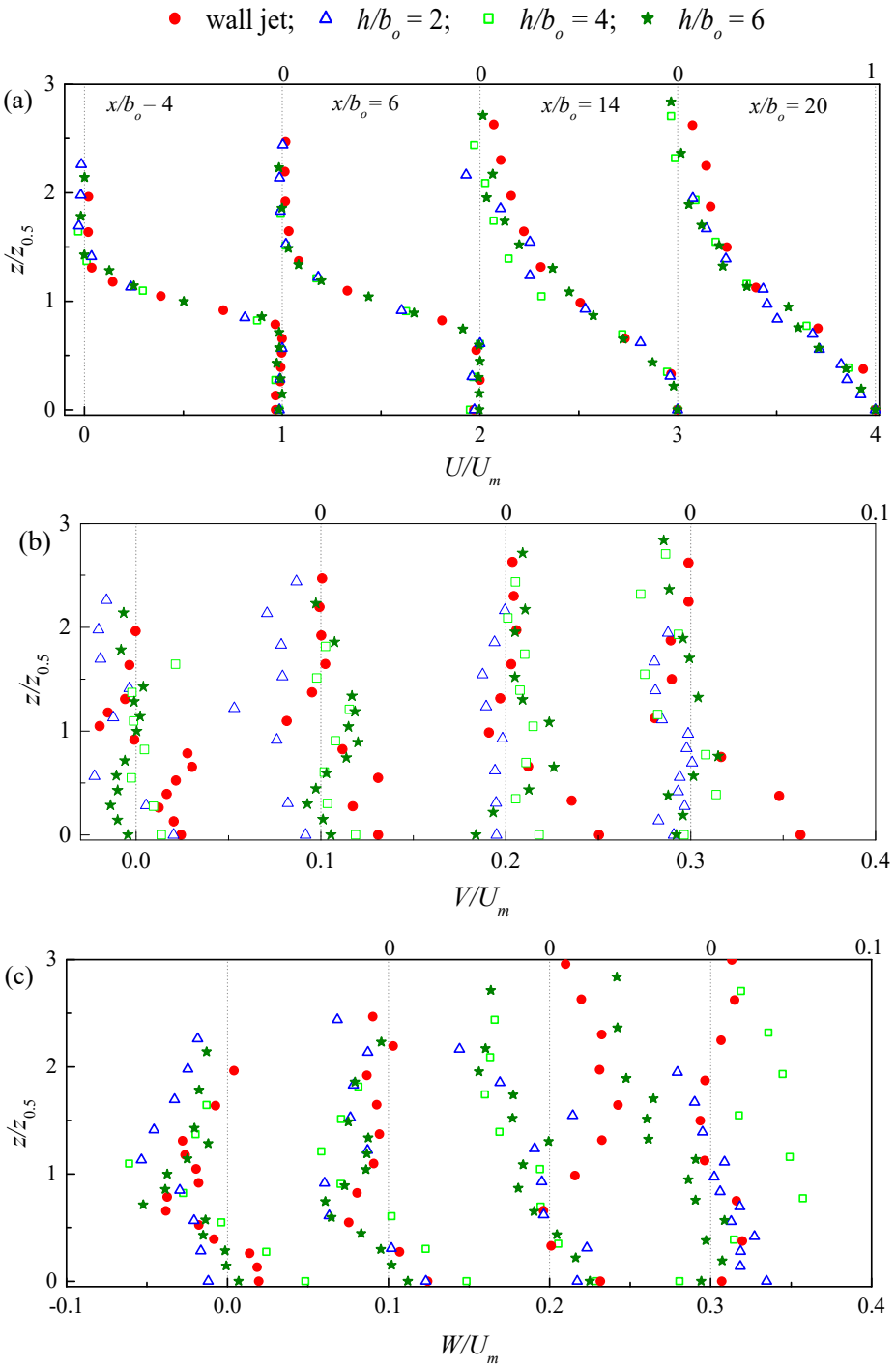

Figure 8.5 Profiles of (a) streamwise, (b) wall-normal and (c) lateral mean velocities in the lateral plane

8.4.1.3 Reynolds stresses

The distribution of the Reynolds normal stresses ($\overline{u^2}$, $\overline{v^2}$, $\overline{w^2}$) and structure parameter within the symmetry plane are shown in Fig. 8.6 at x/b_o = 6 and 25. The presence of the channel bottom in the case of the wall jet suppressed the formation of double peaks for the normal stresses. However, there existed double peaks close to the nozzle exit for h/b_o = 2, 4 and 6 offset jets. The presence of the double peak is an indication of high turbulence production at the edges of the jet where there exist high mean velocity gradients. Due to mixing and spreading of the jet, the double peaks disappeared farther downstream. The present distribution of the normal stresses depicts the highly anisotropic nature (since $\overline{u^2} \neq \overline{w^2} \neq \overline{v^2}$) of the offset jets with the level of anisotropy increasing with increasing h/b_o. The level of large-scale anisotropy would be discussed in detail in the next section in relation to the nozzle expansion ratio. The present results for the normal stresses highlight the drawback of modeling the flow characteristics of 3D offset jets with isotropic turbulence models. Since $\overline{w^2}$ was directly determined in the present investigation, the measured data was compared to the commonly used approximation of $\overline{w^2} = 0.5(\overline{u^2} + \overline{v^2})$. The approximated values of $\overline{w^2}$ are indicated as the solid and dashed lines for x/b_o = 6 and 25, respectively in Fig. 8.6c. For the various jets, the approximation accurately follows the measured data at x/b_o = 6. At x/b_o = 25, the approximation yielded lager values when h/b_o was increased to 4 and 6. The present results suggest that this approximation breaks down in the early development regions of offset jets with large h/b_o and as such a smaller coefficient (other than 0.5) should be used in this region.

Figure 8.6d shows the distribution of the structure parameter which is an important parameter for calibrating turbulence models. In particular, the structure parameter provides a

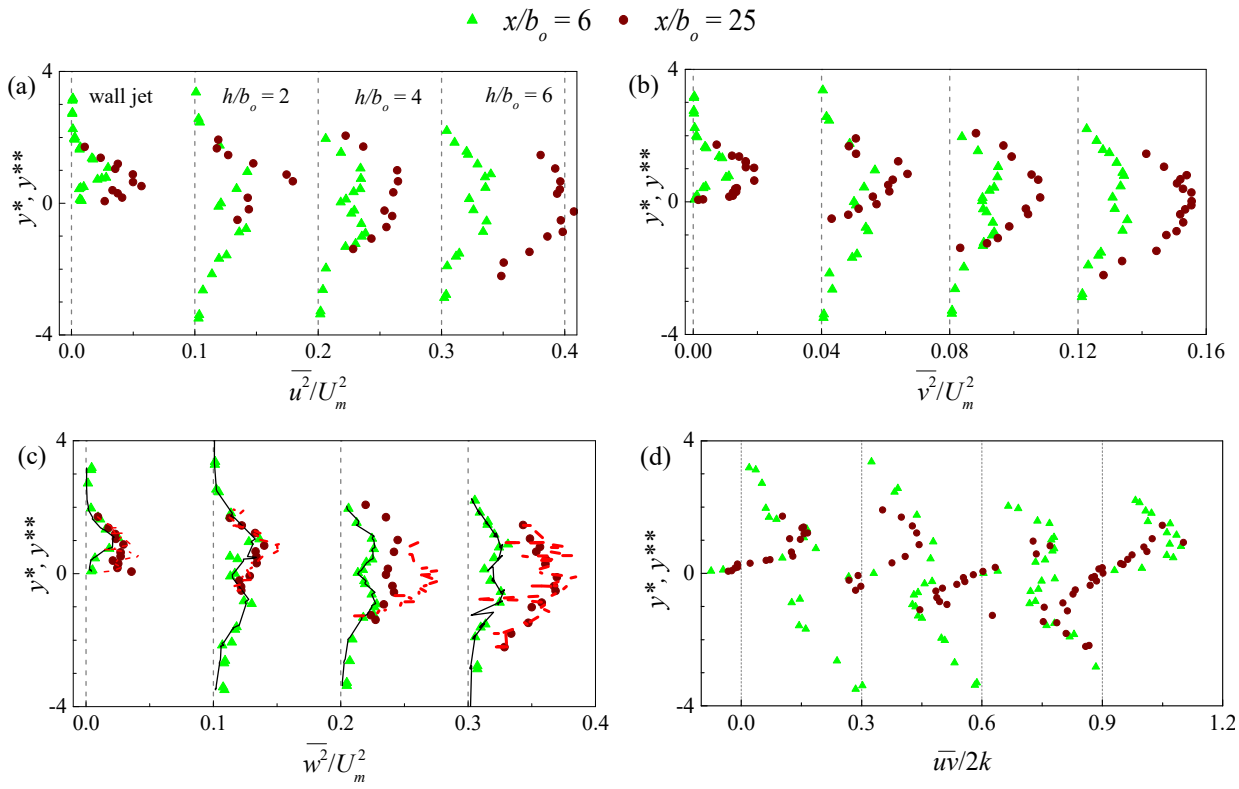

Figure 8.6 Profiles of Reynolds normal stresses and structure parameter; solid and dashed lines represent approximation of $\overline{w^2}$ at x/b_o = 6 and 25, respectively

guide for estimating the modelling coefficient C_μ (where $C_\mu = (-\overline{uv}/k)^2$). This coefficient is used in computing the turbulent eddy viscosity. Based on the assumption of local equilibrium (where production = dissipation rate) and experimental data obtained in the overlap region of boundary layer flows, a structure parameter value of 0.15 is often used which corresponds to C_μ = 0.09. The present results indicate that the peak values of the structure parameter ranged from 0.14 – 0.2 for the 3D offset jets. Predominantly larger values of the structure parameter were attained for the offset jets compared to the wall jet. Figure 6d also shows that it is inappropriate to use a constant value for the structure parameter across the jet since there was no constant Reynolds shear stress region. This observation suggests that standard eddy viscosity models cannot be used to accurately reproduce the flow characteristics of the 3D offset jet.

8.4.2 Nozzle expansion ratio

8.4.2.1 Mean flow properties

Normalized profiles of the streamwise and lateral mean velocities in the symmetry and lateral planes, respectively are presented in Fig. 8.7. The mixed scaling was adopted for distances in the symmetry plane since the conventional scaling did not yield an appropriate collapse of the profiles of U in both the inner and outer shear layers at larger ER. Figure 8.7a shows that a recirculation region was formed between the discharged jet and the bottom of the channel. Increasing the expansion ratio, ER, intensified the negative streamwise mean velocities within the recirculation region. For example changing ER from 0.24 to 0.75 and 1.00 resulted in an increase in negative velocities within the recirculation region by 64% and 80%, respectively. The mixed scaling collapsed profiles of U in both the inner and outer shear layer of the jet for $ER = 0.24$. Due to the dramatic deflection and reattachment of the jets with larger ER, the mixed scaling approach could not completely collapse U profiles in the inner shear layer. Normalized profiles of W in the lateral plane are illustrated in Fig. 8.7b. A negative value of W implies entrainment of ambient fluid into the core region of the jet, with positive values representing outward movement of the jet. Increasing the nozzle ER resulted in predominantly positive values of W, which represents enhanced outward movement of the jet in the lateral plane as a result of the severe curvature and subsequent impingement of the jet towards the channel bottom. Due to the significant levels of the secondary mean velocities (V, not shown, and W), their gradients coupled with large-scale anisotropy of the jets would contribute to the generation of vortices within the flow.

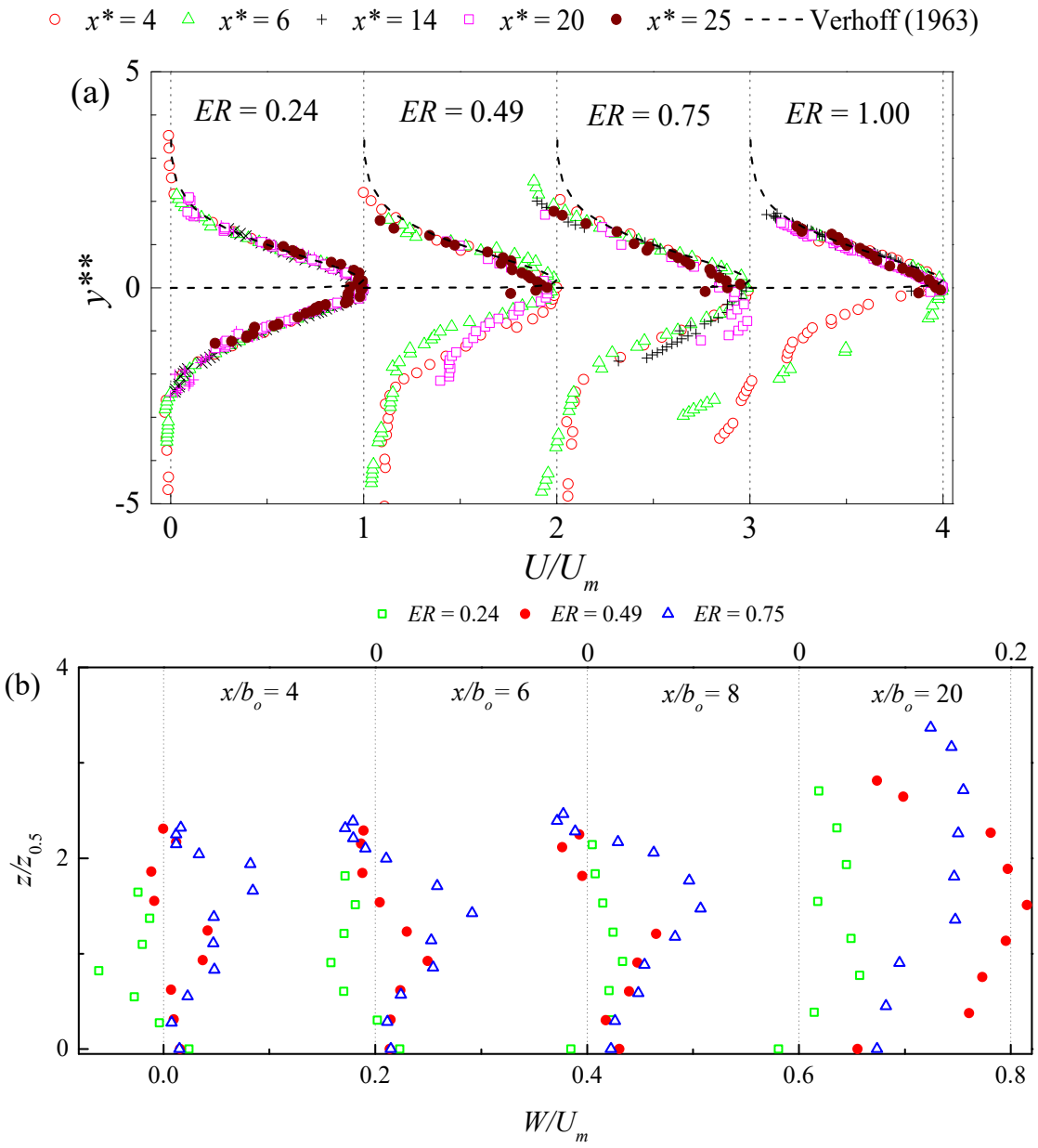

Figure 8.7 Streamwise and (b) lateral mean velocity distributions for the various nozzle expansion ratios (where $x^* = x/b_o$)

8.4.2.2 Flow development

Figure 8.8a shows the decay of U_m. The profiles reveal a higher initial decay of U_m for the larger *ER* nozzles due to a higher entrainment surface compared to *ER* = 0.24. The higher

entrainment level close to the nozzle exit is due to the non-uniform curvature of the azimuthal vortical structures generated. Farther downstream, increasing *ER* decreased entrainment of ambient fluid thereby reducing mixing characteristics of the jet. This means that there was larger near-field mixing for *ER* = 0.49–1.00 nozzles compared to *ER* = 0.24 nozzle. A power law was fitted to the experimental data in order to estimate the decay rates beyond the region $x/b_o \geq 14$. Decay rate values for the different nozzle configurations are shown in Table 8.1. Increasing *ER* resulted in a decrease in the estimated decay rates. This observation however, is in contrast to studies by Quinn (1992) who reported increased decay rates for free jets issuing from larger *AR* nozzles. The contrasting results can be attributed to the dynamic role played by the presence of the channel bottom and side walls on the discharged jet which were absent in the study of Quinn (1992). Increasing *ER* limits the level of entrainment in the lateral plane due to the presence of the side walls. This was evident in the slower decay of the *ER* = 1.00 configuration. From these observations, it is worth highlighting the fact that mixing is enhanced in 3D offset jets compared to plane offset jets.

The development of the inner shear layer is illustrated in Fig. 8.8*b* for the different *ER*. The extent of y_m for *ER* = 0.24 remained fairly constant with the x/b_o considered. However, changing *ER* to 0.49–1.00 caused a drastic decrease of y_m within $x/b_o < 20$ for both *ER* = 0.49 and 0.75 and $x/b_o < 12$ for *ER* = 1. Beyond these limits, the inner shear layer development for the larger *ER* nozzles was similar. It can be seen from Figure 8.8b that the inner shear layer for the larger *ER* nozzles grew at a rate of 0.017 (indicated by the dashed line). The drastic decrease in y_m for the larger *ER* nozzles is attributed to the severe deflection of the jet towards the bottom of the channel when *ER* was increased. Increasing *ER* reduced the jet momentum thereby resulting in severe deflection towards the bottom of the channel (Nozaki, 1986).

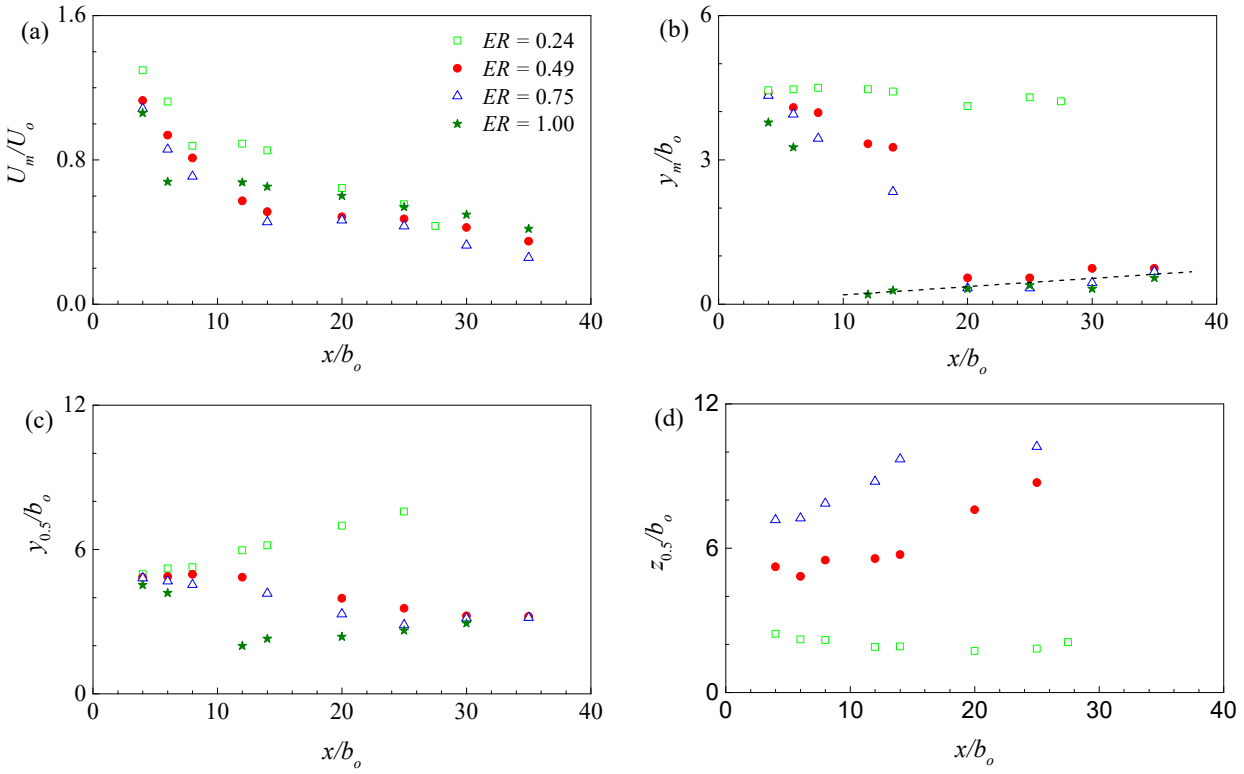

Figure 8.8 Variation of (a) U_m decay, (b) y_m (c) $y_{0.5}$ and (d) $z_{0.5}$; dashed line represents the correlation for y_m development beyond $x/b_o = 10$

The spread of the offset jets within the symmetry and lateral planes is shown in Figs. 8.8c and 8.8d, respectively. Values of $y_{0.5}$ increased monotonically with streamwise distance for the *ER* = 0.24 configuration. Increasing the *ER* resulted in a decrease in estimated values of $y_{0.5}$. The observed decrease in $y_{0.5}$ for the larger *ER* configurations can be linked to the severe curvature of the jet towards the bottom of the channel as explained in the development of the inner shear layer. With the plane offset jet, values of $y_{0.5}$ increased beyond $x/b_o > 12$ which coincides with the region where the deflected inner shear layer begins to grow with x/b_o. Normalized values of $z_{0.5}$ initially decreased close to the nozzle exit and then increased with x/b_o as depicted in Fig. 8.8d. The streamwise extent of the initial reduction in $z_{0.5}$ decreased with increasing *ER*. The dynamics of

the secondary mean motions is expected to have played a vital role in this distribution. The present distribution of $y_{0.5}$ and $z_{0.5}$ can be related to the secondary mean motions as well as the formation of vortical structures in the near field region of the jet. In a free jet study, Abramovich (1982) attributed the initial decrease in $z_{0.5}$ to non-uniform pressure field associated with rectangular vortex rings generated within the shear layer of the jet. From the observations of Abramovich (1982), it can be inferred that these vortical structures were suppressed by the side walls of the channel as *ER* increased and this reduced the streamwise extent of the initial decrease in $z_{0.5}$.

The wall-normal and lateral spread rates were estimated as the gradient ($dy_{0.5}/dx$ and $dz_{0.5}/dx$) of the linear fit to the experimental data for the half-widths. The wall-normal spread rate was estimated beyond $x/b_o \geq 12$ for $ER = 0.24$ and 1.00, and $x/b_o \geq 25$ for $ER = 0.75$. Wall-normal spread rate values of 0.126, 0.030 and 0.046 were obtained for offset jets with $ER = 0.24$, 0.75 and 1.00, respectively, as shown in Table 8.1. The lower wall-normal spread rates for the larger *ER* nozzles compared to $ER = 0.24$ can be attributed to the slower decay rate of the former compared to the latter nozzle configuration. The present wall-normal spread rates for the plane offset jet are smaller than 0.076 reported by Yoon *et al*. (1993) for a plane offset jet with $h/b_o = 4.5$. Due to the non-linear distribution of $z_{0.5}$ in the near-field region of the flow, the lateral spread rate could only be estimated for the $ER = 0.49$ and 0.75 configurations beyond $x/b_o \geq 8$ and shown in Table 8.1. The lateral spread rate of the turbulent offset jet decreased with increasing *ER* due to restrictions by the side walls as the nozzle width increased.

8.4.2.3 Reynolds stresses

Figure 8.9 shows the distribution of the Reynolds stresses at selected x/b_o locations. Close to the nozzle exit the Reynolds normal stresses exhibited distinct double peaks for $ER = 0.24$ which

disappeared with streamwise distance due to the spreading of the jet as well as merging of the shear layers. The distinct double peak diminished when *ER* was increased, an occurrence that is associated with the effective near-field mixing of the jet. The enhanced mixing of the discharged jets for the larger *ER* nozzle can be associated to their shorter potential core lengths compared to nozzles with smaller *ER* (Quinn, 1992). Due to the severe curvature of the discharged offset jet when *ER* was increased to 1.00, high levels of Reynolds normal stresses were produced within the outer shear layer (which falls on the convex side of the curved jet). It is to be emphasized that the curvature of the offset jet has an effect on the turbulence field on both the concave and convex sides of the jet. Pelfrey & Liburdy (1986) reported that curvature has a stabilizing influence on the turbulence field on the concave side and a destabilizing influence on the convex side of a plane offset jet. The destabilizing effect on the convex side of the jet enhances the downstream Reynolds normal stress which is what was observed in the present study when *ER* was increased to 1.00. The high stresses are diffused from the shear layers into the core region of the offset jets with streamwise distance.

Figure 8.9d shows the distribution of Reynolds shear stress for the different *ER* nozzles. The distribution of $\overline{uv}$ was greatly influenced by increasing *ER*. Larger values of $\overline{uv}$ were obtained when the *ER* was increased. This can be explained by the high production of Reynolds shear stress due to the dominant contribution of the mean velocity gradient (Quinn, 1992). The interplay of the inner and outer shear layers modifies the dynamics of the jet. One such feature is the shift in the wall-normal location where $\overline{uv}$ is equal to zero (denoted herein as y_{uv}) from the location y_m. The high turbulent outer shear layer interacts with the inner shear layer thereby displacing y_{uv} towards the bottom of the channel (Abrahamsson *et al*., 1994). Increasing *ER* from 0.24 to 0.49, 0.75 and

1.00 caused a significant displacement of y_{uv} towards the bottom of the channel. This was due to the severe curvature of the offset jet, which resulted in high turbulence levels in the outer shear layer when *ER* was increased. This has been discussed in previous sections.

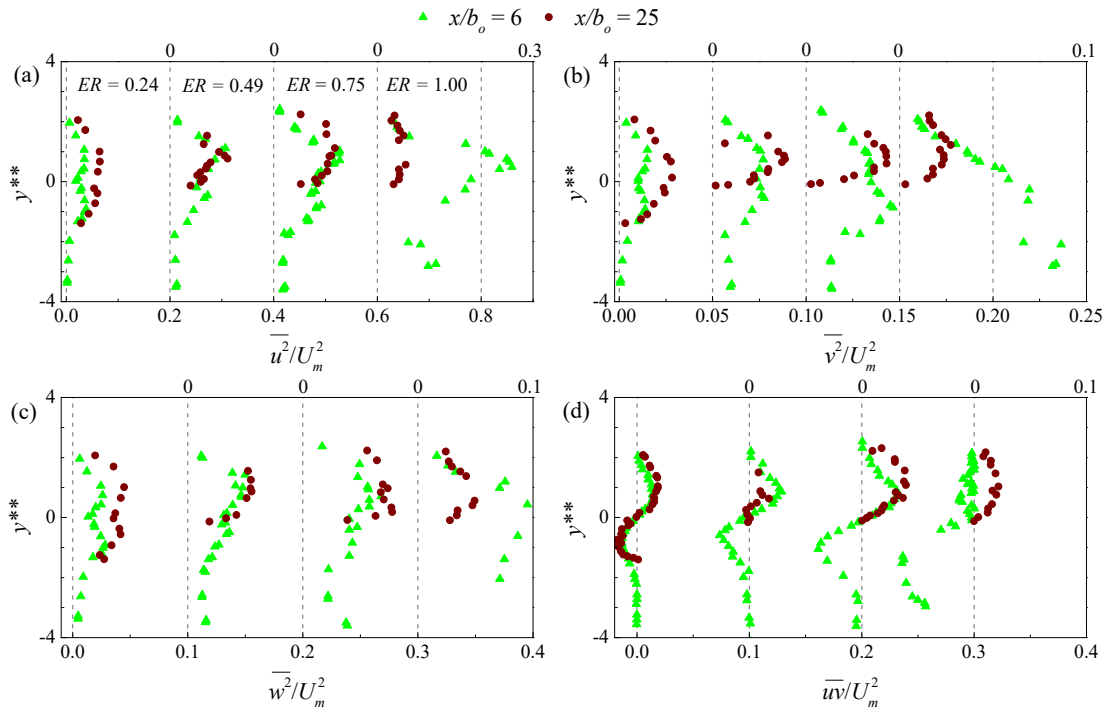

Figure 8.9 Profiles of Reynolds stresses

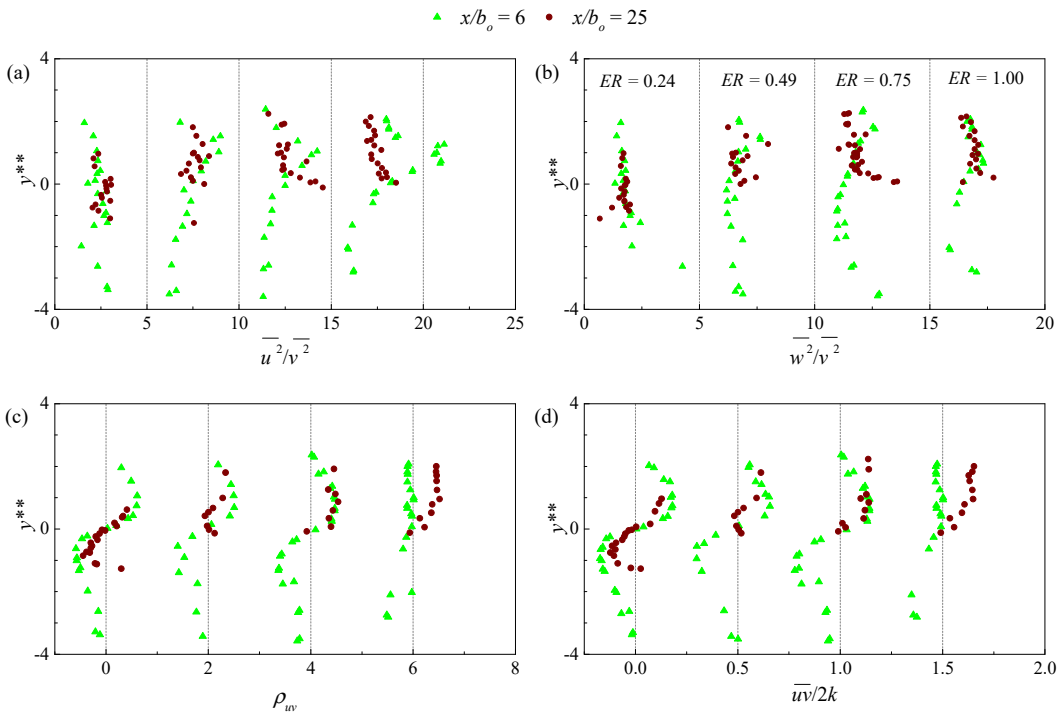

Figure 8.10 Profiles of (a) – (b) Reynolds stress ratios, (c) correlation coefficient and (d) structure parameter

The ratios of the Reynolds stresses were used to provide a guide to large-scale anisotropy in turbulence flows. Figure 8.10 shows the effect of *ER* on large-scale anisotropy, correlation coefficient and the structure parameter at x/b_o = 6 and 25. At lower *ER*, the levels of $\overline{u^2}$ and $\overline{w^2}$ were about twice $\overline{v^2}$ within the core region of the jet. Close to the nozzle exit, the effect of jet curvature enhanced the level of anisotropy in the outer shear layer when *ER* was increased to 1.00. After reattachment of the jet, greater anisotropy occurred close to the bottom channel where $\overline{v^2}$ was greatly damped by the presence of the wall compared to $\overline{u^2}$ and $\overline{w^2}$. The distribution of the correlation coefficient shows a dependence on *ER* in both near and far field. For *ER* = 0.24, 0.49 and 0.75, *u* and *v* were negatively and positively correlated within the inner and outer shear layers, respectively. Figure 8.10c indicate that for *ER* = 1.00, both *u* and *v* are negatively and positively correlated at x/b_o = 6 and 25, respectively. Similar to earlier discussion, Fig. 8.10d shows that the

structure parameter for the different *ER* nozzles varies considerably within the inner and outer shear layers close to the nozzle exit. Farther downstream, the structure parameter attained a more uniform value of 0.15 when *ER* was increased to 1.00. The considerable variation of the structure parameter for the smaller *ER* nozzles is a clear indication that the local equilibrium condition does not apply to the present flow.

8.5 Conclusion

The flow characteristics of turbulent jets issuing from four different offset height ratios (h/b_o = 0, 2, 4 and 6) and expansion ratios (*ER* = 0.24, 0.49, 0.75 and 1.00 at a fixed h/b_o = 4) were experimentally studied using an ADV. The jet was discharged from a sharp-edged rectangular nozzle at an exit Reynolds number of 5.3×10^4. The mean velocity distribution for the different offset jets revealed that the influence of the wall on the discharged jet was minimized when the offset height ratio increased further away from the bottom of the channel. As a result of enhanced entrainment of the ambient fluid with increasing h/b_o, the decay of the local maximum streamwise mean velocity increased with h/b_o with estimated decay rates of 0.756, 0.480, 0.914 and 0.816 for h/b_o = 0, 2, 4 and 6, respectively. The present distribution of the Reynolds stresses signifies their contribution towards the generation of streamwise vortices responsible for entrainment and spreading of the jet. The distribution of $\overline{w^2}$ suggests that the widely used approximation $\overline{w^2} = 0.5(\overline{u^2} + \overline{v^2})$ in boundary layers breaks down in the far field of the jet when h/b_o increases. The present results for the offset jets also reveal that it is inappropriate to use a constant value for the structure parameter when calibrating turbulence models.

For the expansion ratio investigation, due to greater near field mixing and entrainment of ambient fluid as *ER* increases, the discharged jet dramatically deflected towards the bottom of the channel.

The presence of the side walls inhibited entrainment of ambient fluid in the lateral direction thereby resulting in a slower decay of the offset jet when *ER* was increased. Upon reattachment, the inner shear layer of the *ER* = 0.49, 0.75 and 1.00 jets develop at a similar rate. The generation of vortical structures within the flow resulted in a non-linear growth in the near-field region of the jet within the lateral plane. Also the streamwise extent of the non-linear portion of $z_{0.5}$ reduced when *ER* was increased. Due to severe curvature, larger levels of Reynolds stresses were observed in the outer shear layer compared to the inner shear layer when *ER* was increased. The present results also reveal that the offset jet is highly anisotropic with the level of anisotropy increasing with *ER*. The present results for the 3D offset jets also provide a guide for the calibration of turbulence models.

CHAPTER NINE

9 CONCLUSIONS AND RECOMMENDATIONS

9.1 Conclusions

This study focused on the effect of various parameters on 3D offset jet issuing from a sharp-edged rectangular nozzle in an open channel application. The effect of offset height ratio (h/b_o = 0, 2, 4, 6 and 8), expansion ratio (0.24, 0.49, 0.75 and 1.00), surface roughness (of height of 12.7 mm) and streamwise rib position were investigated. For the surface roughness study, the roughness was made up of 2D acrylic ribs spanning the entire width of the channel (arranged to yield p/k = 2, 4 and 8) and gravels. Velocity measurements were conducted using both acoustic Doppler velocimetry (ADV) and particle image velocimetry (PIV) techniques. In order to investigate the effect of offset height ratio, surface roughness and expansion ratio, the results were compared to the wall jet, flow over a smooth surface and plane offset jets obtained from the same facilities, respectively. Measurements were conducted in both the symmetry (x–y) and lateral (x–z) planes using the PIV and ADV techniques. The effect of the different test cases on the maximum mean velocity decay, wall-normal and lateral spread of the offset jets was investigated. The mean velocity and Reynolds stress profiles were also used to characterize the effect of the different test cases on the 3D offset jet. The features of large-scale vortical structures present in the offset jet flow were investigated. Both two-point correlation and POD techniques were applied to the PIV data to identify the size, inclination and the energy content of these large-scale vortical structures. A summary of the salient observations are provided below:

- Increasing h/b_o enhanced the mixing and entrainment of the discharged jet and the ambient fluid. This process resulted in an increase in the decay rate of the maximum mean velocity

when h/b_o was increased. For the expansion ratio configuration, increasing the expansion ratio enhanced near-field mixing and entrainment of the ambient fluid. However, the estimated decay rate decreased for the larger expansion ratios due to restriction of the discharged jet by the side walls of the channel.

- The wall-normal spread rate increased by 27% when h/b_o was increased. However, increasing the nozzle expansion ratio decreased the wall-normal spread rate by 63%, and this was a result of limited entrainment in the lateral plane due to the presence of the side walls.
- For the current flow configuration, the introduction of surface roughness did not affect the estimated decay rate for the streamwise range considered.
- The estimated mean reattachment length of the discharged jets increased with increasing h/b_o. Also at a constant h/b_o, changing the streamwise location of a surface mounted rib resulted in an increase in the mean reattachment length of the discharged 3D offset jet. Also at a fixed h/b_o, the introduction of surface roughness did not influence the mean reattachment length of the discharged 3D offset jet.
- Profiles of the streamwise mean velocity revealed that the 3D wall jet became self-similar at a shorter streamwise distance compared to the 3D offset jets. The farther streamwise extent for the 3D offset jets indicates a slower relaxation of the discharged jet after reattachment.
- Within the recirculation region, the Reynolds stresses were independent of h/b_o. Larger turbulence intensities and Reynolds shear stresses existed in the near-field region of the discharged jet due to enhanced near-field mixing of the larger expansion ratio jets. The structures generated within the recirculation and developing regions enhanced the

production of Reynolds stresses. The distribution of the Reynolds stresses within the symmetry and lateral planes suggest strong anisotropy in the turbulence field of 3D offset jets.

- Based on the present results, standard turbulence models based on the eddy viscosity concept cannot accurately predict the flow characteristics of the 3D offset jet.
- A two-point correlation analyses showed that larger structures existed within the recirculation region compared to the developing region where the flow structures were broken down as a result of the reattachment process. Within the recirculation region, the size of these structures increased with increasing h/b_o. As a result of merging of the broken down structures downstream of the nozzle exit, much larger structures dominated the self-similar region compared to both the recirculation and developing regions.
- Large-scale structures dominated the outer shear layer compared to the inner shear layer. Within the inner shear layer of the self-similar region, the inclination of these structures (12° ±0.2°) was in the range of values reported in boundary layer flows. However, the inclination of these structures within the outer shear layer was largely controlled by the direction of the mean shear gradient.
- The POD analysis revealed the dominance of energetic modes within the self-similar region compared to the developing region of the 3D offset jet flow. A two-point correlation analysis on the POD modes revealed that the energetic modes contained larger structures compared to the less energetic modes.

9.2 Contributions

The present investigation has improved our understanding of 3D offset jets and the turbulence phenomena controlling them. Some of the contributions have been listed below.

- The present study on 3D offset jet is the first conducted in an open channel flow application with the jet discharging from a sharp-edged rectangular nozzle.
- The ADV technique has been applied for the first time to investigate 3D offset jets. Information of all the Reynolds stress tensors was acquired to give a better understanding of the flow. This study also investigated the level of large-scale anisotropy since all three normal stresses were directly determined. Based on this information, a guide was provided for estimating some of the constants used in calibrating turbulence models.
- This investigation is also among the pioneering works in quantitatively studying large vortical structures in the flow regions of 3D offset jets using the spatial information obtained from the PIV technique.
- The present investigation extensively explored coherent structures using the PIV data and also reported the contributions of these structures towards the mixing and entrainment properties of the jet.
- The present investigation also provides new information of effect of expansion ratio and surface roughness on the velocity fields and entrainment process of 3D offset jets.

9.3 Recommendations for future work

Some recommendations for future work on 3D offset jets are summarized below.

- The presence of the backflow within the outer shear layer of the jet affected the flow behavior downstream. Future experiments can be designed to eliminate this effect on the discharged offset jet.
- Further experimental work is needed to determine the behavior of the large vortical structures responsible for the entrainment of ambient fluid by the jet in the off-symmetry plane. That is, different measurement planes in both the off-the-symmetry and lateral planes can be taken to analyze these flow structures.
- The ADV technique provides a measure of all three velocity components simultaneously but it is a pointwise measuring device. Hence, it is challenging to obtain spatial gradients of the velocity data which are relevant to completely explaining the physics of the flow. Future studies can be conducted using holographic PIV which can allow the opportunity of extracting 3D velocity fields to investigate the coherent structures.
- Roughness elements of heights larger than considered in the present investigation can be used to study roughness effect on the evolution of offset jets through the different flow regions.

10 REFERENCES

Abrahamsson, H., Johansson, B. and Lofdahl, L. (1997). The turbulence field of a fully developed three-dimensional wall jet. *Internal Report 97/1*, Department of Thermo and Fluid Dynamics, Chalmers University of Technology, Sweden, 1-37.

Abrahamsson, H., Johansson, B. and Lofdahl, L. (1994). A turbulent plane two-dimensional wall jet in a quiescent surrounding. *European Journal of Mechanics, B/Fluids*, 13, 533-556.

Abramovich, G. N. (1982). On the deformation of the rectangular turbulent jet cross-section. *International Journal of Heat and Mass Transfer*, 25(12), 1885-1894.

Adrian, R. J., Christensen, K. T., and Liu, Z.-C. (2000). Analysis and Interpretation of Instantaneous Turbulent Velocity Fields. *Experiments in Fluids*, 29: 275-290.

Agelinchaab, M., and Tachie, M. F. (2011a). Characteristics of turbulent three-dimensional wall jets. *Journal of Fluids Engineering*, 133, 021201-1-9.

Agelinchaab, M., and Tachie, M. F. (2011b). Characteristics of turbulent three-dimensional offset jets. *Journal of Fluids Engineering*, 133, 051203-1-9.

Agelinchaab, M., and Tachie, M. F. (2011c). Characteristics and structure of turbulent 3D offset jets. *International Journal of Heat and Fluid Flow*, 32(3), 608-620.

Agelinchaab, M., and Tachie, M. F. (2008). PIV study of separated and reattached open channel flow over surface mounted blocks. *Journal of Fluids Engineering*, 130, 061206-1 – 061206-9.

Agelinchaab, M., and Tachie, M. F. (2006). Open channel turbulent flow over hemispherical ribs. *International Journal of Heat and Fluid Flow*, 27(6), 1010-1027.

Ahlman, D., Brethouwer, G. and Johansson, A. V. (2007). Direct numerical simulation of a plane turbulent wall-jet including scalar mixing. *Physics of Fluids*, 19, 1-13.

Alfonsi, G. (2006). Coherent structures of turbulence: methods of eduction and results. *Applied Mechanics Reviews*, 59(6), 307-323.

Alfredsson, P. H., and Johansson, A. V. (1984). On the detection of turbulence-generating events. *Journal of Fluid Mechanics*, 139, 325-345.

Anthony, D. G., and Willmarth, W. W. (1992). Turbulence measurements in a round jet beneath a free surface. *Journal of Fluid Mechanics*, 243, 699-720.

Antoniou. J., and Bergeles, G. (1985). Development of the reattached flow behind surface mounted two-dimensional prisms. *Journal of Fluids Engineering*, 110, 127-133.

Ayukawa, K., and Shakouchi, T. (1976). Analysis of a jet attaching to an offset parallel plate. *Bulletin of JSME,* 19: 395-401.

Azim, M. A. (2013). On the structure of a plane turbulent wall jet. *Journal of Fluids Engineering,* 235, 084502-1 – 084504-4.

Ball, C. G., Fellouah, H., and Pollard, A. (2012). The flow field in turbulent round free jets. *Progress in Aerospace Sciences*, 50, 1-26.

Banyassady, R., and Piomelli, U. (2015). Interaction of inner and outer layers in plane and radial wall jets. *Journal of Turbulence*, 16, 460-483.

Banyassady, R., and Piomelli, U. (2014). Turbulent plane wall jets over smooth and rough surfaces. *Journal of Turbulence*, 15(3), 186-207.

Bergeles, G., and Athanassiadis, N. (1983). The flow past a surface-mounted obstacle. *Journal of Fluids Engineering,* 105, 461-463.

Bhuiyan, F., Habibzadeh, A., Rajaratnam, N., and Zhu, D. Z. (2011). Reattached turbulent submerged offset jets on rough beds with shallow tailwater. *Journal of Hydraulic Engineering*, 137, 1636-1648.

Boersma, B. J., Brethouwer, G., and Nieuwstadt, F. T. M. (1998). A numerical investigation on the effect of the inflow conditions on the self-similar region of a round jet. *Physics of Fluids*, 10(4), 899-909.

Bogey, C., and Bailly, C. (2009). Turbulence and energy budget in a self-preserving round jet: direct evaluation using large eddy simulation. *Journal of Fluid Mechanics*, 627, 129-160.

Bourque, C. (1967). Reattachment of a two dimensional jet to an adjacent flat plate. *Advances in Fluidics (ed. By F. T. Brown) ASME New York*, 192-204.

Bourque, C., and Newman, B. G. (1960). Reattachment of a two-dimensional incompressible jet to an adjacent flat plate. *Aeronautical Quarterly*, 11: 201-232.

Bradshaw, P., and Wong, F. Y. F. (1972). The reattachment and relaxation of a turbulent shear layer. *Journal of Fluid Mechanics*, 52, 113-135.

Bradshaw, P. (1966). The effect of initial conditions on the development of a free shear layer. *Journal of Fluid Mechanics*, 26(2), 225-236.

Castro, I. P. (1979). Relaxing wakes behind surface-mounted obstacles in rough wall boundary layers. *Journal of Fluid Mechanics,* 93, 631-659.

Christensen, K. T., and Wu, Y. (2005, June). Characteristics of vortex organization in the outer layer of wall turbulence. *Proc. Fourth International Symposium on Turbulence and Shear Flow Phenomena*, Williamsburg, Virginia, 3, 1025-1030.

Coleman, H. W., and Steele, W. G. (1995). Engineering application of experimental uncertainty analysis. *AIAA Journal*, 33, 1888-1896.

Craft, T. J., and Launder, B. E. (2001). On the spreading mechanism of the three-dimensional turbulent wall jet. *Journal of Fluid Mechanics*, 435, 305-326.

Cui, J., Patel, V. C., and Lin, C. L. (2003). Large eddy simulation of turbulent flow in a channel with rib roughness. *International Journal of Heat and Fluid flow*, 24(3), 372-388.

Davis, M. R., and Winarto, H. (1980). Jet diffusion from a circular nozzle above a solid plane. *Journal of Fluid Mechanics*, 101: 201-221.

Dejoan, A., and Leschziner, M. A. (2006). Separating the effects of wall blocking and near-wall shear in the interaction between the wall and free shear layer in a wall jet. *Physics of Fluids*, 18, 0651101-1–065110-17.

Deo, R. C., Mi, J., and Nathan, G. J. (2007). The influence of nozzle-exit geometric profile on statistical properties of a turbulent plane jet. *Experimental Thermal and Fluid Science,* 32(2), 545-559.

Dey, S., and Sarkar, A. (2008). Characteristics of turbulent flow in submerged jumps on rough beds. *Journal of Engineering Mechanics*, 134(1), 49-59.

Durand, Z. M. J. (2014). Experimental study of tailwater level and asymmetry ratio effects on three-dimensional offset jets. MSc. Thesis, University of Manitoba.

Ead, S. A., and Rajaratnam, N. (2004). Plane turbulent wall jets on rough boundaries with limited tailwater. *Journal of Engineering Mechanics*, 130, 1245-1250.

Ead, S. A., and Rajaratnam, N. (2002). Plane turbulent wall jets in shallow tailwater. *Journal of Engineering Mechamics*, 128(2), 143-155.

Ead, S. A., and Rajaratnam, N. (2001). Plane turbulent surface jets in shallow tailwater. *Journal of Fluids Engineering*, 123, 121-127.

Eaton, J. K., and Johnston, J. P. (1981). A review of research on subsonic turbulent flow reattachment. *AIAA Journal*, 19, 1093-1100.

Eriksson, J. G., Karlsson, R. I., and Persson, J. (1998). An experimental study of a two-dimensional plane wall jet. *Experiments in Fluids*, 25: 50-60.

Essel, E. E., Tachie, M. F., Agelin-Chaab, M., Koupriyanov, M., and Tully, B. (2013). Particle image velocimetry measurements in curved turbulent jets produced from a slot diffuser. *Experimental Thermal and Fluid Science*, 49, 169-184.

Etheridge, D., and Kemp, P. H. (1978). Measurement of turbulent flow downstream of a rearward-facing step. *Journal of Fluid Mechanics*, 545-566.

Faghani, E., Maddahian, R., Faghani, P., and Farhanieh, B. (2009). Numerical investigation of turbulent free jet flows issuing from rectangular nozzles: the influence of small aspect ratio. *Archive of Applied Mechanics*, 80(7), 727-745.

Fellouah, H., Ball, C. G., and Pollard, A. (2009). Reynolds number effects within the development region of a turbulent round free jet. *International Journal of Heat and Mass Transfer*, 52, 3943-3954.

Forliti, D. J., Strykowski, P. J., and Debatin, K. (2000). Bias and precision errors of digital particle image velocimetry. *Experiment in Fluids*, 28, 436-447.

Gao, N., and Ewing, D. (2007). Experimental investigation of planar offset attaching jets with small offset distances. *Experiments in Fluids*, 42, 941-954.

Garcia, C. M., Jackson, P. R., and Garcia, M. H. (2006). Confidence intervals in the determination of turbulence parameters. *Experiments in Fluids*, 40(4), 514-522.

Goring, D. G., and Nikora, V. I. (2002). Despiking acoustic Doppler velocimeter data. *Journal of Hydraulic Engineering*, 128(1), 117-126.

Grass, A. J., Stuart, R. J., and Mansour-Tehrani, M. (1993). Common vortical structure of turbulent flows over smooth and rough boundaries. *AIAA Journal*, 31(5), 837-847.

Gui, L., Longo, J., and Stern, F. (2001). Biases of PIV measurement of turbulent flow and the masked correlation-based interrogation algorithms. *Experiments in Fluids*, 30, 27-35.

Hall, J. W., and Ewing D. (2007). Three dimensional turbulent wall jets issuing from moderate aspect ratio rectangular channels. *AIAA Journal*, 45: 1177-1186.

Hashiehbaf, A., and Romano, G. P. (2013). Particle image velocimetry investigation on mixing enhancement of non-circular sharp edge nozzles. *International Journal of Heat and Fluid Flow*, 44, 208-221.

Hattori, H., and Nagano, Y. (2010). Investigation of turbulent boundary layer over a forward-facing step via direct numerical simulation. *International Journal of Heat and Fluid Flow*, 31, 284-294.

Hoch, J., and Jiji, L. M. (1981). Two-dimensional turbulent offset jet-boundary interaction. *Transactions of the ASME. Journal of Fluids Engineering*, 103, 154-161.

Holman, J. P. (2001). Experimental methods for engineers. Seventh Edition.

Holmes, P., Lumley, J., and Berkooz, G. (1996). Turbulence coherent structures, dynamical systems and symmetry. Cambridge University Press: Cambridge.

Hsiao, F.-B., Lim, Y.-C., and Huang, J. M. (2010). On the near-field flow structure and mode behaviors for the right-angle and sharp-edged orifice plate jet. *Experimental Thermal and Fluid Sci*ence, 34(8), 1282-1289.

Hussein, H. J., Capp, S. P., and George, W. K. (1994). Velocity measurements in a high- Reynolds number, momentum-conserving, axisymmetric, turbulent jet. *Journal of Fluid Mechanic*, 258, 31-75.

Hussain, A. K. M. F., and Clark, A. R. (1977). Upstream influence on the near field of a plane turbulent jet. *Physics of Fluids*, 20(9), 1416-1426.

Hwang, R. R., Chow, Y. C., and Peng, Y. F. (1999). Numerical study of turbulent flow over two-dimensional surface-mounted ribs in a channel. *International Journal for Numerical Methods in Fluids*, 31, 767-785.

Irwin, H. P. A. H. (1973). Measurements in a self-preserving plane wall jet in a positive pressure gradient. *Journal of Fluid Mechanics*, 61(1), 33-63.

Islam, M. R., and Zhu, Z. D. (2013). Kernel density-based algorithm for despiking ADV data. *Journal of Hydraulic Engineering*, 139(7), 785-793.

Jimenez, J. (2004). Turbulent flows over rough walls. *Annual Review Fluid Mechanics*, 36, 173-196.

Keane, R. D., and Adrian, R. J. (1991). Optimization of particle image velocimeters. Part II: multiple pulse systems. *Measurement Science and Technology*, 2, 1202-1215.

Keane, R. D., and Adrian, R. J. (1992). Theory of cross-correlation analysis of PIV images. *Applied Scientific Research*, 49, 191-215.

Koso, T., and Ohashi, H. (1981). Turbulent diffusion of a three-dimensional wall jet: 1st Report, Mean and Turbulent Characteristics of Velocity and Temperature Field. *Transactions of the Japan Society of Mechanical Engineers*, 47(418), 1002-1014.

Kostas, J., Soria, J., and Chong, M. S. (2005). A comparison between snapshot POD analysis of PIV velocity and vorticity data. *Experiments in Fluids*, 38, 146-160.

Kostas, J., Soria, J., and Chong, M. S. (2002). Particle image velocimetry measurements of a backward-facing step flow. *Experiments in Fluids*, 33, 838-853.

Krogstad, P.-A., and Antonia, R. A. (1999). Surface roughness effects in turbulent boundary layers. *Experiments in Fluids*, 27(5), 450-460.

Krogstad, P.-A., and Antonia, R. A. (1994). Structure of Turbulent Boundary Layers on Smooth and Rough Walls. *Journal of Fluid Mechanics*, 277, 1-21.

Krogstad, P.-A., Antonia, R. A., and Browne, L. W. B. (1992). Comparison between rough and smooth wall turbulent boundary layers. *Journal of Fluid Mechanics*, 245, 599-617.

Kumar, A. (2015). Mean flow characteristics of a turbulent dual jet consisting of a plane and parallel offset jet. *Computers and Fluids*, 114, 48-65.

Launder, B. E., and Rodi, W. (1983). The turbulent wall jet-measurement and modeling. *Annual Review of Fluid Mechanics*, 15, 429-459.

Launder, B. E., and Rodi, W. (1981). The turbulent wall jet. *Progress in Aerospace Sciences*, 19, 81-128.

Law, A., and Herlina, W-K. (2002). An experimental study on turbulent circular wall jets. *Journal of Hydraulic Engineering*, 128: 161-174.

Lee, S-J., and Baek, S J. (1994). The effect of aspect ratio on the near-field turbulent structure of elliptic jets. *Flow Measurements and Instrumentation*, 5(3), 170-180.

Liu. M., Rajaratnam, N., and Zhu, D. Z. (2004). Turbulence structure of hydraulic jumps of low Froude numbers. *Journal of Hydraulic Engineering*, 130, 511-520.

Lu S. S., and Willmarth, W. W. (1973). Measurement of the structure of the Reynolds stress in a turbulent boundary layer. *Journal of Fluid Mechanics*, 60, 481-511.

Lykossov, V. N. (1992). The momentum turbulent counter-gradient transport in jet-like flows. *Advances in Atmospheric Sciences*, 9(2), 191-200.

Madnia, C. K., and Bernal, L. P. (1994). Interaction of a turbulent round jet with the free surface. *Journal of Fluid Mechanics*, 261, 305-332.

Martinuzzi, R., and Tropea, C. (1993). The flow around surface-mounted rib, prismatic obstacles placed in a fully developed channel flow. *Journal of Fluids Engineering*, 115, 85-92.

Mei, M., Adrian, R. J., and Hanratty, T. J. (1991). Particle dispersion in isotropic turbulence under stokes drag and basset force with gravitational settling. *Journal of Fluid Mechanics*, 255, 481-495.

Meyer, E. K., Pedersen, J.M., and Ozcan, O. (2007). A turbulent jet in crossflow analyzed with proper orthogonal decomposition. *Journal of Fluid Mechanics*, 583, 199-227.

Mi, J., Xu, M., and Zhou, T. (2013). Reynolds number influence on statistical behaviors of turbulence in a circular free jet. *Physics of Fluids*, 25(7), 075101-1 – 075101-30.

Miozzi, M., Lalli, F., Romano, G. P. (2010). Experimental investigation of a free-surface turbulent jet with coanda effect. *Experiments in Fluids*, 49(1), 341-353.

Miyake, Y., Tsujimoto, K., and Agata, Y. (2001). Direct numerical simulation of rough wall heat transfer in a turbulent channel flow. *International Journal of Heat and Fluid Flow*, 22(3), 237-244.

Moin, P., and Kim, J. (1985). The structure of the vorticity field in turbulent channel flow. Part 1: analysis of instantaneous and statistical correlation. *Journal of Fluid Mechanics*, 155, 441-464.

Mossa, M., Petrillo, A., and Chanson, H. (2003). Tailwater level effects on flow conditions at an abrupt drop. *Journal of Hydraulic Research*, 41(1), 39-51.

Nagano, Y., Hattori, H., and Houra, T. (2004). DNS of velocity and thermal fields in turbulent channel flow with transverse-rib roughness. *International Journal of Heat and Fluid Flow*, 25(3), 393-403.

Nasr, A., and Lai, J. C. S. (1998). A turbulent plane offset jet with small offset ratio. *Experiments in Fluids*, 24, 47-57.

Nasr, A., and Lai, J. C. S. (1997). Comparison of flow characteristics in the near field of two parallel plane jets and an offset plane jet. *Physics of Fluids*, 9, 2919-2931.

Newman, B. G., Patel, R. P., Savage, S. B. and Tjio, H. K. (1972). Three-dimensional wall jet originating from a circular orifice. *Aeronautical Quarterly*, 23, 188-200.

Nolan, K. P., Walsh, E. J., and McEligot, D. M. (2010). Quadrant analysis of a transitional boundary layer subject to free-stream turbulence. *Journal of Fluid Mechanics*, 658, 310-335.

Nozaki, T. (1983). Reattachment flow issuing from a finite width nozzle: effects of aspect ratio of the nozzle. *Bulletin JSME,* 26, 1884-1890.

Nozaki, T., Hatta, K., Nakashima, M., and Matsumura, H. (1979). Reattachment flow issuing from a finite width nozzle. *Bulletin JSME*, 22: 340-347.

Nyantekyi-Kwakye, B., Clark, S., Tachie, M. F., Malenchak, J., and Muluye, G. (2015a). Flow characteristics within the recirculation region of 3D turbulent offset jet. *Journal of Hydraulic Research*, 53(2), 230-242.

Nyantekyi-Kwakye, .B, Clark, S. P., Tachie, M. F., Malenchak, J., and Muluye, G. Y. (2015b). Experimental study of the flow structures of 3D turbulent offset jet. *Journal of Hydraulic Research*, 53(6), 773-786.

Okomato, S., Seo, S., Nakaso, K., and Kawai, I. (1993). Turbulent shear flow and heat transfer over the repeated two dimensional square ribs on ground plane. *Journal of Fluids Engineering*, 115(4), 631-637.

Ong, L., and Wallace, M. (1998). Joint probability density analysis of the structure and dynamics of the vorticity field of a turbulent boundary layer. *Journal of Fluid Mechanics*, 367, 291-328.

Padmanabham, G., and Lakshmana Gowda, B. H. (1991a). Mean and turbulence characteristics of a class of three-dimensional wall jets-Part 1: Mean flow characteristics. *Journal of Fluids Engineering*, 113, 620-628.

Padmanabham, G., and Lakshmana Gowda, B. H. (1991b). Mean and turbulence characteristics of a class of three-dimensional wall jets-Part 2: Mean flow characteristics. *Journal of Fluids Engineering*, 113, 629-634.

Pani, B. S., and Dash, R. N. (1983). Three-dimensional reattached wall jet. *La Houille Blanche*, No.1, 27-32.

Pelfrey, J. R. R., and Liburdy, J. A. (1986). Mean flow characteristics of a turbulent offset jet. *Transactions of ASME. Journal of Fluids Engineering*, 108, 82-88.

Pelfry, J. R. R. (1984). Characteristics of a turbulent plane offset jet. Ph.D. Thesis, Clemson University, New York, USA.

Perry, A. E., Schofield, W. H., and Joubert, P. N., (1969). Rough wall turbulent boundary layers. *Journal of Fluid Mechanics*, 37(2), 383-413.

Pope, S. B. (2000). Turbulent flows. University Press, Cambridge.

Pramanik, S., and Das, M. K. (2013). Numerical characterization of a planar turbulent offset jet over an oblique wall. *Computers and Fluids*, 77, 36-55.

Prasad, A. K., Adrian, R. J., Landreth, C. C., and Offutt, P. W. (1992). Effect of resolution on the speed and accuracy of particle image velocimetry interrogation. *Experiments in Fluids*, 13, 105-116.

Quinn, W. R. (2006). Upstream nozzle shaping effects on near field flow in round turbulent free jets. *European Journal of Mechanics, B-Fluids*, 25(3), 279-301.

Quinn, W. R. (1992). Turbulent free jet flows issuing from sharp-edged rectangular slots: the influence of slot aspect ratio. *Experiments in Thermal and Fluid Science*, 5(2), 203-215.

Quinn, W. R. (1989). On mixing in an elliptic turbulent free jet. *Physics of Fluids*, 1(10), 1716-1722.

Quinn, W. R., and Militzer, J. (1988). Experimental and numerical study of a turbulent free square jet. *Physics of Fluids*, 31(5), 1017-1025.

Ra, S. H., Chang, P. K., and Park, S. O. (1990). Measurement of the forward-flow fraction using a split film sensor. *Experiments in Fluids*, 10, 57-59.

Raffel, M., Willert, C. E., and Kompenhaus, J. (1998). Particle image velocimetry: a practical guide. Springer Verlag.

Rajaratnam, N., and Subramanya, N. (1968). Plane turbulent reattachment wall jets. *ASCE Journal of Hydraulic Division*, 94, 95-112.

Rathore, S. K., and Das, M. K. (2013). Comparison of two low-Reynolds number turbulence models for fluid flow study of wall bounded jets. *International Journal Heat and Mass Transfer*, 61(1), 365-380.

Ren, H., and Wu, Y. (2011). Turbulent boundary layers over smooth and rough forward-facing steps. *Physics of Fluids*, 23, 045102-1 – 045102-16.

Rostamy, N., Bergstrom, D. J., Sumner, D., and Bugg, J. D. (2011a). An experimental study of a turbulent wall jet on smooth and transitionally rough surfaces. *Journal of Fluids Engineering*, 133, 1-8.

Rostamy, N., Bergstrom, D. J., Sumner, D., & Bugg, J. D. (2011b). The effect of surface roughness on the turbulence structure of a plane wall jet. *Physics of Fluids*, 23(8), doi: (10.1063/1.3614478).

Sawyer, R. A. (1963). Two dimensional reattaching jet flows including the effect of curvature on entrainment. *Journal of Fluid Mechanics*, 17: 481-498.

Sawyer, R. A. (1960). The flow due to a two dimensional jet issuing parallel to a flat plate. *Journal of Fluid Mechanics*, 9, 543-561.

Schultz, M. P., & Flack, K. A. (2005). Outer layer similarity in fully rough turbulent boundary layers. *Experiments in Fluids*, 38, 328-340.

Schwarz, W. H., and Cosart, W. P. (1961). The two-dimensional turbulent wall-jet. *Journal of Fluid Mechanics*, 10(4), 481-495.

Sfeir, A. A. (1976). The velocity and temperature fields of rectangular jets. *International Journal of Heat and Mass Transfer*, 19, 1289-1297.

Sforza, P. M. and Herbst, G. (1970). Study of three-dimensional incompressible turbulent wall jets. *AIAA Journal*, 8, 276-283.

Shah, M. K. (2009). Effects of Pressure Gradient on Separated and Reattached Turbulent Flows. Ph.D. Thesis, University of Manitoba, Winnipeg, Canada.

Shah, M. K., and Tachie, M. F. (2009a). Proper orthogonal decomposition analysis of separated and reattached pressure gradient turbulent flows. *AIAA Journal*, 47, 2616-2631.

Shah, M. K., and Tachie, M. F. (2009c). PIV investigation of flow over a transverse square rib in pressure gradients. *Journal of Turbulence*, 10, 1-22.

Shakouchi, T. (1986). A study on the three-dimensional reattached jet. *Bulletin of JSME*, 29, 2508-2514.

Shim, Y. M., Sharm, R. N., and Richards, P. J. (2013). Proper orthogonal decomposition analysis of the flow field in a plane jet. *Experimental Thermal and Fluid Science*, 51, 37-55.

Shinneeb, A.-M., Balachandar, R., and Bugg, J. D. (2008). Analysis of coherent structures in the far-field of an axisymmetric free jet identified using particle image velocimetry and proper orthogonal decomposition. *Journal of Fluids Engineering*, 130, doi:10.1115/1.2813137.

Sirovich, L. (1987). Turbulence and the dynamics of coherent structures, Part 1: coherent structures. *Quarterly of Applied Mathematics*, 45(3), 561-571.

Sun, H., and Ewing, D. (2002). Effect of initial boundary conditions on the development of three-dimensional wall jet. *Proceedings of 40th AIAA Aerospace Sciences and Exhibit*, Reno, USA. Paper No. AIAA 2002-0733.

Swamy, N. V. C., and Bandyopadhyay, P. (1981). The structure of three-dimensional wall jets. *Indian Journal of Technology*, 19, 390-394.

Tachie, M. F., Balachander, R., and Bergstrom, D. J. (2004). Roughness effects on turbulent plane wall jets in an open channel. *Experiments in Fluids*, 37, 281-292.

Tachie, M. F., Bergstrom, D. J., and Balachander, R. (2003). Roughness effects in low-Re_θ open channel turbulent boundary layers. *Experiments in Fluids*, 35(4), 338-346.

Todde, V., Spazzini, P. G., and Sandberg, M. (2009). Experimental analysis of low-Reynolds number free jets: evolution along the jet centerline and Reynolds number effects. *Experiments in Fluids*, 47, 279-294.

Tomkins, D. D. and Adrian, R. J. (2003). Spanwise Structure and Scale Growth in Turbulent Boundary Layers. *Journal of Fluid Mechanics*, 490: 37-74.

Tsikata, J. M., Tachie, M. F., and Katopodis, C. (2014). Open-channel turbulent flow through bar racks. *Journal of Hydraulic Research*, 52(5), 630-643.

Tsuchiya, Y., Horikoshi, C., and Sato, T. (1986). “On the spread of rectangular jets.” *Experiments in Fluids*, 4(4), 197-204.

Venas, B., Abrahamsson, H., Krogstad, P.-A., and Lofdahl, L. (1999). Pulsed hot-wire measurements in two and three-dimensional wall jets. *Experiments in Fluids*, 27, 210-218.

Verhoff, A. (1963). The two-dimensional turbulent wall jet with and without an external free stream. Report No. 626, Princeton University, New Jersey, USA.

Volino, R. J., Schultz, M. P. and Flack, K. A. (2007). Turbulence Structure in Rough and Smooth Wall Boundary Layers. *Journal of Fluid Mechanics*, 592, 263-293.

Wang, X. K. and Tan, S. K. (2007). Experimental investigation of the interaction between a plane wall jet and a parallel offset jet. *Experiments in Fluids*, 42: 551-562.

Westerweel, J., Draad, A. A., van der Hoeven, Th. J. G. and van Oord, J. (1996). Measurement of Fully Developed Turbulent Pipe Flow with Digital Particle Image Velocimetry. *Experiments in Fluids*, 20, 165-177.

Wheeler, A. J., and Ganji, A. R. (2004). Introduction to engineering experimentation. Second Edition.

Wygnanski, I., Katz, Y. and Horev, E. (1992). On the applicability of various scaling laws to the turbulent wall jet. *Journal of Fluid Mechanics*, 234, 669-690.

Wygnanski, I., and Fiedler, H. (1969). Some measurements in the self-preserving jet. *Journal of Fluid Mechanics*, 38(3), 577-612.

Xu, G., and Antonia, R. A. (2002). Effect of different initial conditions on a turbulent round free jet. *Experiments in Fluids*, 33(5), 677-683.

Yaghoubi, M., and Mahmoodi, S. (2004). Experimental Study of turbulent separated and reattached flow over a finite blunt plate. *Experimental Thermal and Fluid Science*, 29, 105-112.

Yoon, S. H., Kim, K. C., Kim, D. S., and Chung, M. K. (1995). Effect of surface roughness on a turbulent wall-attaching offset jet. *Experiments in Fluids*, 19(1), 38-42.

Yoon, S. H., Kim, K. C., Kim, D. S., and Chung M. K. (1993). Comparative study of turbulent wall-attaching offset jet and a plane wall jet. *Journal of Mechanical Science and Technology*, 7, 101-112.

Appendix A

The techniques for error analysis and measurement uncertainties in the PIV measurements are reported in this section.

Error Analysis

Measurement is generally assigning values to physical variables. The accuracy of the measurement is determined by the closeness of the assigned quantity and the true value. The difference between the experimentally measured value and the true value is termed as the measurement error or uncertainty. The procedure to determine the uncertainty (i.e. the bias, B, and precision, P) in the measured quantities follows that given by Holman (2001) and Wheeler & Ganji (2004). Detailed uncertainty analysis for PIV measurements are presented by ITTC (2008). The total error in experimental measurements can be categorized into two main components: the bias, B, and precision, P, components. The primary sources of the bias uncertainties arise from systematic errors such as camera resolution, as well as the field of view calibration, and the errors created in the basic measurements. Errors are classified as precision when they contribute to the scatter of the measured data (Coleman & Steele, 1995). Some other sources of error include selection of inappropriate time between pulses, insufficient sample size, spatial resolution and sub-pixel displacement bias. The uncertainties also include the response time of the particle to the fluid motion, position of the laser sheet and error arising from algorithms in determining the average particle displacement. Investigations by Forliti *et al*. (2000) revealed that both the evaluation of bias and their gradients can be effectively minimized by using Gaussian digital masks on the interrogation window. This will also reduce the measurement uncertainty. Both bias and precision errors are reduced by increasing the number of separately obtained samples.

Carefully selecting the appropriate time between the image pairs can minimize some of the experimental errors. Another major contributor to bias error is peak locking. In order to minimize the errors associated with peak locking, steps need to be taken during image acquisition and processing. Raffel *et al*. (1998) recommended that in order to reduce peak locking, the particle image diameter should be close to 2.0 pixels. The large sample size (4000 instantaneous images) used in the computation of the statistics in the present study also minimized the precision error. There are also errors associated with the velocity gradients since these tend to broaden the displacement peak while reducing the amplitude. To obtain acceptable gradients when using a cross-correlation technique at a 95% probability, Keane & Adrian (1992) suggested the use of the expression below:

$$\frac{M_f \Delta U_y \Delta t}{d} < 0.03 \qquad \text{(A.1)}$$

where M_f is the magnification factor, $\Delta U_y = (\partial U/\partial y)/(d/2)$, Δt is the time between the two laser pulses and d is the length of the interrogation area size. This check was conducted for the wall jet where M_f = 0.125, Δt = 962.28 × 10^{-6} s and $\partial U/\partial y$ within the inner region of the flow is approximately 24.41 s^{-1}. From these parameters, the left hand side of Eqn. (A.1) yielded a value of 0.003, which satisfies the relationship provided. Similar analyses were done for the various offset jets and the results obtained again satisfied the expression provided.

Bias error

The equation for the determination of the instantaneous velocity in PIV measurements is given as (Gui *et al*. 2001):

$$u_i = \frac{\Delta s L_0}{\Delta t L_1} \qquad \text{(A.2)}$$

where i can be 1 and 2 representing the x and y coordinates respectively, Δs is the particle displacement, L_0 and L_1 are the width of the camera view in the object plane and width of the digital image respectively. To determine the corresponding bias error, the root of the sum of the squares (RSS) of the elementary bias limits based on their sensitivity coefficients given in Eqn. (A.2) is used:

$$B_{u_i}^2=\eta_{\Delta s}^2 B_{\Delta s}^2+\eta_{L_0}^2 B_{L_0}^2+\eta_{\Delta t}^2 B_{\Delta t}^2+\eta_{L_1}^2 B_{L_1}^2 \equiv \sum_{v=\Delta s,L_0,\Delta t,L_1} \eta_v B_v^2 \quad \text{(A.3)}$$

where η_v is the generic form of the four sensitivity coefficients defined as:

$$\eta_v=\frac{\partial u_i}{\partial v} \quad \text{(A.4)}$$

Based on the equations provided, the bias errors were performed for U and V for the various test conditions. A typical case has been presented for the inner shear layer of the wall jet in Tables A.1 and A.2. The percentage bias error (%Bias error) for both U and V cases are expressed as a percentage of U.

Table A.1 Bias limits of the local streamwise mean velocity (U) within the inner region of the wall jet (self-similar region)

Variable	Magnitude	B_v	η_v	$B_v\eta_v$	$(B_v\eta_v)^2$
L_0 (m)	1.20E-01	5.00E-04	3.16E-01	1.58E-04	2.49E-08
L_1 (pix)	2.05E+03	5.00E-01	-1.85E-05	-9.25E-06	8.56E-11
Δt (s)	9.62E-04	1.00E-07	-3.94E+01	-3.94E-06	1.55E-11
Δs (pix)	6.22E-01	1.27E-02	6.09E-02	7.73E-04	5.98E-07
U (m/s)	3.79E-02				
				$\Sigma(B_v\eta_v)^2$	6.23E-07
				Bias error	7.89E-04
				%Bias error	2.08%

Table A.2 Bias limits of the local wall-normal mean velocity (V) within the inner region of the wall jet (self-similar region)

Variable	Magnitude	B_v	η_v	$B_v\eta_v$	$(B_v\eta_v)^2$
L_o (m)	1.20E-01	5.00E-04	1.71E-02	8.54E-06	7.30E-11
L_I (pix)	2.05E+03	5.00E-01	-1.00E-06	-5.00E-07	2.50E-13
Δt (s)	9.62E-04	1.00E-07	-2.13E+00	-2.13E-07	4.54E-14
Δs (pix)	3.37E-02	1.27E-02	6.09E-02	7.73E-04	5.98E-07
V (m/s)	-2.05E-03				
				$\Sigma(B_v\eta_v)^2$	5.98E-07
				Bias error	7.73E-04
				%Bias error	2.04%

Precision error

The precision component of the error estimation is determined from the standard deviation as well as the mean of the data. The precision error, P, of the measured variable, η is given by

$$P_\eta = \frac{t\sigma}{\sqrt{N}} \tag{A.5}$$

where t is the confidence coefficient having a value of 2 for 95% confidence level according to Holman (2001), N is the sample size (4000) and σ is the standard deviation, defined as

$$\sigma = \sqrt{\frac{1}{n\text{-}1}\sum_{j=1}^{n}\left(\eta_j - \bar{\eta}\right)^2} \tag{A.6}$$

where $\bar{\eta}$ is the mean and it is given by:

$$\bar{\eta} = \frac{1}{n}\sum_{j=1}^{n}\eta_n \tag{A.7}$$

In order to obtain the standard deviations of U and V, the number of images was grouped into 8 sub-data of 500 images. This means that the number of readings for the present study is n = 8. The values of U and V were determined at the same locations of the flow. From the 8 sub-datasets, the

standard deviation for U and V was approximately 2.84% and 0.25% respectively. With known values of t, N and σ, the precision error was estimated from Eqn. (A.5) to be approximately 2.4% and 0.2% for U and V respectively.

Total error

The total measurement uncertainty, E, is the root-sum-square of the bias and precision errors and is given by

$$E_\eta = \sqrt{B_\eta^2 + P_\eta^2} \tag{A.8}$$

The total measurement uncertainty for U and V was obtained to be 3.2% and 2.1% respectively. Likewise, the uncertainty in the turbulence intensities, Reynolds stresses and triple velocity products were obtained to be ±8, ±12, and ±14 respectively.

Appendix B

Conference Paper (Turbulence and Shear Flow Phenomenon 9 – 2015)

PIV Study of a 3D Turbulent Offset Jet Flow Over Square Ribs

Abstract

An experimental study was conducted to investigate a three-dimensional offset jet flow over a surface mounted square rib using particle image velocimetry. The square rib was mounted at three different streamwise locations, $1.25b_o$, $3.45b_o$ and $6.25b_o$ from the nozzle exit (where b_o is the nozzle height). An increase in reattachment length of the offset jet was observed when the placement of the rib was increased from the nozzle exit. Increasing the location of the rib from the nozzle exit resulted in a faster decay of the maximum streamwise mean velocity. In the near-field of the jet, the rib location modified the turbulent kinetic energy, Reynolds shear stress and triple velocity correlations. Results from the Reynolds normal stresses highlighted the highly anisotropic nature of the flow field of three-dimensional offset jets. A quadrant analysis revealed that all four events were affected by changing rib location. Contrary to boundary layers both interaction events contributed to the total Reynolds shear stress.

Introduction

Three dimensional (3D) offset jets are encountered in diverse engineering and environmental applications such as fuel injection systems, environmental transport and mixing of effluent in lakes and rivers as well as in energy dissipation structures. The flow field of an offset jet can be divided into the following three main regions: recirculation, reattachment and wall jet region. The features of the recirculation and reattachment regions are qualitatively similar to prototypical separated and reattached turbulent shear flows. The wall jet flow, which is formed downstream of the reattachment region, is a composite shear layer with an inner region that is similar to a turbulent boundary layer, and an outer region that is akin to a free jet. In view of their complex flow physics, refined measurements in turbulent offset jets are essential to optimize a multitude of mixing devices, and also to provide the physical understanding and benchmark datasets required to facilitate the development of accurate numerical models and validate numerical results.

Considerable research efforts have been made in the past to advance our understanding of two-dimensional (2D) offset jets (Bhuiyan *et al*. 2011; Nasr & Lai, 1998; Pelfrey & Liburdy, 1986). On the other hand, only few investigations on the relatively more complex 3D offset jets have been reported (Chapter 4; Agelinchaab & Tachie, 2011). As a consequence, our understanding of the flow physics for 3D offset jets is deficient compared with their 2D counterparts and other canonical turbulent shear flows. Agelinchaab & Tachie (2011) investigated the effects of Reynolds number and offset height on the reattachment length and turbulent transport phenomena in 3D offset jets. The experiments, which were performed using a particle image velocimetry (PIV), were conducted at three Reynolds numbers, Re = 5000, 10000 and 20000 and four offset height ratio, h/b_o = 0, 0.5, 1.5 and 3.5. The results revealed that the reattachment length was independent of Reynolds number but increased with increasing h/b_o. The development of the mean flow and higher order turbulence statistics showed a distinct dependence on h/b_o. For example, the mean velocity profiles required a longer x/b_o (where x is the streamwise distance with the origin at the nozzle exit) to attain self-similarity when h/b_o was changed from 0.5 to 3.5.

Recently, an experimental research program was initiated to study the effects of h/b_o on the characteristics of 3D offset jets produced from a sharp-edged rectangular slot in an open channel (Chapter 4). The measurements were performed at a fixed Reynolds number of 8000 and three h/b_o = 0, 2 and 4. The reattachment lengths (L_e) for h/b_o = 2 and 4 were, respectively, L_e/b_o = 4.4 and 6.2. As expected, the lateral spread rate was larger than the wall-normal spread rate, irrespective of h/b_o. However, both lateral and wall-normal spread rates decreased with increasing h/b_o.

The focus of the present study is to understand the flow characteristics and turbulent transport phenomena in 3D offset jets over a surface mounted 2D square rib. Specifically, initial conditions such as inlet Reynolds number, Froude number and offset height were kept constant while the streamwise location of the square rib on the wall was varied to investigate the impact on the recirculation and reattachment region as well as the wall jet region.

Experimental setup and procedure

The experiments were performed in an open channel with dimensions 2500 mm long and a square cross section of 200 × 200 mm. The side walls as well as the bottom of the test section were made from a smooth acrylic to facilitate optical access. The Cartesian coordinate system was used with x and y representing the streamwise and wall-normal distances, respectively. The 3D offset jet was generated from a rectangular nozzle with dimensions 8 mm high (b_o) and 48 mm wide. The experiments were conducted for an h/b_o of 2. A 2D acrylic rib of 10 × 10 mm square cross section as shown in Fig. B.1, spanning the entire channel width was positioned at x/b_o = 1.25, 3.45 and 6.25 from the nozzle exit which are represented herein as $R1$, $R2$ and $R3$, respectively. Locations $R1$, $R2$ and $R3$ corresponded to streamwise locations within the recirculation, reattachment and developing regions, respectively, of a reference experiments performed at similar test conditions but with no rib mounted on the wall (Chapter 4). The tailwater depth, y_t, was maintained constant at 116 mm. The bulk velocity, U_o, was 0.95 ms^{-1} yielding a Reynolds number (Re = $(b_oU_o)/\nu$) and Froude number (Fr = $U_o/(gb_o)^{0.5}$) of 7600 and 3.4, respectively, where ν is the kinematic viscosity of water and g is the acceleration due to gravity.

The velocity measurements were performed using a planar particle image velocimetry system. The flow was seeded with 10 μm silver coated hollow glass spheres having a specific gravity of 1.4. A New Wave Solo Nd:YAG double-pulsed laser with maximum energy of 120 mJ per pulse at 532 nm wavelength was used to illuminate the flow field. The laser sheet was aligned with the mid-span of the test section for measurements in the x–y plane, which coincided with the centre of the nozzle. Scattered light from the tracer particles were captured with a 12-bit FlowSenseEO 4M charge-coupled device camera that has a resolution of 2048 × 2048 pixels and a pixel pitch of 7.4 μm. A camera field of view of 120 × 120 mm was used with an acquisition rate of 4 Hz. The interrogation area size was set to 32 × 32 pixels with 50% overlap in both directions within the x–y plane. The instantaneous images were post-processed using the adaptive correlation option of DynamicStudio developed by Dantec Dynamics. Based on preliminary convergence tests the mean velocities and turbulence statistics were calculated using 4000 instantaneous image pairs. The time between acquisitions of images pairs was set to 0.25 s in order to ensure that consecutive velocity fields were statistically independent.

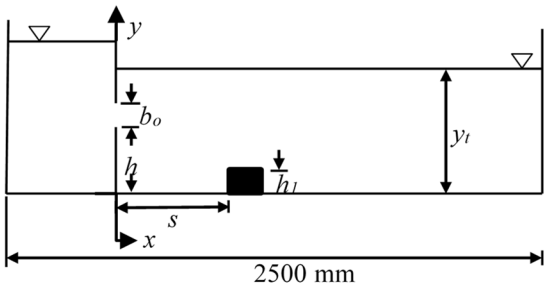

Figure B.1 Schematic of experimental setup

Results

Mean velocity

Contour plots of the streamwise mean velocities (U) are shown in Fig. B.2 to reveal the salient features of the mean flow pattern. In this and subsequent contour plots, all flow statistics are normalized by U_o. Results are presented for test cases $R1$ and $R3$ only. In all cases, the vena contracta effect produced by the sharp-edged nozzle caused an acceleration of U. The increase in U occurred in two stages for $R1$. The first stage, caused by the vena-contracta effect, occurred at $x^* \leq 2.6$, and the second stage, caused by the presence of the rib, occurred between $2.8 \leq x^* \leq 4.6$, where $x^* = x/b_o$. The increase in U for $R2$ (not shown) and $R3$ occurred within the regions $x^* \leq 2.2$ and $x^* \leq 3.4$, respectively. The magnitude of maximum reverse velocity within the recirculation region was about $0.02U_o$, $0.21U_o$ and $0.14U_o$ for $R1$, $R2$ and $R3$, respectively. These values are greater than $0.001U_o$ obtained for the reference case where there was no mounted rib. The increased negative velocities can be attributed to an enhanced adverse pressure gradient caused by the presence of the mounted ribs. Also, since the rib was mounted at the reattachment point in the case of $R2$, the leading edge of the rib deflected part of the reattaching fluid into the recirculation region thereby increasing the negative velocity compared to $R1$ and $R3$. A secondary recirculation region was formed beyond the trailing edge of the rib for $R2$ (not shown) and $R3$. This was not the case for $R1$ since it was mounted within the recirculation region of the flow. The reattachment lengths (L_e) were $4.75b_o$, $7.05b_o$ and $8.60b_o$ for $R1$, $R2$ and $R3$, respectively. The estimated L_e for $R1$ was similar to $L_e = 4.4b_o$ obtained for the reference case. For the $R2$ and $R3$ ribs, secondary reattachment lengths of $3.05b_o$ and $6.0b_o$, respectively, were obtained.

Profiles of U at the following streamwise locations were used to investigate the effects of rib location on the mean flow: s_1, m_1, L_e, and $5h_1$, where the symbols s_1 and m_1 represent the mid-point from the nozzle exit to the leading edge of the rib ($0.5s$, where s is the distance from the nozzle exit to the leading edge of the rib) and mid-point on top of the rib, respectively. Location $5h_1$ corresponds to 5 rib heights downstream the trailing edge of the rib. The streamwise location s_1 is situated within the recirculation region of the flow. These profiles are shown in Fig. B.3(a), and the velocity and length scale used were U_m and b_o, respectively (where U_m is the local streamwise maximum mean velocity). The rib location increased the negative velocities at location s_1. The peak value of U at m_1 for $R3$ occurred at a higher y location compared to both $R1$ and $R2$. This is as a result of deflection of the flow in the wall-normal direction by the rib. Beyond the reattachment point, U profiles for $R2$ and $R3$ developed at a similar rate compared to $R1$. Also, the U profiles for $R2$ and $R3$ at the reattachment point and beyond, showed a considerable spread of the jet compared to $R1$.

The decay of U_m is shown in Fig. B.3(b) for the three test cases. There was an initial increase in U_m due to the vena-contracta effect and then a decrease with the minimum value occurring within the vicinity of the rib. The minimum values occurred at about x/b_o = 2.5, 4.5 and 6.0 for $R1$, $R2$ and $R3$, respectively. Beyond these locations, the values of U_m increased to a second peak and then gradually decayed with x/b_o. The second peaks for the jets occurred at $1.8h_1$, $3.0h_1$ and $1.6h_1$ from the trailing edge of the rib for $R1$, $R2$ and $R3$, respectively (where h_1 is the rib height). Increasing the rib location from the nozzle exit resulted in a faster decay of the local maximum streamwise mean velocity. For the streamwise range considered, the decay of U_m after the second peak was similar for $R2$ and $R3$.

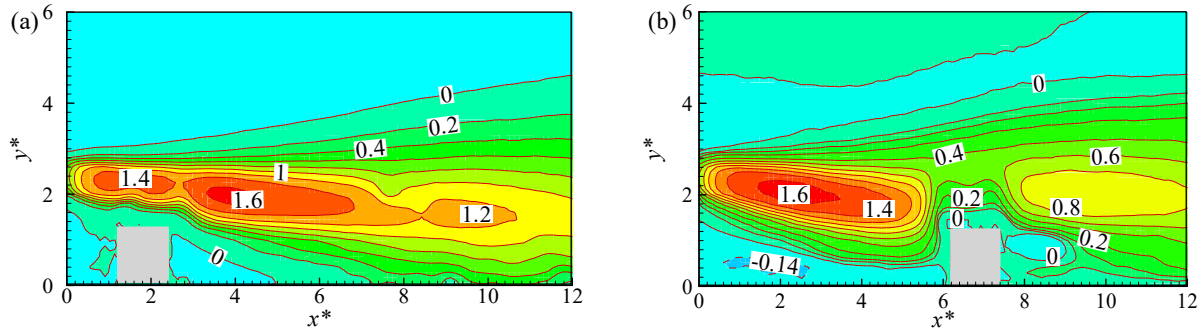

Figure B.2 Streamwise mean velocity contours for (a) $R1$ and (b) $R3$ ($x^* = x/b_o$; $y^* = y/b_o$).

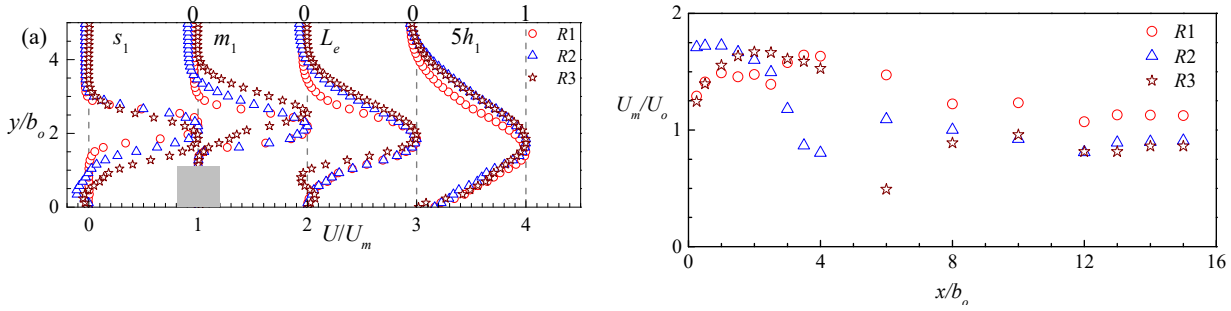

Figure B.3 Profiles of (a) U and (b) decay of U_m.

Turbulent kinetic energy and profiles of turbulence statistics

Figure B.4 shows contours of the turbulent kinetic energy (k) for $R1$ and $R3$, which was approximated as: $k = 0.75(\overline{u^2}+\overline{v^2})$, since the w component of the fluctuating velocity was not measured. Here u, v and w represent the fluctuating velocity component in streamwise, wall-normal and lateral directions, respectively. The peak value of k occurred at $x^* = 0.5$ for $R1$ and at $x^* = 12$ for both $R2$ and $R3$. The obtained peak values are larger than 0.032 reported by Kasagi & Matsunaga (1995) for a backward-facing step flow. The larger values can be attributed to the formation of a second recirculation region downstream of the ribs as well as enhanced mixing of the jets. In all test cases, k was diffused from the core region of the jet into the outer and inner shear layers. Large scale anisotropy was investigated by evaluating the ratio of $\overline{v^2}$ and $\overline{u^2}$ for the jets. Figure B.5 shows that at s_1, high levels of $\overline{v^2}/\overline{u^2}$ occurred at the edges of the jet. As the jet reattached, the ratio of $\overline{v^2}/\overline{u^2}$ decreased. Within the developing region of the flow, the presence of the wall dampened the wall-normal Reynolds normal stress leading to ratios of $\overline{v^2}/\overline{u^2}$ being less

than one close to the wall (Durao *et al*. 1991). Since the distribution of $\overline{v^2}/\overline{u^2}$ is less than one within the flow domain, it suggests that the Reynolds normal stresses are not equal within the early development of the jet. The present results suggest that the flow field of the offset jet is not isotropic.

The effect of rib location on the Reynolds shear stress, $-\overline{uv}$, and wall-normal transport of k and $-\overline{uv}$ are presented in Fig. B.6. Within the near field of the jets, the distribution of $-\overline{uv}$ profiles was anti-symmetric which is consistent with the orientation of the mean shear layer. Predominantly positive values of $-\overline{uv}$ were observed at s_1 for all the test cases (Fig. B.6a). Changing the rib location from $R1$ to $R2$ and $R3$ resulted in a 34% and 58% decrease in $-\overline{uv}$ values within the recirculation region, respectively. For $R1$, the Reynolds shear stress is significantly larger within the recirculation region compared to the reattached regions. The enhanced levels of the Reynolds shear stress within the recirculation region may be attributed to the predominantly large-scale structures generated due to the separation of the jet (Etheridge & Kemp, 1978). As a result of mixing and entrainment of the reattached jet, the maximum value of $-\overline{uv}$ decreased with streamwise distance in the case of $R1$. Levels of $-\overline{uv}$ increased for $R2$ and $R3$ at the reattachment point and then subsequently decreased beyond the reattachment point.

The triple velocity correlations are important statistics since their gradients constitute the turbulent diffusion terms in the turbulent kinetic energy and Reynolds stress budget equations. Thus, profiles of the triple velocity correlations can provide guidance to modelling the turbulent diffusion terms in these two transport equations. The triple velocity correlations reported are the transport of k (expressed as $\overline{u^2v} + \overline{v^3}$) and $-\overline{uv}$ (denoted as $-\overline{uv^2}$) in the wall-normal direction as shown in Figs. B.6(b) and B.6(c) instead of the conventional individual terms. The transport of k was predominantly positive for all test cases at s_1 and m_1 with $R1$ yielding the lowest peak value. The positive values suggest that the diffusion of k was largely from the core region of the jet into the outer shear layer. The transport of $-\overline{uv}$ shown in Fig. B.6(c) was also enhanced for $R2$ and $R3$ compared to $R1$. The enhanced transport of $-\overline{uv}$ for both $R2$ and $R3$ can be attributed to the dominance of large-scale structures which may have been as a result of the second recirculation region downstream of the rib.

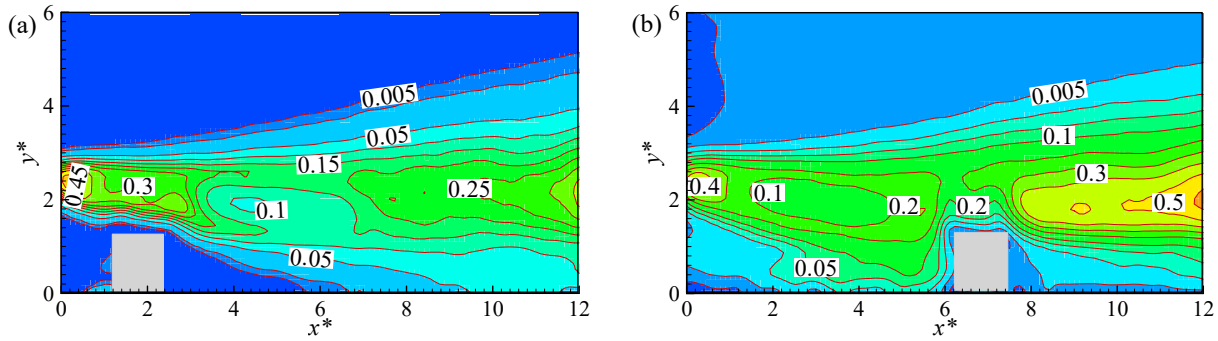

Figure B.4 Contours of k for (a) $R1$ and (b) $R3$.

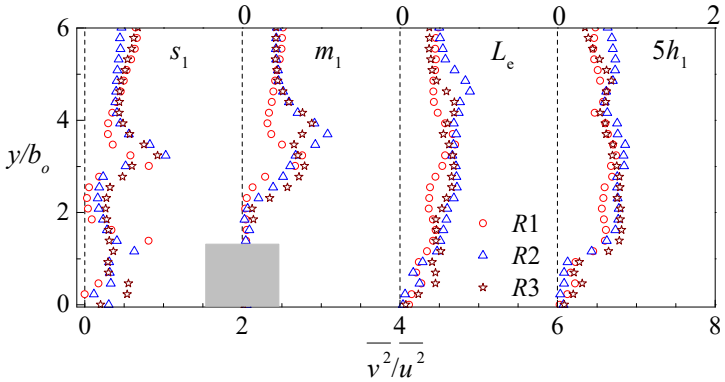

Figure B.5 Profiles of stress ratio for the various jets.

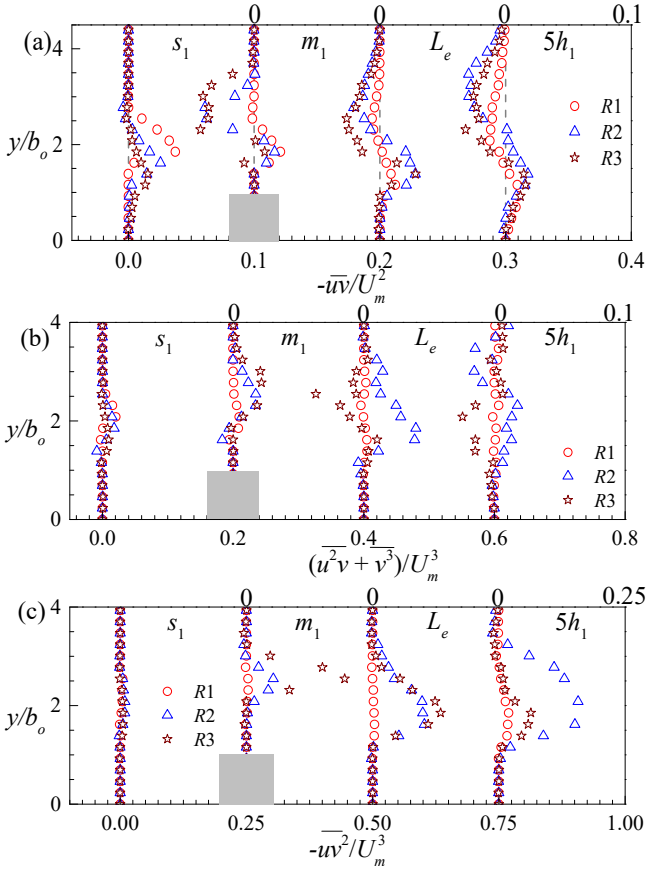

Figure B.6 Profile plots of (a) $-\overline{u}\overline{v}$ (b) wall-normal transport of k and (b) wall-normal transport of $-\overline{u}\overline{v}$.

Quadrant analysis

The quadrant analysis was used to decompose the active motions that contribute to the Reynolds shear stress. This involves investigating the relationship between the fluctuating velocity components, u and v and sorting them into four different quadrants with $Q1$ ($u > 0$, $v > 0$), $Q2$ ($u < 0$, $v > 0$), $Q3$ ($u < 0$, $v < 0$) and $Q4$ ($u > 0$, $v < 0$) representing the outward interaction, ejection, inward interaction and sweep events, respectively. Following the methodology proposed by Lu

and Willmarth (1973), the Reynolds shear stress at each grid point was decomposed into contributions from the four quadrants excluding a hyperbolic hole size, H as follows:

$$\overline{uv}_Q(x,y,H)=\frac{1}{N}\sum_{i=1}^{N} u_i(x,y)v_i(x,y)I_Q(x,y,H) \quad \text{(B.1)}$$

where N is the total number of instantaneous velocity vectors at each grid point and I_Q is the indicator function given by

$$I_Q(x\,y,H)=\begin{cases}1, \; when\ |u_i(x,y)v_i(x,y)|_Q \geq Hu'(x,y)v'(x,y)\\ 0\end{cases}$$

For the present analysis, a hole size, $H = 0$ was used. Contours of $Q1$, $Q2$, $Q3$ and $Q4$ are presented for $R1$ and $R3$ in Fig. B.7 and Fig. B.8, respectively. All four events contributed significantly to the production of Reynolds shear stress according to the orientation of the mean shear layer. In the case of $R1$, the relative peaks of the quadrant events were identical with values of -0.03, 0.05, -0.03 and 0.03 for $Q1$, $Q2$, $Q3$ and $Q4$, respectively. This means that $Q2$ and $Q4$ events contributed 62.5% and 37.5% towards the positive Reynolds shear stress. The result indicates dominance of the ejection events in the Reynolds shear stress production. Changing the location of the rib enhanced contributions from the various events towards the Reynolds shear stress, with peak values of -0.04, 0.08, -0.08 and 0.04 for $Q1$, $Q2$, $Q3$ and $Q4$, respectively as can be seen from Fig. B.8. The present results suggest that both interaction events are relevant to the production of Reynolds shear stress. It is interesting to note from Figs. B.7 and B.8 that the contribution from both $Q2$ and $Q4$ events to the total Reynolds shear stress close to the nozzle exit was not affected by changing rib location. However, beyond the reattachment point, a more pronounced contribution was observed for the ejection events compared to the sweep events. The ejection events contributed about 50% more towards the Reynolds shear stress compared to the sweep events beyond the reattachment point when the rib location was changed from $R1$ to $R3$. Changing the rib location from $R1$ to $R2$ and $R3$, respectively resulted in a 56% and 50% contribution towards the total $-\overline{uv}$ in $Q2$ quadrant. Profiles of normalized $Q1$, $Q2$, $Q3$ and $Q4$ were extracted at four x locations and presented in Fig. B.9. Similar to the contours, all four events contributed immensely towards $-\overline{uv}$. Predominantly larger values of $Q2$ and $Q4$ occurred within the recirculation region for both $R1$ and $R3$. However, contributions from $Q2$ and $Q4$ events decayed further downstream for $R1$. For example, the maxima of $Q2$ decreased by 51% at L_e compared to s_1. In contrast to $R1$, a much larger contribution from all four events occurred at the reattachment point and beyond in the case of $R3$. This can be attributed to the separation of the flow downstream of the rib. At the reattachment point, the peak of $Q2$ and $Q4$ occurred closer to the wall compared to $Q1$ and $Q3$. For example, in the case of $R1$, the peaks of $Q2$ and $Q4$ occurred at y/b_o = 1.42 and 1.15, respectively at the reattachment point. This was lower than y/b_o = 2.62 and 2.26 for $Q1$ and $Q3$, respectively. The present results revealed that the Reynolds shear stress distribution at any streamwise location is influenced by all four quadrant events.

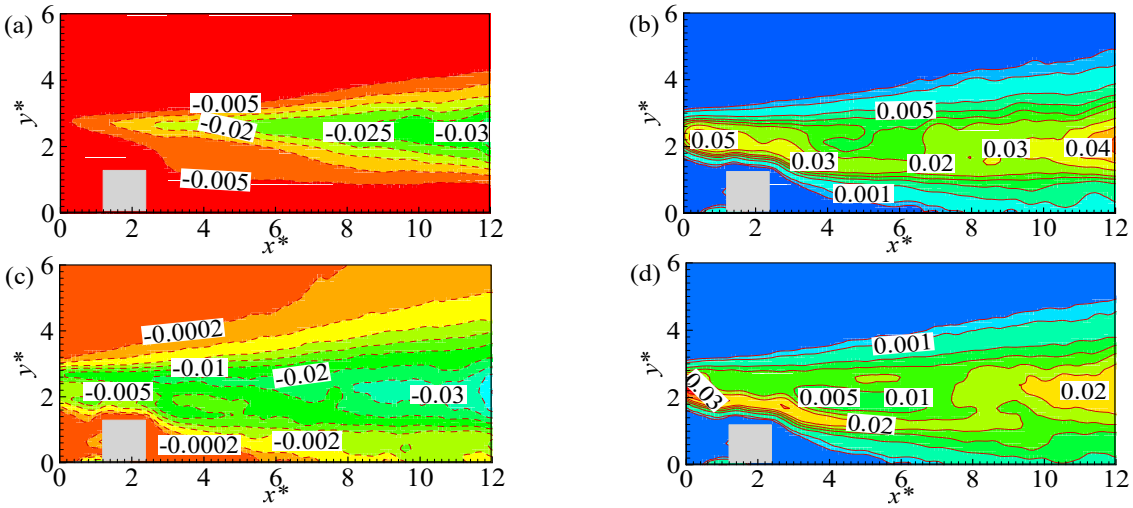

Figure B.7 Contours of (a) $Q1$, (b) $Q2$, (c) $Q3$ and (d) $Q4$ for $R1$.

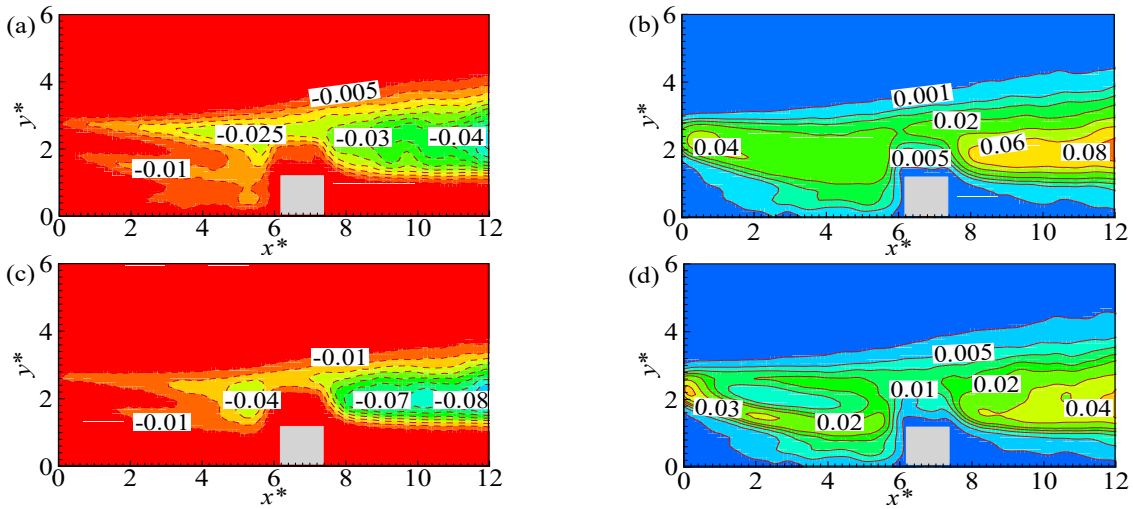

Figure B.8 Contours of (a) $Q1$, (b) $Q2$, (c) $Q3$ and (d) $Q4$ for $R3$.

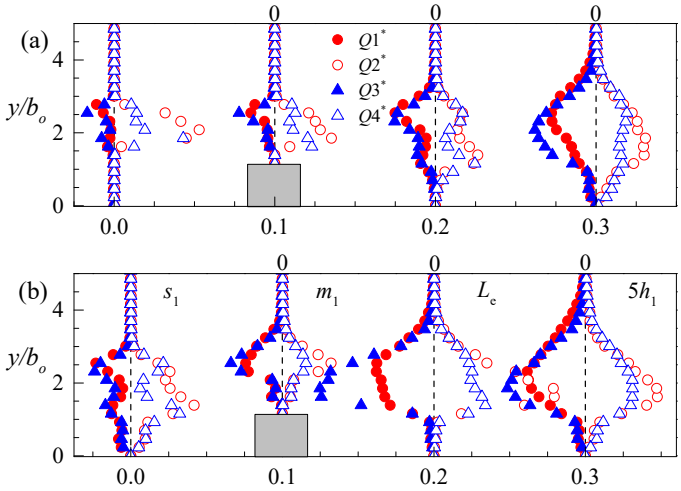

Figure B.9 Profiles of all four events for (a) $R1$ and (b) $R3$ at selected streamwise locations

Conclusion

A PIV technique was used to investigate the flow characteristics of 3D offset jet flow over surface mounted rib. The experiment was conducted for an offset jet with offset height ratio of 2. The square rib was mounted at three different streamwise locations, $1.25b_o$, $3.45b_o$ and $6.25b_o$ represented herein as $R1$, $R2$ and $R3$, respectively. These locations corresponded to streamwise distances within the recirculation region, mean reattachment point and developing region of the flow, respectively. Contour plots of U revealed that the offset jet accelerated upon discharge as a result of the vena-contracta effect. The distribution of U also revealed enhanced spreading of the jet with increasing rib location. Changing the rib location from $R1$ to $R2$ and $R3$ resulted in a rapid decay of the maximum streamwise mean velocity of the discharged jet. The placement of the rib affected the reattachment length of the discharged jet with reattachment lengths of $4.75b_o$, $7.05b_o$ and $8.60b_o$ recorded for $R1$, $R2$ and $R3$, respectively.

The turbulence statistics (such as k, $-\overline{uv}$ and the triple velocity correlations), were influenced by the rib location. The Reynolds shear stress within the recirculation region of the flow decreased by 34% and 58%, respectively, when the rib location was changed from $R1$ to $R2$ and $R3$. Profile plots of the triple velocity correlations indicated that $-\overline{uv}$ was largely transported from the core region of the jet into the outer shear layer. A quadrant analysis was used to decompose the contribution of the active motions towards $-\overline{uv}$. The analysis revealed significant contributions from all four quadrant events. However, the ejection event was the dominant event in all test cases. Changing the rib location from $R1$ to $R2$ and $R3$ resulted in 56% and 50% contribution by the ejection event towards the total $-\overline{uv}$, respectively.

References

Agelinchaab, M., and Tachie, M. F., 2011, "Characteristics of turbulent three-dimensional offset jets", *Journal of Fluids Engineering*, Vol. 133, pp. 051203-1-9.

Antonia, R. A., Browne, L. W., Bisset, D. K., and Fulachier, L., 1987, "A description of the organized motion in the turbulent far wake of a cylinder at low Reynolds number", *Journal of Fluid Mechanics*, Vol. 184, pp. 423-444.

Bhuiyan, F., Habibzadeh, A., Rajaratnam, N., and Zhu, D. Z., 2011, "Reattached turbulent submerged offset jets on rough beds with shallow tailwater", *Journal of Hydraulic Engineering*, Vol. 137, pp. 1636-1648.

Durao, D., Gouveia, P., and Pereira, J., 1991, "Velocity characteristics of the flow around a square cross section cylinder near a channel wall", *Experiments in Fluids*, Vol. 350, pp. 341-350.

Etheridge, D. W., and Kemp, P. H., 1978, "Measurements of turbulent flow downstream of a rearward-facing step", *Journal of Fluid Mechanics*, Vol. 86(3), pp. 545-566.

Kasagi, N., and Matsunaga, A., 1995, "Three-dimensional particle-tracking velocity measurement of turbulence statistics and energy budget in a backward-facing step flow", *International Journal of Heat and Fluid Flow*, Vol. 16, pp. 477-485.

Lu, S. S., and Willmarth, W. W., 1973, "Measurement of the structure of the Reynolds stress in a turbulent boundary layer", *Journal of Fluid Mechanics*, Vol. 60(3), pp. 481-511.

Nasr, A., and Lai, J. C. S., 1998, "A turbulent plane offset jet with small offset ratio", *Experiments in Fluids*, Vol. 24, pp. 47-57.

Nyantekyi-Kwakye, B., Clark, S., Tachie, M. F., Malenchak, J., and Muluye, G., 2015, "Flow characteristics within the recirculation region of 3D turbulent offset jet", *Journal of Hydraulic Research*, 53(2), 230-242.

Pelfrey, J. R. R., and Liburdy, J. A., 1986, "Mean flow characteristics of a turbulent offset jet", *Transactions of the ASME*, Vol. 108, pp. 82-88.

Appendix C

Reconstructed POD modes for the offset jets

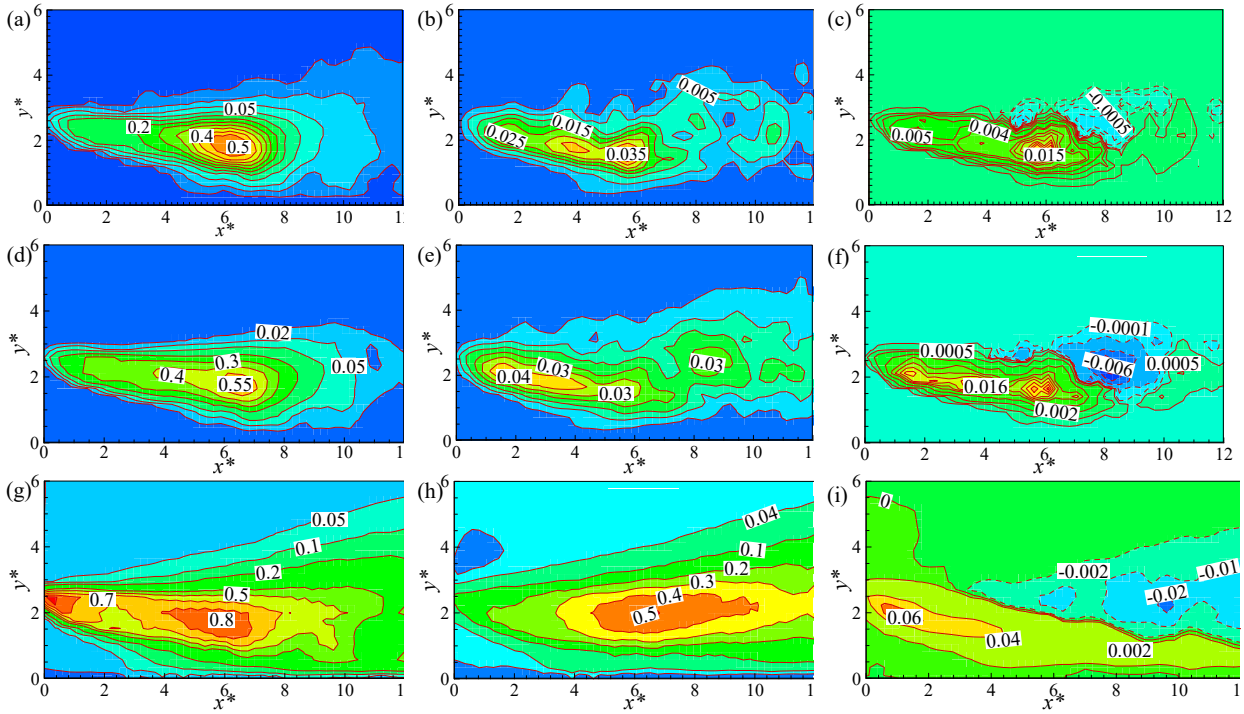

Figure C.1 Contour plots of u', v' and $-\overline{uv}$ for mode 1 (a - c), mode 2 (d - f) and PIV data (g - i), respectively for $h/b_o = 2$ offset jet

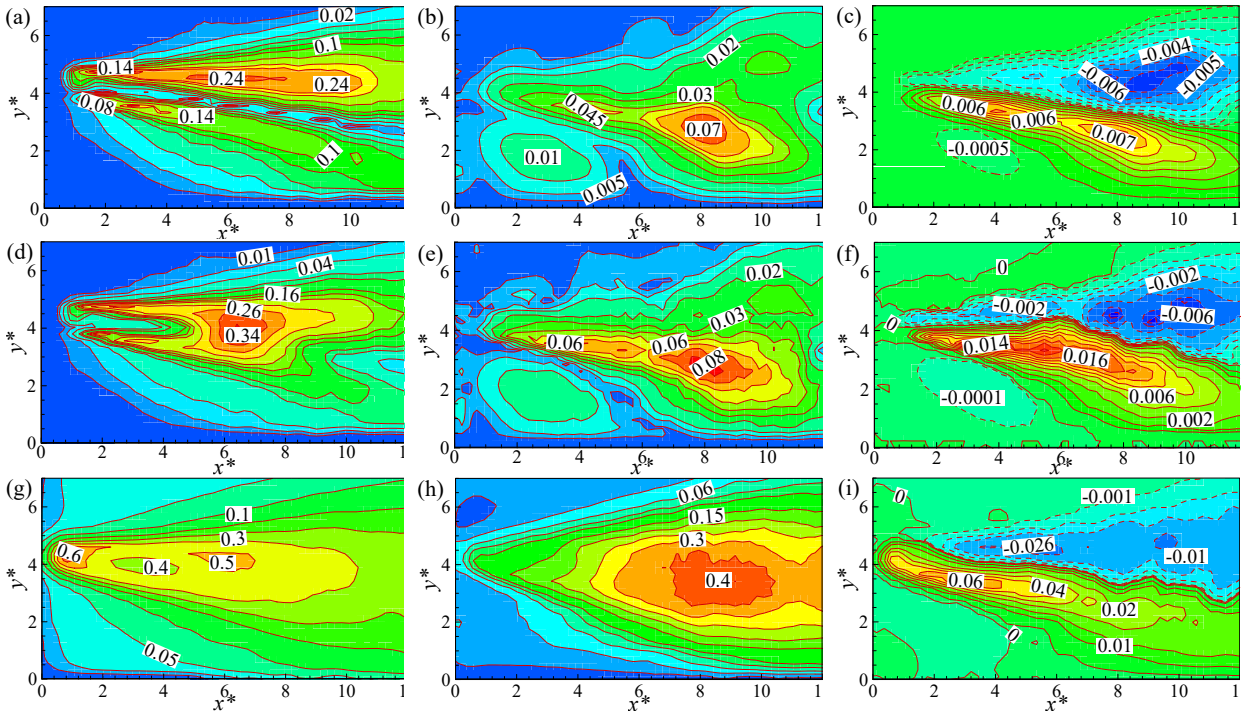

Figure C.2 Contour plots of u', v' and $-\overline{u'v'}$ for mode 1 (a - c), mode 2 (d - f) and PIV data (g - i), respectively for $h/b_o = 4$ offset jet